UNIVERSITA' DELLA CALABRIA

Dipartimento di Chimica e Tecnologie Chimiche - CTC

Dottorato di Ricerca in

Scienze e Tecnologie Fisiche, Chimiche e dei Materiali (STFCM)

Con il contributo di

Regione Calabria - POR FSE/FESR 2014 – 2020

CICLO

XXXV

Nanofillers doped buckypaper membranes for highly enhanced recovery of pollutants from wastewater

Settore Scientifico Disciplinare CHIM/02

Coordinatore: Ch.mo Prof. Gabriella Cipparrone

Firma Firma oscurata in base alle linee guida del Garante della privacy

Supervisore/Tutor: Ch.mo Prof. Giovanni De Filpo

Firma Firma oscurata in base alle linee guida del Garante della privacy

Dottoranda: Dott.ssa Mariafrancesca Baratta

Firma oscurata in base alle linee guida del Garante della privacy

“La borsa di dottorato è stata cofinanziata con risorse del Programma Operativo Regionale Calabria FSE/FESR 2014 – 2020 (CCI 2014IT16M2OP006)”

TABLE OF CONTENTS

Abstract

L'acqua è un bene prezioso, fonte di vita sulla Terra. Sin dalla notte dei tempi, questa minuscola molecola fatta di soli due elementi e tre atomi, ha assistito all'alternarsi di ere geologiche, ha conosciuto epoche e visto lo sviluppo e il declino di civiltà che attorno all'acqua hanno costruito la loro ricchezza e il loro sostentamento. Dall'acqua dipende la vita e attorno all'acqua si è costruita la vita. L'idea che questa risorsa naturale sia sempre stata presente sulla Terra ha fatto credere per molto tempo che essa sia una fonte inesauribile, a cui tutti possono accedere illimitatamente per soddisfare i propri bisogni. Tuttavia, se fino al secolo scorso, il rapporto tra la domanda e l'offerta si è mantenuto pressoché unitario, con l'avvento della civiltà moderna e, dunque, con lo sviluppo economico che ciò ha comportato, si è assistito a un progressivo aumento della disuguaglianza tra questi due termini, con il primo, quello della domanda, che è letteralmente schizzato alle stelle. La richiesta d'acqua da parte della popolazione mondiale, che attualmente ammonta a 8 miliardi, per il soddisfacimento dei propri bisogni quotidiani ha portato, nel corso degli anni, a un enorme consumo di questa risorsa, senza però che la Terra ricevesse nel frattempo un efficiente ricambio di acqua pulita. Non solo, infatti, il consumo d'acqua è notevolmente aumentato, e le risorse del pianeta nel frattempo sono rimaste pressoché uguali, ma gran parte di questa grossa quantità di acqua è stata sprecata e costantemente inquinata. Inquinata da quella stessa popolazione che ne fa domanda, attraverso il rilascio improprio di rifiuti provenienti dagli impianti di scarico di attività connesse con il sostentamento della vita umana, in primis quelle industriali. Stando a quanto riportato dall'ONU all'Assemblea Generale delle Nazioni Unite del luglio 2010, l'acqua è un diritto umano universale e a tutti deve essere garantito l'accesso all'acqua potabile, al fine di prevenire l'insorgere di malattie infettive. Pratiche di igiene e sanificazione sono dunque necessarie e obbligatorie per rimuovere gli inquinanti presenti nelle acque, prima che queste vengano nuovamente introdotte sulla superficie terrestre e giungano poi sulla nostra tavola. A seguito della notevole diversificazione delle attività antropogeniche, gli inquinanti comunemente rinvenuti nelle acque sono molteplici. Si annoverano

coloranti, pesticidi, metalli pesanti, farmaci e organismi patogeni come batteri e virus. Accanto a queste "molecole", una grossa fonte di inquinamento è poi rappresentata dalla presenza di plastiche, il cui consumo negli ultimi decenni è cresciuto in maniera esponenziale.

Il seguente lavoro di tesi si propone di sviluppare delle nuove membrane a base di nanotubi di carbonio (CNTs) da impiegare nella rimozione di inquinanti dalle acque mediante processi di fotocatalisi o di assorbimento. Le membrane a base di CNTs, anche note come *buckypapers*, si presentano come dei fogli sottili, perfettamente autosostenuti, in cui i CNTs sono assemblati formando una vera e propria rete. Le prestazioni di tali membrane dipendono molto dal tipo di CNTs utilizzati (SWNTs o MWNTs); in generale, però, a differenza delle membrane polimeriche attualmente in commercio, esse sono stabili anche ad alte temperature, sono inoltre flessibili, presentano una buona stabilità chimico-fisica e una buona conduttività elettrica. Al fine di migliorare le loro performances, tali membrane sono state dopate con opportune nanoparticelle, introdotte allo scopo di incrementare selettivamente il recupero dei seguenti inquinanti: piombo e cerio, per quanto concerne la categoria dei metalli pesanti, e, per la categoria dei farmaci, le molecole di diclofenac, ketoprofene e naprossene, tutte comunemente impiegate come antinfiammatori. Nell'ottica della degradazione di inquinanti mediante processi fotocatalitici, sono state inoltre sviluppate nuove membrane composite della forma semiconduttore/buckypapers, in cui questi ultimi espletano la funzione di supporto a uno strato fine di semiconduttore depositato sulla loro superficie. In tal caso, una nuova applicazione nella degradazione di coloranti e antinfiammatori è stata rinvenuta per tali membrane, le quali hanno mostrato delle ottime efficienze di rimozione per gli inquinanti investigati.

Introduction

"The earth, the air, the land and the water are not an inheritance from our forefathers but on loan from our children. So we have to hand over to them at least as it was handed over to us." - Mahatma Gandhi

"Water is essential to life. It need not be spelt out exactly how important it is. Yet water pollution is one of the most serious ecological threats we face today." – WWF

Water is a precious resource and access to water is officially recognized as a universal human right. Its ubiquity on the planet, in the form of lakes, seas, glaciers, rain, rivers, has led humanity to believe that this natural resource is practically unlimited. The rising demand for water coming from the entire world's population is responsible for the exponentially increasing that water consumption has experienced over time, with the last decades, in concomitance with the beginning of the third industrial revolution, contributing in a substantial way to this brutal escalation. The aims of progress and development carried out by modern society through the fulfilment of anthropogenic activities necessarily prevailed and this natural resource, even if it must be preserved precisely as being a resource, has been wasted and polluted over the years. Today humanity has to deal with the consequences arising from this excessive, uncontrolled and unrestricted use of water. First, water is not unlimited: even if Earth surface is prevalently covered by water, the amount of fresh water immediately available is slightly less than 2%, a few percent considering that 8 billion people demand for water each day. Second, water is full of pollutants, such as heavy metals, dyes, pesticides, pharmaceuticals, exhibiting different levels of toxicity to human health. This means that separation and purification technologies are required to remove contaminants from water, before entering the environment once more. Currently wastewater treatment technologies for pollutants removal from water are often known with the acronym WWTPs, standing for wastewater treatment plants. These systems are often older, designed more than 30 years ago, thus failing in the complete removal of contaminants, especially those discovered very early and grouped under the

name of emerging contaminants (ECs). Moreover, the removal of these contaminants often requires more appropriately and specific treatment technologies leading to a major processing cost, which industries and owners of WWTPs are not always willing to pay. Nevertheless, water pollution is an environmental growing concern and cannot be avoided anymore.

This project, titled "*Nanofillers doped buckypaper membranes for highly enhanced recovery of pollutants from wastewater*", aims to develop new carbon nanotubes-based membranes, called buckypapers (BPs), opportunely doped with different types of nanofillers, such as graphene oxide or metal organic frameworks, to improve their separation performances. After a detailed physico-chemical characterization, the as prepared membranes were tested for the removal of several pollutants from water, including heavy metals, dyes, and pharmaceuticals, by adsorption processes. Considering great removal efficiencies reached in advanced oxidation processes (AOPs), buckypapers were also employed as support for the deposition of a thin layer of photocatalyst, such WO_3, and tested in water purification treatments by photocatalytic processes.

In order to better explain the aim of the project, the present dissertation has been structured in two sections, *Theoretical* and *Experimental Part*, and 10 chapters, five for each section. *Theoretical Part* has the objective to provide a general framework on water pollution. Starting from Chapter 1, focused on the description of contemporary water crisis and contaminants commonly found in wastewaters, including legislations currently in force worldwide, the discussion continues in Chapter 2, where a detailed overview of wastewater treatment technologies is provided. Chapter 3 is largely devoted to membranes and carbon nanotubes membranes, the core of this project, presenting the state-of-art of this field up to the latest developments. Chapter 4 and Chapter 5 briefly describe techniques employed in membrane characterization and theory of adsorption, respectively, both fundamental in the designing of high-performance membranes. Finally *Experimental Part*, to which Chapter 6 to Chapter 10 are dedicated, presenting the scientific work in its entirely, from the

preparation of buckypaper membranes and nanofillers doped BPs up to results obtained for pollutants removal from water by adsorption and photocatalytic processes. Except for Chapter 6, providing a detailed description of contaminants investigated in this project, scientific publications are directly attached in the subsequent chapters. The structure in chapters is due to the organization of scientific publications for BP typology (BP-MOF and BP-GO) and treatment technology employed (adsorption or photocatalysis). Lastly, considering the enormous environmental threat arising from microplastics (MPs) in aquatic systems, a comprehensive review on sources, accumulation, impact, and removal technologies of MPs is also included in Chapter 10.

Chapter 1

1.1 Water pollution: a real time problem

Water is essential to life. This is a fact, without any doubt. If there is something in our life of which every living being can be sure, this is certainly the fact that its live depends on a constant and continuous supply of water. Fresh, clean, uncontaminated water, to be exact.

Today, the importance of water in everyday life is not only a scientific consideration. With the Resolution 64/292, approved by the United Nations General Assembly in July 2010, ONU establishes that water and sanitation are universal human rights and recognizes also the importance of clean drinking water and sanitation for the realization of all human rights [1]. As a matter of fact, in November 2002, with the *General Comment No. 15* adopted on the right to water, the Committee on Economic, Social and Cultural Rights had already drawn attention about the importance of "sufficient, safe, acceptable and physically accessible and affordable water for personal and domestic uses" to everyone [2]. The difference is that Resolution introduces an important correlation: it is not only the right to water, but also the most reliable right to sanitized water, on which life on the planet undoubtedly depends.

From the beginning of XIX century, with the advent of industrialization and urbanization phenomena and the development of more profitable human activities, the demand for water, for industrial and domestic purposes, which was always contained up to that time, has experienced a remarkable surge to meeting growing human needs, without too much attention on concept such as waste or contamination. This has inevitably brought to an excessive, unscrupulous and unrestrained use of water and consequently to a waste of this important natural resource. Reason why today humanity has to face up with which are the consequences of this "wicked behaviour": a) How much water can Earth supply in real time? Is it sufficient to satisfy actual human needs? b) Can this water supply be effectively used for industrial and domestic purposes?

From a technically point of view, in reference to question a), the amount of water of the Earth today is the same of many years ago, the same of many

centuries ago. Earth is rich in water, especially considering that 70% of terrestrial surface is entirely covered by this natural resource. The problem, the real problem relies in the abundance of fresh water, which is the water of which humanity really needs. Of the totally amount of water currently available on Earth, only a short percentage, 2%, can be counted as fresh water while the remaining 98% is seawater, impossible to use because of the presence of salt in it. This becomes more problematic when one considers that only 0,036% of fresh water, which is already an insignificant slice of this "water pie", is available and accessible for use. The residual 1,96% is trapped in polar ice caps, aquifers, and underground wells, not always easy to access. It is estimated that, only for Mediterranean Region, the water demand, which was around 280 km^3/year in 1990, has increased of nearly 50% in the last 25 years, with a water consumption which if it was equal to 357 km^3/year in 2010, it is estimated to reach 500 km^3/year by 2025 [3]. Constant access to Earth "blue water" (fresh surface water and groundwater) is strictly dependent on availability of this natural resource, but during last years climate changes and unqualified social and economic politics have affected negatively on it bringing to light the most alarming problem of water scarcity. Mekonnen and Hoekstra (2016) estimated that today four billion people live in areas characterized by physical water scarcity at least one month per year [4]. The study, which monitors the water monthly availability through the monthly blue water scarcity index (WS), clearly evidences that regions affected by high water scarcity are those characterized by high population density (China, India, Greater London), presence of too much irrigated agriculture (High Plains in the United States) or both (eastern China, Nile delta, India). Last but not least, it must also be added to the list those regions (Gobi, Taklamakan, Sahara, Central Australia deserts) which have already a low water availability for natural circumstances (*Fig. 1*).

Thus, if on the one hand water scarcity comes forward, on the other it must be considered that fresh water sources, even where they are available, cannot always be used because of a large presence of pollution, which is absolutely a danger for human life. It is legitimate to ask where water pollution comes from.

The great amount of contaminants found in water is totally due to domestic, agricultural, and industrial activities, too often focused on profit and not enough interested in environment preservation. As a result, the same activities which contributed to waste this natural resource are those which today pay the worst consequences. And the world population, too. One of the last estimation reports in fact that around 80% of the world population has to cope with problems of water supply and water sanitation today [5]. Concerning water sanitation, actually 2.1 billion people live without safe drinking water at home [6]. It is clearly evident that a change of direction is required, hoping a strict collaboration between government, human and industrial authorities to promote policies turned to safeguard this precious resource. In 1746, Franklin wrote "When the Well's dry, we know the worth of water". Now more than ever these words are the truest ones anyone can read.

Before dealing with a problem and suggesting a solution, it is necessary to investigate its causes and to understand its origin. Therefore, in order to evaluate and understand what water pollution is, next paragraph is entirely dedicated to the identification and description of pollutants actually found in water, pointing out what are the major threats for human health resulting from unsafe water.

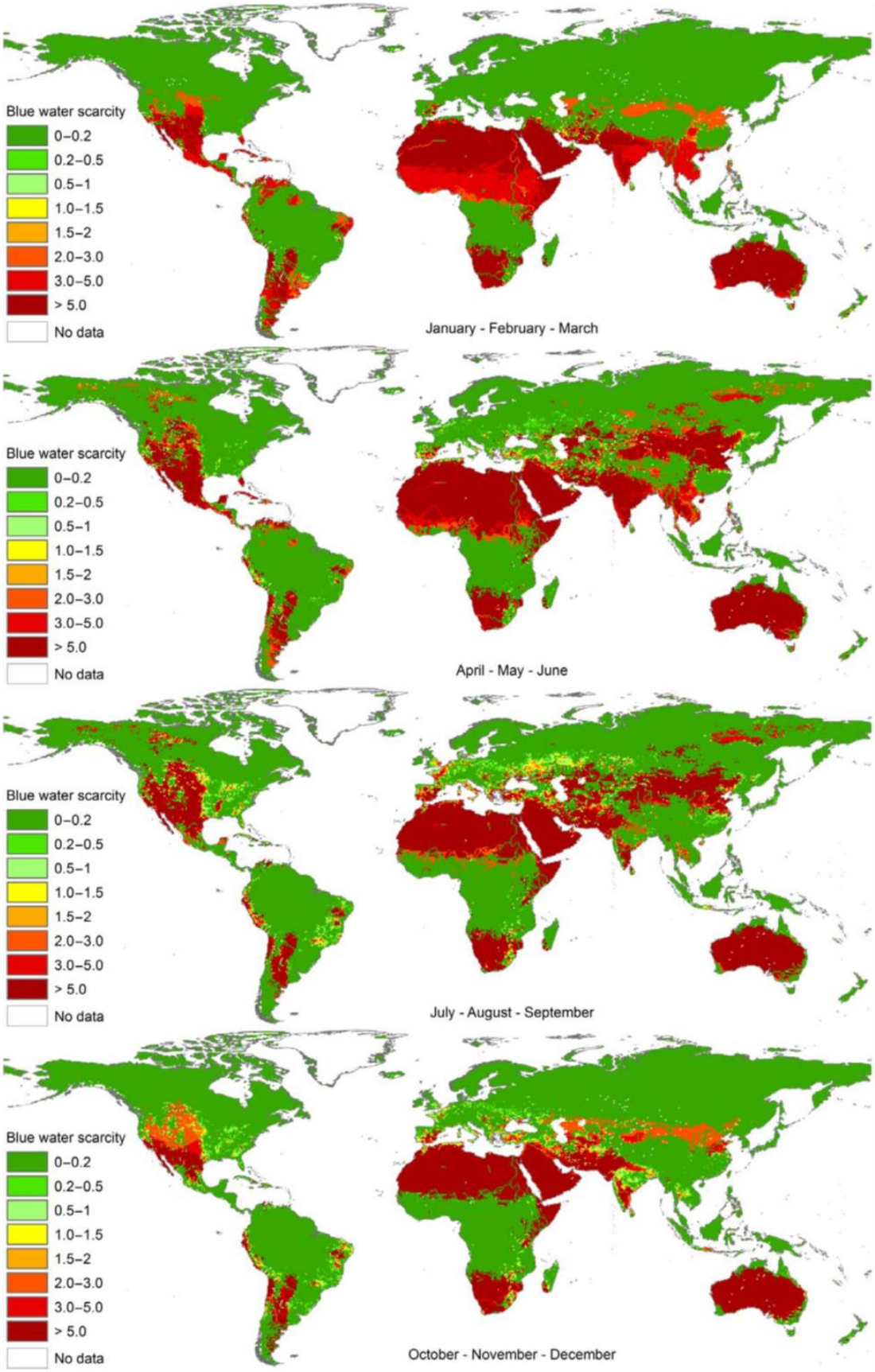

Fig. 1. Monthly blue water scarcity (1996-2005). *Source: M. M. Mekonnen and A. Y. Hoekstra, Sci. Adv., 2016, 2, e1500323..*

1.2 Water contaminants: classifications, sources and human health potential adverse effects

Where does water pollution come from? (*Fig. 2*) Anthropogenic activities are the primarily responsible for water contamination, releasing every day a lot of pollutants directly into the environment. Another large contribution originates from municipal discharges, with wastewater treatment technologies being often obsolete and thus failing the process of sanitation and purification. The wide plethora of organic and inorganic pollutants which can be currently found in water includes dyes and pigments, plastics, heavy metals, pharmaceuticals, and pathogens. A comprehensive description of these classes of pollutants is provided below.

Fig. 2. Main sources of water pollution.

1.2.1 Dyes and pigments

Because of their widespread use, dyes and pigments can count today on a global market of millions of dollars. 26.53 billion of dollars was the market value in 2017, but this sum is set to increase in the next years [7]. Similar onerous numbers are those of waste: $7x10^7$ tons of synthetic dyes are produced annually worldwide, of which 10,000 tons come entirely from textile industry and more than 80% are azo dyes [8]. Use of pigments and dyes is now completely included in many industrial production cycles involved in several sectors such as paints, printing inks, coatings, paper and textiles, plastics, glass, construction and automotive, food and cosmetics. Compounds belonging to the group of pigments and dyes, including synthetic dyes, are very large in number, reason why different types of classifications were proposed over the years according to their source, chemical structure, color, solubility, and application methods. Even if the classification based on chemical structure is the most suitable because of its uniqueness, it must also be considered that colorants are complex molecules and IUPAC names are very long and often difficult to remember. Classification based on application methods is therefore preferred, counting on a better ease of identification of these compounds through those properties which allow them to be used in one process or another [7]. *Fig. 3* shows briefly how dyes and pigments are classified according to their chemical structure and application methods. Colorants applied in food and cosmetics [9] are subjected to a strict legislation because of their direct contact with human health. Food industry has built an empire on these compounds considering that the appearance of the food, especially in terms of its color, plays an important role in the capacity to attract the consumer to consume. It has been shown that food or beverage color can influence the flavor perception, in fact [10]. Natural colorants are the most used in this sector, being the ones considered harmless or even healthy. In this direction, plant pigments like chlorophylls, betalains, anthocyanins and carotenoids are the new emerging class of food colorants because of their beneficial effects on human health as antioxidants [11]. Regarding to cosmetics, the picture is not so favorable. Even if serious health hazards have been rarely associated with cosmetic products, colorants used in this sector are

not always harmless, some of these suspected to be carcinogenic or with long-term effects. Instead, skin irritations and allergic reactions, such as rashes and contact dermatitis, are effects much more reported, proving that dyes and pigments in these products are less healthy than many people would believe [12].

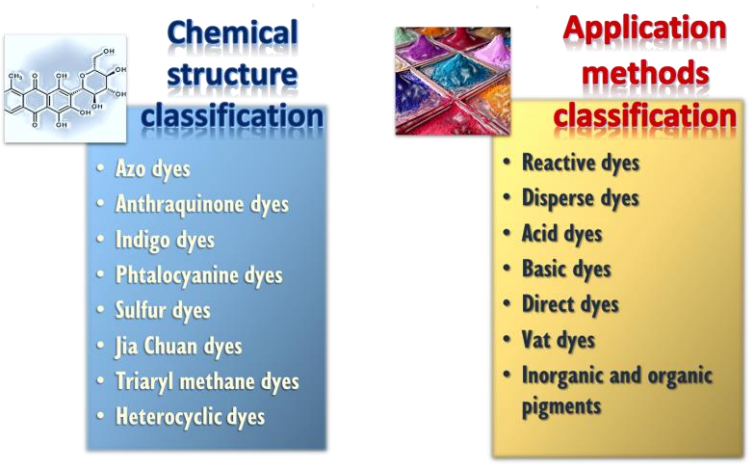

Fig. 3. Dyes classifications according to chemical structure and application methods.

The major concern associated with dyes and pigments comes from manufacturing sector, leaded by textile industries, which discharges effluents full of colorants directly in water and in the environment [8]. Even if a legislation exists and requires that effluents must not contain colorants before their disposal, it is also true that it is often circumvented because treatment technologies needed to remove colorants are missing or, where they are adopted, they are inadequate. Water pollution caused by dyes and pigments can bring to a lot of detrimental effects. Colorants, also detectable in small concentrations (less than 1ppm) due to their brilliance, can absorb and reflect the sunlight in the water, reducing the amount of light entering the photic zone of the aquatic environment. Photosynthetic activity of algae decreases, plant flowering and germination change, influencing the entire food chain and causing eutrophication [13]. Negative effects have been observed in most living organisms [8]. Genotoxic effects and diseases to the immune system have been reported for fishes. Concerning human health, dyes and pigments can be responsible of less negative effects such as dermatitis, skin and eye irritation, up to the most harmful ones like problems to the central nervous system,

ovulation and spermatogenesis interference and carcinogenesis. Degradation of dyes and pigments promoted by water treatment technologies as chlorination or anaerobic digestion can lead to the origination of aromatic amines, known for their mutagenic potential and therefore harmful for human health [14]. This phenomenon needs also to be monitored in order to prevent negative effects coming from what would be thought to be a solution to colorants removal from water.

1.2.2 Emerging contaminants (ECs)

Emerging contaminants (ECs) class is very large and includes all chemicals compounds characterized by low concentrations in water, from ng/L to µg/L [15]. These emerging contaminants are not new, probably their occurrence in water is the same of other pollutants. However, they are referred as emerging contaminants because their discovery in water is relatively recent, made possible by the development and improvement of new analytical techniques able to detect compounds even at low concentrations or trace levels (ng/L). Although their potential negative impacts on human health and environment have been reported, ECs detection drives too fast, so many compounds still remain out of a regulatory legislation or are actually under a regularization process. Emerging contaminants class includes pharmaceuticals, personal care products, pesticides and disinfection byproducts, all belonging to the group of EDCs, endocrine disrupting compounds.

Pharmaceuticals or Pharmaceutically Active Compounds (PhACs) are considered one of the categories of greater concern [16]. Their occurrence in water is due to different sources [17]: landfill leachates, hospital effluents, industrial and domestic wastewater not sufficiently and properly treated. Human assumption of pharmaceuticals is undoubtedly accountable for the largest release of PhACs into water. After their assumption, pharmaceuticals are metabolized by human body and can be transformed in glucuronide or sulfate conjugates or can be subjected to hydrolysis, oxidation, reduction or alkylation reactions. After the metabolization process, PhACs are excreted via bile or urine in the form of more polar and hydrophilic metabolites, even if the occurrence of the pristine

pharmaceutical in a little percentage cannot be excluded. Pharmaceuticals from veterinary medicine and those coming from intensive livestock farming represent the other common pathway through which PhACs enter the water. Whatever the release source, it has been shown that common wastewater treatment plants (WWTPs) are often unable to remove PhACs due to their complex molecular structure and low concentrations in water [18–21], with a maximum removal percentage of 10% in the worst cases. Antidepressants, antibiotics, anti-inflammatories, analgesics, antacids, antipyretics, hormones, lipid-lowering, beta-blockers, stimulants, drugs, tranquilizers and steroids are the most common pharmaceuticals found in water treatment effluents. Therefore, even if pharmaceuticals occurrence in water cannot be avoided because current wastewater treatment technologies are not sufficient, it must also be said that there are not too many concerns about PhACs in water. Effluents from farms are often released into surface water without any treatment while animal excrements, feces especially, are usually used in agriculture as fertilizers, directly damaging the food chain in this way. Pharmaceuticals are developed to treat and prevent human and animal diseases, reason why they have to be biologically active and persistent in the organism enough time to exhibit their therapeutic effect. However, these imperative properties are at the same time the reason for which PhACs removal from wastewater is difficult. It has been shown that many pharmaceuticals can mimic the activity of endogenous steroid hormones by inducing similar hormonal responses [19,21,22]. Many of them are classified as endocrine disrupting compounds because they can interfere and block endocrine systems in humans. Serious consequences such as diabetes, endometriosis, obesity, abnormal reproductive growth and cancer can be caused by this alteration of endocrine systems [23]. Another evidence shows that a mixture of therapeutic drugs can inhibit human embryonic cell growth [24]. In fact, drugs as naproxen, sulfamethoxazole and erythromycin can persist for more than one year in the environment while this time can be longer in the case of clofibric acid. One of the major risks associated with pharmaceuticals is that antibiotics occurrence can bring to antibiotic resistance genes (ARGs) and antibiotic resistant bacteria

(ARB) [25–27], with the consequence that their therapeutic potential towards human and fauna pathogens can be reduced or even suppressed. Another aspect often underestimated is represented by the huge number of new transformation products, produced by metabolization processes of pharmaceuticals in living organisms, whose toxicity is not always known or investigated.

Sunscreens, disinfectants, antifungal agents, fragrances and insect repellents are all classified as personal care products (PCPs) [28,29]. Being designed for external use only, PCPs main difference with pharmaceuticals resides in the fact that the formers are not subjected to metabolization processes. However, on the other hand, personal care products are released in the environment in huge quantities, reaching surface waters without any difficulty, especially by wash-off during bathing or showering. Recent studies have shown that PCPs are bioactive, persistent and can bioaccumulate [30,31]. Considering the major threat coming from pharmaceuticals, personal care products are not often investigated and little is known about their toxicity. A preliminary hazard assessment about potential chronic toxicity has been found for triclosan and triclocarban, two biphenyl ethers used as antimicrobials in deodorants, soaps, toothpaste, skin creams and plastics [29].

The exponential rise in food demand during the last century has forced agriculture to increase crop yields of huge quantities. To achieve this goal and ensure the complete yield of each single crop without economical waste, agriculture has begun to use pesticides [32], chemicals which led to a better control of pests and diseases, by reducing insect-borne diseases (encephalitis, filariasis, malaria, dengue, etc.) in the human health sector. Nonetheless, these compounds are often released in the environment without any care, consequently enriching surface waters. In spite of agriculture being the main source of pesticides in water, these chemicals have been also found in WWTPs whose origin, instead, comes from applications in public health (rodent-control areas, mosquito-abatement districts and aquatic areas), in grass-management (educational facilities, cemeteries, golf courses and parks), in and in non-

agricultural crops (horticulture, plant-nurseries and commercial forestry) and in industrial vegetation control (electric utilities, industrial facilities, roadways, pipelines and railroads) [33]. Literally, the term pesticide is a contract name and indicates all compounds able to kill living organisms. Considering this definition, pesticides include fungicides, herbicides and insecticides. Because they are designed with the objective of killing living organisms, pesticides are biologically active substances and, therefore, exhibit variable levels of toxicity for humans. Human exposure routes to pesticides include inhalation, ingestion and dermal contact. It has been shown that prolonged or acute exposure can cause neurobehavioral disorders, immunosuppression and autoimmune diseases, allergy, myoglobinuria, reproductive abnormalities such as mal-descent of testes, spermatogenetic dysfunction and malformations of penis, leukemia and cancer (malignant lymphoma, multiple myeloma) [34–36].

Current water disinfection processes employ sanitizers to remove or inactivate pathogens from water and avoid water-borne diseases in order to achieve the quality parameters required for a safe drinking water consumption. Among them, chlorine and chlorine-based disinfectants are the most common and widely used thanks to their economy of operation, convenience, taste improvement, persistence in the distribution network and high efficiency towards many pathogens. Disinfection byproducts (DBPs) represent a side effect of these treatments since these substances originate from the reactions between natural organic matter (NOM), contained in waste and raw water, and inorganic ions (chlorine, bromide and iodide), of which disinfectants are made [37,38]. Being more specific, DBPs formation depends on different factors, including wastewater composition (NOM, pesticides, pharmaceuticals etc.) and water treatment operational parameters such as temperature, pH, contact time and disinfection agent type and concentration. The first DBP to be identified was trichloromethane, in 1974, and since then a lot of epidemiologic studies have been done to evaluate human health risks resulting from DBPs exposure. What is clearly observed is that iodinated DBPs are generally more carcinogenic than their brominated analogues, which are in turn more toxic than the

chlorinated ones [39]. Increased incidences of pregnancy abnormalities and cancer to bladder and colorectal have been related to consumption of disinfected drinking water [39]. Recent studies have paid attention to new emerging DBPs, such as iodo-acids, iodo-trihalomethanes, halofuranones, halonitromethanes, haloamides, halobenzoquinones and nitrosamines, which are resulted extremely toxic and responsible for serious adverse effects on human health [40–43]. Even if many disinfection byproducts can be potential carcinogenic, mutagenic and teratogenic, risk assessments revealed that the magnitude of these effects can not only be associated to DBPs, which is why further studies are required.

1.2.3 Heavy metals

Despite the adjective "heavy", the class of metalloids is often included in the group of heavy metals. Not taking into consideration the contribution coming from natural sources (Earth's crust) and natural causes (geological weathering, soil erosion, metal corrosion, metal evaporation from soil and water and sediment re-suspension, volcanic activity), in the last decades their concentration in water increased significantly as a result of anthropogenic activities [44]. Industrial operations such as electroplating, electrolysis, metal smelting and chemical synthesis processes, together with coal driven power plants, waste incinerators and medical waste represent the primarily responsible for the release of metals in the environment. Following, the second major contribution comes from the agricultural field. In contrast to organic pollutants, heavy metals and metalloids could not be degraded by simple biological treatments. As a consequence, they are more easily transported in the environment and, depending on the conditions (oxic/anoxic, presence/absence of microorganisms), they can react through redox, complexation, precipitation/dissolution and adsorption processes, promoting in this way their accumulation and bioaccumulation. Once entered in human and animal organism, metals can escape control mechanisms such as transport, homeostasis, compartmentalization, and, more importantly, can cross cell membranes and bind to specified cell constituents such as proteins and DNA,

leading to the modification of protein structures, to the alteration of enzyme functions and, in the worst cases, to DNA damage [45,46]. Teratogenicity, carcinogenicity, and detrimental health problems represent sufficient evidence to consider heavy metals and metalloids extremely toxic for human and animal beings. Aluminum, Arsenic, Cadmium, Chromium, Cobalt, Copper, Lead, Mercury, Nickel and Zinc are the most priority aquatic pollutants because of their toxicity [46]. Metal concentration levels at which they are toxic for human beings are strictly dependent on the peculiar characteristics of the metal, which is why some of them (As, Hg, Pb) are extremely toxic even at low concentrations while others, such as Al, Co and Zn, become toxic upon a certain concentration value [44,47]. For example, it has been shown that persistent exposure to arsenic can cause the damage of skin, liver, cardiovascular, endocrine and central nervous systems, and is connected with the appearance of various types of cancer [48]. High exposure to mercury, considered the most toxic metal, can produce deleterious effects on the cardiovascular system, on the immune and reproductive systems and on the central nervous system and can also bring to blindness and deafness [49]. Adverse effects on the kidney, stomach and nervous system have been observed for lead, which is extremely persistent in the human body [50].

1.2.4 Fluoride

With a concentration of about 0.3 g/kg, fluorine is the 13th most abundant element in the Earth's crust, normally found in water in its ionic form, as fluoride. It is classified as an essential environmental element and recognized as beneficial [51]. However, its environmental accumulation registered in the last decades, due to anthropogenic practices like coal burning, hydrofluoric acid, phosphate fertilizers and enamel production, aluminum smelting, textiles and dyeing, and glass and ceramic manufacturing, provoked a rise in its concentration big enough to observe fatal consequences both to human, animal and plant health. In human beings, in fact, when dosages are low (<1 mg/L), fluoride is useful for the development of normal bones and teeth [52]. On the contrary, if concentration exceeds 1.5 mg/L or the organism is subjected to

chronic exposure, adverse effects such as dental fluorosis, skeletal and dental lesions and dysfunctions, enamel discoloration, together with growth and development problems, have been observed [51]. At the present time, water contamination from fluoride represents a serious problem in arid, semi-arid and mid-latitude world countries, such as India, China, Poland and Africa [53–55].

1.2.5 Microplastics

Plastic occurrence in water and marine environments is one of the most relevant global concerns. Just in 2020, annual plastic production amounted to 367 million tons while more than 10 billion tons of plastic have been produced from 1950 [56]. Land-based sources and microbeads are responsible for around 80% of all plastic currently polluting the oceans and marine environment [57,58]. Contrary to what one would expect, maritime operations are not the main source of ocean plastic pollution. Plastic reaches the marine environment through wind, tides, internal waterways and wastewater outflows and comes mainly from industrial, coastal and domestic activities, followed by coastal tourism, aqua industries and commercial fishing [59]. Plastic particles found in water differ in shape, size, chemical composition and specific density. Polystyrene, the least dense (40 kg/m^3), polypropylene and polyethylene are usually visible on the sea surface as, being very light, they float. Therefore they can be easily transported through wind and currents and be found even in the most remote places on the planet. Plastic particles whose density is greater than that of seawater, on the other hand, sink and settle on the seabed. Among them there are polyamide, polyester, acrylic, PVC and the densest of all, polytetrafluoroethylene (2020 kg/m^3). According to their size, plastic particles are classified in megaplastics (diameter >50 cm), macroplastics (5–50 cm), mesoplastics (0.5–5 cm) and microplastics (<0.5 cm). Megaplastics (MEPs) and macroplastics (MAPs) are easy to see due to large dimensions of debris. These fragments come mainly from disposable products [60] and can cause the death of aquatic living organisms by suffocation, since they often ingest plastic debris mistaken them for food or end up entangled by debris [61]. Mesoplastics (MePs) are particles with lower dimensions, principally produced by degradation and

fragmentation of mega and macroplastics. Microplastics (MPs) can be released in water both from marine coatings, tires, road markings, personal care products, synthetic textiles, plastic pellets and city dust (primary sources), both from degradation and fragmentation of large plastic debris by physical, chemical and biological processes (secondary sources) [62]. Microplastics are generally found in the oceans in the form of fibers, pellets or fragments. They can directly reach the oceans from domestic and industrial drainage systems. Due to their small size, in fact, wastewater treatment plants fail very often to retain these particles which, inevitably, remain in the effluents (about 50% of the initial concentration) and from there arrive in the water bodies [63,64]. Carried by wind and currents, floating microplastics and microbeads reach the subtropical gyres where they tend to accumulate, creating real "special accumulation zones" [65] denoted by the term "ocean garbage patches" [66] (*Fig. 4*).

Fig. 4. Geographical collocation of "ocean garbage patches".

The first "hotspot" entirely made of plastic was discovered in the North Pacific central gyre [67]. Today there are at least 6 gyres: South Indian, South Pacific, North Pacific, South and North Atlantic and the zone of Barents Sea [68,69]. Data is alarming to say: estimates show that the number of microplastic particles in

the South Pacific garbage patch is at least 30,000 particles/km^2 [70], with 270,000 tons of plastic for each subtropical gyre [68]. Numbers regarding plastic pollution of the beaches are no longer comforting. 25 beaches along the coastal area of Hong Kong are occupied by 90% of microplastics, estimating around 5,600 particles/m^2 [71]. In Belgium, studies show that the percentage of MPs along the coast is around 93 particles/kg of dry sediment [72]. Also, along the beaches of the island of Malta the presence of MPs is about 1,000 particles/m^2 on the surface, while the beaches of Guanabara Bay, in Brazil, have been counted among those with the highest percentage of MP pollution [57]. Anthropogenic activities are clearly the major contributor to microplastic pollution. Guoin et al. (2011) showed that the US population annually produces 263 tons of polyethylene for use of personal care products, an amount responsible for about 25% of the microplastic intake that ends up in the North Atlantic subtropical gyre [73]. In 2016, Varinsky showed that around 29 tons of plastic microfibers are released into the oceans every day, 35% of which comes entirely from clothing [74]. In 2018, Resnick estimated that through a single laundry wash it is possible to release a very high number of plastic microfibers into the oceans, equal to 22,992 microfibers for poly-cotton, 121,465 in the case of acrylic fabrics and 82,672 for polyester [74]. Another important way of introducing microplastics into the marine environment is certainly due to sewage sludges, which contain an even greater quantity of microplastics than effluents, and to the degradation of plastic debris promoted by weathering [64]. Last but not least, an important component of microplastics is added to the oceans through wind, currents and storm sewers. Rivers, for example, are among the main carriers of microplastics up to the coasts [75]. Here, the transported sediment, which includes both macroplastics and microplastics, ends up in shallow marine sediment deposits and from here it can follow two paths: to reach submarine canyon head or to be reworked by coastal phenomena such as longshore drift [76].

Due to their small size, microplastic particles are of greater concern since they can bioaccumulate in organisms through the food chain, resulting in several detrimental effects such as disruption of immune functions, alteration of

metabolism, oxidative stress, cytotoxicity up to the most threatening one, carcinogenicity [77,78].

1.2.6 Pathogens

Among water pollutants of greater concern, pathogens must also be considered. Pathogens are disease-causing microorganisms and include viruses, bacteria, protozoa, helminths and fungi [79,80]. The reason why they represent a threat for human health is essentially due to these three characteristics: a) pathogens spread in the environment in high numbers and are highly infectious to humans even at low concentrations; b) if environmental conditions are favorable, pathogens can also multiply outside of a host; c) pathogens are often highly resistant to currently water treatments, surviving in the environment for a long time during which they continue to remain highly infectious. The main route through which pathogens contaminate water bodies is by human and animal feces, which represent the natural habitat for microorganisms such as Salmonella, Aeromonas, Campylobacter, Leptospira, Vibrio, Shigella and so on. Contributions to this fecal waste come from different discharge sources, ranging from raw sewage to industrial drains, and from non-point source discharges such as forestry, agriculture, wildlife and urban run-off, whose waste, due primarily to anthropogenic activities, is typically introduced in water bodies without any control [81]. Even if origin and source of contamination can be easily identified, pathogens removal from water represents one of the hardest challenges of these years. Historically, the presence of pathogens of the form of viruses, bacteria and protozoa is monitored by the fecal indicator bacteria (FIB), including total and fecal coliforms and enterococci [82]. It is useful to consider that this analysis gives results only in a probabilistic way: if FIB is upon a certain value, this may indicate fecal pollution and there may be a possible association with enteric pathogens. In addition, because of the number of pathogens is extremely high, these routine microbiological water analyses are based on the detection of few indicator organisms, chosen in term of population (the most numerous) and with the same natural habitats. This inevitably introduces a lot of limitations, both in terms of selectivity, since numerous uncommon

pathogens remain undetected, and in terms of sensibility, since the method is poorly performing at low concentration levels [83]. Consequently, although new fecal indicators have been proposed, none of those currently used meet all ideal criteria required for water quality assessment [84]. Generally, the major risk for human health is associated with the ingestion of fecal contaminated water. It has been shown that the main bacterial diseases transmitted through drinking water are cholera, typhoid fever and other serious salmonellosis, gastroenteritis caused by vibrios, bacillary dysentery or shigellosis, acute diarrheas and gastroenteritis [79]. These diseases are particularly diffused in developing countries, especially in Africa and Asia, where poor financial resources preclude the adequate and appropriate sanitation of hygienic facilities, becoming in turn the suitable habitat for pathogens proliferation [85,86].

Once in water, all these pollutants interfere with flora and fauna ecosystems and, as a result, enter the food chain. The main route of ingestion for humans is represented by drinking water, immediately followed by food consumption. Taking into consideration hazardous effects for which these contaminants are responsible for human health, the World Health Organization has issued new 2022 Guidelines for drinking water, which are briefly resumed in the following paragraph.

1.3 2022 Guidelines for drinking water: WHO and EPA

Access to safe drinking water is a human right and it is strictly important in effective policy of health protection. Since 1958, when the first document was published, World Health Organization provides on a regular basis reports examining the current state of water on a global scale, by posing attention to problematics such as access to safe drinking water, water scarcity and water pollution. The first editions of these reports bore the name *WHO International standards for drinking water* and were published in 1958, 1963 and 1971. Subsequently, the name has been changed in *Guidelines for drinking-water quality*. Four editions have been released: 1983-1984, 1993-1997, 2004 and 2011. Considering the large number of studies and the speed at which results are published, *Guidelines* are constantly updated in order to include the most recent findings. This leads to the introduction of major new recommendations and modifications of acceptable limits for assessed pollutants but also to the inclusion of new chemicals in the list of water pollutants. Therefore, it is strongly advisable to always access the latest updates of these Guidelines. Recalling the words in the Preface of the latest edition, "*The primary goal of the Guidelines is to protect public health associated with drinking-water quality*". Guidelines objectives are briefly described below:

- *"provide an authoritative basis for the effective consideration of public health in setting national or regional drinking-water policies and actions";*
- *"provide a comprehensive preventive risk management framework for health protection, from catchment to consumer, that covers policy formulation and standard setting, risk-based management approaches and surveillance";*
- *"emphasize achievable practices and the formulation of sound regulations that are applicable to low-income, middle-income and industrialized countries alike";*
- *"summarize the health implications associated with contaminants in drinking water, and the role of risk assessment and risk management in disease prevention and control";*
- *"summarize effective options for drinking-water management";*

- *"provide guidance on hazard identification and risk assessment".*

Guidelines are always supported by a series of scientific publications regarding both internationally peer-reviewed risk assessments for specific chemicals and the scientific basis underpinning their development. The latest updates to the fourth edition (first published in 2011) have been included in March 2022.

U.S. EPA is the acronym of United States Environmental Protection Agency and it is an American organization, born with the scope to "*improve the lives of millions of Americans by reducing pollution in neighborhoods where people live, work, play, and go to school; accelerating environmental justice efforts; and tackling our biggest climate challenges*". Water pollution and water sanitation practices fall perfectly within the environmental topics of which EPA takes particularly care. Actually, EPA has drinking water regulations for more than 90 pollutants and, in the same way of WHO, periodically publishes its list of contaminants, called Contaminant Candidate List or CCL. For each pollutant in CCL, EPA defines two important limits: the maximum contaminant level goal (MCLG) and the maximum contaminant level (MCL). The first represents "*the maximum level of a contaminant in drinking water at which no known or anticipated adverse effect on the health of persons would occur, allowing an adequate margin of safety*". Once MCLG has been determined, EPA introduces an enforceable standard, the maximum contaminant level. MCL is "*the maximum level allowed of a contaminant in water which is delivered to any user of a public water system*". EPA limits and regulations are always reported in the document *National Primary Drinking Water Regulation*s (NPDWR), online available here: https://www.epa.gov/ground-water-and-drinking-water/national-primary-drinking-water-regulations.
Latest updates have been introduced in January 2022.

Table 1 briefly resumes currently acceptable limits in drinking water for the most common pollutants set by WHO and EPA [87,88].

Table 1. Currently acceptable limits in drinking water for the most common pollutants.

Contaminant	Category	WHO limit (µg/L)	EPA MCLG (µg/L)	EPA MCL (µg/L)
Alachlor	herbicide	20	0	2
Aldicarb	pesticide	10	1	3
Aldrin and dieldrin	chlorinated pesticides	0.03	-	-
Arsenic		10	0	10
Atrazine	herbicide	100	3	3
Cadmium	heavy metal	3	5	5
Carbofuran	pesticide	7	40	40
Chloramines	disinfection by-products	3000	4000	4000
Chlordane	insecticide	0.2	0	2
Chromium	heavy metal	50	100	100
Copper	heavy metal	2000	1300	1300
DDT	insecticide	1	-	-
Lead	heavy metal	10	0	15
Manganese	heavy metal	80	-	-
Mercury	heavy metal	6	2	2
Nickel	heavy metal	70	-	-
Perchlorate	anion	70	-	-
Polynuclear aromatic hydrocarbons (PAHs)	organic pollutant	0.7	-	-
Selenium	metal	40	50	50
Styrene	organic pollutant	20	100	100
Trihalomethanes:	organic pollutant			
Bromoform		100	0	80
Chloroform		300	70	80
Vinyl chloride	organic pollutant	0.3	0	2

Chapter 2

Water pollution: most currently employed treatment technologies for water purification

The world entire has a constant need for water. In fact, in addition to drinking, which is undoubtedly vital for humanity, water is widely used in a large part of human activities such as agricultural and industrial operations, food processing and cleaning. However, increasing water pollution on the one hand and the appearance of the problem of water scarcity, due also to climate changes, on the other make water supply even more difficult. Concepts such as water remediation and water reuse are not an innovation of the last century. According to literature, Mesopotamian civilization already took care of sanitation problems building latrines leading to cesspits and a drainage system to carry away wastes from homes [89]. Greeks and Romans are undoubtedly forerunners of modern sanitation technologies: their water systems included latrines, sewers and drainage systems in order to convey waste outside the city [89]. The main difference compared to then is that the 21st century has to deal with a water demand which, considering the currently world population of about 8 billion, is strictly high while water sources are in short supply and the problem of water pollution continues to grow. Wastewater reuse is undoubtedly a crucial step to meet and accommodate the living standards of modern society. Considering the large number of contaminants found in water, wastewater need to be properly managed prior to enter again water bodies and be reused. Wastewater treatment plants (WWTPs) are the currently adopted systems to remove contaminants from water and achieve high quality standards required for a correct public hygiene [90]. The first WWTP dates back to the beginning of 20th century when the outbreaks of waterborne diseases such as typhoid and cholera made evident that they originated from drinking water contamination by pathogens transported from wastewater [90].

Depending on its origin, wastewater is classified in domestic, industrial and commercial or urban sewage. Domestic wastewater originates from residential sources such as laundry, bathing, toilets and sinks and can contain contaminants such as detergents, soaps, drugs, personal care products, bacteria

or other pathogenic organisms. Industrial wastewater is the sewage produced by manufacturing facilities and industrial operations including commercial wastewater from stores, offices, hotels and other enterprises. Urban wastewater is usually a mix between domestic, industrial and commercial sewage and, if the city disposes of an only one sewer system, municipal wastewater also includes stormwater. Bearing in mind that pollutant types in wastewater are strictly dependent on the sewage origin, WWTPs need to be correctly engineered to ensure the proper decontamination of water from pollutants. This involves the design of each single step of treatment, evaluating benefits and potential risks of each unit operation in the WWTP, i.e. from the moment when the influent enters the system up to when the effluent is released into water bodies. According to the method employed, currently conventional treatments are divided in physical operations, chemical and biological processes. Physical operations include all type of operations in which pollutants are removed only by physical forces while, in chemical and biological processes, contaminants removal is operated respectively by chemical and biological activity. Water decontamination usually requires the use of more than one treatment, reason why it is also strictly important the order with which removal methods are employed. Generally, WWTPs include the following stages of treatment: 1) preliminary treatments; 2) primary treatments; 2) secondary treatments; 3) tertiary treatments (not always applied) [91]. In order to achieve water quality standards required by EPA and WHO, it is absolutely necessary that each treatment in a WWTP provides highest performances, both in terms of results and lifetime [92]. For this reason, quality of influents and effluents entering and exiting each step must be constantly monitored. Generally, wastewater quality is evaluated through the following parameters: fraction of suspended solids (SS), biochemical oxygen demand (BOD) and chemical oxygen demand (COD) [93,94]. It must be noted that BOD measures only the fraction of organic matter which can be biodegraded in terms of oxygen demand while COD quantifies organics and a portion of certain inorganics, such as ferrous iron, sulfites and sulfides, nitrites and chlorides, which can undergo chemical oxidation. The sum of BOD and COD constitutes the total oxygen demand (TOD). These parameters

can provide only a preliminary view about wastewater quality. It is beyond any doubt that more sensitive analytical determinations and specific analysis must be also added to the list [90,95–98], in order to evaluate nutrient availability, pH conditions, occurrence of heavy metals or other toxic contaminants, whose removal can also require more specific treatments.

A brief description about tasks and role of each treatment unit is now proposed, to better understand benefits and limits coming from each step of a WWTP and the reason why tertiary treatments often turn out to be indispensable before releasing water into water bodies.

Preliminary processes. Preliminary processes have the scope of removing all floating large material, often found in raw wastewater, and the portion of inorganic solid heavy enough to settle, making use of only physical operations. This includes the removal of pieces of paper, cloth, wood, plastics, garbage but also sand, gravel, glass, metal and some fecal matter [99].

Primary treatments. Organic and inorganic suspended solids, unaffected by preliminary processes, are generally removed during primary treatments through sedimentation and flotation [93,99]. In sedimentation, wastewater containing grit, silt and suspended solids (SS) is collected in large tanks and left undisturbed/semidisturbed for a certain period of time, depending on the size and density of solids to remove. Solids and other suspended inorganic material settle by gravity at the bottom tank. Because this process can also take a long time, generally some chemicals are introduced in the tanks with the scope to adjust pH to the value at which process is faster [100]. Removal percentage of oils with sedimentation is about 99% while suspended solids are reduced of approximately 60%. In the flotation process, suspended and biological solids, greases and oils are removed by adhering them to air or gas bubbles. After being captured in bubbles, these pollutants form agglomerates which, due to the lower density, accumulate at the water surface and can be easily removed. To ensure a good quality process, gas or compressed air are generally insufflated from the bottom tank in order to go through all wastewater volume and help

bubbles lift until the water surface. As in sedimentation, flotation is also promoted by adding some chemicals such as activated silica or alum. Compared to sedimentation, the fraction of suspended solids removed by flotation is increased of an extra 15% while removal percentage of oils and greases are almost the same (99%).

Secondary treatments. In terms of solid fraction, effluents from primary treatments contain generally 30% of suspended solids and about 65% of dissolved solids, while the colloidal portion is about 6%. Secondary treatments are therefore employed to remove this organic matter using typical biological processes adopted by microorganisms under a specific and controlled environment [93]. Water is circulated in a reactor in which microbe concentration is preserved high and organic matter is converted in water, CO_2 and NH_3, even if secondary products such as nitrate, glucose and alcohol can also be originated. Because degradation occurs through typical biological pathways, it is extremely important at this stage to have the complete absence of toxic organic and inorganic pollutants which can inevitably interfere with metabolization reactions of microorganisms, making them harmless or, in the worst cases, causing their death even before degradation can start. Secondary treatments are divided in aerobic and anaerobic processes, depending on the presence or absence of oxygen and on the rate at which microbes metabolize organic matter [101]. In aerobic conditions, parameters which must be monitored are temperature, retention time, oxygen availability and biological activity of microbes. To promote bacterial growth, some chemicals can be added. More than 90% of biodegradable organic matter can be removed, including volatile/non-volatile suspended and dissolved organics. One of the major problems of this process is the high production of biosolids, whose management and disposal require an expensive cost. In anaerobic conditions, degradation of organic matter is operated by microbes which can live in absence of oxygen and whose metabolization processes release, as waste products, gases such as methane, nitrogen, ammonia and hydrogen sulfide. Because of their toxicity, anaerobic treatment does not reach common standard permitted

discharge levels and it is often used as a primary step, previously to aerobic process, to treat high strength wastewaters [102]. Compared to the aerobic treatment, which needs energy to transfer oxygen, anaerobic process produces energy in the form of methane. One of the disadvantages of this process is that initial startup may take a time even greater than 45-60 days.

Depending on the type with which bacteria are cultivated in the reactor, secondary treatments can be classified in attached growth (biofilms) and suspended growth (activated sludge) systems. In the first case, bacteria attach and grow on a fixed substrate such as rock or plastic [103]. In suspended growth systems, wastewater and biomass are maintained under a constant process of mixing and the reactor is designed so that new wastewater and the fraction of solids, already treated but not yet sedimentable, can continuously flow in up to when all organic matter is degraded [104].

Tertiary treatments. Generally, after secondary treatments, influent BOD and SS are reduced of about 85% to 95% while influent COD of only 65% [99]. Tertiary treatments involve recent advanced technologies to eliminate any other contaminant whose occurrence in water has not been affected by the previous units or to remove eventual microbes left by biological processes employed during the secondary treatment step. Several technologies and chemical processes have been developed to achieve this task: disinfection, advanced oxidation processes (AOPs) and membrane technologies are the most commonly employed tertiary treatments.

Disinfection. Water disinfection has the aim of removing all pathogenic microorganisms from water [105]. Conventional technologies employ chemical disinfectants such as chlorine, the most common, chlorine dioxide, peracetic acid and ozone [106–108]. Chlorine, used in the form of gaseous chlorine, sodium hypochlorite or chloramines, interferes with metabolic activities of pathogens, modifying chemical structures of enzymes which regulate their nutrition, thus inhibiting their development and their proliferation. Chlorine dioxide acts in the same way of chlorine towards bacteria but its disinfectant power is equal or

higher than that of chlorine. Peracetic acid is highly reactive and decomposes producing acetic acid and oxygen, whose oxidizing power is used against pathogens. Oxygen or reactive hydroxyl radicals, originated during the disinfection process, attack and destroy bacterial cell walls and membranes, as well as some enzymes and DNA. Because of the production of acetic acid, this process causes the increase of BOD and COD on the final effluent. Ozone is an extremely reactive gas with oxidizing power, able to kill bacteria through the disruption of cell walls. Its disinfectant efficiencies are better than chlorine. Regardless of the type of chemical disinfectant, one main disadvantage of disinfection process is the possibility to originate organic and inorganic disinfection byproducts, whose toxicity has been already discussed in the previous chapter [109–112]. Alternatively, UV radiation can also be used, reducing the problem of byproducts [113].

Advanced oxidation processes. Advanced oxidation processes (AOPs) have been proposed for water purification for the first time in 1980 [114]. As the name suggests, water pollutants are removed through oxidation processes activated by hydroxyl ($OH^{\cdot}$) or sulfate ($SO_4^{\cdot-}$) radicals, directly generated in situ. Compared to chlorine or ozone, which can be used both as oxidants and disinfectants, AOPs are predominantly employed as removers of organic and inorganic contaminants in polluted waters. This can be ascribed to the short half-life (about 10^{-6} seconds) of hydroxyl and sulfate radicals, thus implying too low concentration levels for the detention times required by disinfection. The final purpose is to degrade these contaminants into less or, hopefully, non-toxic products in order to release high-quality water, ready to be reused. Except for sulfate radical-based AOPs, all the other processes are based on the generation of hydroxyl radical and can be classified in ozone-based AOPs, UV-based AOPs and Fenton-related AOPs [115]. Hydroxyl radical is certainly one of the strongest oxidants in water, able to operate both in acid and basic conditions. Its high potential is related to the fact that it is not selective, rapidly reacting with numerous species. Principal mechanisms of oxidation are hydrogen abstraction, electron transfer, radical addition and radical combination, through which

organic pollutants are transformed into more reactive species which undergo chemical degradation and mineralization. Due to its short half-life, $OH^{\cdot}$ is always generated in situ.

In ozone-based AOPs, the precursor of hydroxyl radical is ozone (O_3) according to the following reaction $3O_3 + H_2O \rightarrow 2OH^{\cdot} + 4O_2$ [116]. To be honest, ozone itself is an oxidant but it is rarely employed because its oxidation reaction is more selective, preferring ionized and dissociated forms of organic compounds. If irradiation or other oxidants are used, $OH^{\cdot}$ yield can be raised.

Photocatalysis (UV-based AOPs) generates hydroxyl radicals by irradiation of semiconductors (TiO_2, ZnO, WO_3, SnO_2) with UV light of appropriate wavelength, depending on semiconductor energy band gap [117–119]. As the name suggests, the core of the process lies in the absorption of energy carried by UV radiation in the form of photons to promote electrons from the semiconductor valence band (VB), populated by electrons in the ground state, to the semiconductor conduction band (CB) [120]. Due to ejection of electrons, VB becomes positively charged with the creation of positive holes (hv_{vb}^{+}) and CB host negative electrons (e_{cb}^{-}) ejected during absorption of incident photons (*Fig. 5*), thus generating electron-hole pairs.

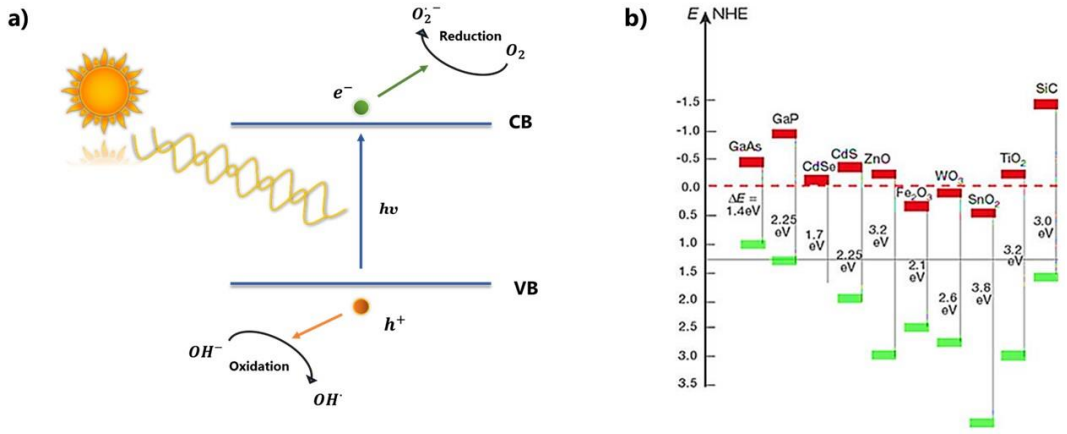

Fig. 5. a) Schematic representation of photocatalysis working principle. b) Band gaps of common semiconductors employed in photocatalysis.

Positive holes are characterized by very strong oxidizing power (1.0-3.5 V vs. NHE, depending on semiconductor and pH): their role consists exactly in the formation of $OH^{\cdot}$ radicals by oxidation of OH^{-} anions and H_2O molecules absorbed on semiconductor surface through the following equations:

$$OH^{-} + hv_{vb}^{+} \rightarrow OH^{\cdot} \quad (1)$$

$$H_2O + hv_{vb}^{+} \rightarrow OH^{\cdot} + H^{+} \quad (2)$$

Once formed, $OH^{\cdot}$ radicals attack organic molecules, triggering a wide range of radical chain reactions which bring to their complete degradation. Contemporaneously, electrons in the CB reduce oxygen molecules contained in the air to superoxide anions. These species can also react with intermediate products originated during organic matter degradation, by forming peroxide derivatives which are in turn converted to hydrogen peroxide molecules and at the end to water, therefore promoting an alternative pathway of degradation for organic pollutants. Because electrons in the conduction band are in excited states, reverse process of electron-hole pair generation can commonly occur, by recombination of holes in the VB with electrons in the CB, leading to the disappearance of both charge carriers on semiconductor surface and thus to a reduction of the photocatalytic efficiency. The annihilation of charge carriers returns the energy previously absorbed in the form of light (radiative recombination) or heat (non-radiative recombination) [121]. Photocatalysts exhibiting high efficiency are metal oxides such as TiO_2, ZnO and CeO_2 while metal sulfides [122]and metal selenides are not stable and consequently discarded from the list of semiconductors with potential photocatalytic applications [120,122]. Among metal oxides, TiO_2 excels and is currently the most employed photocatalyst, due to its high chemical stability both in acidic and basic conditions, high oxidizing power, cheapness, nontoxic behavior, and environmental safety [122]. Apart from recombination processes, photocatalytic efficiency is strongly affected by the following parameters: structure, size, shape, and surface area of the catalyst, amount of catalyst, light intensity, reaction temperature, pH, and concentration of wastewater [120,123]. Semiconductors can exhibit more than one solid phase, each characterized by a

peculiar photocatalytic activity, depending on how atoms are organized in the crystal structure. TiO_2, for example, exhibits three different solid phases: anatase, rutile and brookite. In terms of photocatalytic activity, anatase is preferred among the three for the position of its conduction band, the higher degree of hydroxylation, which means higher amount of $OH^{\cdot}$ radicals, its stability and adsorption power. Photocatalytic activity strongly depends on semiconductor surface area: the larger surface area, the bigger efficiency. In this direction, spherical particles and nanoscale dimensions are recommended for their high surface-to-volume ratio. Catalyst amount should also be considered. Higher quantities of semiconductor can ensure a major number of active sites, originating more $OH^{\cdot}$ radicals, but if semiconductor amount exceeds optimum concentration, light penetration in the solution reduces and photocatalytic activity also decreases. Even temperature must be monitored because, if it is too high, recombination processes are favored. pH is a crucial parameter, driving the formation and occurrence of charge carriers on semiconductor surface. Lastly, increasing light intensity means raising the number of photons reaching the semiconductor surface and consequently the number of active sites which can be originated, improving photocatalytic efficiency. One of the major drawbacks of photocatalysis is represented by catalyst recovery. Due to their high surface-to-volume ratios and surface energy, semiconductor particles tend to agglomerate, leading to surface area reduction and having detrimental effects in terms of catalyst reusable lifespan. Efforts have been done in this direction by preparation of new composite systems, in which semiconductor nanoparticles are immobilized on a support, such as cellulose, silica, polymeric materials, and activated carbons [121,124,125]. Regardless of the substrate type, a good support must respect the following criteria: a) photocatalyst reactivity must be independent from the technique employed during anchoring process; b) strong interactions between photocatalyst and support are required, thus avoiding leaching under various experimental reactions; c) high surface area must be preserved; d) the new composite system must be stable over a period of time; e) the support should not be easily degraded during the photocatalytic process. Polymeric materials have been investigated a lot in recent years, being

good support candidates due to their cheapness, abundance, chemical and mechanical stability during photocatalytic processes. Because photocatalysis involves electrons transfer, conductive polymers appear the most appropriate choice in their role of support, enhancing the efficiency of the process. Interesting results have been found when TiO_2 or ZnO are incorporated with polythene (PE), polyvinyl alcohol (PVA), polyethylene terephthalate (PET), polymethyl methacrylate (PMMA) and polyaniline (PANI) [126–129]. The activation of the photocatalytic process often requires higher energies, which cannot be achieved using visible light. Recent developments are directed towards the reduction of semiconductor band gap by preparing new mixed metal oxides nanocomposites, obtained through semiconductor doping with metal ions such as Pt, Au, Pd, Ag, Co, Cu, Mn, Ce or non-metal elements as N, C, Cl and S [130–132]. These dopants possess a different electronic structure, introducing new energetic levels placing inside the semiconductor band gap, without altering its original value (*Fig. 6*). This can include the creation of a more energetically VB, closer to CB of the host, or the introduction of a less energetically level, below the CB, which diminishes the gap with the semiconductor valence band. Along this path, carbon materials such as graphene, carbon nanotubes and carbon quantum dots (CQDs) have been also investigated for visible light photocatalysis [133]. Due to their excellent electrical conductivity and high surface area, graphene and graphene oxide (GO) exhibited the most interesting results among carbon materials [134–136].

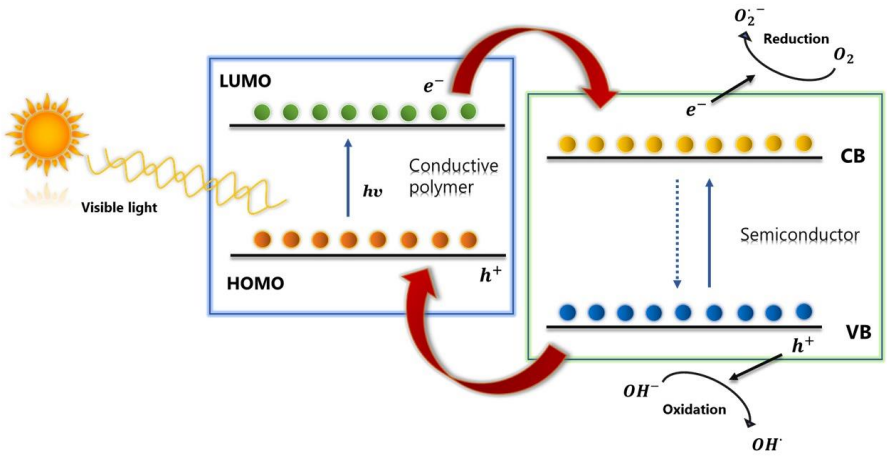

Fig. 6. Schematic diagram of visible light photocatalysis when conductive polymers are employed.

In Fenton-related AOPs, $OH^{\cdot}$ precursor is H_2O_2 [137]. Reaction is catalyzed by Fe^{2+} ion, through the following subsequent steps:

$$Fe^{2+} + H_2O_2 \rightarrow Fe^{3+} + OH^{\cdot} + OH^{-} \quad (3)$$

$$Fe^{3+} + H_2O_2 \rightarrow Fe^{2+} + HO_2^{\cdot} + H^{+} \quad (4)$$

$$OH^{\cdot} + H_2O_2 \rightarrow HO_2^{\cdot} + H_2O \quad (5)$$

$$OH^{\cdot} + Fe^{2+} \rightarrow Fe^{3+} + OH^{-} \quad (6)$$

$$Fe^{3+} + HO_2^{\cdot} \rightarrow Fe^{2+} + HO_2^{+} \quad (7)$$

$$Fe^{2+} + HO_2^{\cdot} + H^{+} \rightarrow Fe^{3+} + H_2O_2 \quad (8)$$

$$2HO_2^{\cdot} \rightarrow H_2O_2 + O_2 \quad (9)$$

Even if Fe^{2+} is re-generated through reaction (4), rate constant of this reaction is several orders of magnitude less than that of reaction (3). Consequently, the largest part of Fe^{3+} remains unconverted, resulting in the production of iron sludge. The problem is that iron sludge requires to be disposed separately, thus increasing treatment complexity and operational costs. In addition, high yields of Fenton reaction are obtained only in acidic conditions. Therefore, in order to render the process more feasible, modifications to the original Fenton reaction have been proposed, such as Fenton-like system (Fe^{3+} precursor), photo-Fenton system (UV irradiation) and electro-Fenton system [137]. During sulfate radical-based AOPs, the role of hydroxyl radicals is assumed by sulfate radicals, obtained from $S_2O_8^{2-}$ through heat, UV irradiation, elevated pH or transition metal catalysts (Fe^{2+}, Fe^{3+}, Cu^{+}, Ag^{+}) [138,139]. Just as hydroxyl radicals, sulfate radicals have also a short half-life but they preferably tend to remove electrons from organic compounds to produce organic radical cations.

Membrane technologies. Although the application of membranes in wastewater treatments is not recent (the first industrial application dates back to 1960), membrane technologies have experienced a big development in the

last 20 years becoming one of the most popular and employed purification technologies in a wide range of sectors, from wastewater treatments to sea and brackish water desalination, passing through gas and vapor separation, food and beverage production, energy conversion and storage and so on [140–145]. Their success can be ascribed almost entirely to the reduction in the size of equipment and to the low energy requirement and capital cost, which allow them to bridge the economical and sustainability gap and embrace concepts such as environmental friendliness and easy accessibility to many. From a technical point of view, a membrane is a system which acts as a barrier between two phases, restricting the transport of the components contained in these two phases in a selective way. Membranes can be classified according to the nature of the membrane material (organic/inorganic), to their geometry (flat/tubular/hollow fiber) and morphology (homogeneous/heterogeneous) but also according to preparation methods, separation regime and processes. Concerning separation processes, it is clear that a driving force is required to ensure a movement of media through membranes. In this regard, processes can be divided in equilibrium and non-equilibrium based membrane processes, pressure driven and non-pressure driven processes [146,147]. Among these, pressure driven membrane processes are the most employed technology in wastewater tertiary treatments. Depending on membrane pore size and pressure requirements, pressure driven processes are divided in microfiltration (MF), ultrafiltration (UF), nanofiltration (NF) and reverse osmosis (RO). Table 2 resumes briefly the main characteristics of these four processes.

Table 2. Most relevant characteristics of pressure driven membrane processes.

PRESSURE DRIVEN PROCESS	PRESSURE REQUIREMENTS (BAR)	PORE SIZE DIAMETER (NM)	MOLECULAR WEIGHT CUT-OFF (MWCO) (KDA)	POLLUTANTS RETAINED
REVERSE OSMOSIS (RO)	15-75	0,1-1	0,2-2	All pollutants, including monovalent ions
MICROFILTRATION (MF)	1-3	10^2-10^4	100-500	Bacteria, colloids, oil, grease, fat, organics, microparticles
ULTRAFILTRATION (UF)	2-5	1-10^3	20-150	Sugar, organics, microplastics, proteins, pigments, oils
NANOFILTRATION (NF)	5-15	1-10	2-20	Pigments, divalent anions, divalent cations, sulfates, sucrose, lactose, sodium chloride

In order to obtain better performances and high-quality treated water, hybrid membrane processes (HMPs) have been developed in the recent years. Hybrid processes include the combination of membrane processes among themselves (MF/UF, FO[1]/RO) and with other wastewater treatments (coagulation, adsorption, biological processes) [148–151]. In this regard, membrane bioreactors (MBRs)[152], combining activated sludge processes with a MF, UF or NF membrane technology, have received greatest attention due to the possibility of cope with fluctuations in effluent composition and flow rates and meet effluent discharge limits for reuse purposes, two main disadvantages commonly found when only activated sludge processes are employed. MBRs can provide high-quality effluents (BOD/TSS <5 ppm), high biodegradation efficiency and a very low excess sludge production, working in a comparatively small configurational system. Considering the problem of membrane fouling, previous treatments such as sedimentation, coagulation or membrane processes

[1] Forward osmosis (FO) is generally used to indicate the natural process of osmosis.

themselves are required before the application of one of these hybrid processes [153].

In contrast to disinfection and advanced oxidation processes, where contaminants removal from water occurs by chemical degradation, converting them into less or non-toxic species, in membrane technologies pollutants remains undamaged and are removed from water through filtration or adsorption processes. Therefore, the design and choice of materials for membrane preparation is of outmost importance to ensure best process performances, both in terms of pollutants removal and in terms of durability and endurance of the membrane itself. Concerning the first one, it is important to use materials whose affinity with contaminants is strong enough to retain them from water but, at the same time, weak enough to release them during the subsequent step of washing, when membrane is regenerated and reused once again. Membrane technologies requires different operational conditions in terms of temperature, pressure, pH conditions, additives occurrence and so on. Therefore, it is extremely important considering all these factors during the choice of the appropriate adsorbent, which must remain unaffected and not damaged by the specific working conditions used during a membrane technology process. Having regard to this background, a membrane must possess at least the following characteristics: a) high selectivity (rejection); b) high flux; c) mechanical stability; d) tolerance to temperature variations and to all feed stream components (fouling resistance); e) low manufacturing cost; f) ability to be packaged into high surface area modules; g) manufacturing reproducibility.

Next chapter describes common adsorbents employed in membrane technologies, highlighting for each of them advantages and disadvantages, until to arrive to the most recent advances proposed in the field of membranes.

Chapter 3

Common materials employed in membrane technologies

The quality of a membrane and consequently of the entire technology depend in the first instance by the choice of the membrane material, since material is responsible for membrane separation performance, operational stability, process design and cost. According to the type of material, membranes can be divided in organic, inorganic, and mixed-matrix membranes (MMMs).

3.1 Organic membranes

Organic membranes are often referred as polymeric membranes, being polymers the most employed organic materials in the field of membranes (only exception is represented by liquid membranes). Despite the huge number of natural and synthetic polymers currently available, organic membranes choose from a very little group of polymers, made up as follows: polysulfone (PSU), polyethersulfone (PES), polyvinylidene fluoride (PVDF), polyacrylonitrile (PAN), poly vinyl alcohol (PVA), polyimide (PI), polytetrafluoroethylene (PTFE), polypropylene (PP), cellulose acetate (CA), cellulose nitrates and cellulose regenerated [154–159]. Polymeric membranes are characterized by an excellent mechanical strength, good selectivity, wide range of temperature (20°C - 150°C) and pressure (up to 137 bar), thus they are widely employed in water purification and desalination processes. In general, permeability and selectivity in these membranes are inversely proportional: the more permeable, the less selective and viceversa. Among polymers above mentioned, PSU and PES present the best characteristics in terms of permeability, selectivity of permeate, mechanical stability and chemical resistance. Just to give some data: the glass transition temperature T_g for PES is equal to 225°C, PSU resist to different oxidation and pH conditions. Thanks to these properties, PES and PSU are the most employed polymers in ultrafiltration processes and the best supports in nanofiltration and reverse osmosis. Concerning microfiltration, best candidates are instead PP and PVDF. In all these cases, the choice of the polymer aims to ensure the best possible performances of the separation process, whose

operational conditions depends on the type of the process itself (MF, UF, NF etc.). Anyway, it is truly difficult find a polymer which satisfies simultaneously all the necessary requirements for a good membrane, which means mechanical strength, chemical/thermal stability, oxidation/pH resistance. In the recent years, several efforts have been done to improve polymeric membranes performances, both in terms of permeation flux and operation stability pressure and in terms of pollution resistance and membrane service life. Being widely hydrophobic (except for cellulose and its derivatives), one of the major drawbacks coming from these polymers is the high tendency of polymeric membranes to fouling, primarily caused by organics and inorganics, proteins, microorganisms and microbial communities depositing on the membrane surface. Because of fouling, selectivity decreases, as well as membrane lifetime, operation costs become greater, making the separation process unsustainable. In response to this problem, the attention of scientific research shifted in the last years to the application of surface modification methods [157,160–163], such as plasma treatment, blending, cross-linking, surface grafting, surfactant methods, surface segregation methods with amphiphilic block copolymers, surface coatings with hydrophilic polymers and gamma ray and UV irradiation, in order to make polymeric membranes more hydrophilic. In addition to less hydrophobicity, membranes from self-assembly of block copolymers are characterized by high selectivity, due to their narrow pore-size distribution, high porosity and consequently high permeability. Recent developments also include the fabrication of tunable membranes [164–166], obtained mixing a certain percentage of additives (usually polymers) in the pristine polymers, whose conformational state can change depending on the process operational conditions, such as pH or temperature. For example, polymethyl methacrylate (PMMA) and polyacrylic acid (PAA) can induce shrinking–swelling of the membrane pores by deionization of carboxyl group (–COOH) and ionization ($–COO^-$) around their pK_a value, rendering membrane permeability affected by pH, ions and solute concentrations [164]. Functionalization with poly(N-vinylcaprolactam)-based microgels, applied as coating to commercially available hollow-fiber membranes for MF and UF, produces a reversible

thermoresponsive permeability and rejection [167]. With a supply of about 700 billion tons per year, cellulose is the most abundant natural biomaterial on Earth. Its availability and natural origin, as well as its low cost and hydrophilicity have led cellulose to be one of the best promising materials in the field of membranes, so much that cellulose-based membranes are the first type of polymeric membranes to receive industrial application. It was 1963 when Loeb and Sourirajan proposed for the first time an asymmetric CA membrane exhibiting high salt rejection and flux values [168]. Despite the good hydrophilicity, which avoids the problem of fouling, cellulose acetate membranes suffer of long-term chemical, biological and thermal stability, being intolerant to chlorine and able to work only in specific ranges of pH and temperature. To obtain the best from each material and do not lose typical cellulose-based membranes hydrophilicity, currently cellulose and its derivatives are often used as additives of hydrophobic polymers, such us PVDF, PSF, PES, with the purpose of preparing membranes with good chemical resistance, thermal stability, mechanical strength and enhanced hydrophilicity [169–171].

3.2 Inorganic membranes

Offering high thermal, chemical and mechanical stabilities, inorganic membranes, obtained from oxides, metals and ceramics, represent a good alternative to polymeric membranes. With a higher chemical stability and organic solvent resistance, ceramics are, among inorganics, the most employed materials in the fabrication of membranes, prevalently used in microfiltration processes [158,172]. Generally, the morphology of ceramic membranes consists of multiple layers, positioned on a coarse support and opportunely spaced through smaller particles which control and determine the final pore size of the membrane itself. Desired physical and electrochemical properties, such as strength, crystallinity, density, thermal and electrical conductivity, require a starting thermal treatment with temperatures even going over 1000°C. Al_2O_3, ZrO_2, TiO_2, SiO_2, SiC, ZnO are the most common materials of which ceramic membranes are made of [173–176]. Among them, particular attention has been paid

in recent years to TiO_2 and TiO_2-composites due to its high photocatalytic efficiency, especially useful in wastewater remediation practices, and its superhydrophilicity, which allows to avoid the problem of membrane fouling [173,177,178]. Ceramic membranes overcome the two major disadvantages coming from polymeric membranes, i.e. fouling and low chemical stability. On the other hand, ceramic membranes are characterized by lower permeability, due to the greater layer thickness, and are recommended for small-scale processes due to their high cost of production. In brief, ceramic and polymeric membranes are the one the complement of the other, opportunely employed depending on the specific requirement of the separation process [174,179]. Recently, good developments have regarded the use of zeolites [180]. Zeolites are crystalline inorganic materials constituted of Si, Al and O, which, disposing in a tetrahedron, are responsible of specific cavities and channels in the material, making zeolites characterized by high porosity with well-established pore dimensions at molecular level. Therefore, these materials exhibit high adsorption capacity and molecular sieving ability, becoming good candidates in the fabrication of membranes to be used in gas separations, reverse osmosis, pervaporation, catalytic membrane reactors and removal of heavy metals and ammonium for water softening [180–184]. Anyway, high production costs and the presence in the material structure of intercrystalline defects, which lower the reproducibility of membrane performances, still remain the two big constraints to the wide use of zeolites in membrane technologies. Along with zeolites, much attention has also been paid to carbon nanotubes (CNTs) in the last years. Because part of this project is focused on development of carbon nanotubes membranes, it is essential to provide much space to these materials in order to better elucidate their potentiality. For this reason, next paragraph is totally devoted on CNTs and CNTs membranes.

3.3 Carbon Nanotubes Membranes

Carbon nanotubes (CNTs) are one of the allotropes of carbon, discovered for the first time in 1991 by Sumio Ijima, while he was working with arc-discharge technique in his laboratory [185]. CNTs are tubular structures characterized by nanometric diameters and lengths of the order of microns, commonly depicted as graphite sheets rolled up in a cylinder [186]. Depending on the number of graphite sheets, CNTs can be classified in Single-Walled Carbon Nanotubes (SWCNTs o SWNTs), if the sheet is just one, and Multi-Walled Carbon Nanotubes (MWCNTs o MWNTs), if the sheets are more than one (*Fig. 7*). Table 3 shows SWNTs and MWNTs principal characteristics. Because CNTs are constituted entirely of sp^2 carbon atoms, carbon nanotubes exhibit high thermal and electrical conductivity and excellent mechanical properties [187]. Some remarkable characteristics include C-C bonds 100 times stronger than those in steel and electrical and thermal conductivities higher than copper (2 orders of magnitude above) and diamond, respectively. Due to their extraordinary properties, CNTs have been proposed in a lot of applications, such as field emission displays, sensors, high-strength conductive composites, hydrogen storage devices and membrane technologies [188–194].

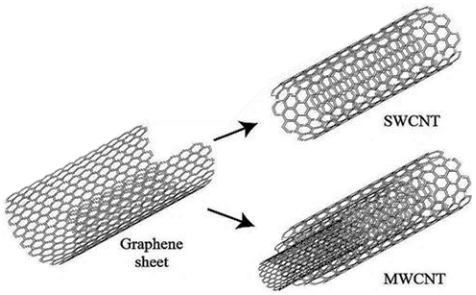

Fig. 7. Schematic representation of SWNTs and MWNTs.

Table 3. Most relevant characteristics of SWNTs and MWNTs.

	SWNTs	MWNTs
Purity	Poor	High
Bulk synthesis	Difficult	Easy
Specific gravity (g cm^{-3})	0.8	1.8
Thermal stability in air (°C)	>600	>600
Thermal conductivity (W m^{-1} K^{-1})	6000	2000
Electrical conductivity (S cm^{-1})	10^2-10^6	10^3-10^5
Electron mobility (cm^2 Vs^{-1})	10^5	10^4-10^5

Carbon nanotubes synthesis can be carried out through three different techniques: arc-discharge, laser ablation and chemical vapor deposition (CVD)

[195,196]. Due to its relative low cost, high production yields with elevated purity and easy scale-up, CVD is actually the most employed technique for CNTs production [197]. Chemical vapor deposition can be briefly resumed in two steps: 1) catalytic decomposition of organic molecules, which constitute the carbon source, in vapor phase; 2) gradual and continuous deposition of carbon atoms on a specific support. Decomposition usually occurs at temperatures around 700°C - 900°C, even if several efforts have been done to lower thermal conditions required by the process such as thermal CVD (TCVD) or plasma-enhanced CVD (PECVD) [197,198]. Regarding organic molecules, best carbon sources are hydrocarbons because, at molecular mass parity with organics such as alkenes and alkynes, they have the higher carbon weight percentage per molecule. Currently, methane, ethylene and carbon dioxide are the most employed carbon precursors [199,200]. The heart of CVD resides in the activation of the catalyst, which is responsible for the decomposition process but also for the high temperatures. In this direction, temperature reactor should be properly selected in order to activate catalyst without bringing to its fusion. Most employed catalysts are transition metals, such as Fe, Ni and Co, in which carbon is soluble even at high temperatures, or alloys in the form of thin films or nanoparticles, useful to increase the surface area of the catalyst [200,201]. Catalysts are often deposited on supports such as graphite, quartz or silicon, acting not only as support but also promoting their catalytic power [200]. Going inside CVD process, bonds breaking of organic molecules generates C atoms and hydrogenated species. The latest are easily removed from the reactor while C atoms, being soluble in the catalyst, deposit on it. Deposition continues and when solubility limit, strictly dependent on the type of catalyst and temperature, is reached, C atoms start to crystallize on the catalyst surface forming a cylinder-type network, i.e. CNTs grow. Catalyst-substrate interactions govern growth mechanism of carbon nanotubes (*Fig. 8*). In tip-growth model, weak interactions between C and catalyst allow carbon atoms to slide on both sides of catalyst surface where, step by step, addition by addition, aided by low catalyst-substrate interactions, carbon nanotubes grow, pushing catalyst to the top and separating it from the substrate. When the metallic

surface is entirely covered by C atoms, the process is concluded and carbon nanotubes stop to grow. In base-growth model, strong interactions between substrate and catalyst stop carbon atoms on both sides of surface catalyst to push it away from the substrate itself. Consequently, C atoms are forced to accumulate on the catalyst surface forming a starting dome on which carbon nanotubes can finally grow. Independently of the model (tip-growth or base-growth), carbon nanotubes are synthesized directly on catalyst so chemical vapor deposition is considered a growth-in-place technique.

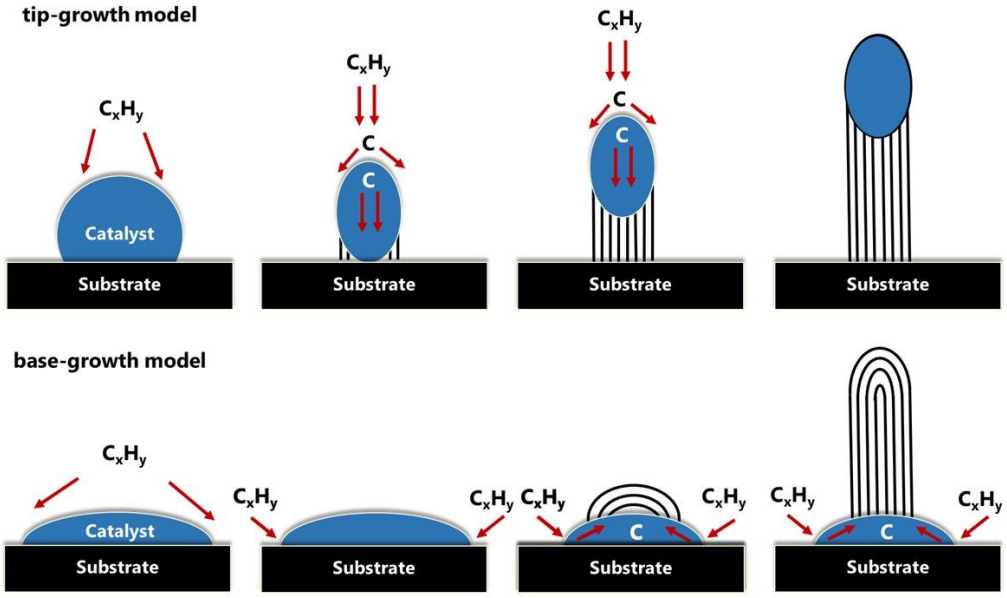

Fig. 8. Carbon nanotubes growth models in CVD.

Arc-discharge and laser ablation belong to the category of growth-then-place techniques [195–197]. During arc-discharge, an electric current is used to heat carbon electrodes to high temperatures, more than 1600°C, in total absence of oxygen. Adding a catalyst on one of two electrodes, carbon nanotubes can be obtained. Considering the high temperatures reached, arc-discharge technique produces carbon nanotubes with an excellent degree of crystallinity, ensuring better and superior mechanical and electrical properties. Anyway, the formation of other carbon products and the presence of catalyst residues, from which CNTs need to be separated, represent the principal disadvantage of this technique. Laser ablation working principle is very similar to arc-discharge technique. The difference lies in the fact that, in laser ablation, energy is

provided by a laser hitting a graphite-pellet containing the catalyst. Carbon and catalyst are vaporized and then condensed on a water-cooled copper collector, where carbon nanotubes form and grow. Considering the high temperatures (1200°C), also laser ablation produces carbon nanotubes characterized by very good crystallinity. After production, CNTs need to be purified in order to remove impurities such as catalyst particles, amorphous carbon from CNTs and soot. Attention is required and purification treatments must be conducted carefully since purification treatments often use chemical agents which can damage and shorten CNTs. The purification step is often followed by one of functionalization, during which capping operations and groups of molecules or commonly organic functional groups (-COOH, NH_2) are attached on CNTs surface. Considering the extraordinary potential of carbon nanotubes, these materials have been immediately employed in the fabrication of membranes [193,202,203]. Carbon nanotubes-based membranes can be essentially divided in a) freestanding CNTs membranes and b) mixed CNT membranes. The last ones are based on the addition of CNTs in the polymer backbone of the membrane so it will be better discussed in the subsequent paragraph, where a panoramic of mixed matrix membranes is presented. Depending on the organization of carbon nanotubes in the membranes, freestanding CNTs membranes are in turn divided in buckypapers (BPs), characterized by a random arrangement of CNTs in a large porous structure, and vertically aligned CNT (VA-CNT) membranes, where carbon nanotubes cylinders are disposed perpendicular to the membrane surface forcing the fluid to pass only inside the tube or between carbon bundles (*Fig. 9*). Considering the high cost of production of vertically aligned carbon nanotubes and the use of harsh chemicals to remove the supporting substrates on which aligned membranes are generally grown, the field of VA-CNT membranes is not too much explored [202]. In BPs, CNTs are randomly disposed originating a large porous network where van der Waals and pi-pi interactions are the only interactions to exist. Even if the lower energy of these interactions, the number of van der Waals interactions per unit volume is extremely high so buckypapers exhibit a very cohesive and strong structure with a large surface area. Lightweight, high porosity (60-70% of the total volume) and high flux,

together with excellent thermal and electrical conductivity are therefore the most important characteristics belonging to buckypapers[193,202], which can vaunt several applications such as sensors, artificial muscles, electrodes and filters [194,204–209].

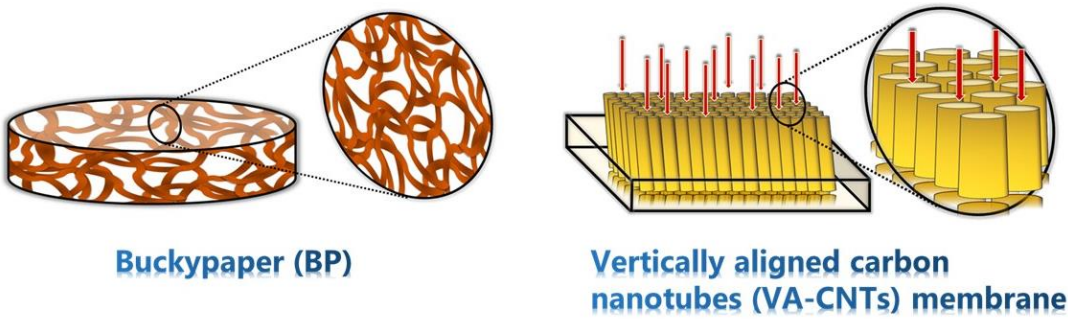

Fig. 9. Classification of carbon nanotubes membranes.

Because of their composition, made up of only C atoms, BP membranes show also a remarkable hydrophobicity, reason why carbon nanotubes membranes are ideal to use for desalination in membrane distillation processes [210]. On the other hand, this strong hydrophobic character represents a problem for BP application in water purification processes. For this reason, functionalized carbon nanotubes or other fillers are often added to improve hydrophilicity of these membranes [211,212]. Great potentialities have also been registered for anti-bacterial activity. Brady-Esétvez et al. (2008) have prepared a BP membrane exhibiting high removal of the model virus MS2 bacteriophage due to depth filtration and high retention of Escherichia coli cells due to size exclusion [213]. Electrospinning, layer-by-layer (LBL) deposition and vacuum assisted filtration are the most common techniques for BPs preparation even though, due to its ease of operation, vacuum assisted filtration is by far the most employed one. In vacuum assisted filtration, BP membranes are obtained by vacuum filtration of a CNTs dispersion on a specific support. Because of their composition, CNTs are extremely hydrophobic and, due to the strong interactions, are always aggregated in micrometric structures, better known as bundles, which resemble very well to miniature ropes. The crucial point of vacuum assisted filtration is undoubtedly represented by CNTs dispersions. BP membranes obtained from higher quantities of untangled nanotubes exhibit superior mechanical and

adsorption properties compared with those obtained by CNTs bundles. Because interactions between CNTs are strong, bundles can be broken making use of physical or chemical treatments. The first method consists in the sonication of CNTs dispersions for a certain period of time, depending on the ultrasonic power applied during the treatment (more power, less time). During sonication, acoustic waves spread inside the liquid forming micrometer sized bubbles which gradually grow through coalescence and diffusion. When the bubble dimensions become high enough to render them instable, bubbles collapse creating microjets of solvent hitting the solid with great force. These jets break the interactions which hold nanotubes in bundles, releasing them separately and resulting in better dispersions. Long periods of sonication are not advisable because the inner structure of carbon nanotube can be altered, introducing defects on the tube which can reduce their mechanical and electrical properties. Chemical treatments include the formation of covalent and non-covalent bonds [203]. Covalent functionalization modifies carbon nanotubes surface through the introduction of amino or carboxylic acid groups, thus reducing their hydrophobic character. In addition, these groups constitute perfect anchoring sites for larger molecules, such as enzymes or antibodies, which can bind much more strongly on CNTs surface and make possible the exploration of carbon nanotubes and carbon nanotubes membranes in much more fields. However, covalent functionalization often requires harsh conditions or harsh chemicals which can damage carbon nanotube structure by converting hybridization of some sp^2 carbons in sp^3 and thus lowering carbon nanotubes peculiar properties. When non-covalent functionalization is pursued, CNTs surface is modified through the attachment of amphiphilic dispersant molecules, such as polymers or surfactants, involving only adsorption processes. Therefore, while the hydrophobic part binds to carbon nanotubes, the polar component of these molecules interacts with solvent through hydrogen bonding and dipole-dipole interactions, favoring a major solubilization of CNTs. Different dispersant molecules have been investigated to improve CNTs dispersions. Due to their composition and molecular partition into a polar (head) and apolar component (tail), surfactants are certainly the most employed dispersants [214,215].

Octylphenolethoxylate, better known as Triton X-100 (Trix), but also sodium dodecylsulfate (SDS) and sodium dodecylbenzenesulfonate (NaDDBS) are the most common surfactants, producing great results even at low concentrations (0.2% w/v of CNTs dispersion). Together with surfactants, biomolecules, such as DNA or lysozyme, were also investigated to improve CNTs dispersions [216]. The great advantage of using biomolecules is due to their lack of toxicity compared with surfactants or other dispersant molecules. Independent of the class, CNTs dispersions containing dispersant molecules have to be stable for long time, ensuring a great solubilization of carbon nanotubes. Compared with sonication or covalent functionalization, non-covalent functionalization does not damage the structure of CNTs, which preserve entirely their properties. The only drawback is to remove molecular dispersant once BP has been filtered. It requires an additional washing step, using a solvent whose affinity with the dispersant molecule is high, to remove all impurities. Vacuum assisted filtration is also well known as the wet method, mainly used in laboratories. In dry approach, instead, BP membranes are directly obtained from micro-molecular hydrocarbons during the process of CNTs production [193,194]. Even if membranes are large in size and costs are low, being therefore particularly useful for commercial purposes, the major drawback of this approach is represented by the high amounts of residual catalyst, which are responsible for the complex and heterogenous composition of BPs.

3.4 Mixed-matrix membranes

Mixed-matrix membranes (MMMs) are essentially composite membranes, developed with the purpose of overcoming the major drawbacks arising during separation processes with polymeric or inorganic membranes [158,217]. MMMs are obtained by dispersion of inorganic or inorganic/organic materials, acting as fillers, in polymeric membranes, in order to combine synergistically the excellent separation performance of fillers with the good processability of polymers, which still maintain their primary role in the formation of membrane backbone. The well-known Robeson plot, which establishes for gas separation processes the upper limit (*upper bound*) of membrane selectivity for each value

of permeability (more permeable, less selective), can be therefore rewritten by the introduction of MMMs which move the upper bound limit towards higher values of selectivity and permeability, ensuring better membrane performances (*Fig. 10*) [218]. Since 1970, when 5A zeolite was incorporated in a rubbery polymer to enhance membrane properties in gas separation processes [219], different types of fillers have been proposed including metal oxides, activated carbon, various zeolites, mesoporous silica and carbon molecular sieves. However, due to poor polymer–filler compatibility, these first mixed-matrix membranes exhibited defects and nonselective voids, with a significant loss of selectivity.

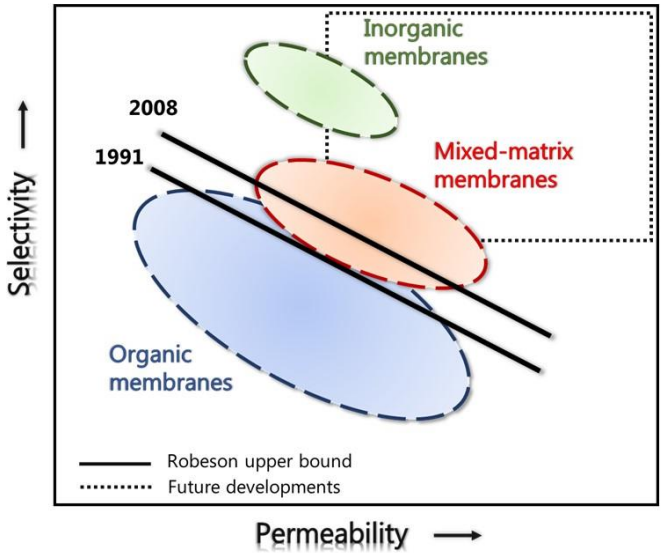

Fig. 10. Robeson plot.

To overcome these problematics, attention has moved towards the introduction of nano-sized inorganic particles and advanced porous materials, such as graphene oxide (GO), TiO_2, CNTs, metal-organic frameworks (MOFs), covalent organic frameworks (COFs), porous organic cages (POCs) and so on [217,220]. With their large surface area, nano-sized materials and polymer can establish a major number of interfacial interactions, resulting in an enhancement of thermal and mechanical properties of the composite membrane. In addition, the presence of functional groups such as carbonyl or hydroxyl on polymer matrix favors interactions with nano-sized materials through the formation of hydrogen bonds, thus improving the level of mixing between them. It has been shown that the incorporation of nanomaterials in polymer membranes produces not

only better mechanical properties but ensure also higher values of permeate flux and surface wettability on the final composite. Following, a brief description of nano-sized materials commonly used in MMMs is proposed, highlighting principal pros and cons of each one of them.

Metal-organic frameworks (MOFs). MOFs are hybrid materials whose porous structure is originated by the presence of inorganic nodes (metals) connected to each other through polytopic organic linkers via coordination bonds [220]. Due to their elevated porosity, tunable pore architectures and diversified pool of chemical functional groups, MOFs have been included in a lot of applications, such as catalysis, chemical sensing, gas storage and separation, proton conduction, thin film devices and biomedical imaging [221–224]. Compared with their inorganic counterpart, i.e. zeolites, MOFs can establish better interactions with polymer chains due to the presence of various organic ligands and chemical functionalities, avoiding defects or nonselective voids in the final MMM. In addition, the judicious design of MOF fillers with specific functional groups, such as amine, hydroxyl, sulfonic, both before or after the incorporation in MMMs, can enhance polymer-filler interactions and, contemporarily, direct MOF selectivity towards certain chemical species over others. MOFs can also be different in terms of pore volumes, pore shapes and surface areas, other tunable characteristics which can be opportunely chosen and governed to fabricate membranes of suitable selectivity and permeability. Considering this huge plethora of possibilities, MOFs are often subclassified as a function of organic ligands and metals occurring in their structure. In this regard, most common examples are ZIFs, the Materials Institute Lavoisier (MIL) series, MOF-74 series, University of Oslo-66 (UiO-66) series and copper-based MOFs (Cu-MOFs) [220] (*Fig. 11*). In ZIFs, the metal cations Zn^{2+} and Co^{2+} are coordinated by imidazolate groups and its derivatives, originating frameworks which are very similar with those of zeolites. ZIFs exhibit different chemical functionalities, tunable pore structures and exceptional chemical resistance toward organic solvents and neutral or weakly basic aqueous solutions as well as facile synthesis process, becoming one of the most employed MOFs subclasses in membrane

technologies [225,226]. To enhance polymer-ZIFs interactions, which represent the major drawback coming from this type of incorporation, different strategies such as ammonia or hydroxyl functionalization, polymer coating and polymer grafting have been proposed, showing good results [220,227,228].

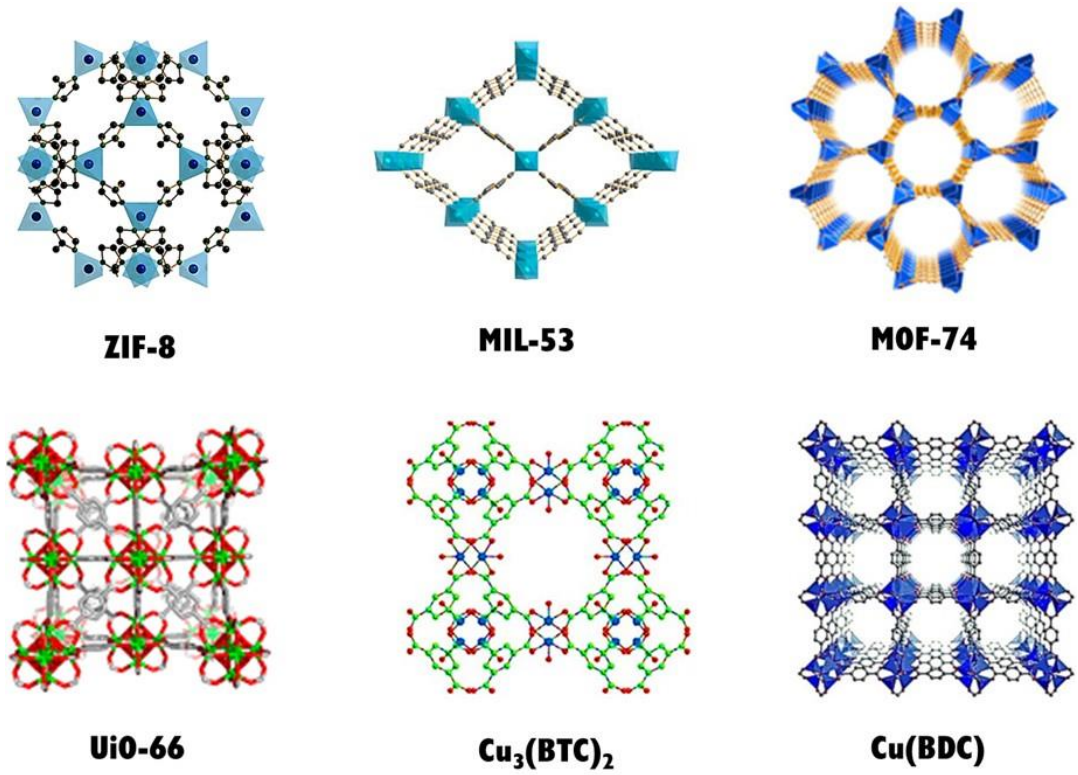

Fig. 11. Base structures of some typical MOFs.

MIL series takes its name from Materials Institute Lavoisier, the institution which first developed and synthesized this class of MOFs. MOFs belonging to this series are characterized by high stability and flexibility, often exhibiting a structural conformational change during adsorption/desorption of guests, referred as "breathing effect". This effect is particularly evident for MIL-53 family, where the adsorption of hydrocarbons or gases such as CO_2 and H_2S results in the alteration of pore size and geometry of MOF. The peculiar feature of MOF-74 series is to be ascribed to its organic ligand, 2,5-dioxido-1,4-benzenedicarboxylate ($dobdc^{4-}$), which, coordinating M^{2+} metals (Mg^{2+}, Mn^{2+}, Fe^{2+}, Co^{2+}, Ni^{2+}, Cu^{2+} or Zn^{2+}), due to its specific chemical structure, originates 1D hexagonal channels rich of unsaturated metal sites, becoming ideal cavities for the selective adsorption of polar and non-polar gases such as CO_2, H_2S, N_2, CH_4. MOFs of UiO-66 series show rich chemical functionality, high porosity and

excellent stability in various organic solvents and water. Since 2008, when the first UiO-66 has been synthesized [229], numerous studies have been done to enhance their properties, especially by introducing a lot of functional groups, as $-(COOH)_2$, $-(COOH)_4$, $-F_4$, $-NH_2$, $-(OH)_2$, $-(OCH_2CH_3)_2$, which enable them applications in various fields, such as catalysis, drug delivery, bioimaging and separation [220,230,231]. Copper-based MOFs (Cu-MOFs) can be essentially classified in $Cu_3(BTC)_2$, also known as HKUST-1, from Hong Kong University of Science and Technology, and CuBDC, where the acronyms BTC and BDC stand for benzene-1,3,5-tricarboxylate and benzene-1,4-dicarboxylate, respectively. The principal difference between $Cu_3(BTC)_2$ and CuBDC resides in their structure: $Cu_3(BTC)_2$ shows a 3D framework intersected by 3D channels with a pore size of 9Å, while CuBDC has a 2D layered structure, where each layer is porous and pore dimensions are equal to 5.2Å.

Porous organic frameworks (POF)s. POFs represent the pure organic counterpart of MOFs, being made of only organic blocks held together by strong covalent bonds [217,220]. POFs exhibit good thermal and chemical stability and rich chemical functionality with structures characterized by high surface area and different pore sizes. Anyway, due to the presence of strong covalent bonds, structures in POFs loss most of that flexibility belonging to MOFs and become more rigid. On the other hand, the pure organic nature of POFs allows much better polymer-filler interactions, completely avoiding cracks or defects in the final membrane. Based on their crystallinity, POFs can be classified in amorphous and high crystalline materials. The former includes polymers of intrinsic microporosity (PIMs), conjugated microporous polymers (CMPs), porous aromatic frameworks (PAFs) and hyper-cross-linked polymers (HCPs); the latter is represented by covalent organic frameworks (COFs). COFs have been attracted much attention due to their high crystallinity and good porosity. After their discovery in 2005 [232], COFs have been progressively developed in order to completely bypass the problems arising from the first generation of these materials, which, being based on boron linkages, showed limited resistance in water, acid and alcohols. Currently, imine-based COFs exhibit much better

chemical stability, even if crystallinity is slightly reduced [233]. Compared with their crystalline counterparts, amorphous POFs are characterized by excellent chemical stability towards harsh conditions. HCPs are the youngest materials to be introduced in this field, with their first application going back to 2016. They are non-expensive materials with simple synthesis process but, considering their young age, they still suffer of poor surface area and irregular pore networks.

Porous molecular compounds. Porous molecular compounds are of recent discovery in the field of MMMs [220]. Growing attention in these materials is to be ascribed to their great solubility in most common solvents used for dissolving the polymer matrix, since MOFs and POFs solubility and chemical stability often reside into a limited group of solvents. For example, it has been shown that immersion in water for 24h causes a loss of crystallinity in $Cu_3(BTC)_2$, reducing its BET surface area from 1,340 to 647 m^2g^{-1} [234]. Most common employed porous molecular compounds are metal-organic cages (MOCs) and porous organic cages (POCs). As their names suggest, MOCs are constituted of metal nodes interconnected by coordination bonds with organic ligands, POCs are completely made of organic blocks. As MOFs and POFs, they exhibit high surface area, high porosity and, as previously mentioned, good solubility in a greater number of solvents. Anyway, with only ten years of research behind, the use of MOCs and POCs as fillers in mixed-matrix membranes is still in its infancy, so next years will be fundamental in the improvement and enhancement of these novel composites.

Inorganic nanoparticles. The category of inorganic nanoparticles is particularly wide. Most relevant fillers employed in MMMs are carbon nanotubes (CNTs), graphene oxide (GO), silica (SiO_2) and titanium dioxide (TiO_2) [235]. Literature is rich of works where high thermal and mechanical properties of CNTs have been exploited with the objective of reinforcing polymeric membranes [202,236,237]. The incorporation of CNTs in the polymer matrix brings to the improvement of final composite properties, exhibiting enhanced salt rejection, major water flux, favored by transport along CNTs tubes, and improved biofouling resistance,

deactivating bacteria and viruses and lowering operational costs of the entire process. In addition, functionalization of CNTs can expand notably the application of these membranes, which can be judicious prepared controlling their properties, in order to satisfy various needs which can occur during separation processes [238]. With its considerable number of covalently attached oxygen-containing groups (epoxy, carbonyl, carboxyl and hydroxyl), graphene oxide (GO) is often employed as a substitute of functionalized-CNTs to enhance membrane hydrophilicity. It also possesses a good compatibility in water, better than CNTs, high surface area and mechanical stability, good electron conductivity, electro- and magneto-controlled ion transport. GO/mixed-matrix membranes are characterized by better mechanical strength and enhanced rejection of gases such N_2 and O_2 [239,240]. SiO_2 is widely employed as an inorganic additive in MMMs due to its mild reactivity, availability of different chemical functionalities, nontoxic nature, convenient operation and mechanical strength. Polymeric membranes, opportunely doped with silica particles, show an improvement of mechanical strength and thermal stability [235]. Great attention has been addressed to TiO_2 nanoparticles, primarily due to their photocatalytic activity, thus promoting decomposition of organic pollutants and reducing, or avoiding, the problem of membrane fouling [241–243]. Mixed-matrix membranes containing TiO_2, essentially based on the exploitation of TiO_2 photocatalytic activity, can also count on the easily tunable morphology and suitable chemical resistance of this inorganic filler, being particularly employed in filtration processes where membrane fouling is the "deal breaker". Other inorganic nanoparticles, such as $CaCO_3$, Ag, Fe_3O_4, Fe-Mn and different types of zeolites, have also been explored as potential fillers in mixed-matrix membranes, but there are still few works that can be found in literature.

Considering the huge number of possibilities and the variety of separation processes, it is worth noting that polymer matrices and fillers can be opportunely combined to better address specific needs coming from each separation process, in order to obtain the best results as possible. Considering the importance of membrane properties in the development of successful

technologies, next chapter is focused on a brief description of the most relevant techniques employed for membrane characterization from a structural, chemical and physical point of view.

Chapter 4

Common techniques employed in membrane characterization

The efficiency of a separation process is closely related to the membrane employed, which has to ensure best performances in terms of permeability, selectivity, rejection, flux, fouling and lifetime. All these parameters strictly depend on membrane surface properties, which in turn are affected from membrane type and membrane materials as well as from interactions between membrane and solute. Therefore, structural, chemical and physical characterization of membranes is strongly required. A short presentation of the most common employed techniques is provided below [158,244,245].

Scanning electron microscopy (SEM). With a resolution ranging from 10 to 50 nm, depending on the owned equipment, SEM is useful to investigate the microstructure of a membrane material, directly giving information about its morphology. Measurement is done in vacuum by exposing the membrane surface to a beam of electrons, previously accelerated at a certain voltage (usually 10-20 kV). Because of the vacuum, the sample must be dried before the measurement and then it is positioned on a support, called *stub*, and coated with an ultrathin layer of conductive material, such as gold, platinum, or carbon. The electrons beam hits the sample and scattered electrons (secondary electrons) are collected on detector, generating an image. It is worth noting that SEM records scattered electrons, thus it is good practice to analyze samples of micrometer thicknesses if inner morphology must be investigated. In addition, dried samples are required, and this can be a problem when hydrophilic polymers are used during membrane preparation, since dehydration can alter the membrane inner structure. Thicknesses can also be measured by SEM through the analysis of specimen cross-sections. In order to avoid defects due to fracture, sample are often cut cryogenically, under liquid nitrogen. Even if it is not the most common method, SEM can also be used to estimate porosity and pore size distribution of membranes.

Transmission electron microscopy (TEM). High resolution analysis can be done by TEM. Measurement is very similar to SEM, except for the fact that the image of membrane morphology is obtained by collecting transmitted electrons by sample. TEM attains almost atomic resolution, being particularly useful to examine thin fine samples smaller than a single column of atoms. Even if resolution is better, TEM is less employed due to the large instrument size, high operation cost and major difficulty in sample preparation, which has to be embedded with epoxy resin and then opportunely cut under cryogenic conditions before the analysis can start.

Atomic force microscopy (AFM). Possessing high atomic resolution, AFM is a tool for imaging and measuring any type of surface (polymer glass, composite, ceramic, biological samples) at the nanoscale level, prior obtaining data about surface roughness, pore size and its distribution, nodule size and aggregate size occurring at the surface of the investigated material. Information is collected through a sharp probe, positioned on a tip of a cantilever and having a radius smaller than 10 nm, which scans the surface material applying a constant force, generally around 5 N/m. The cantilever, usually made of silicon or silicon nitrates, deflects during the surface scanning because of interactions between the tip and the forces on surface material, which can be Van der Waals forces, capillary forces, magnetic and electrostatic forces. Deflection is then measured by a laser beam reflected onto a photodiode and used to create the final surface image. Because forces can have different intensity values, in order to avoid probe breaking, AFM can count on three various operating modes (contact, noncontact, tapping), all conducted at air condition. As the name suggests, during contact mode the tip scans the sample surface in constant contact, but this operating mode can often result detrimental for the sample, since surface damaging can easily occur. As a result, membrane surface investigation is usually conducted in tapping mode. The cantilever oscillates in close proximity of sample surface, coming into contact with it only for brief instants, depending on the cantilever oscillation frequency. Amplitude damping together with the measurement of the position and deflection of the cantilever are then elaborated

to create the surface image. Membrane porosity can also be measured by AFM. However, low surface roughness is required since depression on membrane surfaces can easily be mistaken with pores.

Contact angle (CA) measurement. Water contact angle is a measurement of membrane wettability. This parameter is particularly important in the evaluation of membrane permeability since higher degree of wettability means greater amount of water, and thus greater membrane flux. In addition, high wettability degree enables comparatively low-pressure working conditions, leading to a reduction of energy consumption. Even if membrane water uptake can also be used, consisting in a simple difference between the weights of dry and water saturated samples, membrane wettability is usually evaluated by contact angle measurements. This measurement can be operated in static (sessile drop method) or dynamic mode (captive bubble method), even if, due to its ease of operation and better data accuracy, static mode is the most accredited one. Typically, a droplet of deionized water (2-5 μL) is deposited onto a membrane surface, and the contact angle formed between the droplet and the surface is measured by using a goniometer. The angle amplitude depends on the forces acting on membrane surface. If the cohesion forces, governing bonds inside the material, are stronger than adhesion forces, which are the forces between water and membrane surface, wetting is difficult, and the water droplet remains almost unaltered. On the contrary, if adhesion forces exceed cohesion ones, wetting occurs and the water droplet spreads on the surface, leading to a lower contact angle. In general, when contact angles are smaller than 90°, water intrusion in membrane pores can occur without additional pressure and hydrophilicity increases with decreasing contact angle values, until reaching the ideal limit of zero contact angle, corresponding to a completely hydrophilic membrane. Contact angle measurements can be affected by chemical composition and heterogeneity, surface roughness, swelling, adsorption and desorption processes, energy level of surface electrons and surface configuration change, therefore it is recommendable to repeat

measurements several times in order to make sure that reproducibility is observed.

Zeta potential measurement. Surface charge is the electric charge at the membrane/liquid interface. This property controls membrane adsorption processes through attractions or repulsions of chemical species, both neutral or charged, and is responsible for many colloidal properties. In addition, changes in surface charge can be used to control fouling behavior in order to choose operational conditions where this phenomenon is reduced to a minimum. Considering the large diversity of materials which can be employed in the preparation of membranes, surface charge strictly depends on the material chemical nature and on solution conditions, such as pH, ionic strength and ionic composition. In a common solution, electric charge on membrane surface attracts opposite charge particles from the bulk, which in turn produce a thin countercharge layer shielding membrane electric surface charge. This is often referred as electrical double layer and because the countercharge layer possesses a charge equal to the electric surface charge but opposite in sign, the complete structure is practically neutral. Zeta potential (ζ) measures net surface charge and charge distribution inside the electrical double layer. It can be calculated by the Helmoltz–Schmolukovski equation, shown below:

$$\frac{E}{p} = \frac{\varepsilon \varepsilon_0 \zeta}{\lambda \eta} \tag{4.1}$$

where ε and ε_0 are respectively the solution and vacuum permittivity, λ is the electrolyte conductivity, η the viscosity of the electrolyte solution, p the applied pressure driving the flow and E the streaming potential generated by electrolyte flow through a capillary channel. Considering that E, p and λ are measured experimentally, ε_0 is a constant and ε and η are calculated from temperature measurements, zeta potential can be easily obtained by applying the inverse formula. The isoelectric point, i.e. the pH value at which streaming potential is zero, can also be determined by zeta potential measurement.

Thermal gravimetric analysis (TGA). Because membrane technologies often require high temperatures, the investigation of membrane thermal stability is extremely important, just to avoid the possibility that decomposition or damage can occur, especially during a separation process. TGA is a technique that monitors physical and chemical changes of the sample as a function of increasing temperature, letting heating rate constant, or as a function of time, while temperature or mass loss are kept constant. This technique is useful for the investigation of some properties of glasses, ceramics, polymers, plastics and composite materials. It is worth noting that TGA requires a higher degree of precision for the measurements of mass, temperature and temperature changes.

X-Ray diffraction (XRD). X-Ray diffraction is particularly useful for the analysis of crystalline properties of nanoparticles in mixed-matrix membranes. Generally, the pattern of diffraction is recorded over a specific degree range, depending on the type of filler employed.

Structural and chemical composition of membranes can also be accompanied by spectroscopic measurements, such as IR, Raman and XPS (X-Ray photoelectron spectroscopy). All these techniques contribute to characterization of polymeric membranes and to the monitoring of surface modification and biofouling.

In conclusion, the efficiency of a separation process depends on the correct choice of membrane materials and on their adequate characterization through the techniques described above. All these factors contribute to the success of the adsorption process, which represents exactly the core of each separation technology. Therefore, next chapter briefly focuses on adsorption processes from a thermodynamic and kinetic point of view, highlighting how they can be correctly studied and implemented, properly choosing and considering all the parameters taking part in these processes.

Chapter 5

Adsorption theory

The process of adsorption arises each time a mass transfer occurs between two in contact phases, of which one is always a solid and the other one is a fluid (liquid or gas) [246]. The fluid phase contains the chemicals (adsorbates) to be removed by adsorption on a solid phase, also known as adsorbent. Considering that in the greatest amount of adsorption processes the fluid phase is water, attention will be focused only on solid-liquid adsorption processes.

Once in contact, the adsorbate starts to partition between the two phases and the process goes on until the equilibrium is reached, i.e. an equal quantity of adsorbate is adsorbed on the solid phase and at the same time another equal one is released in the liquid phase, thus concentration does no longer change.

At equilibrium, adsorption processes can be described by the following equation:

$$A_s \rightleftarrows A_l \tag{5.1}$$

where A_s and A_l are respectively the amount of adsorbate on the solid and in the liquid phase. This partitioning of the adsorbate strictly depends on the affinity degree of the adsorbate with the solid and liquid phase. Bearing in mind the scope of adsorption processes, adsorbate must have a major affinity degree with the adsorbent. According to the type of interactions which can be established between adsorbent and adsorbate, adsorption can be classified in chemical adsorption and physical adsorption. Chemical adsorption, also known chemisorption, involves high energy interactions (40-800 KJ/mol) since, due to electron transfer, the adsorbate binds the adsorbent through the formation of covalent or ionic bonds. If chemisorption occurs, desorption is very difficult and the process is considered irreversible. On the contrary, in physical adsorption or physisorption, energies involved are low, ranging from 5 to 40 KJ/mol, and interactions can be electrostatic, van der Waals, dipole-dipole or hydrogen bond type. Physisorption is a reversible process, thus desorption is possible. As before mentioned, the choice of the adsorbent material is fundamental for the good outcome of the adsorption process. From this perspective, a good adsorbent should have the following characteristics: efficiency, high adsorption

capacity, high surface area and pore volume, mechanical, chemical, and thermal stability, availability, low cost, ease of desorption and reuse, and able to provide a fast kinetics.

In a laboratory scale, in order to test the quality of the adsorbent and establish some operational parameters such as pH, temperature, operation time and amount of adsorbent, adsorption experiments are usually conducted in discontinuous batch systems. The adsorbent is put into contact with a solution of the adsorbate and the system is left under stirring at constant temperature until the equilibrium is reached. Starting from an initial adsorbate concentration C_0 and a solution volume V_0, at equilibrium, due to adsorption process, new values of adsorbate concentration and solution volume should be observed, referred respectively C_e and V_e. If q_0 and q_e are the adsorbate amounts entrapped by the adsorbent at time zero and at equilibrium, respectively, the global mass balance of the adsorbate is represented by the following equation:

$$C_0V_0 + q_0m = C_eV_e + q_em \tag{5.2}$$

where m is the mass of the adsorbent. For a virgin adsorbent, q_0 is zero so the term q_0m can be removed from equation (5.2). In addition, the volume variation of the solution, due to aliquot sampling for adsorbate quantification, can be considered negligible so $V_0 = V_e = V$. Rearranging equation (5.2), q_e can be isolated:

$$q_e = \frac{(C_0 - C_e)V}{m} \tag{5.3}$$

Scale-up of adsorption experiments requires fixed bed systems. The solution of the adsorbate (influent) with initial concentration C_0 is pumped through a column of fixed height and packed with a certain amount of adsorbent (m), at a flow rate Q. During the operation, the adsorbate is captured from the adsorbent and the concentration of adsorbate (C_e) in the output solution (effluent) decreases. Equilibrium is achieved when $C_e = C_0$, so the bed saturation occurs and no more adsorption is possible.

Adsorption thermodynamics. At equilibrium, the relation between q_e, the amount of adsorbate caught by the adsorbent, and C_e, the amount of adsorbate remained in solution, is called adsorption isotherm [246]. From adsorption isotherm curves, it is possible to calculate the maximum adsorption capacity of a specific adsorbent under determined experimental conditions. In addition, these curves provide information about the interaction mechanism between adsorbent and adsorbate and are useful for the estimation of thermodynamic parameters, such as standard entropy change (ΔS^0), standard enthalpy change (ΔH^0) and standard Gibbs free energy change (ΔG^0). According to the initial slope, adsorption isotherms are classified into four classes (S, L, H and C) (*Fig. 12*) [247].

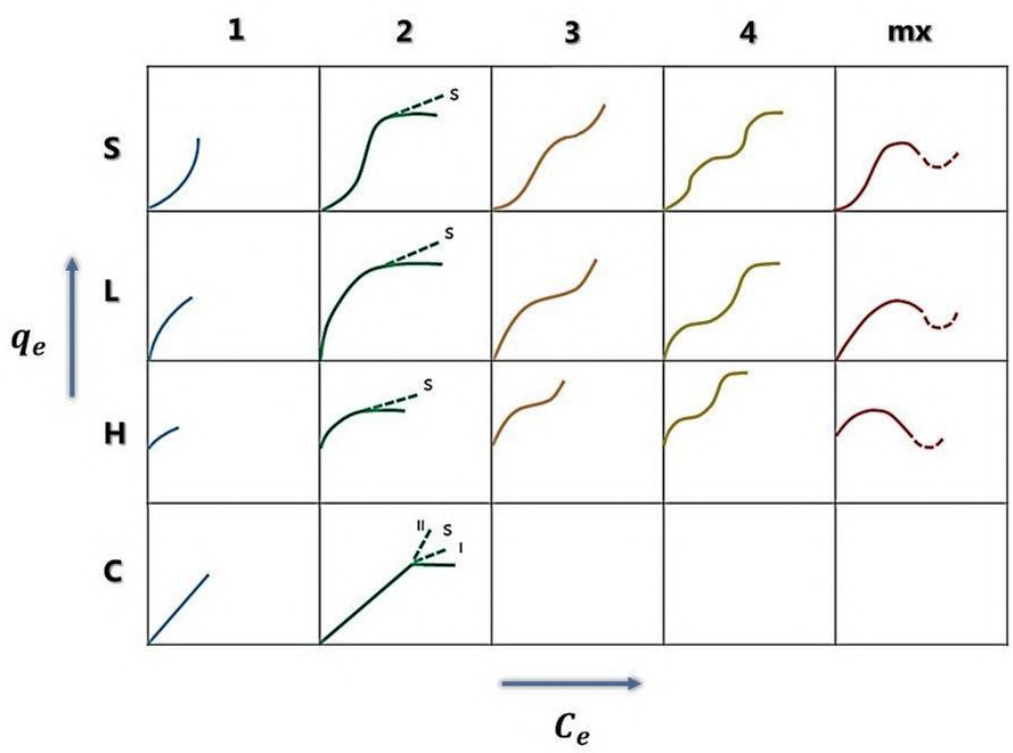

Fig. 12. Classification of adsorption isotherms.

Each class is in turn subclassified in function of the shape of the upper part of the curve and its slope variations. S curves or vertical orientation isotherms are characterized by an inclined slope followed by a vertical orientation. Generally, S curves appear when a) the adsorbate is monofunctional; b) the intermolecular attraction is moderate, leading molecules to pack in regular arrays, parallel or perpendicular to the adsorbent surface; c) for substrate sites, competition

between molecules of the solvent and adsorbate species is very strong. L curves, also called normal or "Langmuir" isotherms, are the most common found adsorption isotherms. The shape of these curves better highlights that in adsorption processes characterized by these curves adsorption capacity rises with increasing the solute concentration until reaching a maximum, corresponding to a total saturation of the adsorbent sites. Generally, molecules are adsorbed flat on the adsorbent surface and interactions between adsorbent and adsorbate are weak, such as Van der Waals forces. H curves or high affinity isotherms are typical of chemisorption processes or of adsorption processes through electrostatic forces. Curves are very similar to Langmuir ones but the first exhibit an initial pronounced vertical orientation, with q_e values usually higher than zero, even when adsorbate concentration in the solution is very low. C curves or constant partition isotherms display a linear behavior of concentration data suggesting that adsorption capacity is proportional to solute concentration. This behavior is preserved until a maximum value of adsorption capacity, over which an abrupt followed by a linear plateau occurs. This phenomenon can be due to 1) higher affinity of the adsorbate with the adsorbent compared to solvent; 2) even if the adsorbent sites are available, interactions between adsorbate and adsorbent are weak and are strictly dependent on liquid phase concentration. Mathematically, adsorption isotherms can be described by three different models: Henry's Law, Monolayer adsorption (Langmuir Isotherm) and Multilayer Adsorption (BET Isotherm). The first model is useful for low solute concentrations and adsorption is uniform on adsorbent surface, thus molecules are perfectly isolated from each other. By analogy with Henry's Law describing solubility of gases in liquid phases, adsorption isotherms in Henry's Law model are of the form below:

$$q_e = K_H C_e \tag{5.4}$$

where K_H is the Henry constant.

Langmuir isotherm model can be used when the following conditions are fulfilled: 1) adsorption is characterized by monolayer coverage (only); 2) each site can hold only one molecule of adsorbate; 3) all sites are energetically equivalent and the surface is uniform; 4) each molecule adsorbs in a given

adsorbent site regardless of the occupation of neighboring ones [246]. In Langmuir model, the fractional coverage θ is defined as the ratio between the number of adsorbent sites occupied by adsorbate molecules and the total number of adsorbent sites [248]. Considering the above assumptions, according to which each adsorbent site can contain only one adsorbate molecule, at equilibrium the number of adsorbent sites occupied can be replaced by q_e and the total number of available sites represents the maximum adsorption capacity q_m. Thus:

$$\theta = \frac{\text{number of adsorbent sites occupied}}{\text{number of adsorbent sites available}} = \frac{q_e}{q_m} \tag{5.5}$$

Pointing the total number of sites with *N* and adsorbate concentration with C_A, adsorption and desorption rates can be described by the following equations:

$$\frac{d\theta}{dt} = k_a C_A N(1-\theta) \tag{5.6}$$

$$\frac{d\theta}{dt} = -k_d N\theta \tag{5.7}$$

with k_a and k_d being respectively the kinetic constant of adsorption and desorption processes. In dynamic adsorption equilibrium, adsorption and desorption rates are equal. Equating (5.6) with (5.7) and solving for θ, the following relation can be obtained:

$$\theta = \frac{K_L C_e}{1 + K_L C_e} \tag{5.8}$$

where K_L is the Langmuir constant, defined as $\frac{k_a}{k_d}$. Considering equation (5.5), (5.8) can be more properly written as following:

$$q_e = \frac{q_m K_L C_e}{1 + K_L C_e} \tag{5.9}$$

better known as Langmuir isotherm equation.

In the case of multiple layer adsorption, isotherm curves are well described by the BET isotherm [249]:

$$q_e = \frac{q_{BET} k_1 C_e}{(1 - k_2 C_e)(1 - k_2 C_e + k_1 C_e)} \tag{5.10}$$

with q_{BET} being the monolayer adsorption capacity (mg/g), k_1 and k_2 the BET constants (L/mg).

Considering the wide variety of interactions which can be established between adsorbent and adsorbates and their chemical complexity, other isotherm

models have been developed to better describe adsorption processes and can be found here [246].

From a thermodynamical point of view, adsorption processes can be considered a reaction between adsorbent (A) and adsorbate (B) in order to form a AB. The two most important equations from which thermodynamical parameters can be extrapolated are the following:

$$\Delta G^0 = \Delta H^0 - T\Delta S^0 \quad (5.11)$$

$$\Delta G^0 = -RT \ln K_e \quad (5.12)$$

where R and T are respectively the universal gas constant and the temperature.

Adsorption kinetics. Adsorption kinetics investigate the rate at which adsorbate (or adsorbates) is removed from the liquid phase and transferred on the adsorbent. Several mathematical models have been developed and are classified into diffusional models and adsorption reaction models [246,250]. In diffusional models, adsorption kinetics is considered on a base of three subsequent steps: external mass transfer, intraparticle diffusion and adsorption on active sites. On the other hand, adsorption reaction models address to the whole process of adsorption as a chemical reaction, not taking into consideration the adsorption diffusion steps mentioned above. Adsorption reaction models are the most common employed models for the kinetic study of adsorption processes. Before going into detail, a brief description on diffusional models is presented below.

In diffusional models, adsorbate molecule is considered a spheric particle of radius R and the process is divided in external mass transfer, intraparticle diffusion and adsorption on active sites [250]. External mass transfer describes the mechanism with which the adsorbate molecule moves from the bulk solution and reaches the adsorbent surface. This process is governed by the external mass transfer coefficient k_f. Concentration of adsorbate in the bulk solution is dependent on time and is often indicated as C_t. Intraparticle diffusion can occur through effective pore volume diffusion, surface diffusion or both. The effective pore volume diffusion regulates the movement of the adsorbate molecules inside the adsorbent pores and is described by the effective pore volume

diffusion coefficient D_P. Surface diffusion regards the transport of adsorbate molecules over the adsorbent surface, moving from sites of higher energy to lower ones, and is represented by the surface diffusion coefficient D_S. The last step is the adsorption on active sites, which precisely considers the interaction between adsorbate molecules and active sites of the adsorbent. One of the most complete diffusional models is PVSDM, the pore volume and surface diffusion model, from which external mass transfer model (EMTM), pore volume diffusion model (PVDM), and surface diffusion model (SDM) can be derived [246,251]. The first assumes that the movement of the adsorbate from liquid phase to adsorbent surface is only governed by external mass transfer. Intraparticle diffusion is instantaneous and concentration gradient inside the adsorbent is absent. PVDM and SDM models can be considered a simplification of the PVSDM model. In PVDM, intraparticle diffusion is only regulated by effective pore volume diffusion while surface diffusion is the only one to govern intraparticle diffusion in SDM. Homogeneous surface diffusion model (HSDM) is another important diffusional model [246]. It is based on the concept that a dual mass transport mechanism in the form of surface diffusion occurs along the hydrodynamic boundary layer surrounding the adsorbent and also governs the intraparticle diffusion inside it.

Adsorption reaction models are frequently used to describe adsorption processes, deriving their equations from the kinetic model developed for a generic chemical reaction. The most common models are pseudo-first-order, pseudo-second-order and Elovich model [246,252]. The pseudo-first-order model developed by Lagergren is based on only one assumption: the solid exhibits a certain adsorption capacity [253]. In this sense, the equation is the following:

$$\frac{dq_t}{dt} = k_1(q_e - q_t) \tag{5.13}$$

where k_1 (min^{-1}) is the kinetic pseudo-first-order rate constant, q_e and q_t (mg/g) are respectively the adsorption capacities at equilibrium and at time t (min). Considering that at $t = 0$ the adsorption capacity $q_t = 0$, and at time t $q_t = q_t$, the integration of (5.13) leads to:

$$q_t = q_e(1 - e^{k_1 t}) \tag{5.14}$$

In the pseudo-second-order model, starting equation is described below [246]:

$$\frac{dq_t}{dt} = k_2(q_e - q_t)^2 \tag{5.15}$$

with k_2 (g mg^{-1} min^{-1}) being the kinetic pseudo-second-order rate constant. As in the pseudo-first-order model, at $t = 0$ $q_t = 0$, and at time t $q_t = q_t$, thus integration of equation (3.15) yields:

$$\frac{1}{q_e - q_t} = \frac{1}{q_e} + k_2 t \tag{5.16}$$

which, by placing $h_0 = k_2 q_e^2$, can be written as follows:

$$q_t = \frac{t}{\left(\frac{1}{h_0}\right) + \left(\frac{t}{q_e}\right)} \tag{5.17}$$

The Elovich model was developed by Zeldowitsch to determine the adsorption rate of carbon monoxide on manganese dioxide and is currently employed for the description of chemisorption processes of gases on heterogeneous surfaces [254]. It starts from the following equation:

$$\frac{dq}{dt} = ae^{-\beta q} \tag{5.18}$$

where a is the desorption constant, β is the initial adsorption rate and q is the amount of adsorbed gas at time t. Fixing that at $t = 0$ $q = 0$ and at time t $q = q$ and assuming that $a\beta t \gg 1$, integration of equation (5.18) gives:

$$q_t = \beta \ln(a\beta) + \beta \ln t \tag{5.19}$$

which can be also written as:

$$q_t = \left(\frac{1}{a}\right) \ln(1 + a\beta t) \tag{5.20}$$

Chapter 6

Introduction to experimental part

This section is totally focused on the presentation of scientific results of the project "*Nanofillers doped buckypaper membranes for highly enhanced recovery of pollutants from wastewater*".

Project has begun with the preparation of carbon nanotubes membranes, better known as buckypapers (BPs), by using the wet method. After optimization of preparation conditions in terms of sonication time, volume of solvent and filtering pressure of CNTs dispersions, the as prepared membranes have been characterized through scanning electron microscopy (SEM), atomic force microscopy (AFM), contact angle and Young modulus measurements. These membranes, which are completely self-standing and lightweight, preserve mechanical and electrical properties of pristine carbon nanotubes. In order to improve membrane performances and adsorption capacities, buckypapers have been also prepared in combination with other materials, such as metal organic frameworks (MOFs) and graphene oxide (GO). Morphological and physicochemical characterizations of these new composites have shown that these fillers are completely incorporated in the BP structure, defining the maximum concentration of dopants which can be introduced in the membranes without altering their mechanical and electrical properties in a substantial way. Finally, buckypaper membranes doped with MOF and GO have been employed for the removal of water pollutants through adsorption processes. In particular, MOF-BP membranes were designed for the removal of lead and cerium while GO-BPs have been investigated for the recovery of lead and non-steroidal anti-inflammatory drugs.

The preparation of new composites in the form of semiconductor/buckypaper membranes was also pursued as one more line of research. In this case, a thin layer of WO_3 semiconductor has been deposited on BPs surface through reactive magnetron sputtering. The as prepared WO_3/BP membranes were then tested for the removal of organic pollutants from water through photocatalysis. A small laboratory system has been developed precisely for this purpose: WO_3/BP is inserted in a round stainless-steel cell, whose diameter is perfectly

compatible with the membrane, and the solution rich of contaminants is allowed to circulate inside the cell by a peristaltic pump. An optical glass, mounted on the top of the cell, exposes the membrane surface to light, allowing the transition of electromagnetic radiation required to activate the photocatalytic process. Three model pollutants, organized in two organic dyes and one non-steroidal anti-inflammatory drug, have been tested for photocatalytic degradation.
A more detailed description on water pollutants investigated in these works is proposed below.

Lead (Pb). The great majority of anthropogenic activities currently include the use of lead in their processes. Thanks to its properties, such as softness, malleability, poor conductivity and slow dissolution in water, lead is employed in several industrial processes such as smelting, electroplating, steel, paint and battery [255,256]. Together with industrial processes, another major input to lead occurrence in the environment comes from land applications of inorganic fertilizers and pesticides, combustion of fossil fuels, recycling and disposal of waste material [257,258]. Considering that lead is one of the most toxic heavy metals, even at low concentrations, developed countries have significantly reduced the use of lead over the years while developing countries still continue to use lead containing products, such as ceramics, pigments and batteries, and, above all, leaded gasoline [259]. First evidence of air pollution from lead dates back to 1969, when it was realized that gasoline combustion produced tetraethyl lead (TEL), subsequently released by car tailpipes in the environment [260]. That year pollution was so high that in some urban areas lead concentration exceeded 20% [259,261]. More recently, a case of extensive water pollution from lead occurred in Flint (Michigan) in 2014-2015 [262]. Corrosion of household pipe systems introduced large quantities of lead in water, with concentrations in samples collected ranging from 217 to 132,000 μg/L, significantly above the current established limit for drinking water of 15 μg/L. Ingestion of lead contaminated waters and inhalation of dust and fumes containing Pb are the primary pathways of human exposure to lead, which is extremely toxic to living beings.

Once in body, Pb can accumulate in bones, kidney, brain, blood, liver and skin [263]. One of the main risks associated with Pb is the formation of reactive oxygen species (ROS) such as $OH^{\cdot}$ or O_2^-, causing oxidative stress and alteration of cell functioning. In addition, Pb can interfere with metabolic processes by inhibiting some enzymatic reactions. Lead is also extremely toxic to central and peripheric nervous systems and can also affect fertility in male [264]. Of the totally amount of adsorbed lead, 80-85% ends up normally in bones, interfering with their formation and development processes [255]. This heavy metal enters the environment from water, dust, soils and paint chips from holder houses [259]. Ingestion of lead contaminated waters is undoubtedly the most common source of human exposure. Lead is primarily released in water by corrosion of older fixtures, lead service lines and lead solder connecting drinking water pipes. Even if in the last few years several cities have replaced lead pipes with copper or polyvinyl chloride (PVC) systems, there are still 9.3 million homes with Pb pipes in United States according to EPA 2017 Report [265]. Currently, the phosphate method is largely employed to control lead concentration levels in water by inhibition, or almost, of its release [266]. Depending on water pH, inhibitors such as orthophosphate, zinc orthophosphate and polyphosphates promote the formation of lead insoluble compounds, like $PbCO_3$ (cerussite), $Pb_5(P0_4)_3(OH)$ (hydroxyl-pyromorphite) and $Pb_3(C0_3)_2(OH)_2$ (hydrocerussite), which in turn prevent further release of lead by creating an insoluble scale within the pipe itself. Older houses, especially those built in 1940-1950 or before, are of concern because they can contain leaded paint, officially banned in 1978. Destruction or restructuring of these houses can introduce large quantities of lead in the environment, which commonly ends up entrapped in small dust particles. Apart from dust, another major source of lead is soil. Soil is characterized by a terrestrial natural abundance of lead ranging from 1 to 200 mg/kg [259]. However, anthropogenic activities, gardening included, can alter considerably this concentration, until to values even greater than 2,000 mg/kg for the most polluted areas. According to the amount of lead contained, soils are classified in low risk ($C_{Pb} < 100\ \frac{mg}{kg}$), of concern ($100\ \frac{mg}{kg} <$

$C_{Pb} < 1200\ \frac{mg}{kg}$) and high risk ($C_{Pb} > 1{,}200\ \frac{mg}{kg}$). Recent growing concerns have been addressed to food. Hore et al. (2019) found that lead occurs in more than 3,000 samples of consumer products [267]. Among them, imported spices have the highest concentration levels of Pb, probably due to lead chromate practice for spice adulteration. Candy is also a product of serious concern. Lead in candies can come from storing or drying processes or when ingredients are grinded inaccurately. Nevertheless, an adequately regulation which can prevent a correct inspection of these products is currently missing, allowing lead to arrive on our tables.

Pb removal from wastewater is performed through several physicochemical techniques [255]. Chemical treatment processes are often avoided due to large amount of reagents required and to the production of huge quantities of toxic sludge, whose disposal is not always user-friendly. To overcome these problems, more cleaner techniques have been developed, including membrane filtration, adsorption, electrochemical and biological treatments. In the field of membranes, MMMs have been largely employed for lead removal, showing prominent results both in terms of adsorption capacity and reusability. Most recent studies are based on PES membranes opportunely doped with amino-functionalized MWNTs [268] or aminated-Fe_3O_4 nanoparticles [269], and on the preparation of PANI based MMMs, in which MOF-808 [270] or GO nanoparticles [271] have been incorporated.

Rare Earth Elements (REEs) or Rare Earth Metals (REMs). The term "rare earth elements" generally refers to the group of lanthanides (Z=57 to Z=71) plus scandium and yttrium, included among REEs because of the similarity between their chemical properties and those of lanthanides. The interest and the demand for REEs have experienced a big step forward with the advent of technology in our daily lives. From that moment, REEs have been progressively employed in industrial applications and advanced technologies, becoming crucial elements in various fields such as medicinal industry, superconductors, metal alloys, batteries, hydrogen storage, nuclear technology, permanent magnets and

military applications [272–275]. Due to their widespread use, REMs are often known as "the vitamins of modern industry". China is responsible for about 90% of REEs supply worldwide but the implementation of a protectionist policy on export of rare earth elements has pushed up their prices remarkably. Considering the high cost on the market and the difficulty of selective extraction of REEs from natural sources due to their similar chemical properties, recovery of rare earth elements from wastewaters has become of utmost importance. Several technologies have been developed, including ion exchange, precipitation, solvent extraction, electrochemical processes and adsorption [276,277]. Solvent extraction lacks in selectivity and, as well as precipitation, produces a lot of waste which absolutely needs further treatment, increasing the cost of the process. In terms of adsorption, recent advances have been done in the development of membrane technologies [277]. Thanks to their porous structure, these membranes offer good selectivity, allowing recovery of rare earth elements in a more environmental friendly pathway. First efforts have been devoted to the fabrication of liquid membranes (LMs) [278], prevalently employed for the capture of lanthanide ions (Ln^{3+}). Anyway, LMs exhibited weak stability and low surface area so they have been early abandoned in favor of more performing systems, such as polymer inclusion membranes (PIMs) [279,280]. These membranes are characterized by long-term stability and low carrier loss, needing small volumes of diluents and having no problems with phase separation, becoming a potential green alternative technology for concentrating, separating and recovering REEs. Cellulose triacetate (CTA), poly-vinylidene fluoride (PVDF) and poly-vinyl chloride (PVC) are the most common polymers employed in PIM technologies [277]. Very recently, nanocomposite membranes based on the incorporation of several fillers, such as metal nanoparticles (Fe, Zr, Ti, Mg etc), carbon nanotubes and graphene oxide sheets, into organic polymer membranes have also been investigated for the recovery of REEs [281–283]. Even if results are very promising, this field is still in its infancy so further studies are required to better implement this technology.

Non-steroidal anti-inflammatory drugs (NSAIDs). Non-steroidal anti-inflammatory drugs are medicinal products developed for pharmacological management of pain [284]. Even if pain can be also treated through opiate/opioid analgesics, NSAIDs are significantly preferred due to long history of clinical use, low abuse potential and robust efficacy. Paracetamol, phenazone and aspirin were the first anti-inflammatory to be discovered, found by serendipity more than 100 years ago [284]. From a chemical point of view, NSAIDs are weakly organic carboxylic acids, whose pK_a ranges between 4.00 and 4.91 [285]. Due to their widespread use, also because their utilization does not require medical prescription, large quantities of anti-inflammatory drugs are released into the environment on a daily basis. After their administration, these pharmaceuticals are excreted by human body as intact substances or metabolites through urines and feces. However, due to their high water solubility, wastewater treatment plants often fail in their removal from water [286]. In Spain, naproxen, ibuprofen and diclofenac were detected in tap water, with average concentrations of respectively 11, 39 and 18 ppb [287]. In Iran, tap water concentration values detected for the same pharmaceuticals are respectively 39, 47 and 24 ppb [288]. It has also been shown that, after sewerage treatment, concentrations of anti-inflammatory drugs in effluents can even increase, resulting in a negative removal efficiency of WWTPs [289]. It can be probably ascribed to the formation of conjugated compounds during wastewater treatment steps, or to an influent-effluent mismatching. Despite their therapeutic effect on human health, high dosages of NSAIDs for long periods can have detrimental effects on a gastrointestinal and cardiovascular level [284]. Prolonged exposure of the gastrointestinal tract to circulating anti-inflammatory drugs often results in an increased risk of upper gastrointestinal bleeding [284]. NSAIDs are also responsible for cardiovascular adverse events, such as hypertension, stroke, heart failure and myocardial infarction [284]. Therefore, NSAIDs removal from water is of utmost importance. Adsorption, photocatalytic degradation, electrochemical and sonochemical processes are the most currently employed technologies in this field [285]. Photocatalytic degradation and, more generally, advanced oxidation processes promote degradation of these pharmaceuticals,

converting them into less toxic or environmentally friendly small organic molecules [290–292]. These methods are characterized by removal efficiencies ranging from 45% up to 90-95%, depending on the type of substrate employed and on operational conditions such as pH, temperature, reaction time. Several materials have been explored for adsorption processes. The vast majority of adsorbents belongs to the category of activated carbons [293] and graphene-based materials [294,295], by themselves or incorporated in polymer organic membranes, particularly indicated for adsorption due to their large surface area and diversity of chemical functionalities. Molecular imprinted polymers (MIPs) have also been developed for NSAIDs capture [296]. Even if selectivity is highly enhanced in these adsorbents, their production costs are currently too high.

Next chapters, having the scope to present the scientific research carried out during this thesis work, are organized as follows:

- **Chapter 7 – MOF/BP membranes:**
    - *Synthesis and Enhanced Capture Properties of a New BioMOF@SWCNT-BP: Recovery of the Endangered Rare-Earth Elements from Aqueous Systems*

      Tursi, A., Mastropietro, T. F., Bruno, R., Baratta, M., Ferrando-Soria, J., Mashin, A. I., Nicoletta, F. P., Pardo, E., De Filpo, G., Armentano, D., *Adv. Mater. Interfaces*, **2021**, 2100730.

    - *Multivariate Metal−Organic Framework/Single-Walled Carbon Nanotube Buckypaper for Selective Lead Decontamination*

      Baratta, M., Mastropietro, T. F., Bruno, R., Tursi, A., Negro, C., Ferrando-Soria, J., Mashin, A. I., Nezhdanov, A., Nicoletta, F. P., De Filpo, G., Pardo, E., Donatella Armentano, D., *ACS Appl. Nano Mater.*, **2022**, 5, 4, 5223.

- **Chapter 8 – GO/BP membranes:**
    - *GO-SWCNT Buckypapers as an Enhanced Technology for Water Decontamination from Lead*
      Baratta, M., Tursi, A., Curcio, M., Cirillo, G., Nicoletta, F. P., De Filpo, G., *Molecules*, **2022**, 27, 4044.

- *Removal of Non-Steroidal Anti-Inflammatory Drugs from Drinking Water Sources by GO-SWCNT Buckypapers*

  Baratta, M., Tursi, A., Curcio, M., Cirillo, G., Nezhdanov, A. V., Mashin, A. I., Nicoletta, F. P., De Filpo, G., *Molecules*, **2022**, 27, 7674.

- **Chapter 9 – WO_3/BP membranes:**
  - *WO_3/Buckypaper Membranes for Advanced Oxidation Processes*

    De Filpo, G., Pantuso, E., Mashin, A. I., Baratta, M., Nicoletta, F. P., *Membranes*, **2020**, 10, 157.

- **Chapter 10 – microplastics pollution:**
  - *Microplastics in aquatic systems, a comprehensive review: origination, accumulation, impact, and removal technologies*

    Tursi, A., Baratta, M., Easton, T., Chatzisymeon, E., Chidichimo, F., De Biase, M., De Filpo, G., *RSC Adv.*, **2022**, 12, 28318.

Chapter 7

ADVANCED MATERIALS INTERFACES
www.advmatinterfaces.de

Synthesis and Enhanced Capture Properties of a New BioMOF@SWCNT-BP: Recovery of the Endangered Rare-Earth Elements from Aqueous Systems

Antonio Tursi, Teresa F. Mastropietro, Rosaria Bruno, Mariafrancesca Baratta, Jesus Ferrando-Soria, Alexander I. Mashin, Fiore P. Nicoletta, Emilio Pardo,* Giovanni De Filpo,* and Donatella Armentano**

Human society is facing—among other environmental threats—an enormous challenge due to human activities. The extensive use of high-tech devices and electronics equipment in the daily life makes, among others, rare-earth elements (REEs) recovery from secondary sources highly required. Here, a novel bioMOF-based single-walled carbon nanotube buckypaper (SWCNTBP) is presented as a new and efficient composite material (BioMOF@SWCNT-BP). The flexible and highly crystalline metal–organic framework (MOF), prepared from the natural amino acid L-threonine, has been homogeneously dispersed within the tangled net of a self-standing SWCNT-BP for lanthanides recovery from water. This MOF-carbon-based membrane exhibits high efficiency, either in static or dynamic regimes, in the recovery of lanthanides from aqueous streams outperforming the state-of-the-art. The capture performances of BPs are successfully improved after incorporation of such MOF featuring hexagonal functional channels decorated with the threonine amino acid residues, pointing toward the accessible void spaces, which boosts the capture properties of the final membrane, providing the adaptable functional environment to interact with lanthanides. This material's preparation presents also a potential for large-scale applications with a potential benefit on natural aquatic ecosystems as well. It is highly demanded because REEs from non-recycled waste materials are potential pollutants for surface waters.

1. Introduction

The enormous appetite for resources of modern society[1] (energy, food, and raw materials) is putting under pressure the planet and it is the cause of, at least, half of greenhouse gas emissions and the almost totality of biodiversity loss, together with water stress. The best practices of a circular economy should be applied as necessary condition to reach climate neutrality by 2050, joined with a judicious resource use within planetary boundaries.[2]

In the last years, the demand for raw materials such as rare-earth elements (REEs) has experienced an exponential increase due to their essential uses in circuits of current technology. The extensive use of high-tech devices in our daily life and the consequent reduction of their primary elements make, among others, REE's recovery from secondary sources highly required. For that reason, REEs are attracting attention to legislators and scientists to develop innovative recovery technologies, for sustainable supply of raw materials. The EU 2020 has listed critical

Dr. A. Tursi, Dr. T. F. Mastropietro, Dr. R. Bruno, M. Baratta, Dr. G. De Filpo, Dr. D. Armentano
Department of Chemistry and Chemical Technologies
University of Calabria
Rende 87036, Italy
E-mail: defilpo@unical.it; donatella.armentano@unical.it

The ORCID identification number(s) for the author(s) of this article can be found under https://doi.org/10.1002/admi.202100730.

DOI: 10.1002/admi.202100730

Dr. J. Ferrando-Soria, Dr. E. Pardo
Department of Inorganic Chemistry/Institute of Molecular Science
University of Valencia
Paterna, Valencia 46980, Spain
E-mail: emilio.pardo@uv.es

Prof. A. I. Mashin
Applied Physics and Microelectronics
Lobachevsky State University of Nizhny Novgorod
Nizhny Novgorod 603022, Russia

Prof. F. P. Nicoletta
Department of Pharmacy
Health and Nutrition Sciences
University of Calabria
Rende 87036, Italy
E-mail: fiore.nicoletta@unical.it

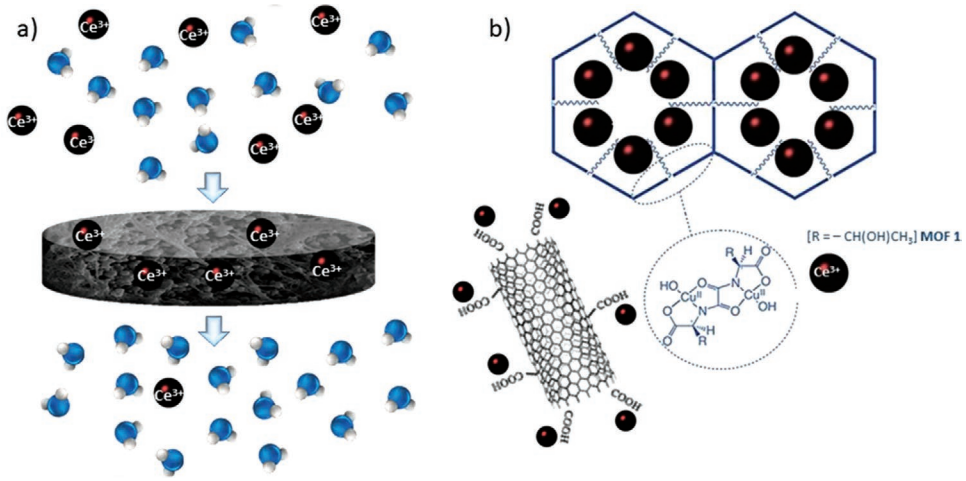

Figure 1. a) Graphical idea of the filtration process to recover REEs by means of a BioMOF@SWCNT-BP membrane in low ion concentration regimes. b) Details of the interaction sites between cerium and functional groups decorating MOF channels and sections of SWCNTs.

raw materials on the basis of their economic importance and supply risk, which are the two main parameters used to determine criticality.[3] REEs, divided into light rare-earth and heavy rare-earth elements, appear already among endangered raw materials. Furthermore, REEs, from non-recycled waste materials, are potential pollutants for surface waters. Nevertheless, the recovery of REEs from industrial waste water streams is still highly challenging, due to their very low concentrations. It requires sophisticated and not economically favored processes, requiring several steps, for the efficient recovery of REEs when present in traces.[4–7] Despite the limitations described above, literature reports some examples of REEs recovery.[6,8,9] In this scenario, it is clear that the development of novel, simpler, and less-costly methods for the separation of REEs is highly important from an industrial point of view. After the pretreatment steps for REEs recycling from e-waste, several methods, based on liquid–liquid extraction, ion exchange, adsorption, or chemical precipitation, have been tested to separate REEs.[10] Among them, adsorption methods emerged, and started to show they can be game changers, thanks to high efficiency and wide-ranging applicability. In this context, metal–organic frameworks (MOFs),[11–13] which are porous materials known for a great potential in separation, are demonstrating their high potentiality even in lanthanide separation.[14–17] Water-stable MOFs offer tunable microporosity and the possibility to tailor their channels with the appropriate functionalities to improve affinity for target elements, even in a selective manner.[18–20] Several works related to MOFs and MOF-based materials have been reported for the recovery of lanthanides.[16,17] However, they exhibit important disadvantages such as difficult handling or leaks of fillers, that compromise any industrial process.

Carbon nanotubes (CNTs) are unique nano-structured porous materials with remarkable electronic and mechanical properties. They are proven as promising candidates for a wide range of environmental applications.[21] Free standing or mixed matrix CNTs membranes have shown a great potential in breaking the trade-off between membrane flux and selectivity, while featuring antifouling properties.[22] More recently, buckypapers (BPs) have been proposed as innovative filtration systems alternative to polymer membranes thanks to their lightweight, high-temperature, and chemical resistance.[23–29] They are entangled assembly of CNTs obtained as the result of filtration of CNT (both single-walled CNTs and multiwalled CNTs) dispersions.[30,31] BPs merge the characteristic properties of polymer membranes such as porosity, flexibility, self-standing, and permeation with those of CNTs such as thermal features, mechanical resistance, and enhanced electric characteristics.[32,33] The morphology of BP membranes is characterized by the presence of a porous and highly disordered structure formed by bundles of CNTs interacting via π–π and van der Waals interactions.[34,35]

2. Results and Discussion

In this context, with the aim to make a step forward on MOF-based technologies for element recovery and water remediation, we present a novel, flexible, and self-standing MOF-based single-walled carbon nanotube buckypaper[33,36] (BioMOF@SWCNT-BPs) as a new and highly performant material in REEs recovery (**Figure 1**). The highly crystalline bioMOF, previously reported by us[17] and prepared from the natural amino acid L-threonine, has been homogeneously dispersed within a thin (150 μm) membrane, made with an entangled CNT network and produced by multiple steps of dispersion and filtration for lanthanide recovery from water. Among the different MOF subfamilies, bioMOFs,[37,38] constructed using biomolecule derivatives as building blocks and often affording water stable materials, emerge as valuable systems to study the capture properties and application in water remediation, either for their chemical functionalization or for being eco-friendly porous materials.[37,39] The presence of such MOF with formula $\{Sr^{II}Cu^{II}_6[(S,S)\text{-threonine}]_3(OH)_2(H_2O)\}\cdot 36H_2O$ BioMOF (where threomox = bis[(*S*)-threonine]oxalyl diamide)[17] featuring hexagonal functional channels decorated with the $-CH(OH)CH_3$ amino acid residues, which point toward the accessible void spaces, unambiguously boosted the capture properties of the final BP membrane, providing the appropriate adaptable functional environment to interact with lanthanides (**Figure 2**).

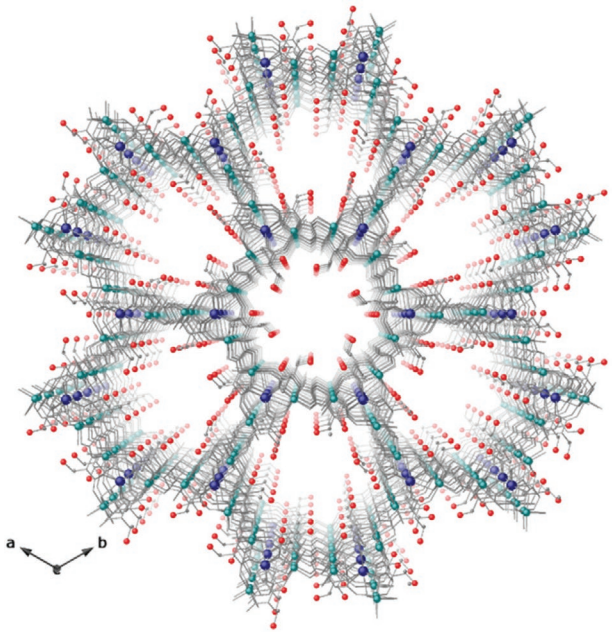

Figure 2. Perspective view of the 3D open-framework of BioMOF along the *c* axis. Cu and Sr atoms are represented by cyan and blue spheres, respectively, whereas the ligands are depicted as sticks. The oxygen atoms from the L-threonine residues are represented as red spheres. Hydrogen atoms and the crystallization water molecules are omitted for clarity.

As a consequence, BioMOF@SWCNT-BP membrane, exploiting the well-known affinity of O atoms for lanthanides, was capable to adsorb, to a certain degree, $CeCl_3$ and equimolar mixtures of lanthanide chlorides from model solutions.

Recently, a number of carbon-based nanomaterials have been applied in adsorption processes for this purpose.[23,26,40,41] Literature shows the studies of the recovery of REEs also using CNTs composites; but SWCNT-based membranes have been only barely explored.[40,42] Up to date, the material with the highest maximum adsorption capacity of REEs reported in the literature is an imprinted chitosan/CNT composite, which exhibits a maximum theoretical recovery of 121.51 mg g^{-1}.[43] Most studies on CNT composites have mainly focused, so far, on sorption experiments using CNTs with several functionalizations which improves their efficiency but increase the number of steps required for their recovery and re-use.[23,24] To the best of our knowledge, no MOF-based SWCNT-BP have been reported so far for the recovery of metal species from water. Herein, we present a green material with potential application in the recovery of lanthanides present in small quantities, for low chemical consuming technologies. This material's preparation presents also a potential for large-scale application. After an initial study on a mono-elemental system with cerium as target ion, investigated both in static and dynamic adsorption regime with both SWCNT-BP and MOF@SWCNT-BP composites, we focused on REE recovery study in a multi-elemental system under dynamic conditions.[44,45]

In this work, we show that the integration of a suitable MOF in a BP, with a specifically designed morphology, yields a membrane that combines the superior capture properties of the MOF, boosting the intrinsic assets of SWCNT-based membrane with improved applicability. The main scope of this work is, indeed, to define, for the first time, a viable protocol to immobilize task-specific MOFs, with a high potential for capturing metal ions, which is related to the high affinity of oxygen atoms toward lanthanides onto a porous and robust support which allows easy manipulation and operability. This particular MOFs, for instance, due to their extremely hydrophilic properties and the presence of functional groups containing oxygen atoms, has already demonstrated its capability as receptor toward lanthanides and great affinity, underpinned by X-ray crystallography, for Cerium^{3+} (**Figure 3**).[17]

In this work, the MOFs has been homogenously dispersed in a highly robust support as a BP for a successful approach to a stable and handy composite, which guarantees high-water fluxes, that is, productivity, and an efficient separation process, that is, purity of the final products.

Polycrystalline samples of MOF (Figure 2) have been prepared even in multigram scale and characterized as previously reported (see Experimental Section in Supporting Information).

A polycrystalline sample of the MOF, with particle dimensions averaging 0.1 µm, was embedded in a SWCNT BP by dispersing in an optimized CNT water solution of SWCNTs and carboxylic acid functionalized SWNTs (COOH-SWCNTs) using

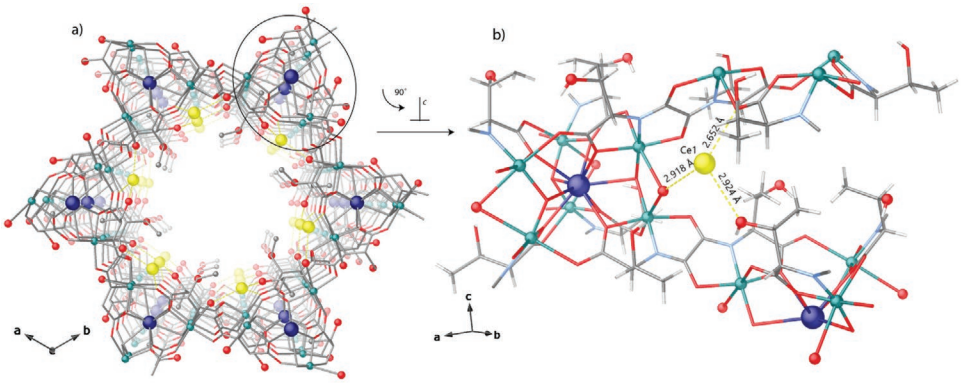

Figure 3. Host–guest interactions at the origin of cerium-MOF affinity previously unveiled by X-ray crystallography: a) Perspective views along the crystallographic *c* axis of a single pore in the $CeCl_3$@MOF crystal structure.[17] b) Details of the Ce···O interaction. Spheres: copper–cyan; calcium–blue; cerium–yellow; oxygen–red; carbon from methyl groups–grey. Sticks: Carbon, nitrogen, and oxygen atoms from the ligand. Free water solvent molecules are omitted for clarity.

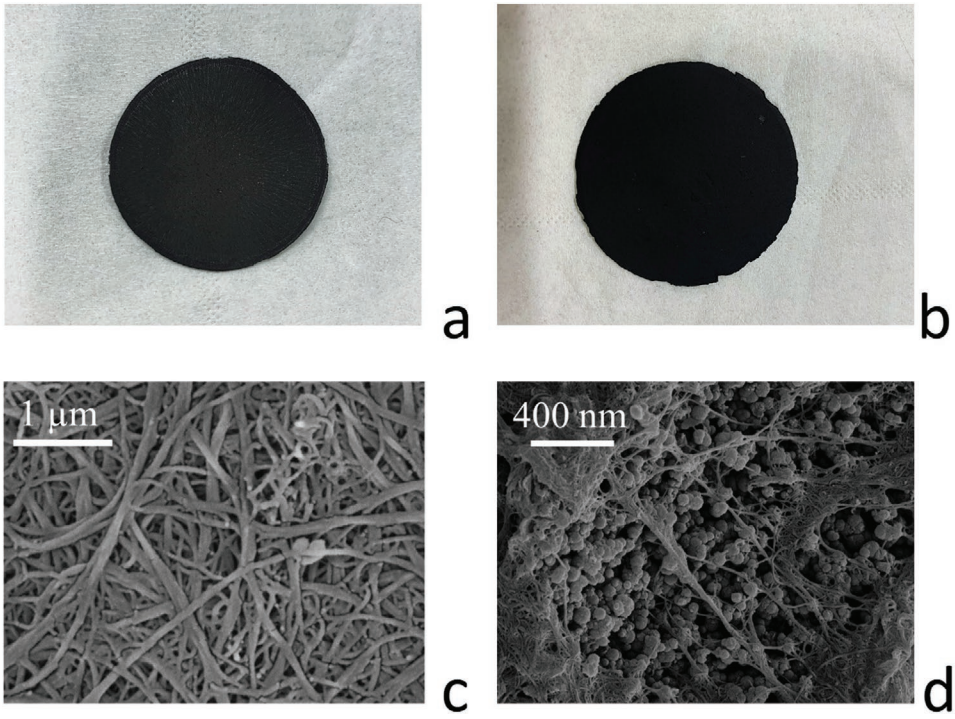

Figure 4. Final appearance of SWCNT-BP (a) and BioMOF@SWCNT-BP (b) obtained under the optimal conditions reported in the Experimental Section of Supporting Information. Circular membranes own an average diameter of 41 ± 1 mm. SEM images of SWCNT-BP (c) and BioMOF@SWCNT-BP (d). It is possible to notice that BioMOF particles are formed by aggregates of smaller nanosized primary particles.

an ultrasonic bath. Then, the solution was filtered through the PTFE disks with a vacuum pump, washed several times with methanol and, finally, dried at room temperature yielding a novel mixed membrane named BioMOF@SWCNT-BP (**Figure 4**b). The detailed procedure is given in the Supporting Information.

TGA analysis assessed the thermal stability of both SWCNT-BPs and BioMOF@SWCNT-BPs. The TGA curves demonstrate that the presence of MOF in BP membrane does not significantly influence the pattern of the neat BP decomposition, showing only slight changes (Figure S1, Supporting Information). The most appreciable variation is probably related to the hydrophilic nature of the MOF and thus to its water content, which is reflected in a weight loss in the temperature range of 50–450 °C for BioMOF@SWCNT-BP. Above 450 °C, there is ≈50% mass loss for both BioMOF@SWCNT-BP and neat SWCNT-BP membrane, which accounts for the partial decomposition of BP (Figure S1, Supporting Information).

As reported in the Experimental Section in Supporting Information several factors influence the integrity and self-standing properties of SWCNT-BP and BioMOF@SWCNT-BP membranes including, in particular, the SWCNT mixture composition (amount of SWCNTs and COOH-SWCNTs) and the percentage of BioMOF loading. After several trials, self-sustaining SWCNT-BPs and BioMOF@SWCNT-BPs were obtained with the weight ratio SWCNT:COOH-SWCNT = 1:2 and 25 wt% of BioMOF.

Figure 4a,b shows SWCNT-BP and BioMOF@SWCNT-BP membranes obtained under the abovementioned optimal conditions. Such circular membranes are characterized by an average thickness of 150 ± 5 μm and an active average diameter of either 41 ± 1 or 37 ± 1 mm (average mass of the disks 40 ± 2 mg) accordingly if they were used in static or dynamic experiments. Both membranes show similar density and porosity values (around 0.60 ± 0.03 g cm^{-3} and 70 ± 5%, respectively).

The morphology of SWCNT-BP and BioMOF@SWCNT-BP membranes was assessed by scanning electron microscopy (SEM). Figure 4c shows the typical microscopic texture of a SWCNT-BP, characterized by bundles and clusters of SWCNTs arising from π–π and van der Waals interactions. The addition of the bioMOFs in SWCNT-BPs is evidenced in Figure 4d by the presence of small spherical aggregates with an average size lower than 1 μm and formed by smaller primary particles with an average diameter of about 0.1 μm. The highly porous and outstanding stable structure of SWCNT-BPs, firmly hosting the nanosized BioMOF particles (no leakage was observed at the end of both static and dynamic experiments), guarantees a high permeability and a large surface area for the contact and successive adsorption of lanthanides present in the test solutions.

Given the high efficiency of MOFs in cerium capture previously demonstrated in their powder form,[17] we started to evaluate the capture properties of BioMOF@SWCNT-BP and compare them with those of the neat SWCNT-BP membrane by experimental set-up reported in **Figure 5**. The study of the Ce^{3+} capture efficiency of both neat SWCNT-BP and BioMOF@SWCNT-BP membranes has been performed by static adsorption in batch (Figure 5a) and dynamic adsorption during permeation, adapting a microfiltration round test cell (Figure 5b, flow rate = 5 mL min^{-1}, feed pressure = 3 bar). In the last case, solutions containing the target ion have been allowed to recirculate through the neat SWCNT-BP and BioMOF@SWCNT-BP membrane, using a peristaltic pump.

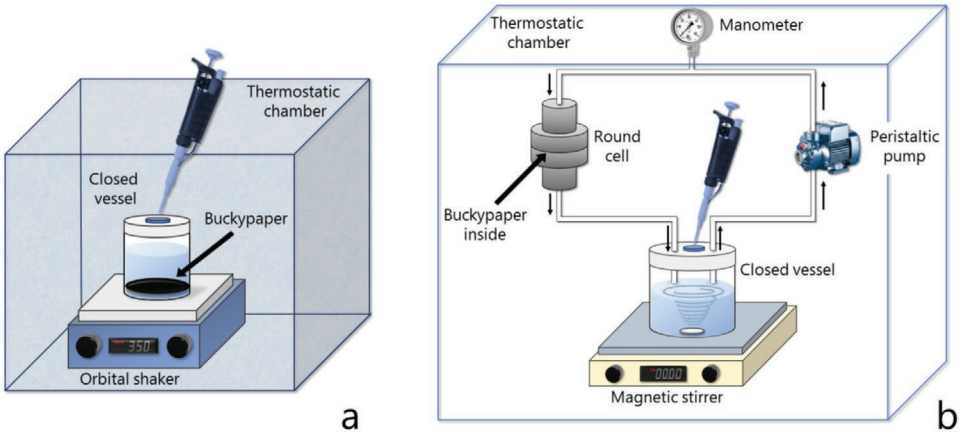

Figure 5. Scheme of the set-up used for the: a) static and b) dynamic adsorption experiments.

In our initial screening, performed under static conditions and different pH values (5, 6, and 8), we found that the pH did not affect in a remarkable way the binding performance, as hydroxyl (of bioMOF) and carboxylic acid groups (of SWCNT) are protonated and deprotonated, respectively, in the whole pH range studied. The Ce^{3+} capture by a SWCNT-BP or a BioMOF@SWCNT-BP disk (diameter 41 mm) during soaking in aqueous solutions of 3.5 ppm Ce^{3+} (volume 80 ml) at different pH values (5, 6, and 8) in the 0–24 h interval is reported in **Figure 6** and Tables S1 and S2, Supporting Information. As it is evident from the time behavior of the Ce^{3+} adsorption static experiments, there is no particular difference among the tested pH conditions for both used membranes: SWCNT-BPs and BioMOF@SWCNT-BPs are able to reduce the initial 3.5 ppm Ce^{3+} concentration to values lower than 20 ppb in 1000 min and to around 0 ppb in 1400 min. A slightly faster adsorption can be noticed by a BioMOF@SWCNT-BP at pH 5, and, consequently, we set the pH value of our solutions for the successive tests under dynamic conditions at 5, which unveiled the best capture properties. In addition, there is no evidence that the presence of MOFs within the BP membranes could meaningfully increase the removal efficiency of the neat SWCNT-BP membranes at all tested pH values.

In the experiments under dynamic conditions two different solutions were used: a Ce^{3+} aqueous solution at different concentrations (1.35, 3, 10, 30, and 50 ppm) in order to unveil if MOFs could enhance capture capacity of the composite material versus the neat SWCNT-BP and a multi-elements solution (REEs standard solution containing Sc^{3+}, Y^{3+}, La^{3+}, Ce^{3+}, Pr^{3+}, Nd^{3+}, Sm^{3+}, Eu^{3+}, Gd^{3+}, Tb^{3+}, Dy^{3+}, Ho^{3+}, Er^{3+}, Tm^{3+}, Yb^{3+}, and Lu^{3+} ions, total concentration 13.4 ppm around 835 ppb for each element) to assess eventually the presence of a selective recovery of REEs by a SWCNT-BP or a BioMOF@SWCNT-BP. Solutions were recirculated in a small continuous plant and the residual concentration values were monitored through ICP-MS analysis, which allowed to follow the adsorption as a function of time.

Under dynamic experiments and at lower Ce^{3+} concentrations (1.35 and 3 ppm), no difference was observed in the adsorption rates of both SWCNT-BP and BioMOF@SWCNT-BP

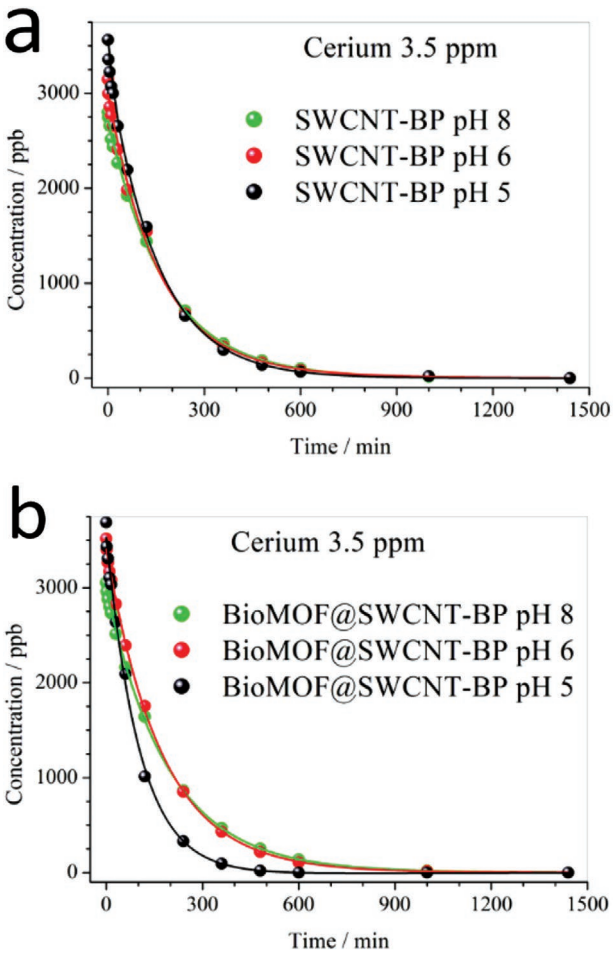

Figure 6. Ce^{3+} capture by neat SWCNT-BP a) and BioMOF@SWCNT-BP disks b) (diameter 41 ± 1 mm) during soaking in aqueous solutions of 3.5 ppm Ce^{3+} (volume 80 mL) at different pH values (5, 6, and 8) in the 0–24 h interval. The cerium residual concentration by neat SWCNT-BP and BioMOF@SWCNT-BP membranes under the same conditions for static adsorption are reported in Tables S1 and S2, Supporting Information. The solid lines in the figures are guides for the eye. The experiments were carried out in triplicate.

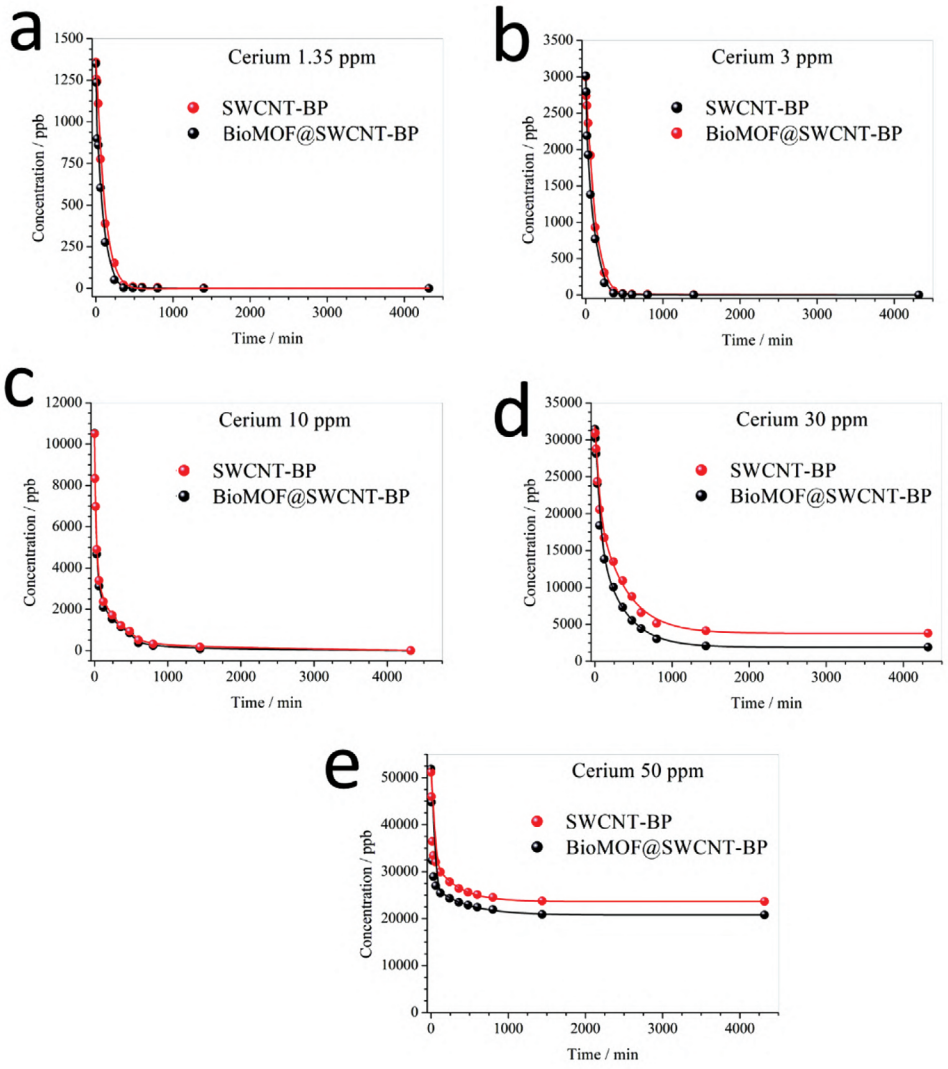

Figure 7. Effect of initial concentrations on the Ce^{3+} capture by SWCNT-BP and BioMOF@SWCNT-BP disks (diameter 37 mm) under dynamic experimental conditions for solutions with a Ce^{3+} concentration of: a) 1.35 ppm, b) 3 ppm, c) 10 ppm, d) 30 ppm, and e) 50 ppm. The solid lines in the figures are guides for the eye. The experiments were carried out in triplicate.

(**Figure 7**a,b and Table S3, Supporting Information). The initial lanthanide concentrations fall to less than 10 ppb in 1400 min and to about 0 ppb in 4320 min. No difference in the adsorption rates between a net SWCNT-BP and a BioMOF@SWCNT-BP is again evident.

For larger Ce^{3+} concentrations (10, 30, and 50 ppm) a different behavior is observed in the recovery efficiency by a neat SWCNT-BP and a BioMOF@SWCNT-BP, (Figure 7c–e and Tables S4 and S5, Supporting Information). SWCNT-BPs show a higher plateau after 72 h in the final Ce^{3+} concentration (3 ppb, 3.79, and 23.64 ppm) than that shown by BioMOF@SWCNT-BPs in similar conditions (≈ 0 ppb, 1.91, and 20.78 ppm, respectively). The recovery efficiencies at 10, 30, and 50 ppm by SWCNT-BPs were, respectively, 99.97%, 87.72%, and 53.77% (calculated uncertainties of ±2%) while the corresponding BioMOF@SWCNT-BP efficiencies were ≈100%, 93.92%, and 59.94%. In order to be sure that the setup did not absorb cerium, Ce^{3+} solutions were recirculated through the cell used in dynamic adsorption conditions without any membrane. There was no meaningful drop in Ce^{3+} concentrations during all test procedures, confirming that there was no considerable Ce^{3+} adsorption by the tubes, pump, or other parts of the experimental setup. These results clearly situate the BioMOF@SWCNT-BP as a potential material for Ce^{3+} capture from water streams. Dynamic experiments using a solution of $[Ce^{3+}] = 50$ ppm, recirculating for a week, showed that SWCNT-BP and BioMOF@SWCNT-BP exhibit a maximum adsorption capacity of about 157 and 263 mg g^{-1}, respectively, which is an adsorption value twice larger than that shown by current most performing carbon-based membranes (chitosan-CNT composite with a maximum theoretical and measured recovery of 121.51 and 88 mg $g^{-}1$, respectively, at 303.15 K).[43] The perfectly synergistic action of threonine arms of the MOF and the −COOH groups of the functionalized SWCNTs added

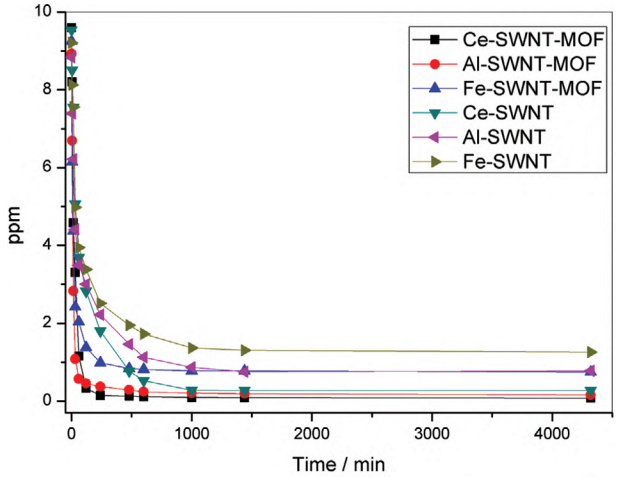

Figure 8. Selectivity measured as residual Ce^{3+}, Fe^{3+}, and Al^{3+} concentrations in an equimolar solution at an initial concentration of 10 ppm for $CeCl_3$, $FeCl_3$, and $AlCl_3$, analyzed with the ICP-MS under static adsorption processes for a neat SWCNT-BP and a BioMOF@SWCNT-BP. The solid lines in the figures are guides for the eye. The experiments were carried out in triplicate.

to not-functionalized SWCNTs in the preparation of SWCNT-BP, outperform the state-of-the-art giving the best performant material for adsorption of REEs. These results not only prove the validity of our approach, but also allow producing a new robust and efficient composite of potential application in the real-world of membranes. Thus, the obtained recovery efficiencies shown by BioMOF@SWCNT-BPs under different Ce^{3+} concentrations demonstrate the suitability of these membranes for the recovery of cerium from water. The maximum recovery capacity reaches 263 mg g^{-1} thanks to the higher surface area of BioMOFs added in SWCNT-BPs, which contributes with a further recovery after the initial adsorption on SWCNT membrane.

Overall, even if, at lower Ce concentrations no significant differences can be observed between SWCNT-BP and BioMOF@SWCNT-BP membranes, BioMOF@SWCNT-BP outperforms SWCNT-BP at higher Ce^{3+} concentrations, which is most-likely due to its larger adsorption capacity, that has special relevance when adsorption sites of SWCNT bundles are saturated.

Aiming at evaluating the efficiency of these two novel materials in the neat adsorption of lanthanides, an equimolar multi-element standard solution of $ScCl_3$, YCl_3, $LaCl_3$, $CeCl_3$, $PrCl_3$, $NdCl_3$, $SmCl_3$, $EuCl_3$, $GdCl_3$, $TbCl_3$, $DyCl_3$, $HoCl_3$, $ErCl_3$, $TmCl_3$, $YbCl_3$, and $LuCl_3$ (about 835 ppb for each lanthanide for a total concentration of about 13.4 ppm) was used as recirculating solution across either a SWCNT-BP or a BioMOF@SWCNT-BP under dynamic conditions at 25 °C and pH 5.

The lanthanide recovery by SWCNT-BP and BioMOF@SWCNT-BP membranes are reported in Figures S2–S5 and Tables S6–S13, Supporting Information. All lanthanides were almost totally recovered by neat SWCNT-BPs with capture percentages near 100% in all cases, in strict analogy with dynamic experiments previously described for Ce^{3+} under lower concentration conditions (1.35, 3, and 10 ppm). As expected, at these low concentrations of such standard solutions, no selective lanthanide recovery was observed for SWCNT-BPs and BioMOF@SWCNT-BPs. However, considering their outstanding capture properties, both materials situate among the best alternatives for the recovery of the scarce and valuable metals.

Overall, capture experiments described above, undoubtedly suggests that the presence of the MOF within the BioMOF@SWCNT-BP can be useful to increase the recovery efficiency of the pure SWCNT-BP membrane at higher lanthanide concentrations. The role of the MOF is undoubtedly defined by the comparison with neat SWCNT-BP performance at different [Ce^{3+}].

In turn, under dynamic conditions and at lower concentrations, the Ce^{3+} cations—and also $ScCl_3$, YCl_3, $LaCl_3$, $CeCl_3$, $PrCl_3$, $NdCl_3$, $SmCl_3$, $EuCl_3$, $GdCl_3$, $TbCl_3$, $DyCl_3$, $HoCl_3$, $ErCl_3$, $TmCl_3$, $YbCl_3$, and $LuCl_3$ when using an equimolar standard solution—is/are almost totally recovered by both SWCNT-BP and a BioMOF@SWCNT-BP membranes, confirming the suitability of both neat BP and MOF-loaded BP for the recovery of lanthanides from water by a simple recirculation through the same membrane for less than one day. In addition, it is evident the fundamental role of the MOFs in the increase of lanthanides recovery.

Anyway, a further prove of the cooperative mechanism of capture can be inferred by SEM coupled with energy dispersive X-ray (EDX) measurements carried out for SWCNT-BP and BioMOF@SWCNT-BP after the recovery of $CeCl_3$ (Figure S6, Supporting Information). The EDX color mapping images of the two membranes after their use show a homogeneous distribution of red dots in SWCNT-BP membrane arising from the Ce(III) adsorption, while in BioMOF@SWCNT-BP the BioMOF particles (green dots) are close together and overlapping in some cases to red dots from cerium. Such results suggest that cerium atoms are linked to the alcohol groups of threonine, as previously unveiled by X-ray crystallography,[17] confirming the relevant role of MOFs in the capture properties of the final composite and that such a mechanism is still operating when MOFs are within the SWCNT-BP membrane.

The stability of the membrane for a potential regeneration process was also evaluated, in order to test their potentiality in industrial applications. In that perspective, the development of extremely efficient, reusable, and selective sorbents is needed.[46]

It is known that both SWCNT-BP[33] and BioMOF in polymer matrices[47] are stable after regeneration processes showing integrity and reusability over several successive cycles of adsorption and regeneration. Such properties were also confirmed for BioMOF@SWCNT-BPs, which were reused thrice after regeneration in 250 mL ethanol for the release of adsorbed lanthanides. Both SWCNT-BP and BioMOF@SWCNT-BP membranes showed still significant efficiency recovery after each regeneration process, losing less than 5% of the original adsorption capacities and confirming the suitability of such BPs in industrial applications (data in Table S14, Supporting Information).

Finally, experiments evaluating the selectivity of SWCNT-BP and BioMOF@SWCNT-BP membranes toward competing ions such as Fe^{3+} and Al^{3+}, as well as the kinetic profile of these processes, were designed and carried out in duplicate. Membranes of 3.7 cm as diameter were soaked in 10 ppm aqueous solutions of $CeCl_3$, containing also 10 ppm of other salts usually competing in water such as $FeCl_3$ and $AlCl_3$, respectively,

during 72 h at pH = 5. ICP-MS analyses indicated that the cerium salt was adsorbed by SWCNT-BP and BioMOF@SWCNT-BP with a modest selectivity toward Fe^{3+} (**Figure 8** and Table S15, Supporting Information). Results indicate two main features, the first is that, for both SWCNT-BP and BioMOF@SWCNT-BP membranes, the Al^{3+} is the most competing ion and Ce^{3+} moderately separated from Fe^{3+} at low concentrations. The second one is related to different degree of selectivity; while BioMOF@SWCNT-BP confirms its better adsorption capacity with respect to SWCNT-BP membrane (Figure 8), it is scarcely performant in terms of selectivity, being able to recover Ce^{3+} versus Fe^{3+} in somewhat degree, but failing when compared with Al^{3+}, which is captured almost efficiently as Ce^{3+}. Despite the extraordinary affinity of Fe^{3+} and Al^{3+} for oxygen atoms, these preliminary results show a sufficient selectivity at least versus iron(III) metal ion. The kinetic profiles suggest also some insights about possible mechanisms implied, which is most likely indicative of a fast adsorption of first raw transition metal ions by −COOH chemical functionalization of CNT, leaving MOF's threonine moieties for further uptake of lanthanide ions. The interaction of lanthanide ions with the carboxylate functional groups decorating the surface of the SWCNT-BP is likely to be the kinetically favored step. These hard acid–hard base interactions mainly driven by Coulombic forces[48] can be easily established between the lanthanide ions and the freely exposed carboxylate groups. On the contrary, the adsorption within the BioMOF structure most likely encompasses a surface adsorption/diffusion step within the porous network, followed by the establishment of interactions between the Ce(III) cations and both the OH− groups from the threonine residue and a carboxylate oxygen atom from the oxamate network, as already proven by crystal structure determination.[17] Experimental results (see Figure 7) suggest that the first mechanism predominates at low lanthanide concentration and in the very early stages of adsorption/filtration experiments, while the second one mainly contributes in improving the overall membrane performances observed at higher REEs concentration.

In order to characterize surface properties, hydrophilic, and hydrophobic characteristics of the given SWCNT-BP and BioMOF@SWCNT-BP membranes, contact angle have been determined by measuring the contact angle. The hydrophilic character of SWCNT-BP and BioMOF@SWCNT-BP top surfaces was confirmed, measurements gave average contact-angle values of 50.8° ± 0.5° and 51.5° ± 0.5°, respectively (Figures S7a and S7b, Supporting Information), highly desirable for water treatment membranes.[49]

3. Conclusions

In summary, in this paper the preparation, characterization, and potential applications of SWCNT-BPs and BioMOF@SWCNT-BPs in the recovery of REEs from model water solutions were reported. Flexible and self-standing BPs were obtained by simple filtration of SWCNT and BioMOF/SWCNT solutions and characterized by SEM, TGA, porosimetry, XRD, EDX, and contact angle measurements. The ability of SWCNT-BPs and BioMOF@SWCNT-BPs in recovering lanthanides from water solutions was investigated both in static and dynamic conditions as a function of pH values and initial lanthanide concentrations. These experiments showed that the adsorption is not influenced by pH of lanthanide solutions and BioMOFs in SWCNT-BPs play a beneficial role in the increase of Ce^{3+} recovery at higher concentrations thanks to the alcohol functionalities of threonine, decorating the MOF pores. We found a relative recovery percentage after a week recirculation in higher concentration (50 ppm of cerium) solutions—recirculating through the same membrane—with a 263.30 mg of cerium adsorbed per gram of BioMOF@SWCNT-BP.

Although this worthy result is achieved only after a large recirculation time, suggesting that binding to supported MOF is kinetically slow, it represents a good background to further improve the preparation of kinetically faster adsorbent materials. As previously stated, the interaction of lanthanide ions with the −COOH functional groups of the SWCNT-BP is likely to be the kinetically favored step, then followed by MOF uptake. The self-standing and re-use features with the possibility of an easy up-scale can make SWCNT-BPs and BioMOF@SWCNT-BPs an effective and cheap solution for the minimization of toxic pollutants from environment and waste and boost the recovery of rare elements such as lanthanides from water. The potential of BioMOF-containing BPs in recovery of REEs from water have been demonstrated for the first time. The overall behavior of here reported membranes presents some advantages but also weakness comparable to other ion-exchange materials such as resins, for which moderate selectivity was obtained as well, and further optimization of the resin preparation conditions is needed and expected to improve the final material performances.[50] However, herein, we have described a new and successful strategy for the preparation of a BP embedding a MOF carefully designed by us for a specific purpose. We showed an unprecedented BioMOF@SWCNT-BP built up with SWCNTs and a bioinspired MOF highly performant in the recovery of ions and possessing intrinsic chemical affinity for oxygen atoms. It outperforms the state-of-the-art representing the carbon-based material with the highest maximum adsorption capacity of REEs reported so far. The strategy reported is sustainable, effective, and cheap and can represent a viable solution to be extended to the whole recovery of REEs family from water streams. As indicated from EC, recovery technologies for critical raw materials are highly deliverable to boost the best practice of a circular economy. The potential of application of BioMOF@SWCNT-BPs on water streams, after the first steps of REEs recovery from e-waste, has been demonstrated here at lab-scale. Its performance is undoubtedly related to both the exquisite control of the threonine moieties decorating the MOF pores that are used, and the intrinsic affinity of SWCNTs for lanthanides. The performed dynamic capture experiments, rarely reported, bring this new composite material closer to a large-scale application. These last results represent a step forward toward the synergistic exploitation of MOFs and carbon-based materials, reporting one of the rare examples of MOF-carbon-based materials in applications dealing with recovery and environmental remediation.

4. Experimental Section

See Supporting Information for a detailed description of MOFs and membranes preparation, their characterization and capture experiments.

Supporting Information

Supporting Information is available from the Wiley Online Library or from the author.

Acknowledgements

A.T. and T.F.M. contributed equally to this work. This work was supported by the Ministero dell'Università e della Ricerca (ex 60%) (Italy) and the MINECO (Spain) (Projects CTQ2016-75671-P and Excellence Unit "Maria de Maeztu" MDM-2015-0538). A.T. thanks the project FOREST-COMP – CUP H56C18000080005 – PON "Ricerca e Innovazione 2014–2020" for postdoctoral grant. The Ph.D. of M.B. was funded by a scholarship from Regione Calabria (grant POR Calabria 2014–2020 - Azioni 10.5.6 e 10.5.12). Thanks are also extended to the "2019 Post-doctoral Junior Leader-Retaining Fellowship, la Caixa Foundation (ID100010434 and fellowship code LCF/BQ/PR19/11700011" (J.F.-S.). R.B. thanks Fondazione CARIPLO for the concession of a postdoctoral grant. D.A. acknowledges the financial support of the Fondazione CARIPLO/"Economia Circolare: ricerca per un futuro sostenibile" 2019, Project code: 2019–2090, MOCA. E.P. acknowledges the financial support of the European Research Council under the European Union's Horizon 2020 research and innovation programme/ERC Grant Agreement No 814804, MOF-reactors.

Conflict of Interest

The authors declare no conflict of interest.

Data Availability Statement

Research data are not shared.

Keywords

metal–organic frameworks, nanotube membranes, rare-earth elements recovery, single-walled carbon nanotubes, water remediation

Received: May 21, 2021
Revised: June 14, 2021
Published online:

[1] United Nations, *Transforming our World: the 2030 Agenda for Sustainable Development* **2015**.
[2] European Commission, **2020**, *COM(2020)*, 98 final.
[3] European Commission, **2020**, *COM(2020)*, 474 final.
[4] D. M. Park, A. Brewer, D. W. Reed, L. N. Lammers, Y. Jiao, *Environ. Sci. Technol.* **2017**, *51*, 13471.
[5] C. E. D. Cardoso, J. C. Almeida, B. Lopes, T. Trindade, C. Vale, *Nanomaterials* **2019**, *9*, 814.
[6] T. G. Ambaye, M. Vaccari, F. D. Castro, S. Prasad, S. Rtimi, *Environ. Sci. Pollut. Res.* **2020**, *27*, 36052.
[7] D. Li, B. Zhang, F. Xuan, *J. Mol. Liq.* **2015**, *211*, 203.
[8] L. Yurramendi, L. Gijsemans, F. Forte, J. L. Aldana, C. del Río, K. Binnemans, *Hydrometallurgy* **2019**, *187*, 38.
[9] T. E. Lister, P. Wang, A. Anderko, *Hydrometallurgy* **2014**, *149*, 228.
[10] Y. Hu, J. Florek, D. Larivière, F. G. Fontaine, F. Kleitz, *Chem. Rec.* **2018**, *18*, 1261.
[11] H. Deng, S. Grunder, K. E. Cordova, C. Valente, H. Furukawa, M. Hmadeh, F. Gándara, A. C. Whalley, Z. Liu, S. Asahina, H. Kazumori, M. O'Keeffe, O. Terasaki, J. F. Stoddart, O. M. Yaghi, *Science* **2012**, *336*, 1018.
[12] J. L. C. Rowsell, E. C. Spencer, J. Eckert, J. A. K. Howard, O. M. Yaghi, *Science* **2005**, *309*, 1350.
[13] G. Maurin, C. Serre, A. Cooper, G. Férey, *Chem. Soc. Rev.* **2017**, *46*, 3104.
[14] X. Zhao, M. Wong, C. Mao, T. X. Trieu, J. Zhang, P. Feng, X. Bu, *J. Am. Chem. Soc.* **2014**, *136*, 12572.
[15] X. Wang, A. Dong, Y. Hu, J. Qian, S. Huang, *Chem. Commun.* **2020**, *56*, 10809.
[16] Y. R. Lee, K. Yu, S. Ravi, W. S. Ahn, *ACS Appl. Mater. Interfaces* **2018**, *10*, 23918.
[17] M. Mon, R. Bruno, R. Elliani, A. Tagarelli, X. Qu, S. Chen, J. Ferrando-Soria, D. Armentano, E. Pardo, *Inorg. Chem.* **2018**, *57*, 13895.
[18] M. Mon, F. Lloret, J. Ferrando-Soria, C. Martí-Gastaldo, D. Armentano, E. Pardo, *Angew. Chem., Int. Ed.* **2016**, *55*, 11167.
[19] M. Mon, R. Bruno, E. Tiburcio, M. Viciano-Chumillas, L. H. G. Kalinke, J. Ferrando-Soria, D. Armentano, E. Pardo, *J. Am. Chem. Soc.* **2019**, *141*, 13601.
[20] G. Boix, J. Troyano, L. Garzón-Tovar, C. Camur, N. Bermejo, A. Yazdi, J. Piella, N. G. Bastus, V. F. Puntes, I. Imaz, D. Maspoch, *ACS Appl. Mater. Interfaces* **2020**, *12*, 10554.
[21] S. Gholami, J. López, A. Rezvani, V. Vatanpour, J. L. Cortina, *Chem. Eng. J.* **2020**, *384*, 123348.
[22] B. Sarkar, S. Mandal, Y. F. Tsang, P. Kumar, K. H. Kim, Y. S. Ok, *Sci. Total Environ.* **2018**, *612*, 561.
[23] B. Lee, Y. Baek, M. Lee, D. H. Jeong, H. H. Lee, J. Yoon, Y. H. Kim, *Nat. Commun.* **2015**, *6*, 7109.
[24] A. Khalid, A. A. Al-Juhani, O. C. Al-Hamouz, T. Laoui, Z. Khan, M. A. Atieh, *Desalination* **2015**, *367*, 134.
[25] H. Y. Yang, Z. J. Han, S. F. Yu, K. L. Pey, K. Ostrikov, R. Karnik, *Nat. Commun.* **2013**, *4*, 2220.
[26] K. C. Khulbe, T. Matsuura, *Appl. Water Sci.* **2018**, *8*, 19.
[27] I. Ihsanullah, *Sep. Purif. Technol.* **2019**, *209*, 307.
[28] B. Ribeiro, L. F. P. Santos, A. L. Santos, M. L. Costa, E. C. Botelho, *J. Thermoplast. Compos. Mater.* **2019**, *32*, 62.
[29] M. H. O. Rashid, S. Q. T. Pham, L. J. Sweetman, L. J. Alcock, A. Wise, L. D. Nghiem, G. Triani, M. in het Panhuis, S. F. Ralph, *J. Membr. Sci.* **2014**, *456*, 175.
[30] L. M. Felton, C. Anthony, *Nature* **2005**, *433*, E10.
[31] Y. A. Kim, H. Muramatsu, T. Hayashi, M. Endo, M. Terrones, M. S. Dresselhaus, *Chem. Vap. Deposition* **2006**, *12*, 327.
[32] M. H. O. Rashid, S. F. Ralph, *Nanomaterials* **2017**, *7*, 99.
[33] G. De Filpo, E. Pantuso, A. I. Mashin, M. Baratta, F. P. Nicoletta, *Membranes* **2020**, *10*, 157.
[34] U. Vohrer, I. Kolaric, M. H. Haque, S. Roth, U. Detlaff-Weglikowska, *Carbon* **2004**, *42*, 1159.
[35] C. J. Frizzell, M. in Het Panhuis, D. H. Coutinho, K. J. Balkus, A. I. Minett, W. J. Blau, J. N. Coleman, *Phys. Rev. B* **2005**, *72*, 245420.
[36] J. G. Park, N. G. Yun, Y. B. Park, R. Liang, L. Lumata, J. S. Brooks, C. Zhang, B. Wang, *Carbon* **2010**, *48*, 4276.
[37] A. C. McKinlay, R. E. Morris, P. Horcajada, G. Férey, R. Gref, P. Couvreur, C. Serre, *Angew. Chem., Int. Ed.* **2010**, *49*, 6260.
[38] I. Imaz, M. Rubio-Martínez, J. An, I. Solé-Font, N. L. Rosi, D. Maspoch, *Chem. Commun.* **2011**, *47*, 7287.
[39] M. Mon, R. Bruno, J. Ferrando-Soria, D. Armentano, E. Pardo, *J. Mater. Chem. A* **2018**, *6*, 4912.
[40] J. Pinto, *J. Membr. Sci. Technol.* **2020**, *10*, 204.
[41] J. Lee, Y. Ye, A. J. Ward, C. Zhou, V. Chen, A. I. Minett, S. Lee, Z. Liu, S. R. Chae, J. Shi, *Sep. Purif. Technol.* **2016**, *163*, 109.
[42] A. A. Alshahrani, I. H. Alsohaimi, S. Alshehri, A. R. Alawady, M. R. El-Aassar, L. D. Nghiem, M. in het Panhuis, *J. Mater. Res. Technol.* **2020**, *9*, 9080.

[43] K. Li, Q. Gao, G. Yadavalli, X. Shen, H. Lei, B. Han, K. Xia, C. Zhou, *ACS Appl. Mater. Interfaces* **2015**, *7*, 21047.
[44] K. Kilian, K. Pyrzyńska, M. Pęgier, *Solvent Extr. Ion Exch.* **2017**, *35*, 450.
[45] X. Xu, S. Sturm, Z. Samardzija, J. Scancar, K. Markovic, K. Z. Rozman, *Green Chem.* **2020**, *22*, 1105.
[46] J. Florek, D. Larivière, H. Kählig, S. L. Fiorilli, B. Onida, F. G. Fontaine, F. Kleitz, *ACS Appl. Mater. Interfaces* **2020**, *12*, 57003.
[47] R. Bruno, M. Mon, P. Escamilla, J. Ferrando-Soria, E. Esposito, A. Fuoco, M. Monteleone, J. C. Jansen, R. Elliani, A. Tagarelli, D. Armentano, E. Pardo, *Adv. Funct. Mater.* **2021**, *31*, 2008499.
[48] M. Oh-E, A. Nagasawa, *ACS Omega* **2020**, *5*, 31880.
[49] A. Nogalska, A. Trojanowska, B. Tylkowski, R. Garcia-Valls, *Phys. Sci. Rev.* **2019**, *5*, 1.
[50] M. Laatikainen, C. Branger, K. Laatikainen, T. Sainio, *Sep. Sci. Technol.* **2021**, *56*, 203.

ADVANCED MATERIALS INTERFACES

Supporting Information

for *Adv. Mater. Interfaces,* DOI: 10.1002/admi.202100730

Synthesis and Enhanced Capture Properties of a New BioMOF@SWCNT-BP: Recovery of the Endangered Rare-Earth Elements from Aqueous Systems

Antonio Tursi, Teresa F. Mastropietro, Rosaria Bruno, Mariafrancesca Baratta, Jesus Ferrando-Soria, Alexander I. Mashin, Fiore P. Nicoletta, Emilio Pardo,* Giovanni De Filpo,* and Donatella Armentano**

Supporting Information

Synthesis and Enhanced Capture Properties of a New BioMOF@SWCNT-BP: Recovery of the Endangered Rare Earth-Elements from Aqueous Systems

Antonio Tursi,[§] Teresa F. Mastropietro,[§] Rosaria Bruno, Mariafrancesca Baratta, Jesus Ferrando-Soria, Alexander I. Mashin, Fiore P. Nicoletta, Emilio Pardo,* Giovanni De Filpo,* Donatella Armentano**

Experimental Section

Chemicals:

All chemicals were of reagent grade quality. They were purchased from commercial sources and used as received. SWCNTs (characterized by an average diameter of 1.4 ± 0.1 nm and an average length longer than 5 μm) and carboxylic acid functionalized SWNTs (COOH-SWCNTs with bundle average dimensions ranging from 4 to 5 nm in diameter and from 0.5 to 1.5 μm in length, as reported in the datasheet from Sigma-Aldrich, Milan, Italy) were used for the preparation of SWCNT solutions. Compound $\{Sr^{II}Cu^{II}_6[(S,S)\text{-threonine}]_3(OH)_2(H_2O)\} \cdot 36H_2O$ (MOF) was prepared as reported earlier.[17]

Preparation of membranes:

Buckypaper membranes were obtained by filtration of solutions of SWCNTs and COOH-SWCNTs. Generally, thirty milligrams of SWCNT mixtures were dispersed in 200 mL of a 0.4% TRITON X100 water solution by an ultrasonic bath (model M1800H-E, Bransonic, Danbury, CT, USA) for 30 min. Then, solutions were filtered through PTFE disks with a vacuum pump (pressure = −0.04 bar), washed several times with methanol and, finally, dried at room temperature. All chemicals were purchased from Sigma-Aldrich, Milan, Italy. It is well known that several preparation factors influence the final BP membrane properties, including the SWCNT solution sonication time, the vacuum depression magnitude used during the filtration of SWCNT solutions, the filter porosity and composition.[32] In addition, the main problem found in this study was the best compromise in terms of weight percentage between long SWCNTs, which ensure the gain of self-standing and flexible BP disks, and short COOH-SWCNTs, which ensure a higher lanthanide adsorption. After several trials, the best weight ratio was SWCNTs : COOH-SWCNTs = 1 : 2, which gave detachable SWCNT disks from polymer filters and self-sustaining BPs (Figure 4.a).

BioMOF@SWCNT-BPs were obtained by dispersing MOF in the optimized SWCNT solution and applying the procedure previously outlined for neat **SWCNT-BP**. The largest amount of MOF, which was possible to disperse in the optimized SWCNT solution without losing detachability and self-sustainability of the final BP disks, was 25% w/w (Figure 4.b).

Both **SWCNT-BPs** and **BioMOF@SWCNT-BPs** were flexible disks with an average diameter of 41 ± 1 mm and an average thickness of 150 ± 5 μm.

Chemical-physical techniques:

Elemental (C, H, N) and powder X-ray Diffraction analyses (of the pure MOF) were performed at the Microanalytical Service of the University of Calabria. ICP-MS analyses for the Ce^{3+} and lanthanides capture experiments on membrane (*vide infra*) were performed at the

Department of Chemistry of the University of Calabria. FT–IR spectra were recorded on a Perkin-Elmer 882 spectrophotometer as KBr pellets. All characterizations confirmed the purity of the sample when compared with the previously reported by us.[17]

X-ray Powder Diffraction Measurements:
Polycrystalline sample of bioMOF **1** to test purity of the bulk, was introduced into 0.5 mm borosilicate capillaries prior to being mounted and aligned on a Bruker D2 Phaser powder diffractometer, using Cu Kα radiation (λ = 1.54056 Å). Five repeated measurements were collected at room temperature (2θ = 2–40°) and merged in a single diffractogram.

Membrane characterization:
The morphology of **SWCNT-BP** and **BioMOF@SWCNT-BP** was characterized by scanning electron microscopy with a Leica LEO 420 (Leica Microsystems, Cambridge, England) scanning electron microscope with an accelerating voltage of 10 kV. Samples were covered with an ultrathin gold layer using a sputter coater.
Figures 4.c and 4.d show the morphology of **SWCNT-BP** and **BioMOF@SWCNT-BP** membranes. SWCNT-BP morphology is characterized by the typical BP microscopic texture with bundles and clusters of SWCNTs arising from π–π and van der Waals interactions. The addition of BioMOFs in **SWCNT-BPs** is evidenced in Figure 4.d by the presence of small spherical particles with an average size lower than 1 μm and formed by smaller primary particles with an average diameter of ≈ 100 nm. The highly porous structure of **SWCNT-BPs**, firmly hosting the nanosized BioMOF particles (no leakage was observed at the end of both static and dynamic experiments), guarantees a high permeability and a large surface area for the contact and successive adsorption of lanthanides present in the test solutions. MOFs are homogenously distributed inside the membrane. No particle sedimentation or agglomeration phenomena were observed.

Thermogravimetric analysis:
The thermogravimetric analysis was performed on **SWCNT-BP** and **BioMOF@SWCNT-BP** samples under a dry N_2 atmosphere with a Mettler Toledo TGA/STDA 851^e thermobalance. The experiments were carried out within a temperature range from 25 °C up to 800 °C at a heating rate of 10 °C/min. Approximately 20 mg of each sample were placed in a ceramic pan for the measurement.

Capture experiments:
The REE adsorption performance of **SWCNT-BPs** and **BioMOF@SWCNT-BPs** was tested on $CeCl_3$ (purity ≥99.99%, Merck, Darmstadt, Germany) water solutions and an equimolar multielement standard solution of $ScCl_3$, YCl_3, $LaCl_3$, $CeCl_3$, $PrCl_3$, $NdCl_3$, $SmCl_3$, $EuCl_3$, $GdCl_3$, $TbCl_3$, $DyCl_3$, $HoCl_3$, $ErCl_3$, $TmCl_3$, $YbCl_3$ and $LuCl_3$ (TraceCERT® 50 mg/L of each element, Merck, Darmstadt, Germany diluted to about 835 ppb for each lanthanide) at room temperature and under static or dynamic conditions (Tables S1-S13).
In static experiments, **SWCNT-BPs** and **BioMOF@SWCNT-BPs** were placed in 100 mL beckers containing 80 mL of $CeCl_3$ solution at room temperature (25°C) and different pH values. pH was adjusted to the desired value (5, 6 and 8) by adding HNO_3 or NaOH. Solutions were stirred by an orbital shaker (PSU-10i, Biosan, Italy).
In dynamic experiments, Cerium (1.35, 3, 10, 30 and 50 ppm) and multielement standard solutions (pH 5, volume = 200 mL, temperature = 25°C by a thermostatic bath model 1225, VWR, Milan, Italy) were recirculated in a small continuous plant by a peristaltic system (flow rate 5 mL min^{-1}, Masterflex® L/S®, Cole-Parmer Srl, Cernusco sul Naviglio, MI, Italy) through a round cell with a diameter of 41 mm. The effective permeation area was limited to 10.75 cm^2 by an *o-ring* with a diameter of 37 mm, used to fix membranes. The filtration setup

is illustrated in Figure 5. Both in static and dynamic conditions, at fixed time intervals aliquots of 100 µL were taken for the determination of lanthanide concentrations. The ICP-MS data are reported considering the dilution factor.
For selectivity experiments, **SWCNT-BPs** and **BioMOF@SWCNT-BPs** were placed in 100 mL beckers containing 10 ppm of $CeCl_3$, $FeCl_3$ and $AlCl_3$ aqueous solution at room temperature (25°C) and pH value adjusted to 5. Solutions were stirred by an orbital shaker (PSU-10i, Biosan, Italy).

ICP-MS analyses:
The REE concentrations were determined by utilizing an inductively coupled plasma-mass spectrometer (ICP-MS iCAP™ TQ Thermo Fisher Scientific, USA) equipped with a Peltier cooled high purity quartz baffled cyclonic spray chamber, a concentric borosilicate glass nebulizer, a wide 2.5 mm internal diameter quartz injector, a nickel sample and two skimmer cones with 1.1 mm and 0.5 mm diameter orifices, respectively. The ICP torch was a demountable single piece quartz torch. The samples were collected by a Thermo Scientific™ Autosampler Housing with a peristaltic pump equipped with three-stop flared PVC pump tubing. A multielement standard solution was used to calibrate the instrument using different analytical concentrations (0.5, 5, 10, 20, 50 and 100 ppb, R^2 of calibration curve ≈ 1 and a limit of detection, LOD, of about 0.015 ppb). Ultrapure water (18.3 MΩ cm, Arioso, Human Corporation, Korea) was used for the aqueous solutions preparation after filtration by 0.45 µm filter (Millex Syringe Filter, Merck, Darmstadt, Germany). Each experiment was performed in triplicate and results are reported as average values ± 3 SD. Data reported in Tables S1-S13.

EDX measurements:
Scanning Electron Microscopy (SEM) measurements were carried out for both **SWCNT-BPs** and **BioMOF@SWCNT-BPs** using a HITACHI S-4800 electron microscope coupled with an Energy Dispersive X–ray (EDX) detector. Data were analyzed with a QUANTAX 400 EDS electron microscope analyzer. Both membranes were suspended in a 10 ppm $CeCl_3$ aqueous solution for 24 h.

Contact angle measurements:
Static contact angle values of **SWCNT-BPs** and **BioMOF@SWCNT-BPs** were measured with a goniometer (Nordtest, Serravalle Scrivia AL, Italy) at 25 °C. A drop (2 µL) of water was put onto the sample surface by a micro-syringe and measurements were carried out by setting the tangents on both visible edges of the droplet on five different positions of each sample and calculating the average value of the measurements. The hydrophilic character of **SWCNT-BP** and **BioMOF@SWCNT-BP** top surfaces was confirmed by contact-angle measurements, which gave average contact-angle values of 50.8° ± 0.5° and 51.5° ± 0.5°, respectively, Figures S7.a and S7.b.

Table S1. Residual Ce^{3+} concentration,[a,b] in the stock solutions at an initial concentration of 3.5 ppm and different pH analyzed with the ICP-MS under static adsorption processes for a neat **SWCNT-BP**.

Time / min	$[Ce^{3+}]$@pH8 / ppb	$[Ce^{3+}]$@pH6 / ppb	$[Ce^{3+}]$@pH5 / ppb
0	2798	3145	3563
1	2743	2994	3355
5	2658	2856	3224
10	2518	2767	3072
15	2439	2658	2999
30	2268	2407	2654
60	1924	1982	2193
120	1439	1543	1591
240	709	683	658
360	364	333	298
480	184	166	140
600	98	86	68
1000	15	19	18
1440	≈ 0	≈ 0	≈ 0
Recovery / %	≈ 100	≈ 100	≈ 100

[a]*LOD: 0.015 ppb*. [b]Each experiment was performed in triplicate and results are reported as average values ± 3 SD.

Table S2. Residual Ce^{3+} concentration,[a,b] in the stock solutions at an initial concentration of 3.5 ppm and different pH analyzed with the ICP-MS under static adsorption processes for a **BioMOF@SWCNT-BP**.

Time / min	**[Ce^{3+}]@pH8 / ppb**	**[Ce^{3+}]@pH6 / ppb**	**[Ce^{3+}]@pH5 / ppb**
0	3053	3518	3688
1	2958	3403	3434
5	2877	3266	3308
10	2801	3170	3105
15	2732	3083	3033
30	2514	2828	2639
60	2164	2391	2092
120	1641	1754	1012
240	864	854	330
360	468	431	95
480	252	219	21
600	137	111	0
1000	19	15	0
1440	≈ 0	≈ 0	≈ 0
Recovery / %	≈ 100	≈ 100	≈ 100

[a]*LOD: 0.015 ppb.* [b]Each experiment was performed in triplicate and results are reported as average values ± 3 SD.

Table S3. Residual Ce^{3+} concentration,[a,b] in the stock solutions at an initial concentration of 1.35 ppm and 3 ppm pH 5 analyzed with the ICP-MS under dynamic adsorption processes for a neat **SWCNT-BP** and a **BioMOF@SWCNT-BP**.

	[Ce^{3+}] = 1.35 ppm		**[Ce^{3+}] = 3 ppm**	
Time / min	SWCNT-BP / ppb	BioMOF@SWCNT-BP / ppb	SWCNT-BP / ppb	BioMOF@SWCNT-BP / ppb
0	1359	1350	3001	3013
5	1258	1236	2737	2794
15	1243	899	2604	2189
30	1110	861	2363	1928
60	776	604	1919	1382
120	389	277	931	770
240	152	51	305	167
360	21	4	57	23
480	11	3	19	13
600	8	4	11	5
800	6	1	8	2
1400	2	0	4	1
4320	0	0	≈ 0	≈ 0
Recovery / %	99.96	99.98	99.99	99.99

[a]*LOD: 0.015 ppb*. [b]Each experiment was performed in triplicate and results are reported as average values ± 3 SD.

Table S4. Residual Ce^{3+} concentration,[a,b] in the stock solutions at an initial concentration of 10 ppm pH 5 analyzed with the ICP-MS under dynamic adsorption processes for a neat **SWCNT-BP** and a **BioMOF@SWCNT-BP**.

Time / min	SWCNT-BP / ppb	BioMOF@SWCNT-BP / ppb
0	10510	10531
5	8332	8339
15	6979	6978
30	4901	4675
60	3396	3120
120	2375	2094
240	1717	1537
360	1211	1153
480	944	856
600	509	372
800	323	241
1400	171	79
4320	3	≈ 0
Recovery / %	99.97	≈ 100.00

[a]*LOD: 0.015 ppb*. [b]Each experiment was performed in triplicate and results are reported as average values ± 3 SD.

Table S5. Residual Ce^{3+} concentration,[a,b] in the stock solutions at an initial concentration of 30 ppm and 50 ppm analyzed with the ICP-MS under dynamic adsorption processes for a neat **SWCNT-BP** and a **BioMOF@SWCNT-BP**.

	[Ce^{3+}] = 30 ppm		**[Ce^{3+}] = 50 ppm**	
Time / min	SWCNT-BP / ppb	BioMOF@SWCNT-BP / ppb	SWCNT-BP / ppb	BioMOF@SWCNT-BP / ppb
0	30831	31441	51146	51875
5	29947	30243	45971	44782
15	28769	28128	36457	32374
30	24353	24086	33450	28953
60	20565	18409	32023	27024
120	16736	13843	29950	25471
240	13512	10041	27848	24302
360	10924	7319	26422	23474
480	8782	5542	25611	22890
600	6597	4431	25120	22428
800	5145	3043	24543	21943
1440	4138	2079	23759	20891
4320	3787	1911	23643	20779
Recovery / %	87.72	93.92	53.77	59.94

[a]*LOD: 0.015 ppb*. [b]Each experiment was performed in triplicate and results are reported as average values ± 3 SD.

Table S6. Residual Sc^{3+} and Y^{3+} concentration,[a,b] in an equimolar multielement standard solution at an initial total concentration of 13.4 ppm analyzed with the ICP-MS under dynamic adsorption processes for a neat **SWCNT-BP** and a **BioMOF@SWCNT-BP**.

	Scandium		**Yttrium**	
Time / min	SWCNT-BP / ppb	BioMOF@SWCNT-BP / ppb	SWCNT-BP / ppb	BioMOF@SWCNT-BP / ppb
0	813	830	815	849
5	666	650	672	673
15	524	515	531	538
30	379	368	385	382
60	247	249	267	262
120	121	165	215	187
240	39	91	178	137
480	7	32	99	50
600	4	10	61	24
1440	1	2	22	11
4320	≈ 0	≈ 0	≈ 0	≈ 0
Recovery / %	≈ 100.00	≈ 100.00	99.95	≈ 100.00

[a]*LOD: 0.015 ppb*. [b]Each experiment was performed in triplicate and results are reported as average values ± 3 SD.

Table S7. Residual La^{3+} and Ce^{3+} concentration,[a,b] in an equimolar multielement standard solution at an initial total concentration of 13.4 ppm analyzed with the ICP-MS under dynamic adsorption processes for a neat SWCNT-BP and a **BioMOF@SWCNT-BP**.

	Lanthanum		**Cerium**	
Time / min	SWCNT-BP / ppb	BioMOF@SWCNT-BP / ppb	SWCNT-BP / ppb	BioMOF@SWCNT-BP / ppb
0	800	836	825	871
5	663	660	653	689
15	522	526	515	518
30	383	382	384	386
60	260	257	266	258
120	183	170	179	173
240	143	113	130	108
480	76	46	68	47
600	45	30	40	27
1440	16	7	13	6
4320	≈ 0	≈ 0	≈ 0	≈ 0
Recovery / %	99.97	≈ 100.00	99.97	≈ 100.00

[a]*LOD: 0.015 ppb*. [b]Each experiment was performed in triplicate and results are reported as average values ± 3 SD.

Table S8. Residual Pr^{3+} and Nd^{3+} concentration,[a,b] in an equimolar multielement standard solution at an initial total concentration of 13.4 ppm analyzed with the ICP-MS under dynamic adsorption processes for a neat **SWCNT-BP** and a **BioMOF@SWCNT-BP**.

	Praseodymium		**Neodymium**	
Time / min	SWCNT-BP / ppb	BioMOF@SWCNT-BP / ppb	SWCNT-BP / ppb	BioMOF@SWCNT-BP / ppb
0	829	869	813	843
5	656	685	668	669
15	516	521	527	529
30	386	383	375	371
60	258	257	252	249
120	175	173	170	169
240	124	107	120	105
480	64	45	61	46
600	38	26	36	25
1440	14	6	13	5
4320	≈ 0	≈ 0	≈ 0	≈ 0
Recovery / %	99.97	≈ 100.00	99.97	≈ 100.00

[a]*LOD: 0.015 ppb*. [b]Each experiment was performed in triplicate and results are reported as average values ± 3 SD.

Table S9. Residual Sm^{3+} and Eu^{3+} concentration,[a,b] in an equimolar multielement standard solution at an initial total concentration of 13.4 ppm analyzed with the ICP-MS under dynamic adsorption processes for a neat **SWCNT-BP** and a **BioMOF@SWCNT-BP**.

	Samarium		**Europium**	
Time / min	SWCNT-BP / ppb	BioMOF@SWCNT-BP / ppb	SWCNT-BP / ppb	BioMOF@SWCNT-BP / ppb
0	818	856	816	845
5	676	673	675	667
15	530	534	526	533
30	384	378	391	388
60	254	252	261	258
120	167	170	168	171
240	114	104	119	106
480	57	42	60	44
600	34	24	36	24
1440	12	5	11	4
4320	≈ 0	≈ 0	≈ 0	≈ 0
Recovery / %	99.98	≈ 100.00	99.97	≈ 100.00

[a]*LOD: 0.015 ppb*. [b]Each experiment was performed in triplicate and results are reported as average values ± 3 SD.

Table S10. Residual Gd^{3+} and Tb^{3+} concentration,[a,b] in an equimolar multielement standard solution at an initial total concentration of 13.4 ppm analyzed with the ICP-MS under dynamic adsorption processes for a neat **SWCNT-BP and a BioMOF@SWCNT-BP.**

	Gadolinium		**Terbium**	
Time / min	SWCNT-BP / ppb	BioMOF@SWCNT-BP / ppb	SWCNT-BP / ppb	BioMOF@SWCNT-BP / ppb
0	814	844	835	874
5	677	673	691	691
15	529	533	544	550
30	381	376	393	391
60	257	253	265	262
120	175	174	182	179
240	126	109	133	115
480	65	42	69	55
600	40	27	41	29
1440	14	6	15	6
4320	≈ 0	≈ 0	≈ 0	≈ 0
Recovery / %	99.97	≈ 100.00	99.97	≈ 100.00

[a]*LOD: 0.015 ppb*. [b]Each experiment was performed in triplicate and results are reported as average values ± 3 SD.

Table S11. Residual Dy^{3+} and Ho^{3+} concentration,[a,b] in an equimolar multielement standard solution at an initial total concentration of 13.4 ppm analyzed with the ICP-MS under dynamic adsorption processes for a neat **SWCNT-BP** and a **BioMOF@SWCNT-BP**.

	Dysprosium		**Holmium**	
Time / min	SWCNT-BP / ppb	BioMOF@SWCNT-BP / ppb	SWCNT-BP / ppb	BioMOF@SWCNT-BP / ppb
0	804	833	833	880
5	669	663	694	696
15	525	526	547	550
30	379	379	397	395
60	258	251	270	267
120	180	174	192	184
240	131	113	145	122
480	69	57	77	67
600	43	30	46	34
1440	15	7	16	8
4320	≈ 0	≈ 0	≈ 0	≈ 0
Recovery / %	99.97	≈ 100.00	99.97	≈ 100.00

[a]*LOD: 0.015 ppb*. [b]Each experiment was performed in triplicate and results are reported as average values ± 3 SD.

Table S12. Residual Er^{3+} and Tm^{3+} concentration,[a,b] in an equimolar multielement standard solution at an initial total concentration of 13.4 ppm analyzed with the ICP-MS under dynamic adsorption processes for a neat **SWCNT-BP** and a **BioMOF@SWCNT-BP.**

	Erbium		**Thulium**	
Time / min	SWCNT-BP / ppb	BioMOF@SWCNT-BP / ppb	SWCNT-BP / ppb	BioMOF@SWCNT-BP / ppb
0	809	836	839	876
5	672	660	697	700
15	528	526	551	551
30	401	396	397	395
60	271	269	272	268
120	186	178	196	188
240	149	121	150	127
480	79	67	80	64
600	48	36	48	37
1440	14	8	17	8
4320	≈ 0	≈ 0	≈ 0	≈ 0
Recovery / %	99.96	≈ 100.00	99.96	≈ 100.00

[a]*LOD: 0.015 ppb*. [b]Each experiment was performed in triplicate and results are reported as average values ± 3 SD.

Table S13. Residual Yb^{3+} and Lu^{3+} concentration,[a,b] in an equimolar multielement standard solution at an initial total concentration of 13.4 ppm analyzed with the ICP-MS under dynamic adsorption processes for a neat **SWCNT-BP** and a **BioMOF@SWCNT-BP**.

	Ytterbium		**Lutetium**	
Time / min	SWCNT-BP / ppb	BioMOF@SWCNT-BP / ppb	SWCNT-BP / ppb	BioMOF@SWCNT-BP / ppb
0	796	833	844	879
5	665	658	698	698
15	526	525	551	553
30	394	393	402	398
60	257	253	275	271
120	186	176	200	188
240	148	120	154	131
480	79	69	83	70
600	47	35	50	41
1440	16	8	18	9
4320	≈ 0	≈ 0	≈ 0	≈ 0
Recovery / %	99.96	≈ 100.00	99.96	≈ 100.00

[a]*LOD: 0.015 ppb*. [b]Each experiment was performed in triplicate and results are reported as average values ± 3 SD.

Table S14. Residual Ce^{3+} concentration,[a,b] in the stock solutions at an initial concentration of 30 ppm of neat **SWCNT-BP** and **BioMOF@SWCNT-BP** membranes, reused after three regeneration cycles, analyzed with the ICP-MS, under dynamic adsorption processes.

	Cerium	
Time / min	SWCNT-BP / ppb	BioMOF@SWCNT-BP / ppb
0	30725	30956
5	30685	30755
15	29207	29816
30	25327	25290
60	21593	19145
120	17573	14535
240	13917	10543
480	9221	5875
600	6729	4653
1440	5786	3521
4320	5052	3226
Recovery / %	83.60	89.58

[a]Calculated uncertainties of ± 2%**.** [b]Each experiment was performed in triplicate.

Table S15. Residual Ce^{3+}, Fe^{3+} and Al^{3+} concentrations,[a,b] in an equimolar solution at an initial concentration of 10 ppm for each ion, analyzed with the ICP-MS under static adsorption processes for a neat **SWCNT-BP** and a **BioMOF@SWCNT-BP**.

Time / min	Ce-SWNT-MOF /ppm	Al-SWNT-MOF/ppm	Fe-SWNT-MOF/ppm	Ce-SWNT/ppm	Al-SWNT/ppm	Fe-SWNT/ppm
0	9,599	8,925	9,245	9,537	8,833	9,206
5	8,203	6,695	6,142	8,501	7,390	8,129
15	4,577	2,833	4,374	7,550	6,219	7,556
30	3,306	1,083	2,423	5,061	4,405	4,980
60	1,157	0,575	2,041	3,683	3,495	3,943
120	0,328	0,456	1,379	2,825	3,004	3,389
240	0,145	0,374	0,985	1,804	2,222	2,513
480	0,124	0,286	0,838	0,774	1,462	1,950
600	0,116	0,240	0,818	0,525	1,128	1,731
1000	0,092	0,205	0,782	0,282	0,867	1,367
1440	0,084	0,190	0,777	0,276	0,754	1,305
4320	0,076	0,160	0,749	0,271	0,781	1,261

[a]*LOD: 0.015 ppb.* [b]Each experiment was performed in triplicate and results are reported as average values ± 3 SD.

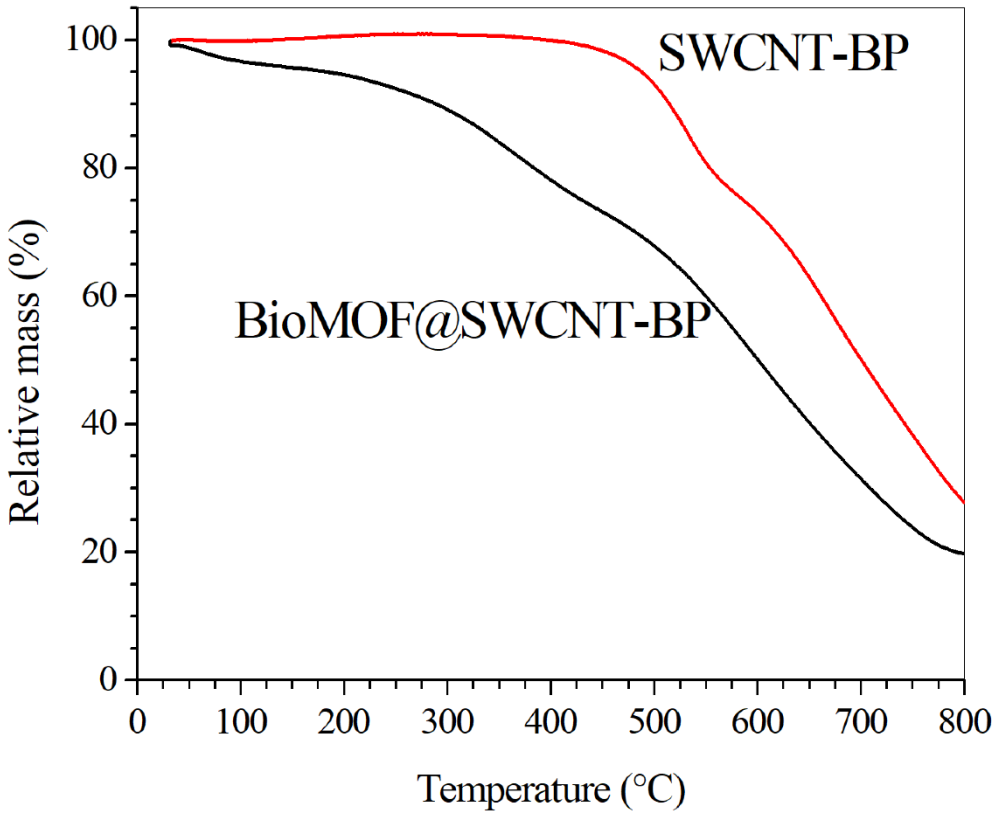

Figure S1. Thermal gravimetrical analyses of a **SWCNT-BP** and a **BioMOF@SWCNT-BP**. The initial relative mass change in **BioMOF@SWCNT-BP** up is due to moisture loss. The degradation of SWCNTs and BioMOFs is observed at larger temperatures.

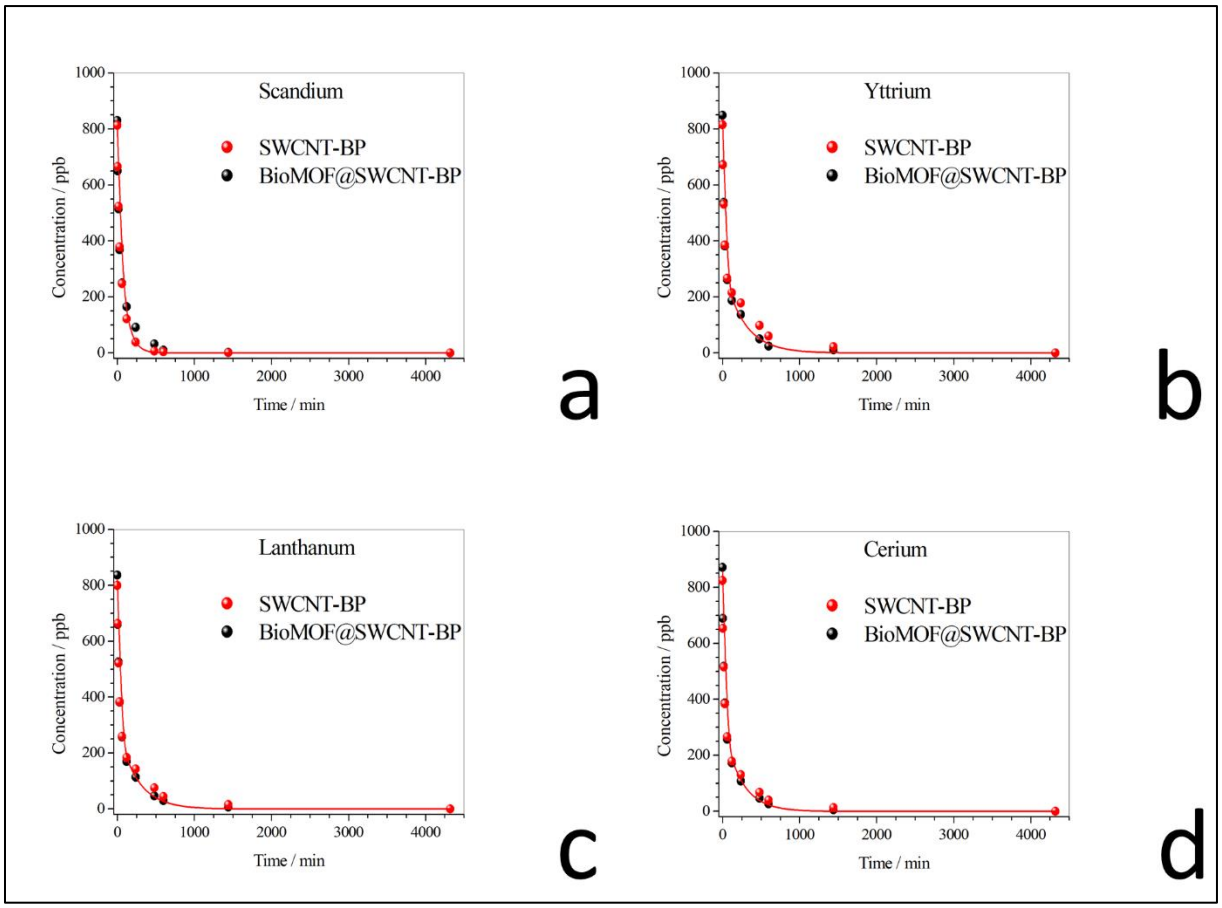

Figure S2. REE recovery by a **SWCNT-BP** and a **BioMOF@SWCNT-BP** from a 13.4 ppm multielement aqueous solution (pH 5) under dynamic experimental conditions: a) Scandium, b) Yttrium, c) Lanthanum, and d) Cerium.

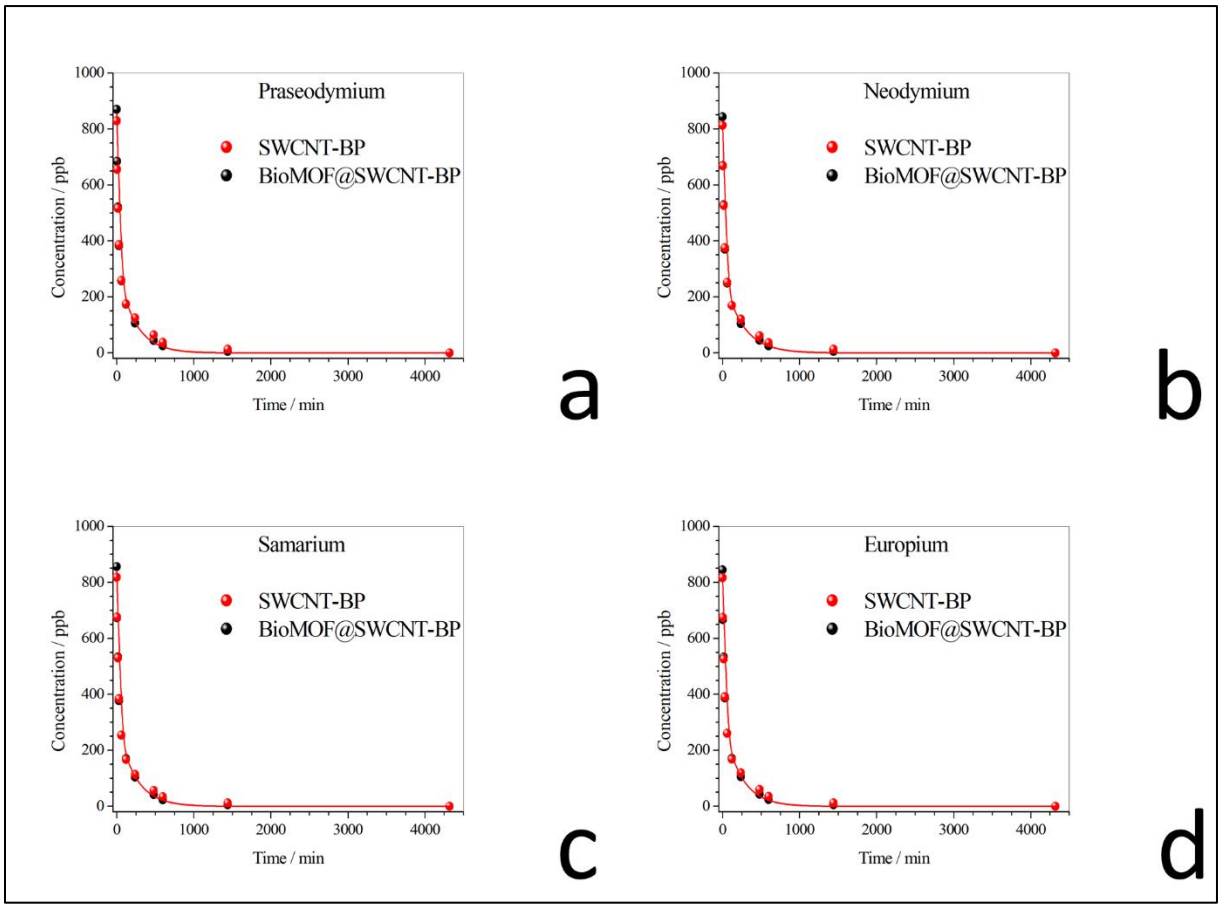

Figure S3. REE recovery by a **SWCNT-BP** and a **BioMOF@SWCNT-BP** from a 13.4 ppm multielement aqueous solution (pH 5) under dynamic experimental conditions: a) Praseodymium, b) Neodymium, c) Samarium, and d) Europium.

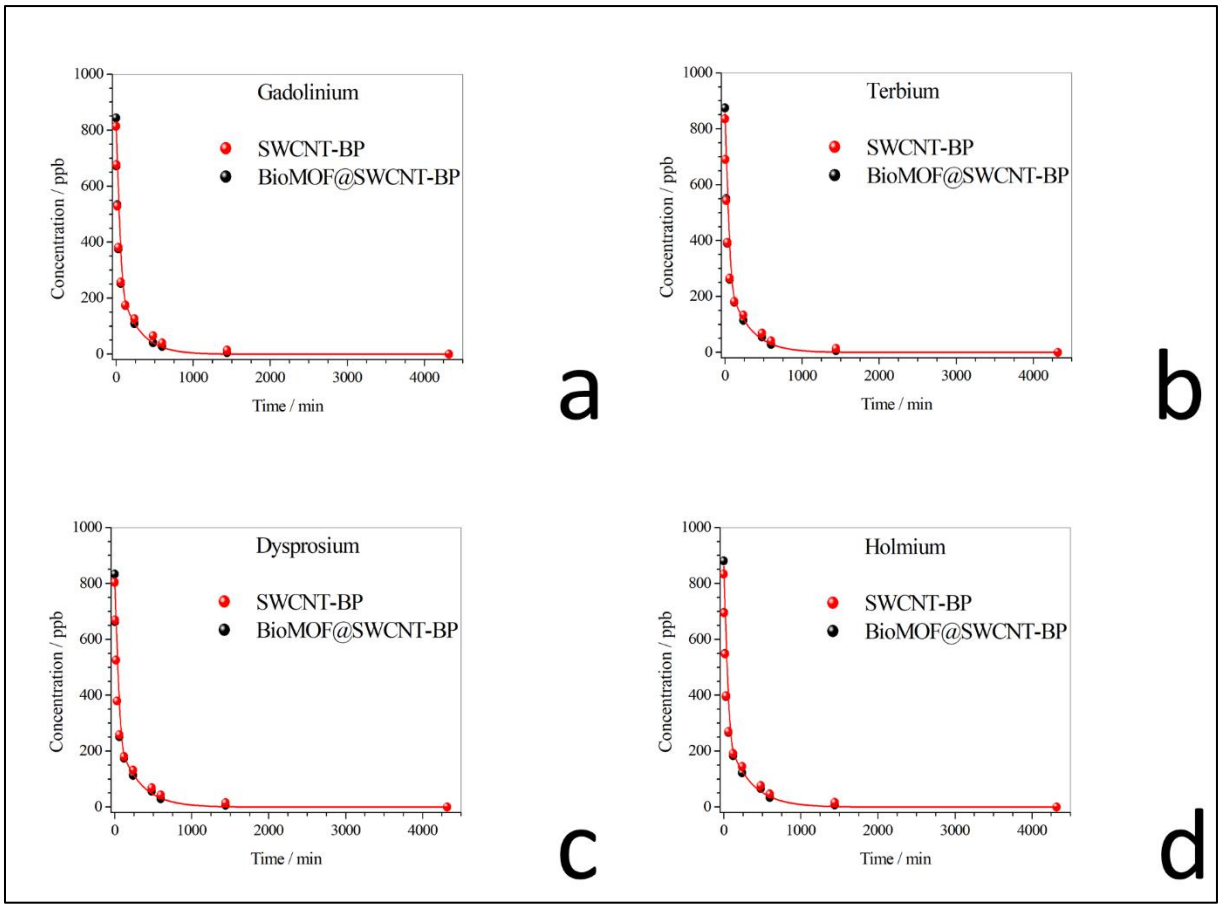

Figure S4. REE recovery by a **SWCNT-BP** and a **BioMOF@SWCNT-BP** from a 13.4 ppm multielement aqueous solution (pH 5) under dynamic experimental conditions: a) Gadolinium, b) Terbium, c) Dysprosium, and d) Holmium.

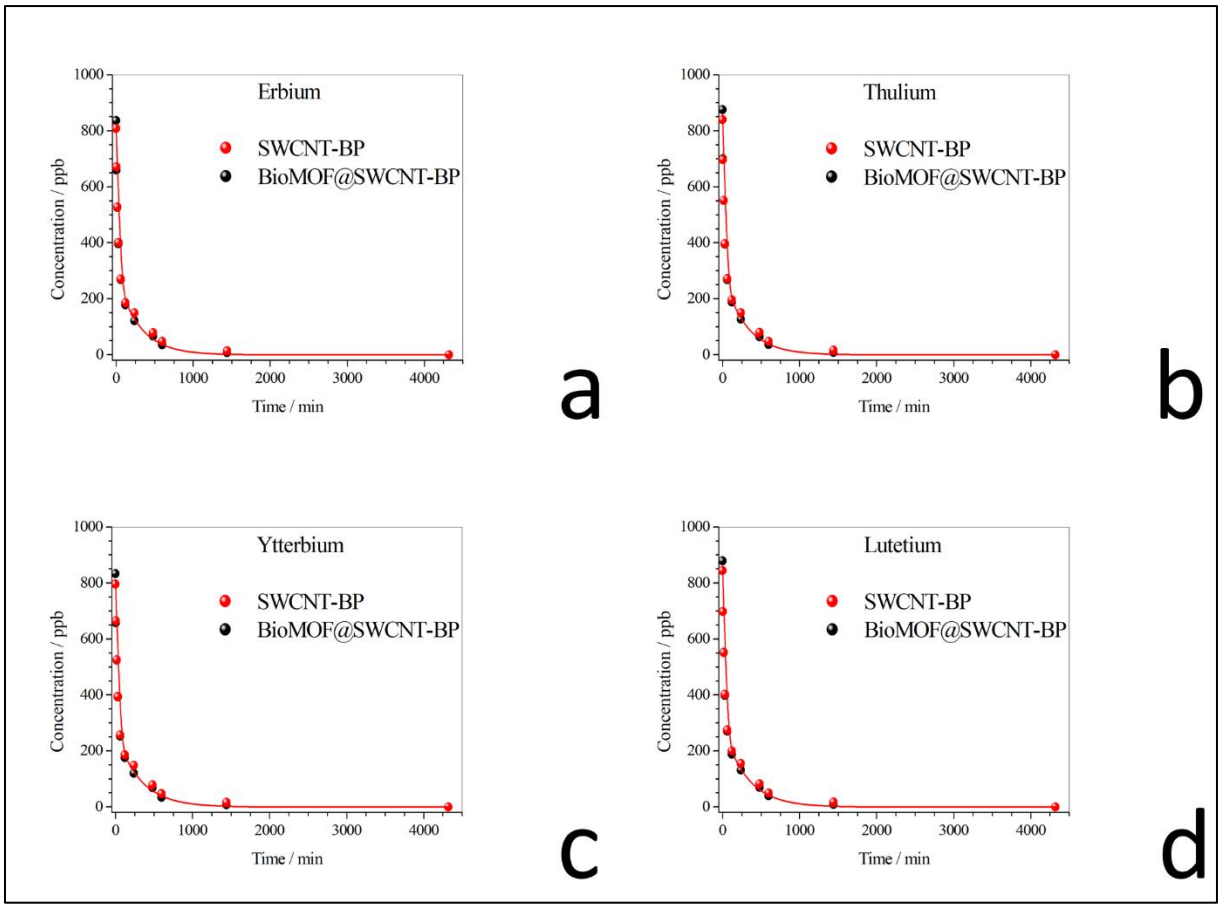

Figure S5. REE recovery by a **SWCNT-BP** and a **BioMOF@SWCNT-BP** from a 13.4 ppm multielement aqueous solution (pH 5) under dynamic experimental conditions: a) Erbium, b) Thulium, c) Ttterbium, and d) Lutetium.

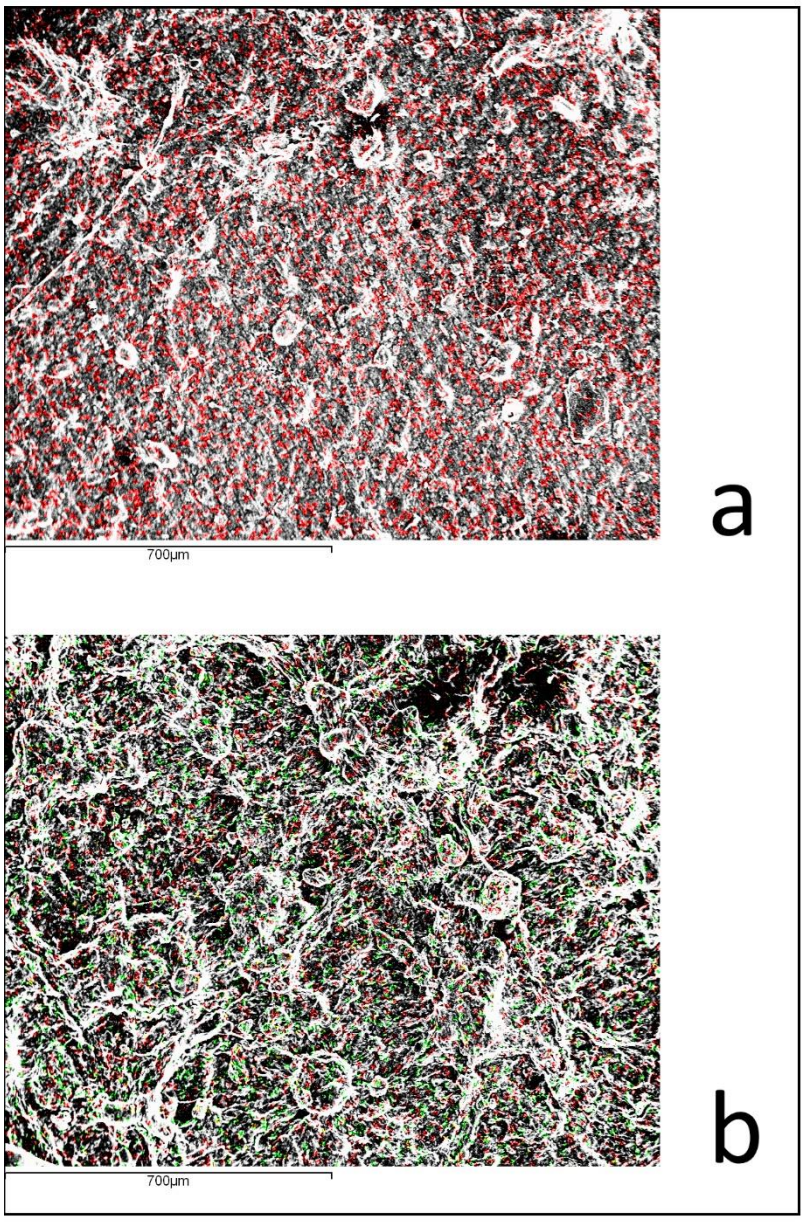

Figure S6. SEM image and the corresponding EDX elemental mapping for Cu and Ce elements from: a) a **SWCNT-BP** and b) a **BioMOF@SWCNT-BP** after their use in the recovery of Ce(III) (red dots). Green dots in (b) are due to Cu(II) atoms present in BioMOFs. Images confirm a homogeneous distribution of BioMOFs in **SWCNT-BPs** and a homogeneous adsorption in both membranes of Ce (III).

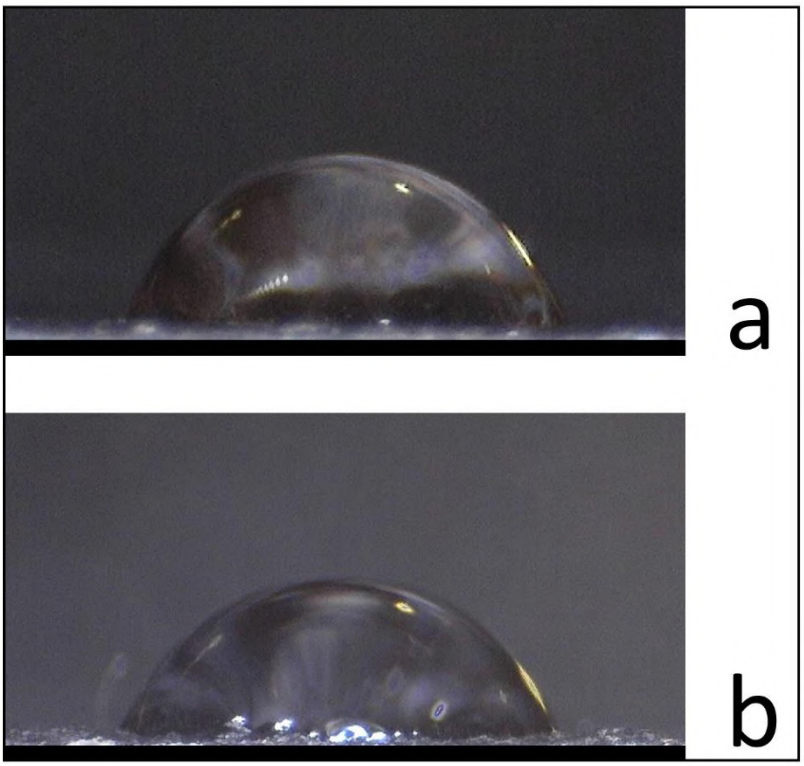

Figure S7. Average contact-angle value of: a) a **SWCNT-BP** and b) a **BioMOF@SWCNT-BP**.

ACS APPLIED NANO MATERIALS

www.acsanm.org Article

Multivariate Metal–Organic Framework/Single-Walled Carbon Nanotube Buckypaper for Selective Lead Decontamination

Mariafrancesca Baratta,[§] Teresa Fina Mastropietro,[§] Rosaria Bruno,[§] Antonio Tursi,[§] Cristina Negro, Jesús Ferrando-Soria,* Alexander I. Mashin, Aleksey Nezhdanov, Fiore P. Nicoletta,* Giovanni De Filpo,* Emilio Pardo,* and Donatella Armentano*

Cite This: *ACS Appl. Nano Mater.* 2022, 5, 5223–5233 Read Online

ACCESS | Metrics & More | Article Recommendations | Supporting Information

ABSTRACT: The search for efficient technologies empowering the selective capture of environmentally harmful heavy metals from wastewater treatment plants, at affordable prices, attracts wide interest but constitutes an important technological challenge. We report here an eco-friendly single-walled carbon nanotube buckypaper (SWCNT-BP) enriched with a multivariate amino acid-based metal–organic framework (MTV-MOF) for the efficient and selective removal of Pb^{2+} in multicomponent water systems. Pristine MTV-MOF was easily immobilized within the porous network of entangled SWCNTs, thus obtaining a stable self-standing adsorbing membrane filter (**MTV-MOF/SWCNT-BP**). SWCNT-BP alone shows a moderately good removal performance with a maximum adsorption capacity of 180 $mg \cdot g^{-1}$ and a considerable selectivity for Pb(II) ions in highly concentrated multi-ion solutions over a wide range of lead concentration (from 200 to 10000 ppb). Remarkably, these features were outperformed with the hybrid membrane filter **MTV-MOF/SWCNT-BP**, exhibiting enhanced selectivity and adsorption capacity (310 $mg \cdot g^{-1}$, which is up to 42% higher than that of the neat SWCNT-BP) and consequently enabling a more efficient and selective removal of Pb^{2+} from aqueous media. **MTV-MOF/SWCNT-BP** was able to reduce $[Pb^{2+}]$ from the dangerous 1000 ppb level to acceptable limits for drinking water, below 10 ppb, as established by the current EPA and WHO limits. Thus, the eco-friendly composite **MTV-MOF/SWCNT-BP** shows the potential to be effectively used several times as a reliable adsorbent for Pb^{2+} removal for household drinking water or in industrial treatment plants for water and wastewater lead decontamination.

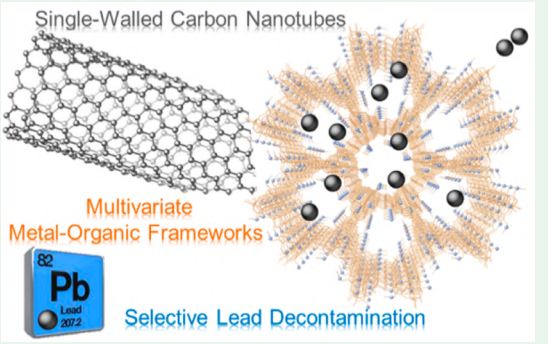

KEYWORDS: *single-walled carbon nanotube membranes, multivariate metal–organic frameworks, lead decontamination, MOF-based composites, water remediation*

INTRODUCTION

Access to safe drinking water is vital for both human life and general public health, as contamination of aquatic environments increases the transmission of life-threatening diseases.[1] Among the wide plethora of organic and inorganic pollutants aquatic environments may contain, which are currently regulated by national and international agencies worldwide,[2−4] water contamination from lead has received particular attention.[2−4] Lead contamination of water sources arises from diverse human activities. For example, some manufacturing and industrial facilities still employ lead in many processes, releasing this toxic metal ion into wastewater at high concentrations.[5,6] However, the main sources of domestic water lead-contamination are the corrosion of household plumbing systems or the erosion of natural deposits.

Exposure to lead has detrimental effects on aquatic ecosystems and human health, as a consequence of its bioaccumulation and the severe diseases it can cause even at minor concentration (>0.4 mg L^{-1}).[7,8] For instance, the maximum contaminant level goal (MCLG), established by the United States Environmental Protection Agency (EPA) through the Safe Drinking Water Act (SDWA),[9] is 0 $\mu g/L$. However, it is extremely difficult to reach such ideal concentration by phosphate dosing, which is the most common technique used to prevent water contamination from lead. In this sense, the maximum contaminant level (MCL) that can be achieved using the best affordable available treatment technologies is fixed to 15 $\mu g/L$ (15 ppb), whereas the maximum allowed levels for lead, established by the EPA[10]

Received: January 19, 2022
Accepted: March 23, 2022
Published: April 1, 2022

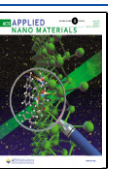

Scheme 1. Graphical Conceptualization of the Work Here Reported Consisting of Enriching SWCNT-BP with MTV-MOF to Produce an MTV-MOF/SWCNT-BP Membrane[a]

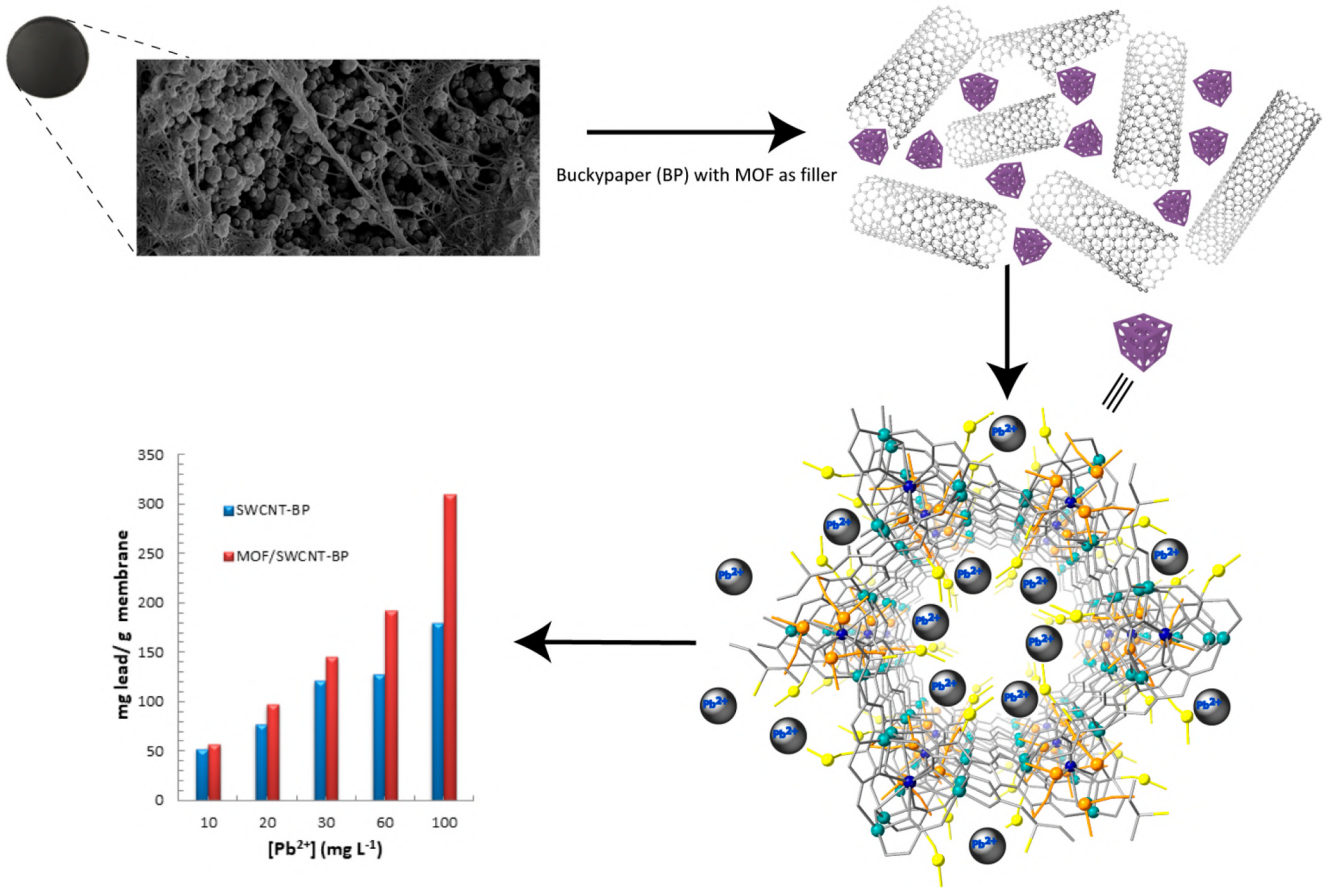

[a]The high chemical affinity of the amino acid residues of methylcysteine and methionine is exploited to recover selectively Pb^{2+} in both low and high ion concentration regimes, even in the presence of interfering ions, with an increase in adsorption capacity up to 42% with respect to neat SWCNT-BP.

and the U.S. Food and Drug Administration (FDA),[11] are 10 μg/L and 5 μg/L (for bottled water), respectively.

A recent tragic example of lead contamination of aquatic environments can be found in Flint (Michigan, United States). The Flint water crisis (2014−2019) was a public health crisis which originated when the Flint River was contaminated with high levels of lead because of excessive pipe corrosion. Pb^{2+} concentration greatly exceeded the established limit and reached very hazardous levels (>5000 μg/L) in several water samples. The highest observed concentration was of 13200 μg/L at the so-called Resident Zero's home.[12] Because this contamination problem would likely have gone undetected indefinitely, without the investigation of Resident Zero, it has renewed the urgency for optimized corrosion controls, as well as for adopting advanced purification systems to prevent similar catastrophic situations in the future, especially in low-incoming countries with old and poorly maintained infrastructures.[13]

Several different techniques have been proposed for Pb(II) removal from aqueous systems, such as chemical precipitation, electrochemical procedures, solvent extraction, ion exchange, flocculation, nanofiltration, and solid-phase adsorption on a wide variety of inorganic and organic materials.[14−16] However, a definitive technique enabling the reduction of Pb^{2+} to safe acceptable limits in contaminated water has not been fully implemented yet.

Metal−organic frameworks (MOFs)[17] are hybrid porous materials that have already shown great efficiency in the removal of both organic[18−21] and inorganic[22−24] contaminants. They combine water stability and highly and well-defined functional[25,26] porous structures with large internal surface areas, which allow for tailorable host−guest interactions and consequently enhanced affinity for target contaminants.[27] In particular, a few water-stable MOFs and MOF-based nanocomposites have been investigated as potential Pb^{2+} adsorbents.[28−40] Some of them show high adsorption capacities[40] and selectivities,[39] even in multicomponent metal ion water systems and/or in the presence of foulants. However, despite these remarkable advances, to the best of our knowledge there is no reported MOF able to clean up contaminated waters within limits accepted for drinking water (10 ppb, 5 ppb for bottled water). Another relevant aspect to be considered is the structuration/process of MOFs powders into more manageable materials.[41] The mass production and large-scale application of MOF adsorbents and nanoadsorbent materials as fine powders are often problematic from a technical point-of-view and very expensive. Also, they present hazard concerns regarding their not-friendly manipulation and likely accidental release into the environment. Thus, the

https://doi.org/10.1021/acsanm.2c00280
ACS Appl. Nano Mater. 2022, 5, 5223−5233

development of structured MOF materials in the form of scalable, and if possible cheap, beads, granules, and membranes is a required step toward real-world applications.[42−44]

Recently, the fabrication of multivariate MOFs[45−49] (MTV-MOFs), possessing different and controlled functional groups within their channels, have emerged as suitable materials aiming at fabricating modular materials containing cooperative functionalities that can act synergistically to capture contaminants of very different natures. As a proof of concept, some of us recently reported outstanding examples of MTV-MOFs[50,51] with environmental application in water remediation. In particular, one of them was reported to simultaneously and efficiently remove both inorganic heavy metals and organic dyes.[51] Although it is quite well-established that the presence of functional groups (amino, thiol, and oxygen-containing groups) decorating MOFs channels is valuable for effective Pb^{2+} removal, much work remains to be done in order to explore, in detail, the interaction mechanisms involved in the capture process. To this end, single-crystal X-ray crystallography (SCXRD) is an extraordinary tool, but it is not frequently used in the elucidation of host−guest interactions for water remediation applications as would be desirable.

Single-walled carbon nanotube buckypapers (SWCNT-BPs) have emerged as very versatile materials in a wide range of applications. For example, they have been revealed as interesting materials for fire protection, heat dispersion systems in microelectronics, TV screens, electromagnetic interferences shielding systems, electrical-conductive tissues, photocatalytic substrates, electrodes for batteries, and supercapacitors.[52] More recently, SWCNT-BPs have been proposed as innovative high-temperature-resistant and lightweight filtration systems.[53,54]

Having in mind the above-mentioned points, and with the aim to make a step forward toward the concrete application of MOF-based technology to water remediation, we have investigated the integration of MTV-MOFs with SWCNT-BPs. In order to do so, we first focused on the development of a novel MTV-MOF, each component of which has been carefully selected on the basis of our knowledge of MTV-MOFs for water remediation. Remarkably, this novel material allowed us to perform an in-depth experimental study through SCXRD of MTV-MOF···Pb^{2+} interactions, which represent the first reported example of such host−guest interaction. Then, we developed an innovative and self-standing membrane, integrating single-walled carbon nanotube buckypaper and prepared multivariate MOF (**MTV-MOF/SWCNT-BP**), as a novel and well-performing material for lead removal from aqueous environments (Scheme 1). We have also compared the lead removal performance of the neat SWCNT-BP with **MTV-MOF/SWCNT-BP**, where we have found for the latter a slight increase in adsorption kinetics and a considerable improvement in terms of both adsorption capacity and selectivity over a wide range of lead concentrations (from 200 to 10000 ppb), even in the presence of background interfering ions. In particular, **MTV-MOF/SWCNT-BP** exhibited an improvement of 42% in adsorption capacity with respect the neat SWCNT-BP and was able to reduce the [Pb^{2+}] from the dangerous 1000 ppb level to acceptable limits for drinking water, below 10 ppb, as the new lead rule from the EPA recently established. These features, together with the nice reusability, good chemical stability, ease of fabrication, and scalability, situate **MTV-MOF/SWCNT-BP** as an appealing technology for large-scale water and wastewater treatment.

RESULTS AND DISCUSSION

Material Preparation and Characterization. We report the preparation of a novel MTV-MOF, obtained from the combination of the metalloligands used in two previously reported MOFs, using oxamidato ligands derived from amino acids,[43,55−63] with formulas $(Me_4N)_2\{Cu_2[(S,S)\text{-methox}](OH)_2\}\cdot 4H_2O$ and $(Me_4N)_2\{Cu_2[(S,S)\text{-Mecysmox}](OH)_2\}\cdot 5H_2O$, where methox and Mecysmox ligands are bis[(S)-methionine]oxalyl diamide and bis[(S)-methylcysteine]oxalyl diamide, respectively. The novel resulting MTV-MOF, prepared by using equimolar amounts of both metalloligands, possess the formula $\{Ca^{II}Cu^{II}_6[(S,S)\text{-methox}]_{1.5}[(S,S)\text{-Mecysmox}]_{1.50}(OH)_2(H_2O)\}\cdot 38H_2O$ (**1**). Single-crystal XRD measurements[64,65] on **1** confirm its isostructurality with a previously reported MTV-MOF, $\{Sr^{II}Cu^{II}_6[(S,S)\text{-methox}]_{1.5}[(S,S)\text{-Mecysmox}]_{1.50}(OH)_2(H_2O)\}\cdot 36H_2O$[50] (crystallographic details are provided in the Supporting Information, Table S1 and Figure S1). The MTV-MOF features hexagonal functional channels decorated with two types of thio-ether groups from the amino acid residues, being either $-CH_2CH_2SCH_3$ or $-CH_2SCH_3$, pointing toward the accessible void spaces, which provides these materials with an excellent task-specific functional environment to sequestrate Pb^{2+} ions into the pores, and they consequently have the potential to enhance the capture properties of the hybrid membrane with respect the neat SWCNT-BP, after the preparation of the hybrid material **MTV-MOF/SWCNT-BP**. Indeed, the high affinity of sulfur toward inorganic pollutants such as Pb^{2+} toxic metal ions is a well-known phenomenon, which makes **1** a promising candidate for the preparation of composite materials—with improved mechanical properties—for metal contaminant removal from water. This approach has been followed before by embedding MOFs in mixed matrix membranes (MMM-MOFs) and evaluating the efficiency for the capture of mercury species.[42] However, the enhanced mechanical properties of **SWCNT-BP** compared to MMMs, provided that the capture properties are maintained, makes this study worthwhile.

The gram-scale preparation of **1** follows a previously reported experimental procedure (see Experimental Section in Supporting Information).[50] The experimental PXRD pattern of **1** is identical to the calculated one (Figure S2), which confirms the homogeneity of the bulk sample and its isostructurality to the single-crystals selected for SCXRD (see below). As a preliminary step to the preparation of **MTV-MOF/SWCNT-BP**, we evaluated the behavior of MTV-MOF **1** in the removal of Pb^{2+} from water (see the Supporting Information for details on preparation of **1**). To this end, 50 mg of a polycrystalline sample of **1** was soaked in an aqueous solution of $Pb(NO_3)_2$ (1 ppm, 10 mL) (see Table S2 and Experimental Section). Overall, **1** was capable of capturing, very efficiently, Pb^{2+} cations from the contaminated solution, as ICP-MS analyses indicate (Table S2). Thus, **1** is capable of reducing [Pb^{2+}] from 1 ppm to less than 5 ppb, sufficiently close to acceptable limits for drinking water. Moreover, PXRD experiments confirm that **1** retains its crystallinity after these capture experiments (Figure S2c), and X-ray photoelectron spectroscopy (XPS) of **1** before and after the capture experiment (Figure S3) indicates that the sulfur oxidation state is not affected by Pb^{2+} loading, as it is observed from the analysis of the S 2p peak. Finally, the N_2 adsorption isotherms at 77 K, for **1**, before and after lead capture are shown in

https://doi.org/10.1021/acsanm.2c00280
ACS Appl. Nano Mater. 2022, 5, 5223−5233

Figure S4. Both isotherms are characteristic of microporous materials, with estimated Brunauer–Emmett–Teller (BET) surface areas of 605 (as synthesized) and 449 $m^2\ g^{-1}$ (after capture experiments). As expected, after the lead capture we observed a reduction of N_2 uptake. Nevertheless, **1** still presents a sizable porosity.

The Pb^{2+} capture was also followed and unambiguously unveiled by single-crystal X-ray diffraction (SCXRD) (see the Supporting Information and Table S1). The crystal structure of **Pb@1**, obtained by soaking crystals of **1** in saturated aqueous solutions of Pb^{2+}, clearly shows Pb^{2+} metal ions residing (with both statistical and large thermal disorder) within the pores of the MTV-MOF, grasped by S···Pb^{2+} linkage [S···Pb^{2+} of 2.7(1) and 2.9(1) Å] (Figures 1, S5, and S6). An auxiliary interaction

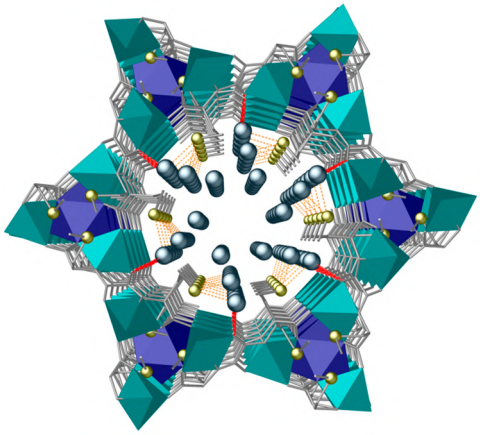

Figure 1. Perspective view down the *c* crystallographic axis of a single channel of **Pb@1** crystal structure determined by SCXRD, showing Pb^{2+} ions captured in pores by sulfur atoms from methionine residues through a supramolecular recognition process. S···Pb^{2+} and O···Pb^{2+} interactions are depicted by orange and red dashed lines, respectively. Color code: copper and calcium atoms from the network are represented by cyan and blue polyhedra, respectively, whereas organic ligands are depicted as gray sticks. Yellow and light blue spheres represent S and Pb atoms, respectively.

of Pb^{2+} with oxygen atoms belonging to oxamidate ligands from the MTV-MOF was also revealed, likely contributing to stabilizing the metal ions in the confined spaces [O···Pb of 2.54(5) Å] (Figure S6b,c). SCXRD data also indicates some clues regarding the Pb^{2+} capture mechanism. It clearly shows that while methionine arms act as scavengers for lead, shorter methylcysteine ones reach their stable conformation upon being confined within the most hindered voids of the crystal structure (Figure S6b). The length of the amino acid residue seems to play a key role in the process of the metal species capture. Hence, the larger length of the ethylmethyl thioether chains decorating the channels imparts more flexibility, allowing a faster approach of the target species.

On the other side, the statistical disorder exhibited by captured Pb^{2+} metal ions can be visualized as a series of snapshots, underpinning the inclusion and somewhat the transport mechanisms behind the capture within nanoconfined spaces. Indeed, the heavy metal ion is detected residing either far or close to the methionine moieties, suggesting a pre- and postrecognition from the amino acid derivative (see Figure S6 and crystallographic details in the Supporting Information). Most likely, the split on two sites with similar occupancy factors is produced by superimposed snapshots of the dynamic process within the porous crystal. It must be clarified that this disorder, as normally occurs for general statistical disorder in a crystal structure, is given by the spatial views averaged in the crystal through only one unit cell.

A polycrystalline sample of **1**, with average particle dimensions of 0.1 μm, was immobilized within the porous network of entangled SWCNT-BP, thus obtaining a stable self-standing adsorbing membrane filter (Figure 2). A powder of **1**

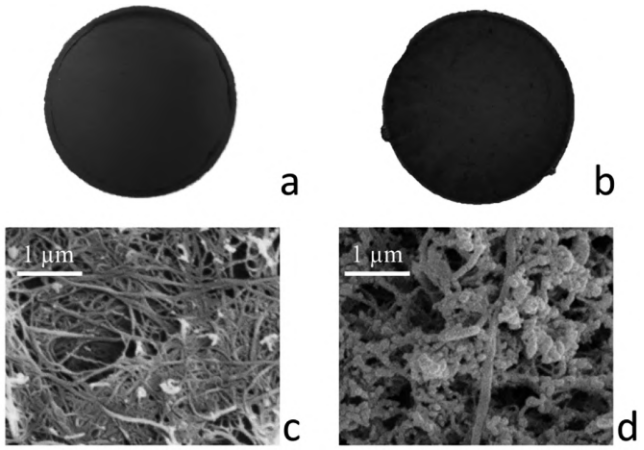

Figure 2. Final appearance of (a) neat SWCNT-BP and (b) **MTV-MOF/SWCNT-BP**. The average diameter of membranes was 38 ± 1 mm. SEM images of (c) SWCNT-BP and (d) **MTV-MOF/SWCNT-BP** unveiling MTV-MOF micrometer particles as aggregates of smaller nanosized primary particles.

was dispersed in an optimized SWCNT-BP water solution using an ultrasonic bath. The as-made solution was filtered through the PTFE disks with a vacuum pump and then washed with ethanol. The novel membrane **MTV-MOF/SWCNT-BP** has been produced by drying the washed composite at room temperature. The detailed procedure for the composite preparation is given in the Supporting Information. Compared to the conventional method for preparing MMM-MOFs, a low cost and simple technique was employed for preparing these **MTV-MOF/SWCNT-BP** membranes, which exhibit relatively high fluxes, porosity, hydro-stability, and mechanical strength. This preparative procedure requires low amounts of eco-friendly solvents (water and ethanol) and no postsynthetic treatment, thus resulting in a more environmentally friendly process.

The SWCNT-BP selected as porous support for MTV-MOF immobilization was not an simply a bystander; it is partially functionalized with carboxylate groups (~3,5%), which can actively and synergically cooperate in the heavy metal sequestration. Nevertheless, the mechanisms underpinning metal ion sorption within carbon nanotubes (CNTs) are very intricate, and they can be explained by the combination of several factors, such as electrostatic attraction, sorption–precipitation, and chemical interaction between the metal ions and the functional groups eventually present on the CNT surface.[66]

The optimum MOF content of 25 wt % in the SWCNT-BP was established by considering both factors: maximum lead uptake/efficiency and mechanical stability of the final membrane. Thermogravimetric analysis (TGA) evaluated the thermal stability of **MTV-MOF/SWCNT-BP**. TGA shows that the presence of MTV-MOF **1** in the hybrid membrane does

https://doi.org/10.1021/acsanm.2c00280
ACS Appl. Nano Mater. 2022, 5, 5223–5233

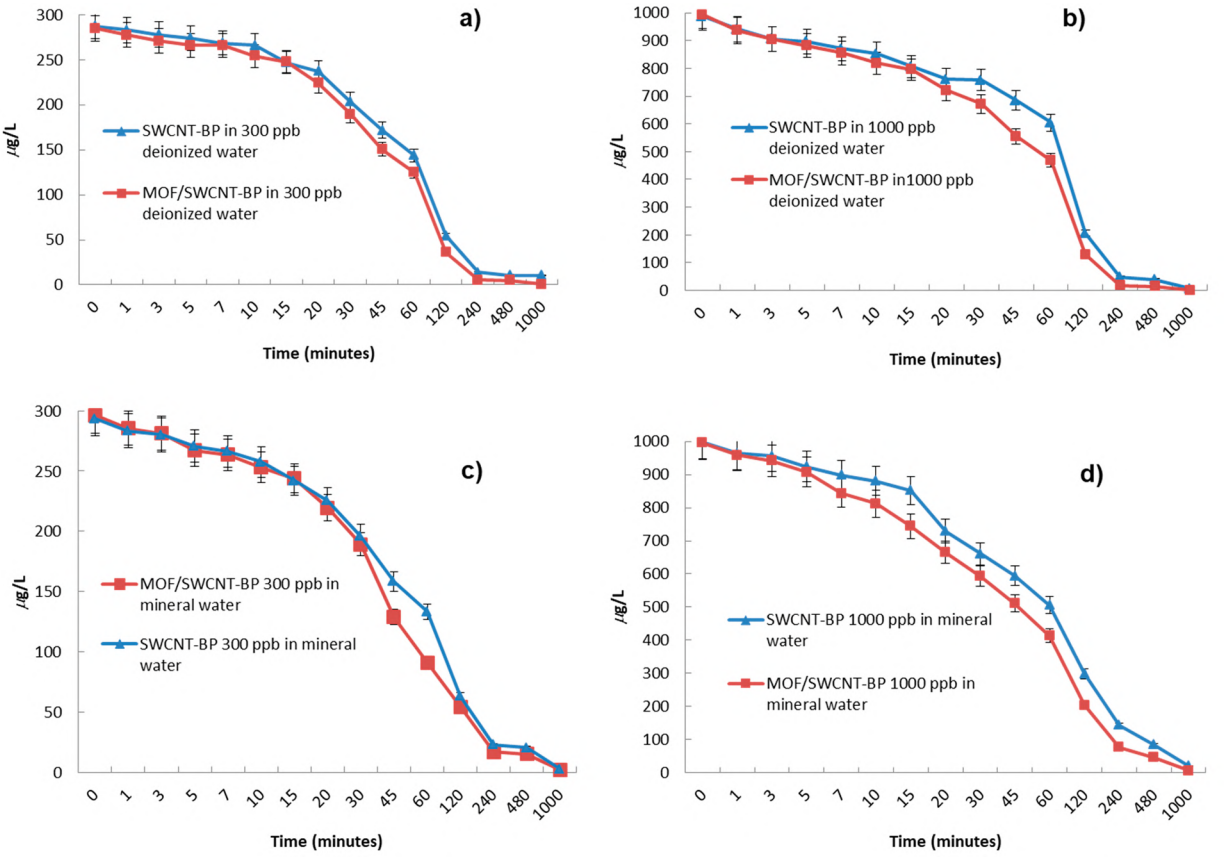

Figure 3. Pb^{2+} capture by neat SWCNT-BP and **MTV-MOF/SWCNT-BP** disks (diameter 38 ± 1 mm) after soaking in 200 mL of aqueous solution with $[Pb^{2+}]$ of 300 and 1000 ppb of deionized (a and b) or mineral water (c and d) in the 0−16 h interval (data from Tables S3−S8). The Pb^{2+} adsorption performance was tested on $Pb(NO_3)_2$ water solutions at room temperature under static conditions. The solid lines in the plots are a guide for the eye.

not significantly influence the shape of the neat buckypaper decomposition (Figure S7). The slight changes observed are likely related to the porosity of the MOF and its water content and were observed in the temperature range of 50−250 °C for the composite membrane of **MTV-MOF/SWCNT-BP**. A mass loss of ∼47% is observed above 450 °C for both **MTV-MOF/SWCNT-BP** and neat SWCNT-BP membrane, accounting for the partial decomposition of BP.

Panels a and b of Figure 2 show neat SWCNT-BP and **MTV-MOF/SWCNT-BP** membranes, respectively, prepared under the above-mentioned optimized conditions. These membranes arranged in a circular pattern exhibit an average thickness of 60 ± 1 μm plus an average diameter of 38 ± 1 mm with a resulting average mass of the disks of 40 ± 2 mg. Density and porosity values for membranes are similar, as expected (0.60 ± 0.03 g cm^{-3} and 70 ± 5%, respectively). The pore distribution (%) for SWCNT-BP and **MTV-MOF/SWCNT-BP** membranes has been evaluated. Figure S8 shows a similar pore distribution for SWCNT-BP and **MTV-MOF/SWCNT-BP** membranes, typical of microporous materials; the estimated Brunauer−Emmett−Teller (BET) surface area for the used SWCNTs is 520 m^2 g^{-1} (from Sigma-Aldrich). Thus, both membranes are potentially good absorbers, with pore diameters, as expected, only slightly reduced after MTV-MOF immobilization in SWCNT-BP.

The morphology of SWCNT-BP and **MTV-MOF/SWCNT-BP** membranes was evaluated through scanning electron microscopy. A typical microscopic texture of a SWCNT-BP is shown in Figure 2c, where bundles and clusters of SWCNTs are evident and likely induced by $\pi-\pi$ and van der Waals interactions. Small spherical aggregates appear after the addition of the MTV-MOF in SWCNT-BP (Figure 2d) featuring an average diameter of roughly 0.1 μm. The stable and porous structure of SWCNT-BPs supports and stabilizes the nanosized MOF particles. Indeed, after capture experiment, no leakage was observed. Thus, the final composite guarantees good permeability together with large active surface area for the adsorption of lead from water solution.

In order to characterize the hydrophilic/hydrophobic surface properties of SWCNT-BP and **MTV-MOF/SWCNT-BP** membranes, the static contact angle has been measured for both materials. The top surfaces of both membranes feature a hydrophilic character. However, it is decreased by the presence of the MTV-MOF, with average contact-angle values of 47.5° ± 0.5° and 78.5° ± 0.5° for SWCNT-BP and **MTV-MOF/SWCNT-BP**, respectively (Figure S9a,b), which is required for water treatment membranes.[67] These results suggest a lower hydrophilic nature for the **MTV-MOF/SWCNT-BP** compared to the neat SWCNTs. In terms of transport mechanisms, it can be seen as an added value of the chosen hybrid support.

PXRD experiments of SWCNT-BP and **MTV-MOF/SWCNT-BP** before and after capture and regeneration process have been also performed (Figure S10). They confirm the integrity of the membranes, showing the common peaks typical of SWCNTs and that the open-framework structure of the filter remains unchanged after the capture of the Pb^{2+} ion and

https://doi.org/10.1021/acsanm.2c00280
ACS Appl. Nano Mater. 2022, 5, 5223−5233

regeneration process (*vide infra*) of **MTV-MOF/SWCNT-BP** (Figure S10).

Capture Properties and Pb^{II} Adsorption Performance. The capture properties of **MTV-MOF/SWCNT-BP** were then evaluated through adsorption experiments and compared with those of the neat SWCNT-BP membrane. Both membrane disks were activated first by immersion in ethanol followed by heating at 80 °C under reduced pressure for 24 h prior to the sorption measurements.

The initial screening was performed in batch, using distilled water and $Pb(NO_3)_2$ at different concentrations (300 and 1000 ppb). The native pH value of the solution was 6.5. At this pH, the carboxylic acid groups of SWCNT are deprotonated, but it is not supposed to affect in a remarkable way the binding performance of the MTV-MOF. The kinetic profiles and adsorption% of lead capture by SWCNT-BP or **MTV-MOF/SWCNT-BP** disk (diameter 38 ± 1 mm), after soaking them at different lead concentrations in the 0−16 h interval, are shown in Figures 3 and 4, respectively (results from the whole time range of 0−72 h are reported in Tables S3−S8).

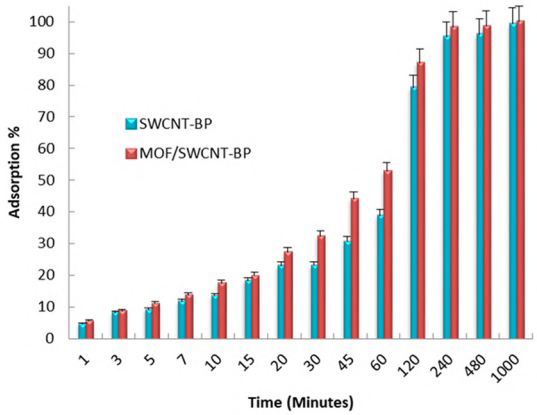

Figure 4. Pb^{2+} capture% by neat SWCNT-BP and **MTV-MOF/SWCNT-BP** disks (diameter 38 ± 1 mm) during soaking in aqueous solutions of 1000 ppb [Pb^{2+}] [volume 200 mL of $Pb(NO_3)_2$ aqueous solution, at room temperature] in the 0−16 h interval (data from Table S4).

Observing the kinetic profiles, some significant differences can be spotted regarding the capture performanc of the two membranes. The SWCNT-BP was able to reduce the lead concentration from the initial value of 300 ppb to values slightly lower than the 15 ppb action level limit in 4 h (13.7 ± 0.2 ppb), while a noteworthy improved removal capacity is observed for the **MTV-MOF/SWCNT-BP** over the same time period, with lead concentration being reduced to 5.5 ± 0.1 ppb; this is much lower than the 10 ppb trigger level and thus within acceptable limits for drinking water (Table S3). A slight increase of adsorption performance of the **MTV-MOF/SWCNT-BP** can be noticed even when the more concentrated solution was used, in line with an increase in maximum adsorption capacity at high concentrations (graphic in Scheme 1) (*vide infra*). The lead concentration was reduced from 1000 to 39.40 ± 0.4 and 14.1 ± 0.1 ppb in 8 h when the neat SWCNT-BP and **MTV-MOF/SWCNT-BP** were used, respectively (Table S3).

A doubled treatment time (16 h) is required to reduce the lead concentration under the imposed trigger level limit with the SWCNT-BP (6.65 ± 0.1 ppb) (Table S4). The obtained results clearly indicate that the presence of the MTV-MOF within the SWCNT-BP membrane improves, significantly, the removal efficiency of the neat SWCNT-BP membrane. Indeed, a considerable reduction of the lead concentration to 0.73 ± 0.02 ppb, which is under the limits required for bottled and drinking water, was observed for the same time (Table S4).

Aiming at evaluating the potential real application of these membranes, additional experiments were performed, in batch, using lead solution at different concentrations (300 and 1000 ppb) prepared with a commercial mineral water containing common and unavoidable background ions (Figure 3c,d and Tables S5−S8) at pH 6.6. The trend in capture performance is preserved, and it is evident that none of the cations present in solution−such as Na^+, K^+, Mg^{2+}, Ca^{2+}−at high concentration noticeably interfere with the adsorption of lead ions (Figures S11 and S12), even when a lower Pb^{2+} concentration of 200 ppb was used (Figure S13 and Tables S9 and S10). These results, confirming the selectivity of this material, are in line with that observed for other MOFs of the same family.[42,43,51] Again, an improved adsorption was observed for the **MTV-MOF/SWCNT-BP** membrane at higher lead concentration. Indeed, while the adsorption ability of the SWCNT-BP and **MTV-MOF/SWCNT-BP** was comparable at 200 and 300 ppb, with lead being reduced below the established limits after 4 and 16 h, respectively, lead concentration falls from 1000 ppb to 13.9 ± 0.1 ppb in 24 h with SWCNT-BP and reached a halved value (6.9 ± 0.1 ppb) in a shorter time (16 h) when the **MTV-MOF/SWCNT-BP** was used, thus further confirming the positive effects of the MTV-MOF on the hybrid membrane performance (Tables S7 and S8).

In addition, the positive effects of the presence of MTV-MOF within SWCNT-BP are evident on the adsorption capacity and selectivity (see below) at high Pb^{2+} concentration.

Kinetic experiments evidence that the rate equation for Pb^{2+} capture in solutions follows the Lagergren first-order equation (capture experiments section, Supporting Information)

$$\frac{dq_t}{dt} = k_1(q_e - q_t) \quad (1)$$

where q_e and k_1 are the lead adsorption capacity per unit of adsorbent mass (mg g^{-1}) at equilibrium and the Lagergren adsorption rate constant (min^{-1}), respectively (Table S11). The capture performance of **SWCNT-BPs** was improved by the incorporation of **MTV-MOF** in **SWCNT-BPs**, increasing the constant rate values for the concentrations of 300 and 1000 ppb from 0.0120 ± 0.0005 and 0.0126 ± 0.0008 min^{-1} to 0.0138 ± 0.0006 and 0.0143 ± 0.0008 min^{-1}, respectively.

In terms of capacity, **MTV-MOF/SWCNT-BP** reaches a value up to 310 mg g^{-1} when soaked in an aqueous solution with [Pb^{2+}] of 100 mg L^{-1}. This quantity, although it could be considered modest if compared to that shown by other bulk MOFs,[32,33,39] is quite remarkable considering that we are dealing with a membrane containing 25% of the MOF. Moreover, it results in a 42% improvement with respect to the neat SWCNT-BP, for which, in the same conditions, a maximum adsorption of 180 mg g^{-1} was observed (bar chart in Scheme 1 and Tables S12−S17). All these results undoubtedly validate that CNTs are good supports to immobilize and prevent leaching of MOFs in target solutions, a drawback often present in MOF-based mixed polymeric membranes.

Finally, in order to ensure the applicability of **MTV-MOF/SWCNT-BP** against any accidental spills, similar to what occurred in Flint, we performed further adsorbing tests by

https://doi.org/10.1021/acsanm.2c00280
ACS Appl. Nano Mater. 2022, 5, 5223−5233

using Pb^{2+} solutions at higher initial concentrations (10000, 20000, 30000, 60000, and 100000 ppb) (Figure 5 and Tables S13–S17). After 72 h of treatment, a removal efficiency up to 90% was observed for the SWCNT-BP membrane at 10000 ppb, with final Pb^{2+} concentration in water of ca. 1200 ppb. With respect to this value, a further reduction of the final concentration of 82% was obtained with the **MTV-MOF/SWCNT-BP** membrane in the same conditions, with the final lead concentration being slightly higher than 200 ppb, corresponding to a removal efficiency of 98% (Table S12). When the initial lead concentration rises further, the removal efficiency of both membranes decreases, with **MTV-MOF/SWCNT-BP** still assuring the better performance: after 72 h of treatment the removal efficiency values were 79 and 94% for initial lead concentration of 30000 ppb (Table S15) and 42 and 66% for initial lead concentration of 60000 ppb (Table S16) for SWCNT-BP and **MTV-MOF/SWCNT-BP**, respectively.

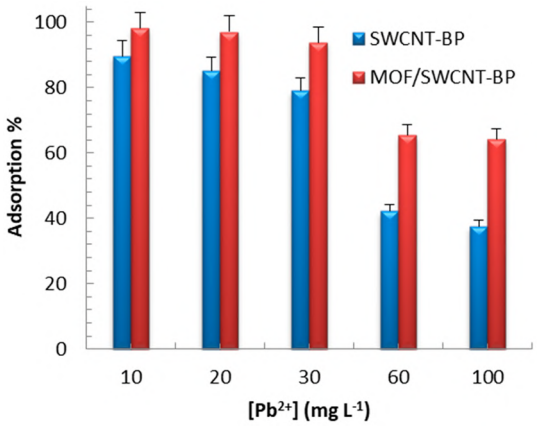

Figure 5. Dependence of Pb^{2+} capture% as a function of concentration by neat SWCNT-BP and **MTV-MOF/SWCNT-BP** disks in 10–100 ppm range of $[Pb^{2+}]$ [volume of 200 mL of $Pb(NO_3)_2$ aqueous solution, at room temperature for 72 h] (data from Table S12).

Selectivity toward Common Interfering Metal Ions Al^{3+} and Fe^{3+}. The already described improved lead uptake efficiency of **MTV-MOF/SWCNT-BP** compared to neat SWCNT-BP is also accompanied by a remarkable increase in selectivity. In particular, we evaluated the lead capture performance of both **MTV-MOF/SWCNT-BP** and SWCNT-BP membranes toward Pb^{2+} in the presence of other interfering metal cations, usually found in drinking water, such as Al^{3+} and Fe^{3+} cations. In order to do so, both **MTV-MOF/SWCNT-BP** and SWCNT-BP were soaked in aqueous solutions containing an initial concentration of 1000 ppb of each metal, where we observed **MTV-MOF/SWCNT-BP** showed higher selectivity toward Pb^{2+} cations (Tables S18 and S19).

Thus, for **MTV-MOF/SWCNT-BP** a removal efficiency of 97.8% for lead can be observed, which corresponds to a final lead concentration of 22 ± 1 ppb, whereas the corresponding removal efficiency for the SWCNT-BP was only 90% for Pb(II) (99 ppb of lead remaining in solution after treatment) (Tables S18 and S19).

The calculation of lead distribution coefficients, K_D, between membranes and solutions both in neat and multicomponent (Pb, Fe, and Al) solutions (see Table S20) confirmed the strong affinity between Pb^{2+} ions and membranes. Even if a decrease in K_D values was observed for increasing lead concentrations and in the presence of competitive ions, it is worth noting that the incorporation of **MTV-MOFs** in **SWCNTs** increased the ion affinity in all cases reported in Table S20.

Overall, all these capture results indicate that **MTV-MOF/SWCNT-BP** is capable of reducing $[Pb^{2+}]$ in contaminated solutions to acceptable limits for drinking water. These results situate **MTV-MOF/SWCNT-BP** among the most efficient materials for lead decontamination and as the most efficient MOF-based material for this purpose.[28−40]

As stated above, a greatly increased absorption ability for Al(III) and Fe(III) was observed only for the SWCNT-BP membrane (removal efficiency of 87 and 57% for Al(III) and Fe(III), respectively), when compared to **MTV-MOF/SWCNT-BP** (removal efficiency of 41 and 30% for Al(III)

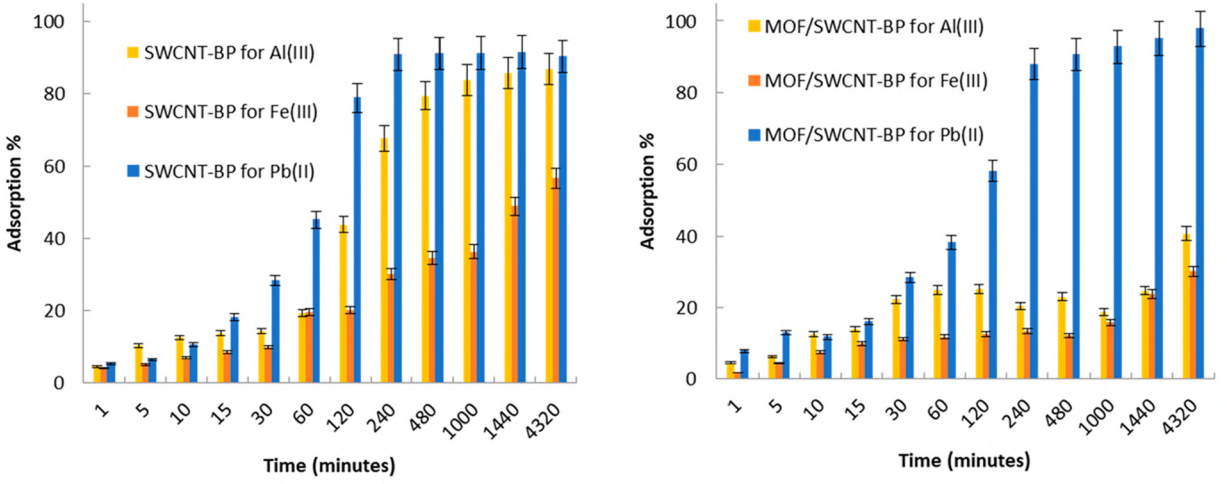

Figure 6. Selectivity for cation adsorption in 1000 ppb $[Pb^{2+}]$, $[Fe^{3+}]$, and $[Al^{3+}]$ solutions by **MTV-MOF/SWCNT-BP** and SWCNT-BP membranes soaked in a volume of 200 mL, in the 0–72 h interval (data from Tables S18 and S19). Membrane disks were placed in 1 ppm $Pb(NO_3)_2$, $FeCl_3$ and $AlCl_3$ aqueous solution at room temperature (25 °C). To avoid precipitation of Fe^{3+} and Al^{3+} as metal hydroxides from the aqueous solution during selectivity experiment, the addition of nitric acid for the stabilization has been performed until pH 2.

https://doi.org/10.1021/acsanm.2c00280
ACS Appl. Nano Mater. 2022, 5, 5223−5233

and Fe(III), respectively). These results are shown in Figure 6 and clearly demonstrate an outstanding selectivity of **MTV-MOF/SWCNT-BP** toward Pb^{2+} (Figure 6b), which decreases, significantly, in neat SWCNT-BP (Figure 6a). Overall, these results further confirm that the introduction of the MTV-MOF brings added value to SWCNT-BP, thus facilitating its real implementation.

These trends are maintained at higher concentrations. When using solutions with an initial concentration of 10000 ppb for each metal (Figure S14 and Tables S21 and S22), **MTV-MOF/SWCNT-BP** still displays higher selectivity and removal efficiency for Pb(II) ions when compared with SWCNT-BP, being as high as 97% for lead for the composite membrane and 64% for the buckypaper. This behavior should be attributed to the high chemical affinity of thioether functions for Pb^{2+} soft metal ions. Methionine residues, pointing within pores of the MTV-MOF, capture Pb^{2+} ions as unveiled by the SCXRD study (Figure 1). These thioether-functionalities, and consequently holding mechanisms, are not present in carbon nanotubes. In neat SWCNT-BP, there exists an oxygen-rich environment related, as above-mentioned, to partial functionalization with carboxylate groups (~3.5%); this and physisorption mechanisms are likely the main actors in the capture processes. These nonspecific interactions are most likely at the origin of the greater affinity unveiled for Al^{3+} and Fe^{3+} in SWCNT-BP (Figure 6). Further evidence of the synergistic effect of MTV-MOF and SWCNT-BP in the hybrid membrane is supported by SEM-EDX analysis on both membranes after Pb^{2+} capture (Figure S15). Images confirm a still homogeneous distribution of MTV-MOF in SWCNT-BP and a homogeneous adsorption in both membranes of Pb(II).

Perspective on Industrial Feasibility and Scale Up: Mechanical Analysis and Regeneration Process. In order to ensure that the excellent mechanical properties of BP are maintained when preparing composites, the mechanical properties of **MTV-MOF/SWCNT-BP** were evaluated and compared to those shown by pure SWCNT-BP. The presence of MTV-MOF in SWCNT-BP causes a slight decrease in the Young's modulus from 1.65 ± 0.03 GPa (neat SWCNT-BP) to 1.54 ± 0.02 GPa (**MTV-MOF/SWCNT-BP**). Nevertheless, these measurements confirm the high mechanical stability of both membranes (see Figure S16).[68]

From the perspective of potential industrial applications, and being aware of the known stability for either SWCNT-BP[68] or MTV-MOF[49] after regeneration processes, the stability of the **MTV-MOF/SWCNT-BP** membrane after a regeneration process was also evaluated. In this regard, recovered Pb^{2+} was extracted after suspension of the membrane in a 10% (v/v %) aqueous solution of 2-mercaptoethanol for 24 h. The reusability of **MTV-MOF/SWCNT-BP** after the extraction process was studied over five subsequent cycles of adsorption and regeneration. The results demonstrate the stability, confirmed by PXRD measurements (Figure S10), and still good efficiency of the hybrid membrane (Table S23), which recovers up to 85.1% of the original adsorption capacity, thus confirming the suitability of **MTV-MOF/SWCNT-BP** for industrial applications.

According to our protocol, we asked a company (potentially involved in the industrial feasibility and scale up) to make a first estimation of the price of the MTV-MOF at a 5−15 kg scale. At 5 kg scale using our procedure they estimate a production cost of 8000 €/kg (including tool depreciation, labor cost, raw materials, and energy) that could be reduced to <4000 €/kg for 15 kg scale by having a more industrial sourcing of methionine and methylcysteine amino acids. As far as BP is concerned, we have an estimation of 1000 €/kg. Of course, the main fraction of the cost comes from the MOF and reactants, but considering that membranes are prepared with a MOF content of 25 wt % in the SWCN-BP, it could be considered cheaper with respect to pure powder of MOF-based technologies.

It is more difficult at this stage to estimate the operating cost of the Pb^{2+} removal (in €/g of Pb^{2+}) and to compare this cost with the expectation of the market or other existing technologies. However, we think that the balance between the membrane production, cost of the regeneration/recovery steps, and their low environmental impact is the key point.

CONCLUSIONS

In summary, we have reported the synthesis, characterization, and lead removal efficiency of a novel material made up of a single-walled carbon nanotube buckypaper incorporating a novel multivariate MOF (**MTV-MOF/SWCNT-BP**). The combination of SWCNT-BP and MTV-MOF, materials that exhibit great capture properties individually, originates a biocompatible, highly stable adsorbent membrane—**MTV-MOF/SWCNT-BP**—with high performance for Pb(II) removal from aqueous solution. It represents a step forward with respect to the previous composite we reported so far,[68] where the MOF embedded inside the CNTs was completely different. In that case, it was prepared with a different amino acid derivative, threonine, owning an alcoholic chemical functionality of the type $-CH(CH_3)OH$ confined within the pores of the MOF and exhibiting a consequent chemical affinity for rare earth elements (REEs) as target metal ions. In the present work we immobilized a multivariate-MOF, which is a new subclass of MOF, exhibiting multiple chemical functionalities. Here, we have used two chemical amino acid derivatives from methionine and methylcysteine, giving a final MTV-MOF with both $-CH_2SCH_3$ and $-CH_2CH_2SCH_3$ functionalities confined within the pores of the MOF and exhibiting a totally different binding affinity when compared with the threonine one. Furthermore, the characterizations of as-prepared composite membranes indicated that the MTV-MOF particles are stably enmeshed into the BP skeleton.

Both the SWCNT-BP and the **MTV-MOF/SWCNT-BP** featured appreciable values of maximum adsorption capacities. However, **MTV-MOF/SWCNT-BP** displayed a remarkable increase of up to 42%, which is the only one exhibiting a remarkable selectivity for Pb(II) ions, even in highly concentrated multicomponent solutions, over a wide range of lead concentrations. These outstanding properties are likely related to MTV-MOF host−guest interactions, unequivocally unveiled by SCXRD measurements. For Pb(II) solution concentration in the range of 200−1000 ppb, the lead content was reduced well below the current established EPA and WHO trigger level and within the drinkable regime (<10 ppb), with the **MTV-MOF/SWCNT-BP** membrane assuring a faster and more efficacious decrease of the lead level in water. When the solution concentration was further increased (10000−50000 ppb), the **MTV-MOF/SWCNT-BP** membrane demonstrated superior removal efficiency with respect to the pristine SWCNT-BP, guaranteeing lead removal higher than 90% for initial lead concentration up to 30000 ppb. To further increase the removal efficiency and reduce the time of treatment, multiple filtration units could be readily connected in series to

https://doi.org/10.1021/acsanm.2c00280
ACS Appl. Nano Mater. 2022, 5, 5223−5233

achieve higher performance and consequently reduce the water concentration under the required limit. The outstanding performance of the composite membrane is retained even in the presence of competitive ions, such as iron(III) and aluminum(III), with removal efficiency up to 97% for lead when solutions containing 10000 ppb of each metal ions were treated, in contrast to what is observed for the neat membrane. Furthermore, the structural stability of the **MTV-MOF/SWCNT-BP** was maintained upon lead adsorption/desorption cycles, and complete regeneration was achieved for up to five cycles. **MTV-MOF/SWCNT-BP** has great potential in the field of water treatment and can be effectively used as a reliable adsorbent for Pb(II) removal for household drinking water, as well as in industrial treatment plants for water and wastewater decontamination.

■ ASSOCIATED CONTENT

Supporting Information

The Supporting Information is available free of charge at https://pubs.acs.org/doi/10.1021/acsanm.2c00280.

Experimental preparation, physical and analytical characterization, and crystallographic refinement details (Tables S1−S20 and Figures S1−S11) (PDF)

CCDC 2128259 (CIF)

CCDC 2128260 (CIF)

■ AUTHOR INFORMATION

Corresponding Authors

Jesús Ferrando-Soria − *Instituto de Ciencia Molecular (ICMol), Universidad de Valencia, 46980 Paterna, Valencia, Spain*; Email: jesus.ferrando@uv.es

Fiore P. Nicoletta − *Dipartimento di Farmacia e Scienze della Salute e della Nutrizione, Università della Calabria, 87036 Rende, Italy*; Email: f.nicoletta@unical.it

Giovanni De Filpo − *Dipartimento di Chimica e Tecnologie Chimiche (CTC), Università della Calabria, Rende 87036 Cosenza, Italy*; Email: giovanni.defilpo@unical.it

Emilio Pardo − *Instituto de Ciencia Molecular (ICMol), Universidad de Valencia, 46980 Paterna, Valencia, Spain*; orcid.org/0000-0002-1394-2553; Email: emilio.pardo@uv.es

Donatella Armentano − *Dipartimento di Chimica e Tecnologie Chimiche (CTC), Università della Calabria, Rende 87036 Cosenza, Italy*; orcid.org/0000-0002-8502-8074; Email: donatella.armentano@unical.it

Authors

Mariafrancesca Baratta − *Dipartimento di Chimica e Tecnologie Chimiche (CTC), Università della Calabria, Rende 87036 Cosenza, Italy*; orcid.org/0000-0002-9966-8312

Teresa Fina Mastropietro − *Dipartimento di Chimica e Tecnologie Chimiche (CTC), Università della Calabria, Rende 87036 Cosenza, Italy*

Rosaria Bruno − *Dipartimento di Chimica e Tecnologie Chimiche (CTC), Università della Calabria, Rende 87036 Cosenza, Italy*

Antonio Tursi − *Dipartimento di Chimica e Tecnologie Chimiche (CTC), Università della Calabria, Rende 87036 Cosenza, Italy*

Cristina Negro − *Instituto de Ciencia Molecular (ICMol), Universidad de Valencia, 46980 Paterna, Valencia, Spain*

Alexander I. Mashin − *Applied Physics & Microelectronics, Lobachevsky State University of Nizhni Novgorod, 603022 Nizhni Novgorod, Russian Federation*

Aleksey Nezhdanov − *Applied Physics & Microelectronics, Lobachevsky State University of Nizhni Novgorod, 603022 Nizhni Novgorod, Russian Federation*

Complete contact information is available at: https://pubs.acs.org/10.1021/acsanm.2c00280

Author Contributions

[§]M.B., T.F.M., R.B., and A.T. contributed equally to this work. Author contributions are as follows: J.F.-S., G.D.F., E.P., and D.A. designed the research; E.P., G.D.F., and D.A. coordinated the whole work; A.T., C.N., T.F.M., and M.B. performed synthetic work; R.B. and D.A. performed single-crystal XRD characterization and analyzed data; A.T. and T.F.M. carried out the capture experiments; A.M., G.D.F., M.B., and A.N. performed physical and mechanical characterization and analyzed data; A.T. performed microscopy measurements; F.N., J.F.-S., G.D.F., E.P., and D.A. wrote and revised the paper.

Notes

The authors declare no competing financial interest.

■ ACKNOWLEDGMENTS

This work was supported by the Ministero dell'Università e della Ricerca (Italy), the MINECO (Spain) (Projects PID2019-104778GB-I00 and Excellence Unit "Maria de Maeztu" CEX2019-000919-M), and the Generalitat Valenciana (Project PROMETEO/2021/054). A.T. acknowledges the project FOREST-COMP − CUP H56C18000080005 − PON "Ricerca e Innovazione 2014−2020" for a postdoctoral grant. The Ph.D. of M.B. is funded by a scholarship from Regione Calabria (grant POR Calabria 2014-2020 - Azioni 10.5.6 e 10.5.12). D.A. acknowledges the financial support of the Fondazione CARIPLO/"Economia Circolare: ricerca per un futuro sostenibile" 2019, Project code: 2019-2090, MOCA; R.B. thanks Fondazione CARIPLO for the concession of a postdoctoral grant. Thanks are also extended to the "2019 Post-doctoral Junior Leader-Retaining Fellowship, la Caixa Foundation (ID100010434 and fellowship code LCF/BQ/PR19/11700011", "Subvenciones concedidas a la excelencia científica de juniors investigadores, SEJI/2020/034", and "Ramon y Cajal Programme (RYC2019-027940-I)" (J. F.-S.). E.P. acknowledges the financial support of the European Research Council under the European Union's Horizon 2020 research and innovation programme/ERC Grant Agreement No. 814804, MOF-reactors.

■ REFERENCES

(1) https://www.who.int/news-room/fact-sheets/detail/drinking-water.

(2) US EPA. *Drinking Water Requirements for States and Public Water Systems 2018 Edition of the Drinking Water Standards and Health Advisories Tables* (EPA 822-F-18-001); 2018.

(3) United Nations. Transforming our world: the 2030 Agenda for Sustainable Development; https://sustainabledevelopment.un.org/post2015/transformingourworld.

(4) U.S. Environmental Protection Agency. *2012 Edition of the Drinking Water Standards and Health Advisories*; https://rais.ornl.gov/documents/2012_drinking_water.pdf.

(5) Kordas, K.; Ravenscroft, J.; Cao, Y.; McLean, E. V. Lead Exposure in Low and Middle-Income Countries: Perspectives and

Lessons on Patterns, Injustices, Economics, and Politics. *Int. J. Environ. Res. Public Health* **2018**, *15*, 2351.
(6) Wani, A. L.; Ara, A.; Usmani, J. A. Lead toxicity: a review. *Interdiscip. Toxicol.* **2015**, *8*, 55−64.
(7) Rai, P. K.; Lee, S. S.; Zhang, M.; Tsang, Y. F.; Kim, K.-H. Heavy metals in food crops: Health risks, fate, mechanisms, and management. *Environ. Int.* **2019**, *125*, 365−385.
(8) Hayes, C. R.; Skubala, N. D. Is there still a problem with lead in drinking water in the European Union? *J. Water Health* **2009**, *7*, 569−580.
(9) https://www.epa.gov/ground-water-and-drinking-water/basic-information-about-your-drinking-water.
(10) https://www.epa.gov/ground-water-and-drinking-water.
(11) https://www.accessdata.fda.gov/scripts/cdrh/cfdocs/cfcfr/CFRSearch.cfm?fr=165.110.
(12) Pieper, K. J.; Tang, M.; Edwards, M. A. Flint Water Crisis Caused By Interrupted Corrosion Control: Investigating "Ground Zero" Home. *Environ. Sci. Technol.* **2017**, *51*, 2007−2014.
(13) Santucci, R. J.; Scully, J. R. The pervasive threat of lead (Pb) in drinking water: Unmasking and pursuing scientific factors that govern lead release. *Proc. Natl. Acad. Sci. U. S. A.* **2020**, *117*, 23211−23218.
(14) Fu, F.; Wang, Q. Removal of heavy metal ions from wastewaters: a review. *J. Environ. Manage.* **2011**, *92*, 407−418.
(15) Carolin, C. F.; Kumar, P. S.; Saravanan, G.; Joshiba, J.; Naushad, M. Efficient techniques for the removal of toxic heavy metals from aquatic environment: A review. *J. Environ. Chem. Eng.* **2017**, *5*, 2782−2799.
(16) Bhattacharya, S.; Gupta, A. B.; Gupta, A.; Pandey, A. *Water Remediation*; Bhattacharya, S., Gupta, A. B., Gupta, A., Pandey, A., Eds.; Energy, Environment, and Sustainability; Springer: Singapore, 2018.
(17) Furukawa, H.; Cordova, K. E.; O'Keeffe, M.; Yaghi, O. M. The chemistry and applications of metal-organic frameworks. *Science* **2013**, *341*, 974.
(18) Dias, E. M.; Petit, C. Towards the use of metal-organic frameworks for water reuse: a review of the recent advances in the field of organic pollutants removal and degradation and the next steps in the field. *J. Mater. Chem. A* **2015**, *3*, 22484−22506.
(19) Ahmed, I.; Panja, T.; Khan, N. A.; Sarker, M.; Yu, J.-S.; Jhung, S. H. Nitrogen-Doped Porous Carbons from Ionic Liquids@MOF: Remarkable Adsorbents for Both Aqueous and Nonaqueous Media. *ACS Appl. Mater. Interfaces* **2017**, *9*, 10276−10285.
(20) Jiang, D.; Chen, M.; Wang, H.; Zeng, G.; Huang, D.; Cheng, M.; Liu, Y.; Xue, W.; Wang, Z. The application of different typological and structural MOFs-based materials for the dyes adsorption. *Coord. Chem. Rev.* **2019**, *380*, 471−483.
(21) Rojas, S.; Horcajada, P. Metal-Organic Frameworks for the Removal of Emerging Organic Contaminants in Water. *Chem. Rev.* **2020**, *120*, 8378−8415.
(22) Kobielska, P. A.; Howarth, A. J.; Farha, O. K.; Nayak, S. Metal-organic frameworks for heavy metal removal from water. *Coord. Chem. Rev.* **2018**, *358*, 92−107.
(23) Li, J.; Wang, X.; Zhao, G.; Chen, C.; Chai, Z.; Alsaedi, A.; Hayat, T.; Wang, X. Metal-organic framework-based materials: superior adsorbents for the capture of toxic and radioactive metal ions. *Chem. Soc. Rev.* **2018**, *47*, 2322−2356.
(24) Bolisetty, S.; Peydayesh, M.; Mezzenga, R. Sustainable technologies for water purification from heavy metals: review and analysis. *Chem. Soc. Rev.* **2019**, *48*, 463−487.
(25) Kalaj, M.; Cohen, S. M. Postsynthetic Modification: An Enabling Technology for the Advancement of Metal-Organic Frameworks. *ACS Cent. Sci.* **2020**, *6*, 1046−1057.
(26) Cohen, S. M. The Postsynthetic Renaissance in Porous Solids. *J. Am. Chem. Soc.* **2017**, *139*, 2855−2863.
(27) Mon, M.; Bruno, R.; Ferrando-Soria, J.; Armentano, D.; Pardo, E. Metal-organic framework technologies for water remediation: towards a sustainable ecosystem. *J. Mater. Chem. A* **2018**, *6*, 4912−4947.
(28) Tahmasebi, E.; Masoomi, M. Y.; Yamini, Y.; Morsali, A. Application of mechanosynthesized azine-decorated zinc(II) metal-organic frameworks for highly efficient removal and extraction of some heavy-metal ions from aqueous samples: a comparative study. *Inorg. Chem.* **2015**, *54*, 425−433.
(29) Ricco, R.; Konstas, K.; Styles, M. J.; Richardson, J. J.; Babarao, R.; Suzuki, K.; Scopece, P.; Falcaro, P. Lead(ii) uptake by aluminium based magnetic framework composites (MFCs) in water. *J. Mater. Chem. A* **2015**, *3*, 19822−19831.
(30) Morcos, G. S.; Ibrahim, A. A.; El-Sayed, M. M. H.; El-Shall, M. S. High performance functionalized UiO metal organic frameworks for the efficient and selective adsorption of Pb (II) ions in concentrated multi-ion systems. *J. Environ. Chem. Eng.* **2021**, *9*, 105191.
(31) Saleem, H.; Rafique, U.; Davies, R. P. Investigations on post-synthetically modified UiO-66-NH_2 for the adsorptive removal of heavy metal ions from aqueous solution. *Microporous Mesoporous Mater.* **2016**, *221*, 238−244.
(32) Chen, D.; Shen, W.; Wu, S.; Chen, C.; Luo, X.; Guo, L. Ion exchange induced removal of Pb(ii) by MOF-derived magnetic inorganic sorbents. *Nanoscale* **2016**, *8*, 7172−7179.
(33) Yu, C.; Shao, Z.; Hou, H. A functionalized metal-organic framework decorated with O^- groups showing excellent performance for lead(II) removal from aqueous solution. *Chem. Sci.* **2017**, *8*, 7611−7619.
(34) Wang, L.; Zhao, X.; Zhang, J.; Xiong, Z. Selective adsorption of Pb (II) over the zinc-based MOFs in aqueous solution-kinetics, isotherms, and the ion exchange mechanism. *Environ. Sci. Pollut. Res.* **2017**, *24*, 14198−14206.
(35) Sun, D. T.; Peng, L.; Reeder, W. S.; Moosavi, S. M.; Tiana, D.; Britt, D. K.; Oveisi, E.; Queen, W. L. Rapid, Selective Heavy Metal Removal from Water by a Metal-Organic Framework/Polydopamine Composite. *ACS Cent. Sci.* **2018**, *4*, 349−356.
(36) Efome, J. E.; Rana, D.; Matsuura, T.; Lan, C. Q. Metal-organic frameworks supported on nanofibers to remove heavy metals. *J. Mater. Chem. A* **2018**, *6*, 4550−4555.
(37) Wu, J.; Zhou, J.; Zhang, S.; Alsaedi, A.; Hayat, T.; Li, J.; Song, Y. Efficient removal of metal contaminants by EDTA modified MOF from aqueous solutions. *J. Colloid Interface Sci.* **2019**, *555*, 403−412.
(38) Boix, G.; Han, X.; Imaz, I.; Maspoch, D. Millimeter-Shaped Metal-Organic Framework/Inorganic Nanoparticle Composite as a New Adsorbent for Home Water-Purification Filters. *ACS Appl. Mater. Interfaces* **2021**, *13*, 17835−17843.
(39) Hakimifar, A.; Morsali, A. Urea-Based Metal-Organic Frameworks as High and Fast Adsorbent for Hg^{2+} and Pb^{2+} Removal from Water. *Inorg. Chem.* **2019**, *58*, 180−187.
(40) Dermanaki Farahani, S.; Zolgharnein, J. Multivariate optimization of high removal of lead(II) using an efficient synthesized Ni-based metal-organic framework adsorbent. *Chin. J. Chem. Eng.* **2021**, *29*, 146−153.
(41) Ryu, U.; Jee, S.; Rao, P. C.; Shin, J.; Ko, C.; Yoon, M.; Park, K. S.; Choi, K. M. Recent advances in process engineering and upcoming applications of metal-organic framework. *Coord. Chem. Rev.* **2021**, *426*, 213544.
(42) Bruno, R.; Mon, M.; Escamilla, P.; Ferrando-Soria, J.; Esposito, E.; Fuoco, A.; Monteleone, M.; Jansen, J. C.; Elliani, R.; Tagarelli, A.; Armentano, D.; Pardo, E. Bioinspired Metal-Organic Frameworks in Mixed Matrix Membranes for Efficient Static/Dynamic Removal of Mercury from Water. *Adv. Funct. Mater.* **2021**, *31*, 2008499.
(43) Mon, M.; Lloret, F.; Ferrando-Soria, J.; Martí-Gastaldo, C.; Armentano, D.; Pardo, E. Selective and Efficient Removal of Mercury from Aqueous Media with the Highly Flexible Arms of a BioMOF. *Angew. Chem., Int. Ed.* **2016**, *55*, 11167−11172.
(44) Mastropietro, T. F.; Bruno, R.; Pardo, E.; Armentano, D. Reverse osmosis and nanofiltration membranes for highly efficient PFASs removal: overview, challenges and future perspectives. *Dalt. Trans.* **2021**, *50*, 5398−5410.

https://doi.org/10.1021/acsanm.2c00280
ACS Appl. Nano Mater. 2022, 5, 5223−5233

(45) Furukawa, H.; Müller, U.; Yaghi, O. M. "Heterogeneity within order" in metal-organic frameworks. *Angew. Chem., Int. Ed.* **2015**, *54*, 3417−3430.
(46) Helal, A.; Yamani, Z. H.; Cordova, K. E.; Yaghi, O. M. Multivariate metal-organic frameworks. *Natl. Sci. Rev.* **2017**, *4*, 296−298.
(47) Osborn Popp, T. M.; Yaghi, O. M. Sequence-Dependent Materials. *Acc. Chem. Res.* **2017**, *50*, 532−534.
(48) Jiao, J.; Gong, W.; Wu, X.; Yang, S.; Cui, Y. Multivariate crystalline porous materials: Synthesis, property and potential application. *Coord. Chem. Rev.* **2019**, *385*, 174−190.
(49) Viciano-Chumillas, M.; Liu, X.; Leyva-Pérez, A.; Armentano, D.; Ferrando-Soria, J.; Pardo, E. Mixed component metal-organic frameworks: Heterogeneity and complexity at the service of application performances. *Coord. Chem. Rev.* **2022**, *451*, 214273.
(50) Negro, C.; Martínez Pérez-Cejuela, H.; Simó-Alfonso, E. F.; Herrero-Martínez, J. M.; Bruno, R.; Armentano, D.; Ferrando-Soria, J.; Pardo, E. Highly Efficient Removal of Neonicotinoid Insecticides by Thioether-Based (Multivariate) Metal-Organic Frameworks. *ACS Appl. Mater. Interfaces* **2021**, *13*, 28424−28432.
(51) Mon, M.; Bruno, R.; Tiburcio, E.; Viciano-Chumillas, M.; Kalinke, L. H. G.; Ferrando-Soria, J.; Armentano, D.; Pardo, E. Multivariate Metal-Organic Frameworks for the Simultaneous Capture of Organic and Inorganic Contaminants from Water. *J. Am. Chem. Soc.* **2019**, *141*, 13601−13609.
(52) Ribeiro, B.; Botelho, E. C.; Costa, M. L.; Bandeira, C. F. Carbon nanotube buckypaper reinforced polymer composites: A review. *Polímeros* **2017**, *27*, 247−255.
(53) Rashid, M. H. O.; Ralph, S. F. Carbon Nanotube Membranes: Synthesis, Properties, and Future Filtration Applications. *Nanomaterials* **2017**, *7*, 99.
(54) De Filpo, G.; Pantuso, E.; Mashin, A. I.; Baratta, M.; Nicoletta, F. P. WO_3/Buckypaper Membranes for Advanced Oxidation Processes. *Membranes* **2020**, *10*, 157.
(55) Mon, M.; Ferrando-Soria, J.; Grancha, T.; Fortea-Pérez, F. R.; Gascon, J.; Leyva-Pérez, A.; Armentano, D.; Pardo, E. Selective Gold Recovery and Catalysis in a Highly Flexible Methionine-Decorated Metal-Organic Framework. *J. Am. Chem. Soc.* **2016**, *138*, 7864−7867.
(56) Grancha, T.; Ferrando-Soria, J.; Cano, J.; Amorós, P.; Seoane, B.; Gascon, J.; Bazaga-García, M.; Losilla, E. R.; Cabeza, A.; Armentano, D.; Pardo, E. Insights into the Dynamics of Grotthuss Mechanism in a Proton-Conducting Chiral bioMOF. *Chem. Mater.* **2016**, *28*, 4608−4615.
(57) Mon, M.; Ferrando-Soria, J.; Verdaguer, M.; Train, C.; Paillard, C.; Dkhil, B.; Versace, C.; Bruno, R.; Armentano, D.; Pardo, E. Postsynthetic Approach for the Rational Design of Chiral Ferroelectric Metal-Organic Frameworks. *J. Am. Chem. Soc.* **2017**, *139*, 8098−8101.
(58) Mon, M.; Bruno, R.; Elliani, R.; Tagarelli, A.; Qu, X.; Chen, S.; Ferrando-Soria, J.; Armentano, D.; Pardo, E. Lanthanide Discrimination with Hydroxyl-Decorated Flexible Metal-Organic Frameworks. *Inorg. Chem.* **2018**, *57*, 13895−13900.
(59) Mon, M.; Bruno, R.; Tiburcio, E.; Casteran, P.-E.; Ferrando-Soria, J.; Armentano, D.; Pardo, E. Efficient Capture of Organic Dyes and Crystallographic Snapshots by a Highly Crystalline Amino-Acid-Derived Metal-Organic Framework. *Chem.—Eur. J.* **2018**, *24*, 17712−17718.
(60) Mon, M.; Bruno, R.; Ferrando-Soria, J.; Bartella, L.; Di Donna, L.; Talia, M.; Lappano, R.; Maggiolini, M.; Armentano, D.; Pardo, E. Crystallographic snapshots of host-guest interactions in drugs@metal-organic frameworks: towards mimicking molecular recognition processes. *Mater. Horizons* **2018**, *5*, 683−690.
(61) Mon, M.; Rivero-Crespo, M. A.; Ferrando-Soria, J.; Vidal-Moya, A.; Boronat, M.; Leyva-Pérez, A.; Corma, A.; Hernández-Garrido, J. C.; López-Haro, M.; Calvino, J. J.; Ragazzon, G.; Credi, A.; Armentano, D.; Pardo, E. Synthesis of Densely Packaged, Ultrasmall Pt_0^2 Clusters within a Thioether-Functionalized MOF: Catalytic Activity in Industrial Reactions at Low Temperature. *Angew. Chem., Int. Ed.* **2018**, *57*, 6186−6191.
(62) Pérez-Cejuela, H. M.; Mon, M.; Ferrando-Soria, J.; Pardo, E.; Armentano, D.; Simó-Alfonso, E. F.; Herrero-Martínez, J. M. Bio-metal-organic frameworks for molecular recognition and sorbent extraction of hydrophilic vitamins followed by their determination using HPLC-UV. *Microchim. Acta* **2020**, *187*, 201.
(63) Tiburcio, E.; Greco, R.; Mon, M.; Ballesteros-Soberanas, J.; Ferrando-Soria, J.; López-Haro, M.; Hernández-Garrido, J. C.; Oliver-Meseguer, J.; Marini, C.; Boronat, M.; Armentano, D.; Leyva-Pérez, A.; Pardo, E. Soluble/MOF-Supported Palladium Single Atoms Catalyze the Ligand-, Additive-, and Solvent-Free Aerobic Oxidation of Benzyl Alcohols to Benzoic Acids. *J. Am. Chem. Soc.* **2021**, *143*, 2581−2592.
(64) Viciano-Chumillas, M.; Mon, M.; Ferrando-Soria, J.; Corma, A.; Leyva-Pérez, A.; Armentano, D.; Pardo, E. Metal-Organic Frameworks as Chemical Nanoreactors: Synthesis and Stabilization of Catalytically Active Metal Species in Confined Spaces. *Acc. Chem. Res.* **2020**, *53*, 520−531.
(65) Young, R. J.; Huxley, M. T.; Pardo, E.; Champness, N. R.; Sumby, C. J.; Doonan, C. J. Isolating reactive metal-based species in Metal-Organic Frameworks - viable strategies and opportunities. *Chem. Sci.* **2020**, *11*, 4031−4050.
(66) Rao, G.; Lu, C.; Su, F. Sorption of divalent metal ions from aqueous solution by carbon nanotubes: A review. *Sep. Purif. Technol.* **2007**, *58*, 224−231.
(67) Nogalska, A.; Trojanowska, A.; Tylkowski, B.; Garcia-Valls, R. Surface characterization by optical contact anglemeasuring system. *Phys. Sci. Rev.* **2020**, *5*, 5.
(68) Tursi, A.; Mastropietro, T. F.; Bruno, R.; Baratta, M.; Ferrando-Soria, J.; Mashin, A. I.; Nicoletta, F. P.; Pardo, E.; De Filpo, G.; Armentano, D. Synthesis and Enhanced Capture Properties of a New BioMOF@SWCNT-BP: Recovery of the Endangered Rare-Earth Elements from Aqueous Systems. *Adv. Mater. Interfaces* **2021**, *8*, 2100730.

https://doi.org/10.1021/acsanm.2c00280
ACS Appl. Nano Mater. 2022, 5, 5223−5233

Supporting Information (SI) for the manuscript:

Multivariate Metal-Organic Framework/Single-Walled Carbon Nanotube Buckypaper for Selective Lead Decontamination

Mariafrancesca Baratta,[†,§] Teresa Fina Mastropietro,[†,§] Rosaria Bruno,[†,§] Antonio Tursi,[†,§] Cristina Negro,[‡] Jesús Ferrando-Soria,*[,‡] Alexander I. Mashin,[◊] Aleksey Nezhdanov,[◊] Fiore P. Nicoletta,*[,#] Giovanni De Filpo,*[,†] Emilio Pardo*[,‡] and Donatella Armentano*[,†]

[†] Dipartimento di Chimica e Tecnologie Chimiche (CTC), Università della Calabria, Rende 87036, Cosenza, Italy

[‡] Instituto de Ciencia Molecular (ICMol), Universidad de Valencia, 46980 Paterna, Valencia, Spain

[◊] Applied Physics & Microelectronics, Lobachevsky State University of Nizhni Novgorod, Nizhni Novgorod, Russian Federation

[#] Dipartimento di Farmacia e Scienze della Salute e della Nutrizione, Università della Calabria, 87036, Rende, Italy

[§]These authors have equally contributed to this work

*E-mail: jesus.ferrando@uv.es; giovanni.defilpo@unical.it; emilio.pardo@uv.es; donatella.armentano@unical.it; f.nicoletta@unical.it

Experimental Section

Chemicals:

All chemicals were of reagent grade quality. They were purchased from commercial sources and used as received. SWCNTs (characterized by an average diameter of 1.4 ± 0.1 nm and an average length longer than 5 μm) and carboxylic acid functionalized SWNTs (COOH-SWCNTs with bundle average dimensions ranging from 4 to 5 nm in diameter and from 0.5 to 1.5 μm in length, as reported in the datasheet from Sigma-Aldrich, Milan, Italy) were used for the preparation of SWCNT solutions.

Compound $\{Ca^{II}Cu^{II}_6[(S,S)\text{-methox}]_{1.5}[(S,S)\text{-Mecysmox}]_{1.50}(OH)_2(H_2O)\}\cdot 38H_2O$ (1) (**MTV-MOF**) was prepared as reported earlier for similar MTV-MOF containing Sr(II).[65]

Synthesis of $\{Ca^{II}Cu^{II}_6[(S,S)\text{-methox}]_{1.50}[(S,S)\text{-Mecysmox}]_{1.50}(OH)_2(H_2O)\} \cdot 38H_2O$ *(**1**):*

Well-shaped hexagonal prisms of **1** suitable for SCXRD were obtained by slow diffusion in H-shaped tubes of aqueous solutions containing stoichiometric amounts of $(Me_4N)_2\{Cu_2[(S,S)\text{-methox}](OH)_2\} \cdot 4H_2O$ (0.131 g, 0.18 mmol) and $(Me_4N)_2\{Cu_2[(S,S)\text{-Mecysmox}](OH)_2\} \cdot 5H_2O$ (0.129 g, 0.18 mmol) in one arm and $CaCl_2$ (0.022 g, 0.2 mmol) in the other. They were isolated by filtration on paper and air-dried. A gram-scale procedure was also carried out successfully by mixing greater amounts of $(Me_4N)_2\{Cu_2[(S,S)\text{-methox}](OH)_2\} \cdot 4H_2O$ (4.37 g, 6 mmol) and $(Me_4N)_2\{Cu_2[(S,S)\text{-Mecysmox}](OH)_2\} \cdot 5H_2O$ (4.32 g, 6 mmol) in water (60 mL). Another aqueous solution of $CaCl_2$ (0.440 g, 4 mmol) was added dropwise to the resulting deep green solution and the final mix was allowed to react, under stirring, for 6 hours. Afterwards, the material was isolated by filtration and characterized by C, H, N, S, analyses to give a final formula of $\{Ca^{II}Cu^{II}_6[(S,S)\text{-methox}]_{1.50}[(S,S)\text{-Mecysmox}]_{1.50}(OH)_2(H_2O)\} \cdot 38H_2O$. Anal. calcd. for **1**: $C_{33}Cu_6CaS_6H_{122}N_6O_{59}$ (2161.04): C, 18.34; H, 5.69; S, 8.90; N, 3.89%. Found: C, 18.21; H, 5.57; S, 8.77; N, 3.96%; IR (KBr): ν = 1625 and 1596 cm^{-1} (C=O).

Preparation of $[Pb(NO_3)_2]_{0.5}@\{Pb^{II}Cu^{II}_6[(S,S)\text{-methox}]_{1.5}[(S,S)\text{-Mecysmox}_{1.50}(OH)_2(H_2O)\}\cdot 7H_2O$

$[Pb(NO_3)_2]$@1.

Well-formed hexagonal green prisms of **[Pb(NO$_3$)$_2$]@1**, which were suitable for X-ray diffraction, were obtained by soaking crystals of **1** (5.0 mg) in a saturated H_2O/CH_3OH (1:1) solution of $Pb(NO_3)_2$ for 6 hours. The crystals were washed with water, isolated by filtration on paper and air-dried. **[Pb(NO$_3$)$_2$]@1:** Anal.: calcd for $C_{33}Cu_6CaH_{60}PbS_6N_8O_{34}$ (1933.76): C, 20.50; H, 3.13; S, 9.95; N, 5.79%. Found: C, 20.67; H, 3.11; S, 9.89; N, 5.90%. IR (KBr): ν = 1623 cm^{-1} (C=O).

[Pb(NO$_3$)$_2$]@1.

Preparation of membranes:

Buckypaper membranes were obtained by filtration of solutions of SWCNT and COOH-SWCNTs. Generally, 40 mg of SWCNT mixtures were dispersed in 200 mL of a 0.4% TRITON X100 water solution by an ultrasonic bath (model M1800H-E, Bransonic, Danbury, CT, USA) for 30 min. Then, solutions were filtered through PTFE disks with a vacuum pump (pressure = −0.04 bar), washed several times with methanol and, finally, dried at room temperature. All chemicals were purchased from Sigma-Aldrich, Milan, Italy. It is well known that several preparation factors influence the final BP membrane properties, including the SWCNT solution sonication time, the vacuum depression magnitude used during the filtration of SWCNT solutions, the filter porosity and composition.[68] In addition, the main problem found in this study was the best compromise in terms of weight percentage between long SWCNTs, which ensure the gain of self-standing and flexible BP disks, and short COOH-SWCNTs, which ensure a higher lead adsorption. After several trials, the best weight ratio was SWCNTs:COOH-SWCNTs = 3:1, which gave detachable SWCNT disks from polymer filters and self-sustaining BPs (Figure 2a).

MTV-MOF/SWCNT-BPs were obtained by dispersing MOF in the optimized SWCNT solution and applying the procedure previously outlined for neat **SWCNT-BP**. The largest amount of MTV-MOF, which was possible to disperse in the optimized SWCNT solution without losing detachability and self-sustainability of the final BP disks, was 25% w/w (Figure 2b).

Both **SWCNT-BP** and **MTV-MOF/SWCNT-BP** were flexible disks with an average diameter of 38 ± 1 mm and an average thickness of 60 ± 1 μm.

Chemical-physical techniques:

Elemental (C, H, N) and powder X-ray Diffraction analyses (of the pure MOF) were performed at the Microanalytical Service of the University of Calabria. ICP-MS analyses for the Pb^{2+} and

interferent ion capture experiments on membrane (*vide infra*) were performed at the Department of Chemistry of the University of Calabria. FT–IR spectra were recorded on a Perkin-Elmer 882 spectrophotometer as KBr pellets. All characterizations confirmed the purity of the sample when compared with the previously work reported by us.[50]

X-ray Powder Diffraction Measurements:

Polycrystalline sample of **1** to test purity of the bulk, was introduced into 0.5 mm borosilicate capillaries prior to being mounted and aligned on a Bruker D2 Phaser powder diffractometer, using Cu Kα radiation (λ = 1.54056 Å). Five repeated measurements were collected at room temperature (2θ = 2–40°) and merged in a single diffractogram. A polycrystalline sample of **1** was also measured after lead capture experiments following the same procedure.

The flexible disks of an average diameter of 34 ± 1 mm for both SWCNT-BP and MTV-MOF/SWCNT-BP have been allocated on a plate sample holder, then mounted and aligned on a Bruker D2 Phaser powder diffractometer, using Cu Kα radiation (λ = 1.54056 Å). Three repeated measurements were collected at room temperature (2θ = 2–60°) and merged in a single diffractogram.

X–ray photoelectron spectroscopy (XPS) measurements:

Samples of **1**, before and after capture experiments, were prepared by sticking, without sieving, the samples onto a molybdenum plate with scotch tape film, followed by air drying. Measurements were performed on a K-Alpha™ X-ray Photoelectron Spectrometer (XPS) System using a monochromatic Al K(alpha) source (1486.6 eV). As an internal reference for the peak positions in the XPS spectra, the C1s peak has been set at 284.8 eV.

Gas adsorption:

The N_2 adsorption-desorption isotherms at 77 K, were carried out, on policrystalline samples of of **1**, before and after capture experiments, with a BELSORP-mini-X instrument. Samples were first activated with methanol and then evacuated at 348 K during 19 hours under 10^{-6} Torr prior to their analysis.

Membrane characterization:

The morphology of **SWCNT-BP** and **MTV-MOF/SWCNT-BP** was characterized by scanning electron microscopy with a Leica LEO 420 (Leica Microsystems, Cambridge, England) scanning

electron microscope with an accelerating voltage of 10 kV. Samples were covered with an ultrathin gold layer using a sputter coater.

Figures 2c and 2d show the morphology of **SWCNT-BP** and **MTV-MOF/SWCNT-BP** membranes. SWCNT-BP morphology is characterized by the typical BP microscopic texture with bundles and clusters of SWCNTs arising from π–π and van der Waals interactions. The addition of MTV-MOFs in **SWCNT-BP** is evidenced in Figure 2d by the presence of small spherical particles with an average size lower than 1 μm and formed by smaller primary particles with an average diameter of ≈ 100 nm. The highly porous structure of **SWCNT-BP**, firmly hosting the nanosized MTV-MOF particles (no leakage was observed at the end of experiments), guarantees a high permeability and a large surface area for the contact and successive adsorption of ions present in the test solutions. MTV-MOF particles are homogenously distributed inside the membrane.

Thermogravimetric analysis:

The thermogravimetric analysis was performed on **SWCNT-BP** and **MTV-MOF/SWCNT-BP** samples under a dry N_2 atmosphere with a Mettler Toledo TGA/STDA 851^e thermobalance. The experiments were carried out within a temperature range from 25 °C to 800 °C at a heating rate of 10 °C/min. Approximately 20 mg of each sample were placed in a ceramic pan for the measurement.

Capture experiments:

The Pb^{2+} adsorption performance of **SWCNT-BP** and **MTV-MOF/SWCNT-BP** were tested on $Pb(NO_3)_2$ water solutions and multielement solution of $FeCl_3$, $AlCl_3$ and $Pb(NO_3)_2$ at room temperature and under static conditions (Tables S3-S10, S12-S19, S21-S23).

SWCNT-BP and **MTV-MOF/SWCNT-BP** membrane disks were placed in beakers containing 200 mL of $Pb(NO_3)_2$ solution (of deionized and mineral water) at room temperature (25°C).

For selectivity experiments, **SWCNT-BP** and **MTV-MOF/SWCNT** membranes were placed in 100 mL beakers containing 1 and 10 ppm of $Pb(NO_3)_2$, $FeCl_3$ and $AlCl_3$ aqueous solution at room temperature (25°C). All solutions were stirred by an orbital shaker (PSU-10i, Biosan, Italy). Each experiment was performed in triplicate and results are reported as average values of ± 3SD. The stabilization of the Pb^{2+} in view of the ICP-MS analysis occurred by adding nitric acid with a purity of 98 %. The ICP-MS data are reported considering the dilution factor. For selectivity experiment, to avoid precipitation of Fe^{3+} and Al^{3+} as hydroxide from the aqueous solution, the addition of nitric acid for the stabilization has been performed until pH =2.

The Pb^{2+} adsorption performance of **SWCNT-BPs** and **MTV-MOF/SWCNT-BPs** reported in Figure 3 (data from Tables S2 and S3) have been fitted under the hypothesis that the lead adsorption capacity of adsorbent (mg g^{-1}) follows the Lagergren-first-order equation[1,2]:

$$\frac{dq_t}{dt} = k_1(q_e - q_t) \qquad (1)$$

where q_e and k_1 are the lead adsorption capacity per unit of adsorbent mass (mg g^{-1}) at equilibrium and the Lagergren adsorption rate constant (min^{-1}), respectively. After integration, the following equation holds:

$$q_t = q_e(1 - e^{-k_1 t}) \qquad (2)$$

The experimental amount of adsorbed metal ions ($q_{exp}(t)$, mg g^{-1}) can be expressed as follows:

$$q_{exp}(t) = \frac{(C_0 - C_t)}{m} V \qquad (3)$$

where C_0 and C_t are the lead concentration in the solution at time zero and t, respectively, m is the mass of the used membranes, and V is the volume of lead solution.

Experimental data were fitted as a function of time by OriginPro 2019 Software.[3] Non-linear optimization method by Origin software was used instead of linear regression in order to avoid any distortions created in the original error distribution.[4]

The obtained Lagergren adsorption rate constants, k_1 (min^{-1}), for **SWCNT-BPs** and **MTV-MOF/SWCNT-BPs** at different initial lead concentrations are reported in Table S11.

The fit of the kinetic profiles of **SWCNT-BP** and **MTV-MOF/SWCNT-BP** membranes agrees with the findings obtained from their direct observation. The capture performance of **SWCNT-BPs** was improved by the incorporation of **MTV-MOF** in **SWCNT-BPs** increasing the constant rate values for the concentrations of 300 and 1000 ppb from 0.0120 ± 0.0005 and 0.0126 ± 0.0008 min^{-1} to 0.0138 ± 0.0006 and 0.0143 ± 0.0008 min^{-1}, respectively.

Distribution coefficients calculation:

The lead distribution coefficients, K_D, between membranes and solutions both in neat and multi-component (Pb, Fe, Al) solutions were calculated, in agreement with reference,[5] according to the following equation:

$$K_D = \frac{[Pb^{2+}]_{mem}}{[Pb^{2+}]_{sol}} \qquad (4)$$

where $[Pb^{2+}]_{mem}$ (mg kg^{-1}) and $[Pb^{2+}]_{sol}$ (mg L^{-1}) are the lead ions concentrations at equilibrium adsorbed onto the membrane and present in the solution, respectively. Table S20 shows the $\log K_D$ values calculated for the lead initial concentrations of 1000 ppb and 10000 ppb in neat and multi-component (Pb, Fe, Al) solutions.

Generally a $\log K_D$ value larger than 5 is indicative for a high affinity of ions to be adsorbed onto a substrate.[6] As reported in Table S20 at Pb^{2+} concentration of 1000 ppb, the $\log K_D$ values for lead neat solutions are larger than 5 both for SWCNT-BPs and MTV-MOF/SWCNT-BPs, confirming the strong affinity between Pb^{2+} and membranes.

As expected, the $\log K_D$ values decrease for increasing lead concentrations as a consequence of the saturation of the active sites present in membranes. Similar trends, but with lower values, were found for the $\log K_D$ in multi-component solutions, confirming the competitive affinity of iron and aluminum ions for both SWCNT-BP and MTV-MOF/SWCNT-BP membranes. It is worth noting that the substitution of SWCNTs with MTV-MOFs increases the ions affinity in all cases reported in Table S20.

ICP-MS analyses:

The Pb^{2+} concentrations together with the Al^{3+}, Fe^{3+}, Na^{+}, K^{+}, Mg^{2+} tested ions were determined by utilizing an inductively coupled plasma-mass spectrometer (ICP-MS iCAP™ TQ Thermo Fisher Scientific, USA) equipped with a Peltier cooled high purity quartz baffled cyclonic spray chamber, a concentric borosilicate glass nebulizer, a wide 2.5 mm internal diameter quartz injector, a nickel sample and two skimmer cones with 1.1 mm and 0.5 mm diameter orifices, respectively. The ICP torch was a demountable single piece quartz torch. The samples were collected by a Thermo Scientific™ Autosampler Housing with a peristaltic pump equipped with three-stop flared PVC pump tubing. A multielement standard solution was used to calibrate the instrument using different analytical concentrations (0.5, 5, 10, 20, 50 and 100 ppb, R^2 of calibration curve ≈ 1 and a limit of detection, LOD, of about 0.015 ppb). Ultrapure deionized water (18.3 MΩ cm, Arioso, Human Corporation, Korea) was used for the aqueous solutions preparation after filtration by 0.45 μm filter (Millex Syringe Filter, Merck, Darmstadt, Germany). Each experiment was performed in triplicate and results are reported as average values ± 3 SD. Data reported in Tables S2-S10, S12-S19, S21-S23.

EDX measurements:

Scanning Electron Microscopy (SEM) measurements were carried out for both SWCNT-BP and BioMOF/SWCNT-BP using a LEO 420 scanning electron microscope (SEM, Zeiss) (Vacuum conditions: 8x10-6 Torr, accelerating voltage: 15 kV) coupled with an Energy Dispersive X–ray (EDX) detector. The EDX module was an INCAx–Sight Oxford Instruments (Vacuum conditions: 8×10^{-6} Torr, iProbe: 650 pA, Current: 15 kV). Samples were gold metallized by an Auto Sputter Coater (Agar). Both membranes were suspended in a 10 ppm $Pb(NO_3)_2$ aqueous solution for 24 h for EDX measurements.

Contact angle measurements:

Static contact angle values of **SWCNT-BP** and **MTV-MOF/SWCNT-BP** were measured with a goniometer (Nordtest, Serravalle Scrivia AL, Italy) at 25 °C. A drop (2 µL) of water was put onto the sample surface by a micro-syringe and measurements were carried out by setting the tangents on both visible edges of the droplet on five different positions of each sample and calculating the average value of the measurements. The hydrophilic character of **SWCNT-BP** and **MTV-MOF/SWCNT-BP** top surfaces was confirmed by contact-angle measurements, which gave average contact-angle values of 47.5° ± 0.5° and 78.5° ± 0.5°, respectively, Figures S5a and S5b.

Mechanical properties:

The mechanical properties of **SWCNT-BP** and **MTV-MOF/SWCNT-BP** were measured with a Sauter TVO-S tensile tester equipped with a Sauter FH-1k digital dynamometer and AFH FAST software (Sauter GmbH, Balingen, Germany). Rectangular strips (width 10 mm and length 34 mm) were tested at a strain rate of 0.1 mm min^{-1}. The test allowed the determination of the mechanical properties such as the tensile strength as the maximum stress and the Young's modulus (Figure S11).

Pore distribution measurements:

Pore size distribution was evaluated by a capillary flow porometer (CFP-1500 AEXL, PMI Porous Materials Inc., Ithaca, NY, USA). Membranes were fully wetted by keeping them in Porewick® (Sigma-Aldrich, Milan, Italy) for 24 h. Then, nitrogen was gradually allowed to flow into the membrane by increasing its pressure and the registration of gas pressure and permeation flow rate allowed the calculation of the pore size distribution (Figure S8).

X-ray crystallographic data collection and structure refinement: Crystals of **1** and **[Pb(NO$_3$)$_2$]@1** with *ca.* 0.16 x 0.12 x 0.10 and 0.14 x 0.08 x 0.10, mm as dimensions were selected and mounted on a MITIGEN holder in Paratone oil. Measurement on single crystal of **1** was performed at room temperature, whereas single crystal of **[Pb(NO$_3$)$_2$]@1** was very quickly placed on a nitrogen stream cooled at 100 K to avoid the possible degradation upon dehydration. Diffraction data were collected on a Bruker-Nonius X8APEXII CCD area detector diffractometer using graphite-monochromated Mo-K$_\alpha$ radiation (λ = 0.71073 Å) for. The data were processed through SAINT[7] reduction and SADABS[8] multi-scan absorption software. The structure was solved with the SHELXS structure solution program, using the Patterson method. The model was refined with version 2018/3 of SHELXL against F^2 on all data by full-matrix least squares.[9-11]

Crystals of **[Pb(NO$_3$)$_2$]@1**, suitable for X-ray diffraction, were obtained by soaking crystals of **1** (5.0 mg) in a saturated aqueous solution of Pb(NO$_3$)$_2$ for 6 hours, after a crystal-to-crystal transformation. For these reasons, it is reasonable to observe a diffraction pattern sometimes affected by expected internal imperfections of the crystals.

All non-hydrogen were refined anisotropically except some carbon and sulfur atoms belonging to the highly thermal disordered methionine and methylcysteine chains pointing within huge pores and disordered Pb atoms in **[Pb(NO$_3$)$_2$]@1.** In the latter, the occupancy factors, of Pb^{2+} metal ions have been defined in agreement with SEM results. Pb^{2+} metal ions exhibit statistic and sever thermal disorder, as normally expected in porous crystals. Indeed, the heavy metal ion is detected residing either far (Pb1A with assigned occupancy factor of 0.08333) or close to the methionine moieties (Pb1 and Pb1B with occupancy factors of 0.16777 and 0.08333, respectively), quite suggesting a pre- and post-recognition from the aminoacidic derivative, with Pb1B representing the first step of migration of Pb1A (the most far from the walls of the MTV-MOF) towards the final site of Pb1, where the Pb^{2+} metal ions interacts both with sulfur atom belonging from methionine derivative and oxygen atoms from the oxamate ligand (Figure S2).

In both crystal structure refinements, the use of some C-C and C-S together with Pb-S bond, in **[Pb(NO$_3$)$_2$]@1**, lengths restrains during the refinements of some highly disordered atoms, has been reasonable imposed and related to ethyl- and methyl-thiomethyl chains of the methox and mecysmox ligands, respectively that are dynamic components of the frameworks. As a consequence Alerts A and B in the checkcifs, also related to short intra H···H, are detected.

The solvent molecules in both models, together with NO_3^- anions expected in **[Pb(NO$_3$)$_2$]@1**, were disordered and no reasonable models have been found to define them. For that reason, the contribution to the diffraction pattern from the disordered water molecules located in the voids was subtracted from the observed data through the SQUEEZE method, implemented in PLATON.[12] The hydrogen atoms of the ligand were set in calculated positions and refined as riding atoms whereas for water molecules were neither found nor calculated.

A summary of the crystallographic data and structure refinement for **1** and **[Pb(NO$_3$)$_2$]@1** is given in Table S1. The comments for the alerts A and B are reported in the CIFs using the validation response form (vrf). The somewhat high R values (levels Alert A and B in checkcifs) is, most likely, affected by the contribution of the highly disordered solvent and anions to the intensities of the low angle reflections. CCDC (Cambridge Crystallographic Data Centre) reference numbers are 2128259-2128260 for **1** and **[Pb(NO$_3$)$_2$]@1**, respectively.

The final geometrical calculations on free voids and the graphical manipulations were carried out with PLATON[12] implemented in WinGX,[13] and CRYSTAL MAKER[14] programs, respectively.

Table S1. Summary of Crystallographic Data for **1** and **[Pb(NO$_3$)$_2$]@1.**

Compound	**1**	**[Pb(NO$_3$)$_2$]@1**
Formula	$C_{33}H_{122}CaCu_6N_6O_{59}S_6$	C_{33} H_{60} Ca Cu_6 N_8 O_{34} Pb S_6
M (g mol^{-1})	2161.04	1933.76
λ (Å)	0.71073	0.71073
Crystal system	hexagonal	hexagonal
Space group	$P6_3$	$P6_3$
a (Å)	17.8511(7)	17.866(2)
c (Å)	12.8014(8)	12.6684(18)
V (Å^3)	3532.8(4)	3502.0(10)
Z	2	2
ρ_{calc} (g cm^{-3})	2.032	1.834
μ (mm^{-1})	2.154	4.520
T (K)	296	100
θ range for data collection (˚)	1.317- 24.620	2.28- 26.45
Completeness to θ = 25.0	94%	99.5%
Measured reflections	37242	59514
Unique reflections (Rint)	3565(0.0469)	4784(0.1047)
Observed reflections [$I > 2\sigma(I)$]	2653	3398
Goof	1.199	1.163
R^a [$I > 2\sigma(I)$] (all data)	0.0615 (0.0811)	0.0773 (0.0998)
wR^b [$I > 2\sigma(I)$] (all data)	0.1762 (0.1840)	0.2198 (0.2352)
CCDC	2128259	2128260

[a] $R = \sum(|F_o| - |F_c|)/\sum|F_o|$. [b] $wR = [\sum w(|F_o| - |F_c|)^2/\sum w|F_o|^2]^{1/2}$.

Table S2. Selected data[a] from the ICP-MS analyses[b] for the aqueous mother solution during the Pb^{2+} adsorption process by 50 mg of a polycrystalline sample of MOF **1**.

Time (min.)	$[Pb^{2+}]$
0	997
1	798
5	734
10	724
15	634
30	259
45	221
60	134
75	79.9
90	46.6
120	23.8
180	22.7
240	17.45
300	7.89
360	6.59
720	5.45
1440	5.12
4320	4.89

[a] Results are given as μg/L. [b] LOD: 0,012 μg/L

Table S3. Residual Pb^{2+} concentration and recovery percentage (RE%) in the stock solutions of deionized water at an initial concentration of about 300 ppb analysed with the ICP-MS for a neat **SWCNT-BP** and **MTV-MOF/ SWCNT-BP**.

Deionized water	**300 ppb**					
	SWCNT-BP			**MTV-MOF/ SWCNT-BP**		
Time	**^{208}Pb**	**SD**	**RE%**	**^{208}Pb**	**SD**	**RE%**
min	**ppb**	**ppb**		**ppb**	**ppb**	
0	287.87	3.39	0.00	285.51	0.80	0.00
1	283.73	2.16	1.44	278.09	1.71	2.60
3	278.53	1.40	3.24	271.39	1.65	4.95
5	274.72	0.31	4.57	266.66	0.84	6.60
7	268.98	0.83	6.56	266.54	1.64	6.64
10	266.37	1.70	7.47	254.68	1.76	10.80
15	247.31	2.42	14.09	248.15	2.52	13.09
20	237.69	1.61	17.43	224.30	4.54	21.44
30	203.85	3.81	29.19	190.13	0.95	33.41
45	172.14	1.60	40.20	150.60	1.59	47.25
60	144.05	1.03	49.96	125.14	0.85	56.17
120	54.77	1.37	80.97	35.97	0.14	87.40
240	13.68	0.18	95.25	5.51	0.04	98.07
480	10.74	0.10	96.27	4.67	0.07	98.36
1000	10.50	0.03	96.35	0.49	0.00	99.83
1440	2.75	0.01	99.05	0.27	0.28	99.90
4320	0.74	0.02	99.74	0.10	0.11	99.97

LOD: 0.015 ppb

Table S4. Residual Pb^{2+} concentration and recovery percentage (RE%) in the stock solutions of deionized water at an initial concentration of about 1000 ppb analysed with the ICP-MS for a neat **SWCNT-BP** and **MTV-MOF/SWCNT-BP**.

Deionized water	**1000 ppb**					
	SWCNT-BP			**MTV-MOF/ SWCNT-BP**		
Time	**^{208} Pb**	**SD**	**RE%**	**^{208} Pb**	**SD**	**RE%**
min	**ppb**	**ppb**		**ppb**	**ppb**	
0	987.61	18.57	0.00	993.21	1.73	0.00
1	941.06	11.23	4.71	936.54	12.93	5.71
3	905.79	8.02	8.28	904.91	8.15	8.89
5	896.23	19.20	9.25	882.24	7.62	11.17
7	870.64	9.37	11.84	855.37	4.69	13.88
10	852.37	6.42	13.69	818.43	7.91	17.60
15	805.98	4.41	18.39	795.13	2.08	19.94
20	760.17	6.96	23.03	720.80	10.74	27.43
30	757.98	8.94	23.25	671.65	6.11	32.38
45	684.44	11.85	30.70	554.84	6.09	44.14
60	603.97	9.13	38.85	468.33	3.28	52.85
120	206.04	2.72	79.14	129.15	0.58	87.00
240	48.25	0.73	95.11	17.41	0.23	98.25
480	39.35	0.43	96.02	14.07	0.05	98.58
1000	6.65	0.06	99.33	0.73	0.02	99.93
1440	5.71	0.07	99.42	0.44	0.01	99.96
4320	4.58	0.11	99.54	0.39	0.12	99.96

LOD: 0.015 ppb

Table S5. Residual Pb^{2+} concentration and recovery percentage (RE%) in the stock solutions of mineral water at an initial concentration of about 300 ppb analysed with the ICP-MS for a neat **SWCNT-BP**. The capture performance was tested also for Na^{+}, Mg^{2+}, K^{+}, and Ca^{2+} ions present in mineral water.

Mineral water 300 ppb – SWCNT-BP											
Time	**^{23}Na**		**^{24}Mg**		**^{39}K**		**^{44}Ca**		**^{208}Pb**		
min	**ppb**	**SD**	**ppb**	**SD**	**ppb**	**SD**	**ppb**	**SD**	**ppb**	**SD**	**RE%**
0	6871.91	74.56	4920.54	62.81	1312.80	11.39	16637.63	153.02	293.73	3.37	0.00
1	6686.03	123.60	4817.24	140.31	1258.96	20.78	16276.08	111.73	283.42	5.16	3.51
3	6696.62	35.51	4845.49	40.44	1172.87	23.91	16276.09	207.81	280.18	3.47	4.61
5	6529.66	84.87	4696.28	41.69	1141.37	17.84	16104.03	95.72	270.61	4.49	7.87
7	6825.34	46.86	4704.86	32.86	1168.61	15.70	16171.00	83.41	266.30	3.24	9.34
10	6849.81	38.35	4474.49	58.41	1142.06	18.72	15585.43	45.48	257.54	5.18	12.32
15	6690.83	86.43	4516.36	66.16	1184.37	13.33	15542.47	60.13	241.88	3.50	17.65
20	6856.03	182.37	4462.22	84.42	1184.80	22.66	15278.75	294.63	225.28	2.87	23.30
30	6820.05	128.55	4475.45	11.15	1166.94	8.24	14995.49	78.03	195.88	2.09	33.31
45	6775.29	147.37	4535.19	10.59	1179.27	10.68	14830.13	104.73	158.33	1.86	46.10
60	6781.49	150.06	4502.74	56.16	1183.65	21.86	14704.52	136.84	133.19	1.03	54.66
120	6320.56	90.84	4433.10	56.74	1175.66	20.20	14545.28	104.93	62.95	0.64	78.57
240	6181.54	135.54	4589.12	14.02	1231.38	10.33	13749.16	209.70	22.94	0.15	92.19
480	6378.30	60.29	4327.91	112.74	1174.71	15.26	13550.60	73.28	20.60	0.13	92.99
1000	6569.74	73.00	4615.92	69.67	1246.08	21.73	13514.85	80.31	2.86	0.03	99.03
1440	6394.11	56.54	4573.10	66.84	1219.59	5.83	13362.88	194.31	2.73	0.03	99.07
4320	6396.42	144.35	4628.81	45.84	1251.99	15.35	13569.02	196.08	0.78	0.01	99.74

LOD: 0.015 ppb

Table S6. Residual Pb^{2+} concentration and recovery percentage (RE%) in the stock solutions of mineral water at an initial concentration of about 300 ppb analysed with the ICP-MS for **MTV-MOF/SWCNT-BP**. The capture performance was tested also for Na^{+}, Mg^{2+}, K^{+}, and Ca^{2+} ions present in mineral water.

Mineral water 300 ppb – MTV-MOF/SWCNT-BP											
Time	**^{23}Na**		**^{24}Mg**		**^{39}K**		**^{44}Ca**		**^{208}Pb**		
min	**ppb**	**SD**	**ppb**	**SD**	**ppb**	**SD**	**ppb**	**SD**	**ppb**	**SD**	**RE%**
0	6712.21	97.47	5099.90	152.52	1668.04	47.45	16921.10	398.73	296.37	4.90	0.00
1	6645.32	160.28	4910.93	155.57	1632.23	50.82	16757.20	220.81	285.51	6.34	3.66
3	6556.25	179.76	4963.62	104.98	1645.33	27.58	16711.04	142.73	281.34	1.24	5.07
5	6567.21	199.20	4930.48	18.26	1684.23	51.67	17051.17	369.40	267.25	3.75	9.82
7	6544.19	134.17	4953.54	106.24	1558.51	11.05	16552.03	318.01	263.57	2.39	11.07
10	6564.92	155.52	4967.77	152.24	1550.63	41.09	16855.55	559.17	252.90	2.89	14.67
15	6571.14	91.39	4958.22	131.60	1498.53	20.04	16433.20	592.65	243.98	1.79	17.68
20	6438.77	71.66	4883.28	63.51	1487.36	22.81	16494.30	366.46	219.48	2.95	25.95
30	6370.28	79.03	4859.73	32.38	1469.68	18.52	16089.10	632.35	189.10	2.37	36.19
45	6313.65	174.78	4737.96	85.99	1365.41	15.99	15476.38	519.60	128.78	0.70	56.55
60	6225.80	72.15	4660.93	78.76	1321.21	14.75	15818.71	411.04	90.98	1.23	69.30
120	6578.66	99.14	4429.78	50.78	1388.73	18.91	15561.95	653.22	54.42	0.38	81.64
240	6452.84	118.17	4337.49	21.50	1362.32	13.57	15052.70	572.06	16.89	0.20	94.30
480	6539.24	382.08	4323.51	80.39	1347.35	5.02	13224.44	445.71	15.14	0.23	94.89
1000	6548.91	119.05	4506.08	26.87	1384.41	27.31	15109.03	270.32	2.24	0.03	99.24
1440	6458.55	118.87	4476.48	67.19	1372.32	11.36	14859.53	445.20	1.88	0.04	99.37
4320	6248.34	150.92	4507.52	101.03	1332.31	4.86	13416.08	580.81	0.01	0.01	100.00

LOD: 0.015 ppb

Table S7. Residual Pb^{2+} concentration and recovery percentage (RE%) in the stock solutions of mineral water at an initial concentration of about 1000 ppb analysed with the ICP-MS for a neat **SWCNT-BP**. The capture performance was tested also for Na^{+}, Mg^{2+}, K^{+}, and Ca^{2+} ions present in mineral water.

Mineral water 1000 ppb – SWCNT-BP											
Time	**^{23}Na**		**^{24}Mg**		**^{39}K**		**^{44}Ca**		**^{208}Pb**		
min	**ppb**	**SD**	**ppb**	**SD**	**ppb**	**SD**	**ppb**	**SD**	**ppb**	**SD**	**RE%**
0	6979.91	55.84	4945.72	81.69	1292.22	25.55	16798.67	93.08	997.60	13.97	0.00
1	6789.47	100.03	4872.17	100.06	1218.08	17.52	16354.61	170.79	963.57	16.42	3.41
3	6883.22	50.57	4849.25	75.10	1157.94	15.91	16123.76	198.43	956.32	10.06	4.14
5	6896.39	86.91	4745.64	53.70	1161.52	23.25	16140.85	256.77	924.19	28.82	7.36
7	6793.70	49.07	4698.50	68.83	1203.30	11.67	15598.11	96.72	898.13	12.75	9.97
10	6605.50	40.76	4597.45	32.84	1214.88	19.59	15601.44	186.47	880.13	9.09	11.78
15	6150.97	74.93	4634.09	98.82	1164.80	10.10	15325.99	213.11	851.95	8.92	14.60
20	6124.14	59.71	4507.51	126.89	1197.72	18.78	15184.39	294.63	729.06	6.24	26.92
30	6115.12	28.80	4531.90	37.07	1179.46	21.45	15018.41	52.02	661.01	12.00	33.74
45	6200.12	77.72	4489.67	63.50	1192.81	17.22	14877.18	219.28	594.69	16.85	40.39
60	6152.46	81.09	4510.62	94.03	1219.19	16.67	14699.75	181.66	506.23	13.70	49.26
120	6295.25	83.82	4387.14	112.71	1182.76	12.29	14206.29	63.35	298.87	7.54	70.04
240	6165.90	90.19	4452.68	73.83	1173.46	8.37	13945.91	79.42	143.53	2.10	85.61
480	6064.32	60.29	4477.50	134.77	1215.68	21.82	13789.65	186.46	84.13	1.02	91.57
1000	6176.15	92.70	4541.63	108.66	1198.57	5.62	13419.96	142.31	20.66	0.57	97.93
1440	6059.76	77.06	4581.69	53.35	1205.95	0.83	13267.45	76.31	13.85	0.04	98.61
4320	6258.11	84.12	4704.93	20.30	1236.08	1.38	13308.08	203.07	7.96	0.19	99.20

LOD: 0.015 ppb

Table S8. Residual Pb^{2+} concentration and recovery percentage (RE%) in the stock solutions of mineral water at an initial concentration of about 1000 ppb analysed with the ICP-MS for **MTV-MOF/SWCNT-BP**. The capture performance was tested also for Na^{+}, Mg^{2+}, K^{+}, and Ca^{2+} ions present in mineral water.

Mineral water 1000 ppb – MTV-MOF/SWCNT-BP											
Time	**^{23}Na**		**^{24}Mg**		**^{39}K**		**^{44}Ca**		**^{208}Pb**		
min	**ppb**	**SD**	**Ppb**	**SD**	**ppb**	**SD**	**ppb**	**SD**	**ppb**	**SD**	**RE%**
0	6759.38	158.40	5023.08	78.88	1498.26	20.88	16995.46	175.71	995.39	4.90	0.00
1	6723.76	90.39	4996.97	96.59	1423.04	7.08	16803.50	134.79	958.89	6.34	3.67
3	6606.57	73.25	4958.48	157.72	1482.65	58.66	16745.37	208.77	941.66	1.24	5.40
5	6598.76	142.24	4947.75	124.24	1403.25	36.38	16702.73	219.48	907.68	3.75	8.81
7	6653.03	107.17	4975.52	68.23	1397.56	47.25	16786.03	154.25	843.22	2.39	15.29
10	6701.31	83.85	4921.93	118.15	1503.62	18.01	17102.86	123.16	812.42	2.89	18.38
15	6698.45	135.39	4903.93	47.72	1516.73	56.07	16817.04	196.11	743.96	1.79	25.26
20	6593.12	128.67	4894.24	91.54	1491.81	39.30	16763.26	201.44	665.21	2.95	33.17
30	6505.85	100.20	4821.09	107.42	1512.69	25.17	16549.09	95.41	593.52	2.37	40.37
45	6723.26	54.72	4786.73	189.75	1438.42	10.55	16296.99	159.62	510.35	0.70	48.73
60	6623.60	164.59	4710.59	63.20	1407.22	44.73	16008.58	103.07	412.76	1.23	58.53
120	6597.81	179.48	4608.19	105.82	1356.89	57.24	15397.34	176.91	204.27	0.38	79.48
240	6687.17	120.19	4593.72	78.23	1349.24	35.71	14996.10	84.88	77.57	0.20	92.21
480	6521.32	85.08	4486.57	45.36	1313.58	5.02	14237.76	142.72	46.04	0.23	95.37
1000	6603.98	52.64	4387.01	142.08	1295.73	31.35	14039.04	119.33	6.85	0.03	99.31
1440	6463.27	175.66	4507.44	175.18	1276.52	23.37	13792.54	245.55	3.88	0.04	99.61
4320	6296.84	94.89	4548.16	97.20	1359.20	29.38	13567.03	156.01	1.76	0.01	99.82

LOD: 0.015 ppb

Table S9. Residual Pb^{2+} concentration and recovery percentage (RE%) in the stock solutions of mineral water at an initial concentration of about 200 ppb analysed with the ICP-MS for a neat **SWCNT-BP**. The capture performance was tested also for Na^{+}, Mg^{2+}, K^{+}, and Ca^{2+} ions present in mineral water.

Mineral water 200 ppb – SWCNT-BP											
Time	**^{23}Na**		**^{24}Mg**		**^{39}K**		**^{44}Ca**		**^{208}Pb**		
min	**ppb**	**SD**	**ppb**	**SD**	**ppb**	**SD**	**ppb**	**SD**	**ppb**	**SD**	RE%
0	6676.80	27.39	5108.88	81.08	1356.60	15.53	16960.68	95.47	183.80	1.17	0.00
1	6592.12	176.15	5022.29	75.30	1281.73	20.53	16788.62	278.11	165.67	1.12	9.86
3	6602.57	92.62	5081.92	76.49	1271.88	9.67	16706.35	169.03	163.59	1.36	11.00
5	6566.34	60.11	4998.03	66.31	1262.21	6.97	15574.14	6.83	158.43	1.25	13.80
7	6729.48	67.63	5067.68	63.21	1285.21	14.21	15670.73	102.46	155.58	1.53	15.35
10	6753.60	76.72	4952.52	64.60	1315.88	5.16	15517.24	84.19	150.14	2.10	18.32
15	6690.83	72.74	4831.15	86.20	1319.48	25.01	15212.41	198.55	142.01	1.83	22.74
20	6759.74	46.64	4867.90	106.42	1323.65	17.55	14993.35	147.56	129.74	0.75	29.41
30	6724.26	49.40	4905.12	102.49	1312.99	10.74	14918.65	80.12	112.20	1.05	38.96
45	6737.23	90.83	4857.80	54.98	1323.79	15.72	14687.97	87.54	91.44	1.26	50.25
60	6686.25	206.08	5044.64	39.06	1348.35	14.97	14896.06	82.07	80.98	0.75	55.94
120	6231.79	97.94	4873.00	86.79	1342.09	5.91	14117.46	106.93	36.11	0.45	80.35
240	6268.36	144.86	4892.03	98.21	1317.63	12.92	14951.69	121.23	13.74	0.13	92.52
480	6288.72	77.53	4976.80	32.02	1316.33	9.55	14676.36	25.34	11.71	0.11	93.63
1000	6551.28	49.99	4995.78	35.33	1331.27	23.00	14276.79	31.83	2.20	0.04	98.80
1440	6304.31	168.83	5062.15	37.08	1367.07	14.88	13584.85	97.98	2.45	0.01	98.67
4320	6396.42	95.25	4980.65	28.27	1238.89	7.21	13231.39	90.40	0.09	0.06	99.95

LOD: 0.015 ppb

Table S10. Residual Pb^{2+} concentration and recovery percentage (RE%) in the stock solutions of mineral water at an initial concentration of about 200 ppb analysed with the ICP-MS for **MTV-MOF/SWCNT-BP**. The capture performances have been tested also for Na^{+}, Mg^{2+}, K^{+}, and Ca^{2+} ions present in mineral water.

Mineral water 200 ppb – MTV-MOF/SWCNT-BP											
Time	**^{23}Na**		**^{24}Mg**		**^{39}K**		**^{44}Ca**		**^{208}Pb**		
min	**ppb**	**SD**	**ppb**	**SD**	**ppb**	**SD**	**ppb**	**SD**	**ppb**	**SD**	**RE%**
0	6923.33	87.34	4918.22	21.94	1287.33	20.17	17139.60	166.35	186.99	1.42	0.00
1	6579.31	96.32	4828.29	26.02	1236.15	26.19	16854.80	73.82	164.35	3.10	12.11
3	6418.45	115.98	4858.95	79.42	1264.22	16.01	16567.79	171.33	162.16	0.71	13.28
5	6376.71	27.72	4717.94	46.62	1227.42	5.67	16682.78	68.22	148.63	1.49	20.51
7	6265.34	114.17	4718.36	87.97	1259.80	27.32	16204.42	224.92	146.20	1.69	21.81
10	6419.24	98.33	4770.07	76.76	1264.72	15.16	16977.31	227.45	139.52	0.99	25.39
15	6332.51	79.84	4694.76	58.54	1262.09	9.42	16767.61	95.20	122.35	1.34	34.57
20	6478.69	190.85	4797.32	31.41	1281.07	5.08	16199.97	137.66	107.08	0.87	42.74
30	6275.34	97.17	4593.38	79.53	1242.04	43.90	16963.21	60.52	79.47	0.69	57.50
45	6323.16	219.89	4627.24	33.93	1259.27	25.99	16257.51	76.89	59.82	0.70	68.01
60	6362.88	63.75	4708.66	91.13	1280.67	2.26	16965.42	464.92	50.32	0.55	73.09
120	6913.36	92.26	4562.43	14.65	1284.77	12.81	16584.59	521.15	24.33	0.23	86.99
240	6988.54	151.57	4571.68	85.95	1276.94	19.78	16519.95	570.09	12.42	0.08	93.36
480	6804.98	101.45	4215.46	52.65	1282.27	7.34	15285.24	446.86	11.26	0.10	93.98
1000	6792.12	83.63	4493.74	37.46	1261.93	4.50	15947.39	706.29	2.49	0.02	98.67
1440	6863.95	155.00	4509.02	15.48	1274.57	5.81	16388.46	396.40	2.15	0.02	98.85
4320	6821.09	242.39	4478.51	67.49	1258.50	40.64	15158.31	847.48	0.00	0.01	100.00

LOD: 0.015 ppb

Table S11. The obtained Lagergren adsorption rate constants, k_1 (min^{-1}), for **SWCNT-BPs** and **MTV-MOF/SWCNT-BPs** at different initial lead concentrations.

ppb	**SWCNT-BPs**	**MTV-MOF/SWCNT-BPs**
300	0.0120 ± 0.0005	0.0138 ± 0.0006
1000	0.0126 ± 0.0008	0.0143 ± 0.0008

Table S12. Adsorption capacities (AC / mg g^{-1}) and recovery percentage (RE%) by neat **SWCNT-BP** and **MTV-MOF/SWCNT-BP** in 10 - 100 ppm Pb^{2+} range.

Pb^{2+}	**SWCNT-BP**		**MTV-MOF/SWCNT-BP**	
ppm	**AC / mg g^{-1}**	**RE%**	**AC / mg g^{-1}**	**RE%**
10	52.00	89.76	57.00	98.15
20	77.00	85.2	97.00	97.1
30	121.00	79.15	145.00	93.91
60	128.00	42.23	192.00	65.5
100	180.00	37.49	310.00	64.31

LOD: 0.015 ppb

Table S13. Residual Pb^{2+} concentration and recovery percentage (RE%) in the stock solutions of deionized water at an initial concentration of about 10 ppm analysed with the ICP-MS for a neat **SWCNT-BP** and **MTV-MOF/SWCNT-BP**.

Deionized water	**10 ppm**					
	SWCNT-BP			**MTV-MOF/ SWCNT-BP**		
Time	**^{208}Pb**	**SD**	**RE%**	**^{208}Pb**	**SD**	**RE%**
min	**ppb**	**ppb**		**ppb**	**ppb**	
0	11681.37	66.93	0	11667.17	154.80	0
1	11489.84	296.53	1.64	11126.69	46.51	4.63
5	11377.41	165.23	2.60	10653.61	108.12	8.69
10	10803.50	17.08	7.52	9639.33	38.18	17.38
15	10278.70	30.77	12.01	8886.27	78.57	23.84
30	9296.89	75.52	20.41	8332.94	64.58	28.58
45	8282.59	58.35	29.10	7925.47	109.90	32.07
60	7373.06	83.56	36.88	6798.52	29.61	41.73
120	5059.86	20.45	56.68	4341.44	49.35	62.79
240	2734.64	31.57	76.59	1977.40	16.59	83.05
480	2194.72	45.24	81.21	1288.87	37.13	88.95
1000	1564.35	27.45	86.61	470.99	4.06	95.96
1440	1263.71	9.27	89.18	331.79	2.19	97.16
4320	1195.88	31.67	89.76	215.35	3.40	98.15

LOD: 0.015 ppb

Table S14. Residual Pb^{2+} concentration and recovery percentage (RE%) in the stock solutions of deionized water at an initial concentration of about 20 ppm analysed with the ICP-MS for a neat **SWCNT-BP** and **MTV-MOF/SWCNT-BP**.

Deionized water	**20 ppm**					
	SWCNT-BP			**MTV-MOF/ SWCNT-BP**		
Time	**^{208}Pb**	**SD**	**RE%**	**^{208}Pb**	**SD**	**RE%**
min	**ppb**	**ppb**		**ppb**	**ppb**	
0	19894.31	103.41	0	20075.97	160.99	0
1	19582.97	98.27	1.56	19189.61	71.63	4.42
5	19057.76	99.93	4.20	18607.41	141.64	7.32
10	18170.47	20.87	8.66	16868.83	34.74	15.98
15	17285.18	41.33	13.11	15931.28	68.36	20.65
30	15868.70	79.66	20.23	14554.07	62.64	27.51
45	14414.43	71.03	27.54	13845.39	108.80	31.04
60	12777.13	87.09	35.77	12470.18	33.16	37.89
120	9158.35	23.26	53.96	8165.90	49.84	59.33
240	6321.42	39.35	68.22	4873.44	18.25	75.73
480	5072.06	56.38	74.50	3072.62	32.30	84.70
1000	3564.07	36.54	82.08	1639.20	13.94	91.84
1440	3261.68	11.55	83.60	1071.05	21.71	94.67
4320	2943.37	32.96	85.20	583.20	13.09	97.10

LOD: 0.015 ppb

Table S15. Residual Pb^{2+} concentration and recovery percentage (RE%) in the stock solutions of deionized water at an initial concentration of about 30 ppm analysed with the ICP-MS for a neat **SWCNT-BP** and **MTV-MOF/SWCNT-BP**.

Deionized water	**30 ppm**					
	SWCNT-BP			**MTV-MOF/ SWCNT-BP**		
Time	**^{208}Pb**	**SD**	**RE%**	**^{208}Pb**	**SD**	**RE%**
min	**ppb**	**ppb**		**ppb**	**ppb**	
0	30592.33	170.56	0	30750.21	200.89	0
1	30131.44	149.96	1.51	29467.92	171.87	4.17
5	28849.97	81.74	5.70	28717.62	194.41	6.61
10	27498.93	108.79	10.11	26435.95	91.81	14.03
15	26048.44	32.43	14.85	25018.37	79.85	18.64
30	24411.60	83.95	20.20	22816.65	64.58	25.80
45	22467.36	77.89	26.56	20663.52	99.05	32.80
60	20497.74	96.64	33.00	19836.96	61.81	35.49
120	16121.79	50.44	47.30	13399.70	53.25	56.42
240	12873.25	19.21	57.92	11352.97	39.75	63.08
480	9612.29	25.36	68.58	7235.52	58.29	76.47
1000	8228.39	24.98	73.10	5433.56	16.57	82.33
1440	7779.28	17.39	74.57	3517.82	4.94	88.56
4320	6379.87	40.09	79.15	1872.68	6.79	93.91

LOD: 0.015 ppb

Table S16. Residual Pb^{2+} concentration and recovery percentage (RE%) in the stock solutions of deionized water at an initial concentration of about 60 ppm analysed with the ICP-MS for a neat **SWCNT-BP** and **MTV-MOF/SWCNT-BP**.

Deionized water	**60 ppm**					
	SWCNT-BP			**MTV-MOF/ SWCNT-BP**		
Time	**^{208}Pb**	**SD**	**RE%**	**^{208}Pb**	**SD**	**RE%**
min	**ppb**	**ppb**		**ppb**	**ppb**	
0	60613.57	848.74	0	61404.79	335.74	0
1	60084.94	945.96	0.87	59072.51	587.86	3.80
5	59722.59	233.57	1.47	58839.87	700.95	4.18
10	55905.96	548.36	7.77	55240.18	642.84	10.04
15	53100.83	219.80	12.39	52347.70	855.39	14.75
30	48269.77	360.10	20.36	47274.89	395.29	23.01
45	47370.00	316.06	21.85	45705.48	542.69	25.57
60	46804.67	680.68	22.78	44537.52	276.20	27.47
120	45148.24	519.83	25.51	39784.47	119.53	35.21
240	44589.97	296.20	26.44	37576.28	274.82	38.81
480	40889.64	309.04	32.54	36764.41	436.75	40.13
1000	37142.55	480.87	38.72	35121.33	393.62	42.80
1440	36200.65	319.02	40.28	28373.77	163.66	53.79
4320	35019.06	296.90	42.23	23027.28	86.58	65.50

LOD: 0.015 ppb

Table S17. Residual Pb^{2+} concentration and recovery percentage (RE%) in the stock solutions of deionized water at an initial concentration of about 100 ppm analysed with the ICP-MS for a neat **SWCNT-BP** and **MTV-MOF/SWCNT-BP**.

Deionized water	**100 ppm**					
	SWCNT-BP			**MTV-MOF/ SWCNT-BP**		
Time	**^{208}Pb**	**SD**	**RE%**	**^{208}Pb**	**SD**	**RE%**
min	**ppb**	**ppb**		**ppb**	**ppb**	
0	95711.39	1188.58	0	96764.29	1282.65	0.00
2880	68080.46	554.53	28.87	42239.43	632.01	56.35
4320	59830.82	523.85	37.49	34535.77	170.12	64.31

LOD: 0.015 ppb

Table S18. Residual concentration and recovery percentage (RE%) in a deionized water solution of Pb^{2+}, Fe^{3+}, and Al^{3+} with an initial concentration of about 1000 ppb for each metal ion, analyzed with the ICP-MS for a neat **SWCNT-BP**.

Deionized water 1000 ppb –SWCNT-BP									
Time	**27Al**			**^{57}Fe**			**^{208}Pb**		
min	**ppb**	**SD**	**RE%**	**ppb**	**SD**	**RE%**	**ppb**	**SD**	**RE%**
0	1079.88	35.69	0.00	1080.97	69.45	0.00	1003.06	0.84	0.00
1	1030.06	44.28	4.61	1036.74	4.83	4.09	948.20	5.86	5.47
5	967.30	50.18	10.43	1024.97	13.62	5.18	938.28	5.08	6.46
10	943.65	45.58	12.62	1005.34	21.05	7.00	897.30	7.01	10.54
15	929.39	36.07	13.94	987.95	11.49	8.61	819.78	4.13	18.27
30	923.95	53.84	14.44	973.12	9.51	9.98	719.24	3.71	28.30
60	869.36	12.81	19.49	869.21	5.24	19.59	549.81	3.57	45.19
120	605.91	33.41	43.89	862.06	5.80	20.25	213.46	2.64	78.72
240	350.20	23.12	67.57	755.27	7.81	30.13	92.66	0.19	90.76
480	222.99	14.81	79.35	706.14	10.71	34.67	90.03	0.10	91.02
1000	176.15	4.13	83.69	687.24	10.37	36.42	88.92	0.85	91.13
1440	153.99	2.22	85.74	552.13	1.82	48.92	86.68	0.44	91.36
4320	143.08	1.96	86.75	467.85	1.84	56.72	98.11	0.39	90.22

LOD: 0.015 ppb

Table S19. Residual concentration and recovery percentage (RE%) in a deionized water solution of Pb^{2+}, Fe^{3+}, and Al^{3+} with an initial concentration of about 1000 ppb for each metal ion, analyzed with the ICP-MS for a **MOF/SWCNT-BP**.

Deionized water 1000 ppb – MTV-MOF/SWCNT-BP									
Time	**^{27}Al**			**^{57}Fe**			**^{208}Pb**		
min	**ppb**	**SD**	**RE%**	**ppb**	**SD**	**RE%**	**ppb**	**SD**	**RE%**
0	1044.68	91.91	0.00	1003.38	171.95	0.00	1043.58	7.07	0.00
1	997.92	73.21	4.48	985.93	82.07	1.74	961.43	2.07	7.87
5	979.56	54.82	6.23	959.20	74.31	4.40	907.87	1.55	13.00
10	913.31	61.94	12.58	927.83	93.69	7.53	921.52	5.87	11.70
15	898.35	66.86	14.01	904.29	56.13	9.88	876.41	3.65	16.02
30	811.74	71.23	22.30	891.66	78.09	11.13	747.75	2.39	28.35
60	785.52	39.22	24.81	885.09	128.61	11.79	644.26	1.08	38.26
120	782.26	59.82	25.12	877.38	69.38	12.56	436.17	1.87	58.20
240	832.42	18.04	20.32	869.51	29.27	13.34	126.76	1.14	87.85
480	804.39	56.64	23.00	881.60	31.34	12.14	98.72	1.36	90.54
1000	849.08	34.31	18.72	844.93	10.29	15.79	75.84	1.30	92.73
1440	786.61	2.01	24.70	765.54	10.36	23.70	51.96	3.30	95.02
4320	619.76	4.84	40.67	701.51	18.72	30.09	22.91	1.25	97.80

LOD: 0.015 ppb

Table S20: $\log K_D$ values calculated for the lead initial concentrations of 1000 ppb and 10000 ppb in neat and multi-component (Pb, Fe, Al) solutions.

	Neat solution		**Multicomponent solution**	
ppb	**SWCNT-BPs**	**MTV-MOF/SWCNT-BPs**	**SWCNT-BPs**	**MTV-MOF/SWCNT-BPs**
1000	5.43	6.50	4.06	4.75
10000	4.04	4.82	3.99	4.59

Table S21. Residual concentration and recovery percentage (RE%) in a deionized water solution of Pb^{2+}, Fe^{3+}, and Al^{3+} with an initial concentration of about 10000 ppb for each metal ion, analyzed with the ICP-MS for a neat **SWCNT-BP**.

Deionized water 10000 ppb – SWCNT-BP									
Time	**^{27}Al**			**^{57}Fe**			**^{208}Pb**		
min	**ppb**	**SD**	**RE%**	**ppb**	**SD**	**RE%**	**ppb**	**SD**	**RE%**
0	10894.88	177.03	0.00	10195.31	123.64	0.00	10045.98	189.18	0.00
1	10569.59	167.83	2.99	10023.13	87.05	1.69	9581.26	118.97	4.63
5	10269.54	90.15	5.74	9877.82	142.85	3.11	9215.70	88.51	8.26
10	10109.34	99.40	7.21	9687.12	112.13	4.98	8997.05	107.92	10.44
15	9984.07	81.09	8.36	9436.66	101.42	7.44	8642.69	136.56	13.97
30	9580.62	68.80	12.06	9279.99	79.44	8.98	8349.39	91.71	16.89
60	9003.96	19.13	17.36	9182.30	58.40	9.94	6837.51	87.26	31.94
120	6400.81	36.00	41.25	9101.81	71.23	10.73	4388.23	109.00	56.32
240	3955.54	32.95	63.69	7987.70	56.48	21.65	2351.79	49.87	76.59
480	3785.62	50.79	65.25	7755.67	93.10	23.93	1941.53	51.89	80.67
1000	3660.85	43.60	66.40	7651.04	69.56	24.96	1345.34	89.85	86.61
1440	3226.73	23.41	70.38	5996.67	23.19	41.18	1149.98	46.27	88.55
4320	3511.46	33.65	67.77	5242.40	34.43	48.58	1140.42	41.23	88.65

LOD: 0.015 ppb

Table S22. Residual concentration and recovery percentage (RE%) in a deionized water solution of Pb^{2+}, Fe^{3+}, and Al^{3+} with an initial concentration of about 10000 ppb for each metal ion, analyzed with the ICP-MS for a **MTV-MOF/SWCNT-BP.**

Deionized water 10000 ppb - MTV-MOF/SWCNT-BP									
Time	**^{27}Al**			**^{57}Fe**			**^{208}Pb**		
min	**ppb**	**SD**	**RE%**	**ppb**	**SD**	**RE%**	**ppb**	**SD**	**RE%**
0	9924.42	191.09	0.00	10503.79	119.54	0.00	10435.77	68.69	0.00
1	9694.66	122.08	2.32	10259.29	82.70	2.33	9572.33	65.70	8.27
5	9472.30	58.24	4.56	10012.97	74.09	4.67	9478.74	34.53	9.17
10	9014.75	39.25	9.17	9983.21	61.65	4.96	8932.13	59.18	14.41
15	8444.53	68.60	14.91	9956.92	55.27	5.21	8547.07	66.47	18.10
30	8036.24	102.31	19.03	9616.56	78.95	8.45	7754.54	39.87	25.69
60	7418.42	92.17	25.25	8979.89	126.10	14.51	5688.65	40.79	45.49
120	7806.91	98.24	21.34	8764.83	97.76	16.56	3614.67	28.66	65.36
240	7408.55	80.45	25.35	8495.14	82.70	19.12	1321.64	19.39	87.34
480	7319.93	66.41	26.24	8321.98	53.38	20.77	1180.16	53.60	88.69
1000	7358.10	43.11	25.86	8049.31	22.88	23.37	567.44	20.50	94.56
1440	7158.16	60.09	27.87	7993.41	35.60	23.90	429.62	17.01	95.88
4320	6765.78	48.41	31.83	7702.12	18.25	26.67	327.15	18.48	96.87

LOD: 0.015 ppb

Table S23. Final residual Pb^{2+} concentration and recovery percentage (RE%) in the stock solutions of deionized water at an initial concentration of about 100000 ppb analysed with the ICP-MS for a neat **SWCNT-BP** and **MTV-MOF/SWCNT-BP** after five consecutive use/regeneration cycles. Cycle # 0 represents the initial Pb^{2+} concentration.

Deionized water	**100 ppm**					
	SWCNT-BP			**MTV-MOF/ SWCNT-BP**		
Cycle #	**^{208} Pb ppb**	**SD ppb**	**RE%**	**^{208} Pb ppb**	**SD ppb**	**RE%**
0	95711.39	1188.58	0	96764.29	1282.65	0
1	59830.82	523.85	37.49	34535.77	1129.08	64.31
2	62224.05	1136.78	34.98	36252.85	1345.10	62.54
3	64530.64	1017.12	32.58	37968.41	1109.76	60.76
4	68802.62	1256.44	28.11	40902.84	1066.28	57.73
5	71756.98	1456.75	25.03	43952.93	1239.76	54.58

LOD: 0.015 ppb

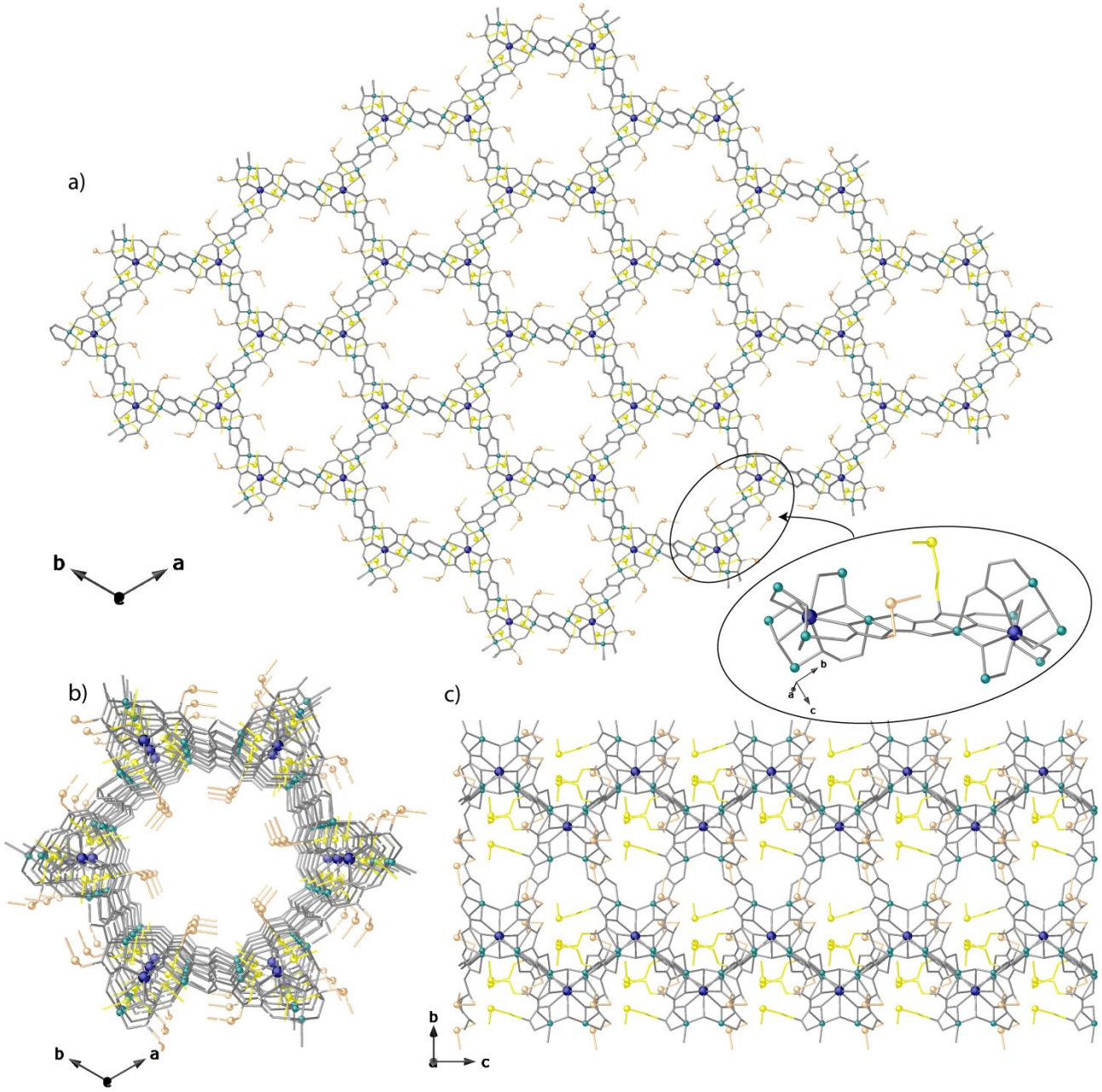

Figure S1. View along *c* crystallographic axis of the porous structure of {$Ca^{II}Cu^{II}_6$[(*S*,*S*)- methox]$_{1.50}$[(*S*,*S*)-Mecysmox]$_{1.50}$ $(OH)_2(H_2O)$} · $38H_2O$ **1**. (b) Perspective view along *c* crystallographic axis of a single channel of the MTV–MOF **1**. (c) View along [011] direction of a single channel of the crystal structure of MTV–MOF **1**. The crystallization water molecules are omitted for clarity. The inset shows the superimposed snapshot of mixed {Cu^{II}_2[(S,S)-methox/mecysmox]} dimers, on which crystallographic model of **1** is based. Organic ligands are depicted as gray sticks, whereas the amino acid residues are represented with the following color code: $–CH_2SCH_3$ (yellow) and $–CH_2CH_2SCH_3$ (orange). Calcium, copper, and sulfur atoms are shown as blue, cyan, and orange (for methylcysteine fragment)/yellow (for methionine fragment) spheres, respectively.

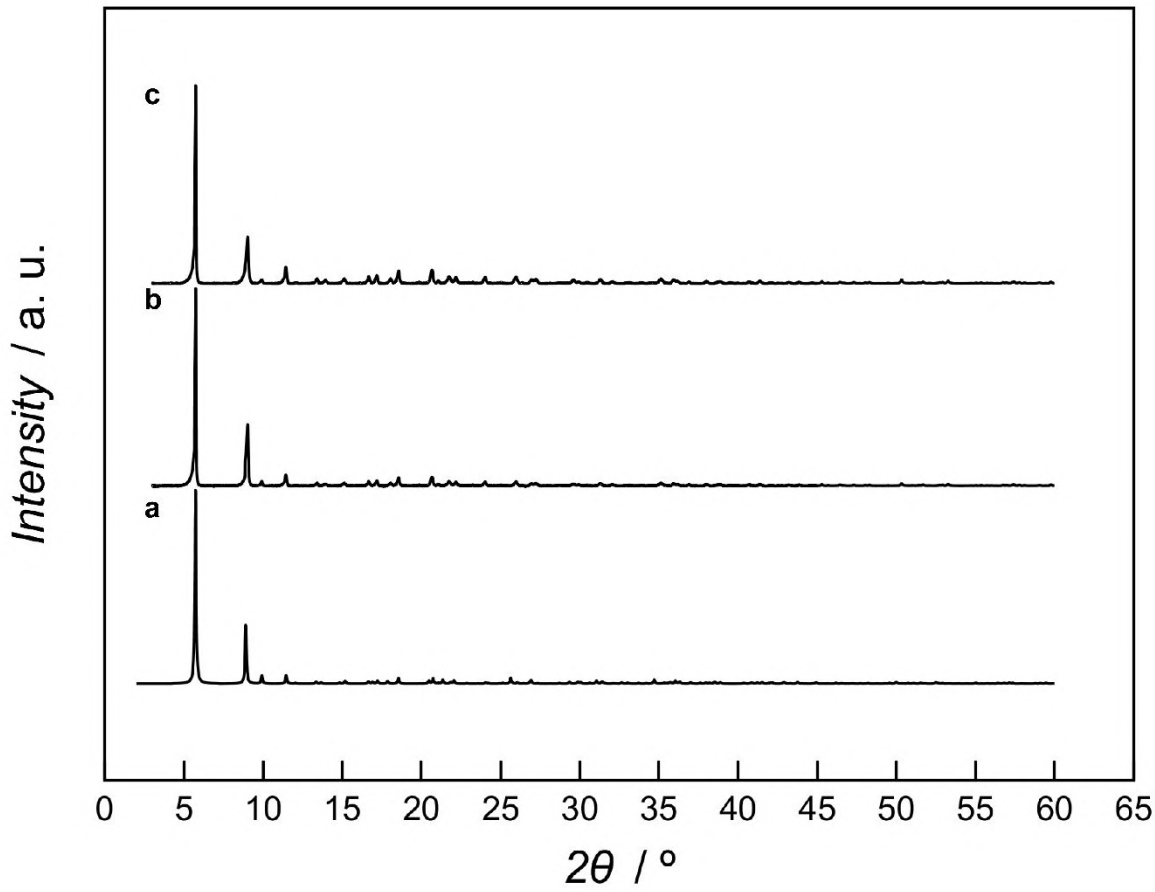

Figure S2. Theoretical (a) and experimental (b) PXRD pattern profiles of **1** in the 2θ range 2–60°. (c) Experimental PXRD pattern profile of **1**, in the 2θ range 2–60°, after the capture experiments with the polycrystalline sample.

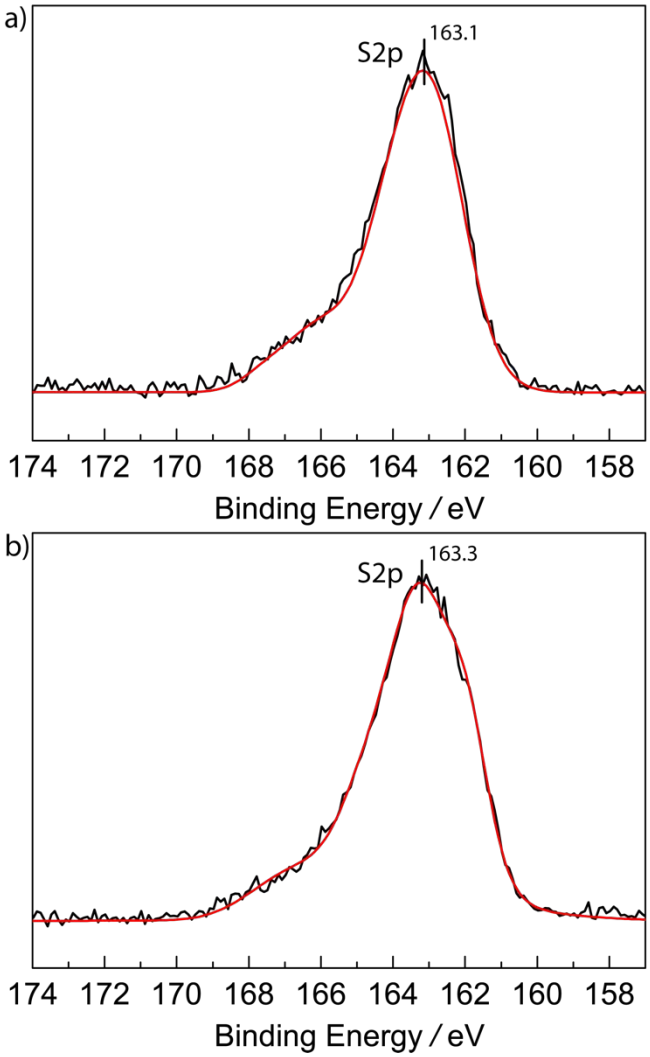

Figure S3. X–ray photoelectron spectroscopy (XPS) of a polycrystalline sample of **1** before (a) and after capture experiments (b).

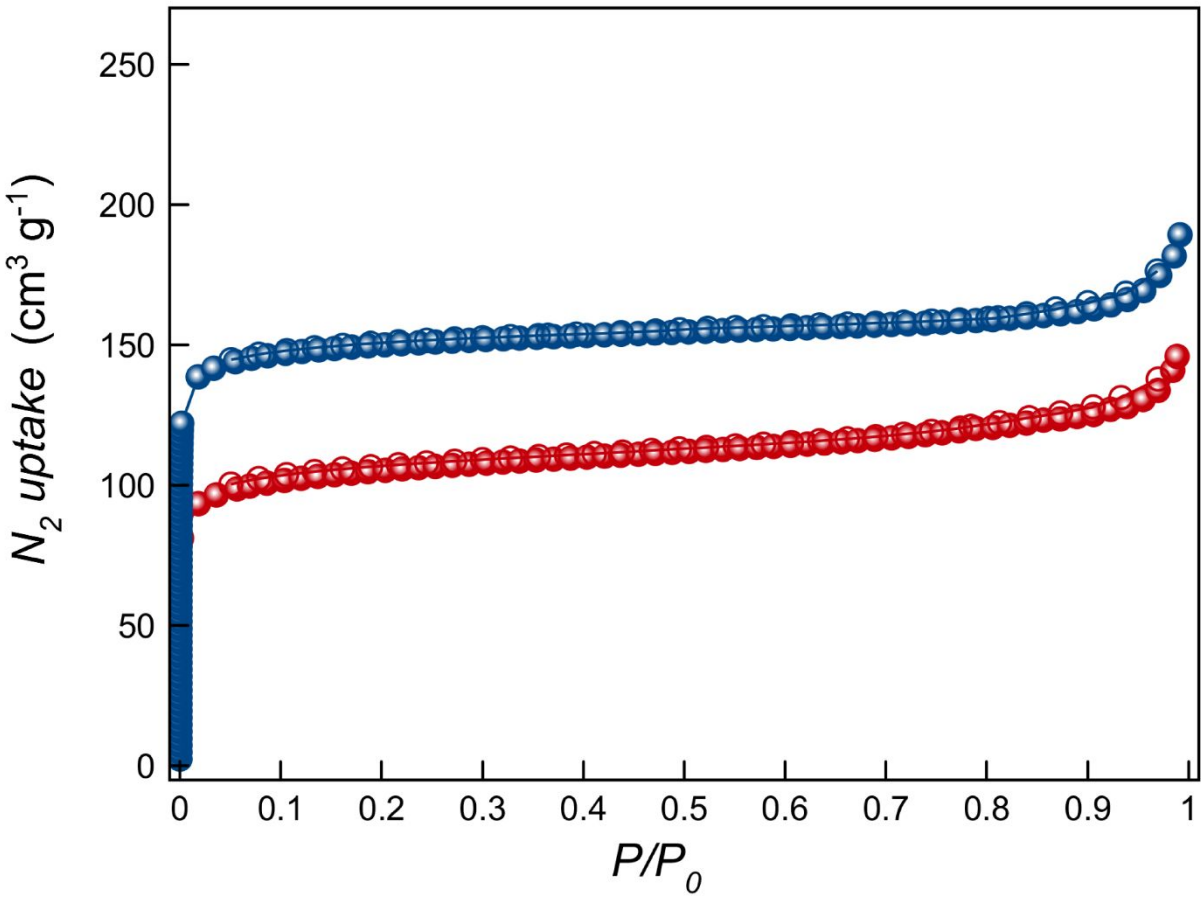

Figure S4. N_2 (77 K) adsorption isotherm for the activated compound **1** before (blue) and after (red) lead capture. Filled and empty symbols indicate the adsorption and desorption isotherms, respectively. The samples were activated at 348 K under reduced pressure for 19 h prior to carry out the sorption measurements.

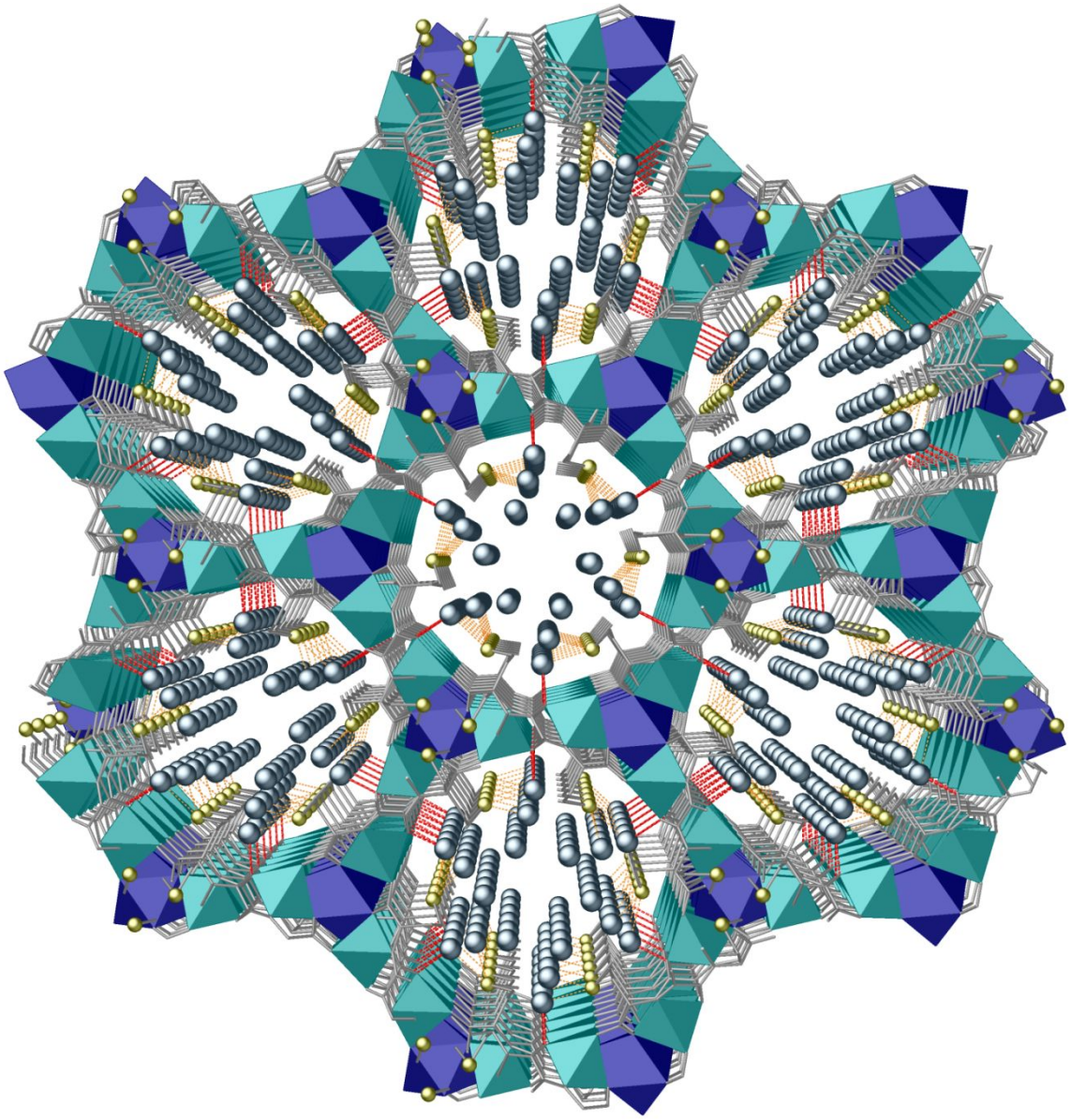

Figure S5. Perspective view along c crystallographic axis of $Pb(NO_3)_2$]@1 crystal structure, showing pores filled by Pb^{2+} metal ions. Color code: copper and calcium atoms from the network are represented by cyan and blue polyhedra, respectively, whereas organic ligands are depicted as grey sticks. Yellow and sky-blue spheres represent S and Pb atoms. S···Pb^{2+} and O···Pb^{2+} interactions are depicted by orange and red dashed lines, respectively.

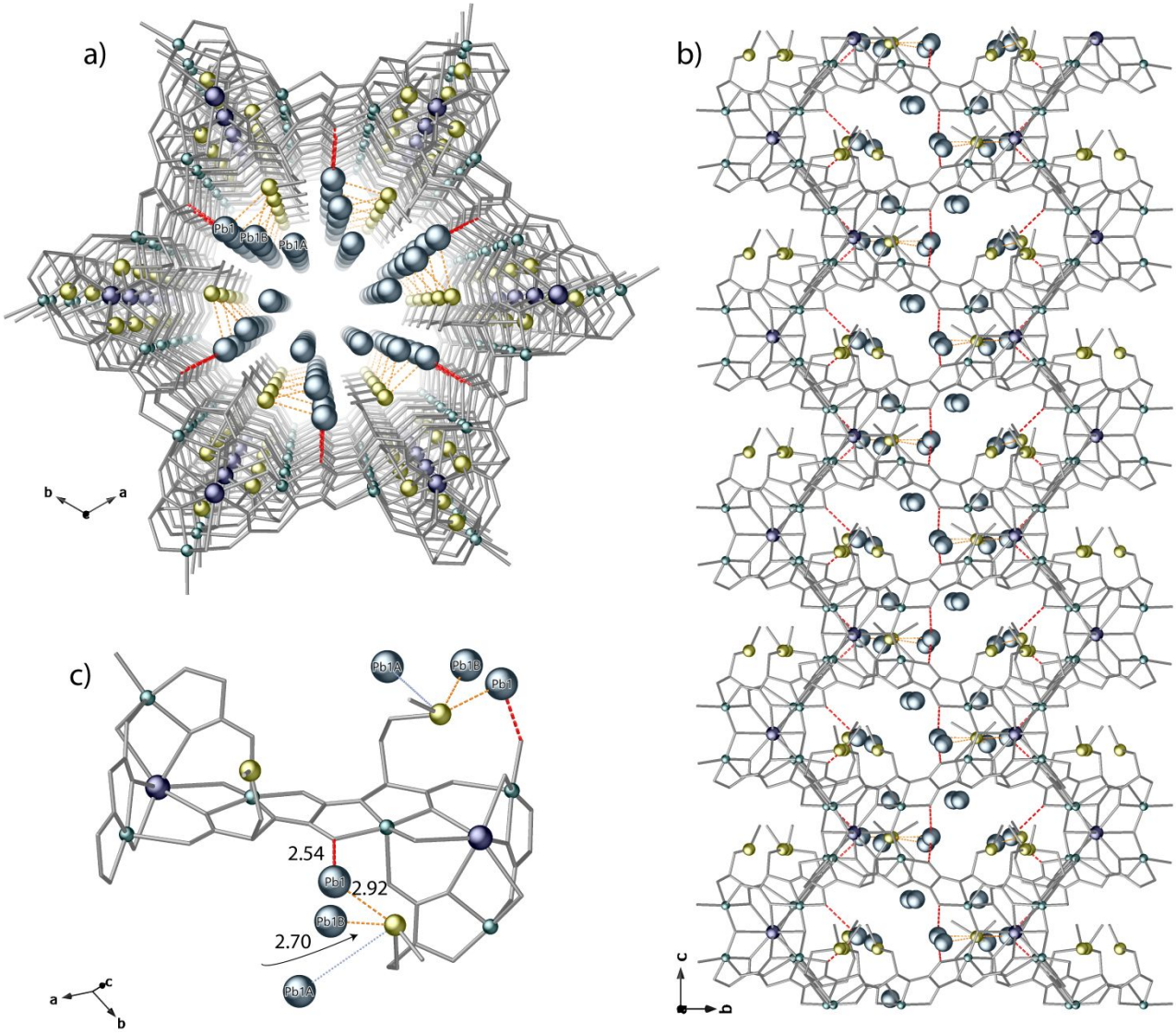

Figure S6. Details of **$Pb(NO_3)_2$]@1** crystal structure**:** perspective view along *c* and *a* crystallographic axis of a single pore filled by Pb^{2+} captured metal ions (a) and (b), respectively. (c) Details of Pb^{2+} interactions with sulfur atoms from methionine moieties and oxygen atoms of the oxamate core of the ligand. Color code: copper and calcium atoms from the network are represented by cyan and blue spheres, respectively, whereas organic ligands are depicted as grey sticks. Yellow and sky-blue spheres represent S and Pb atoms. S···Pb^{2+} and O···Pb^{2+} interactions are depicted by blue and red dashed lines, respectively.

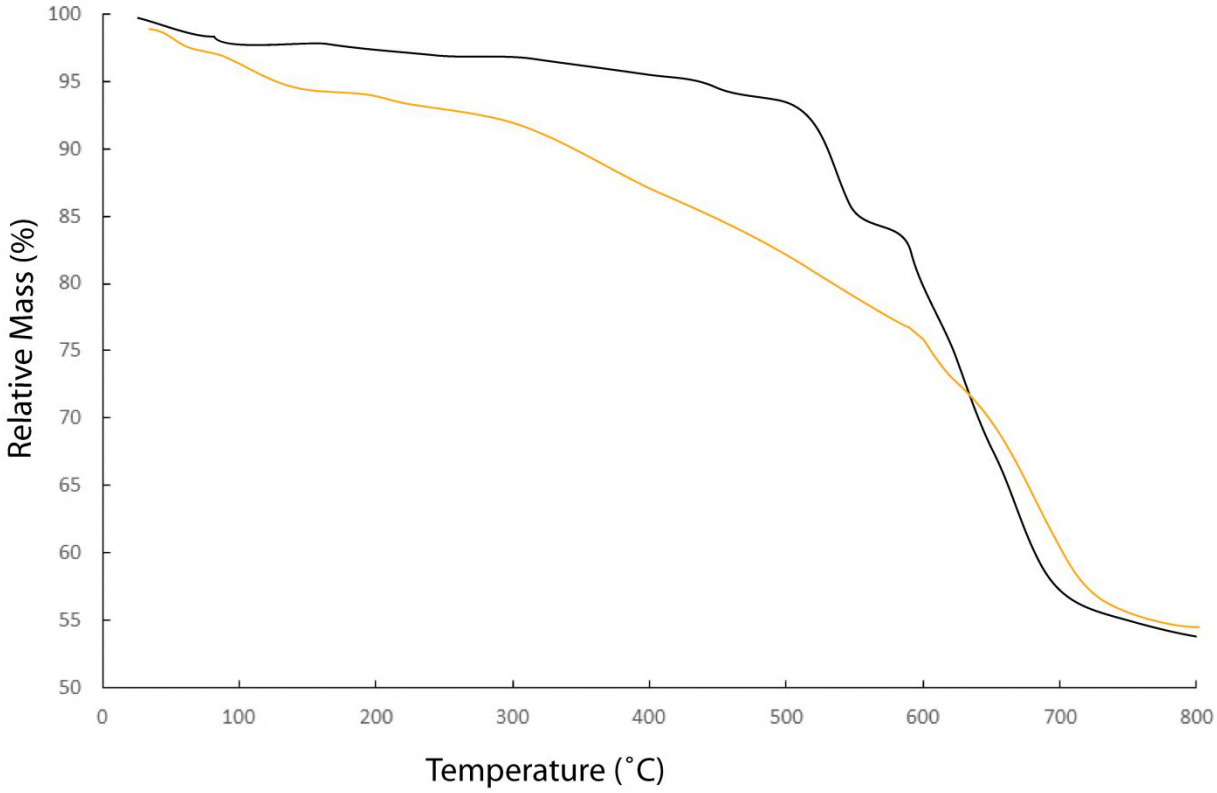

Figure S7. Thermal gravimetrical analyses of a **SWCNT-BP** (black) and a **MTV-MOF/SWCNT-BP** (orange). The initial relative mass change in **MTV-MOF/SWCNT-BP** up to 250 °C is due to solvent loss. The degradation of **SWCNT-BP** and **MTV-MOF/SWCNT-BP** is observed above 450 °C.

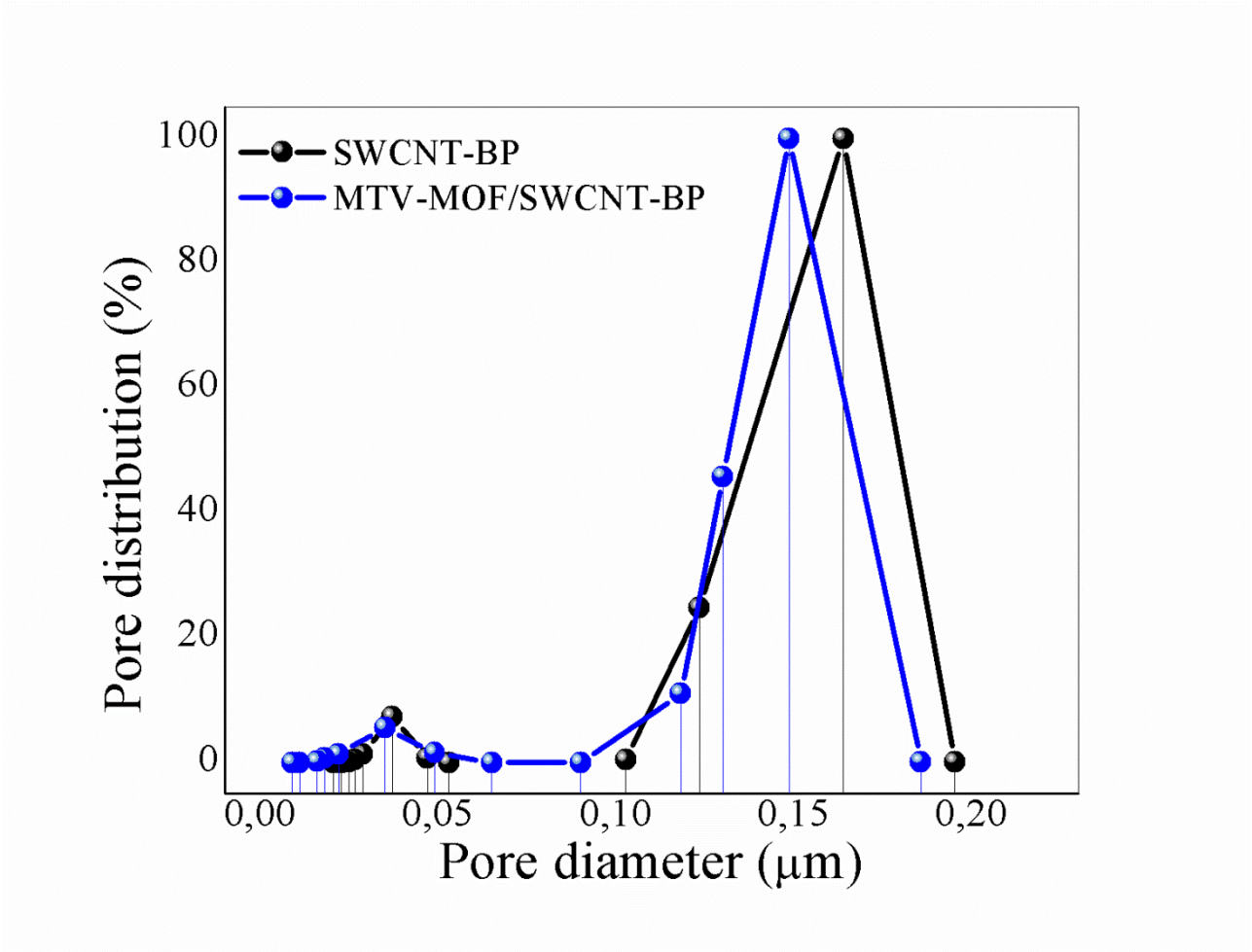

Figure S8. Pores distribution for **SWCNT-BP** and **MTV-MOF/SWCNT** membranes.

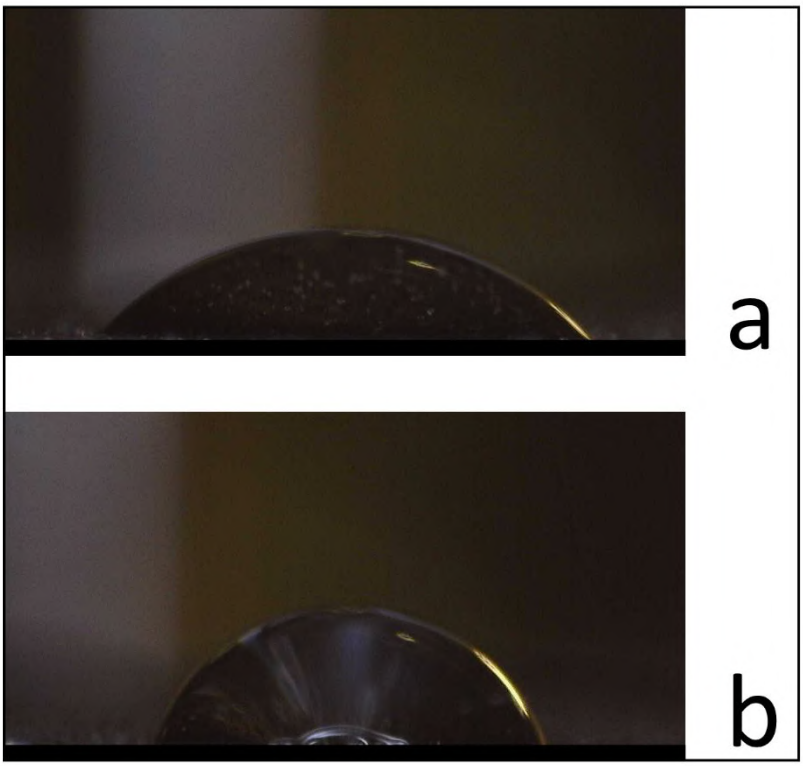

Figure S9. Average contact-angle value of: a) a **SWCNT-BP** (θ = 47.5° ± 0.5°) and b) a **MTV-MOF/SWCNT-BP** (θ = 78.5° ± 0.5°).

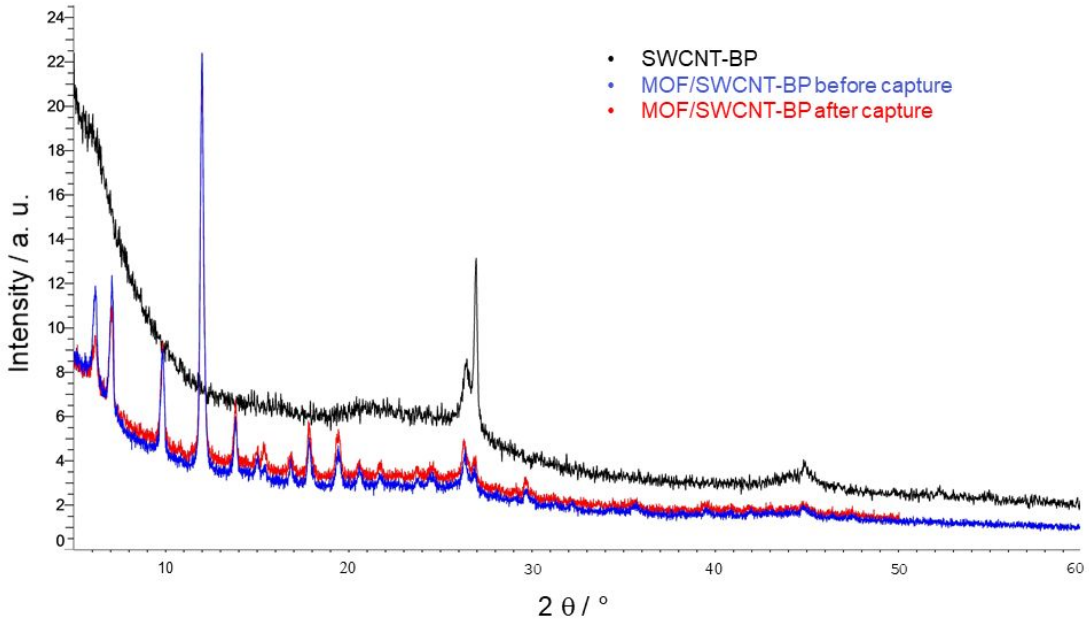

Figure S10. Experimental PXRD pattern profiles of **SWCNT-BP** (black) and **MTV-MOF/SWCNT-BP** membranes before (blue) and after capture and regeneration process (red line) in the 2θ range 2–60°.

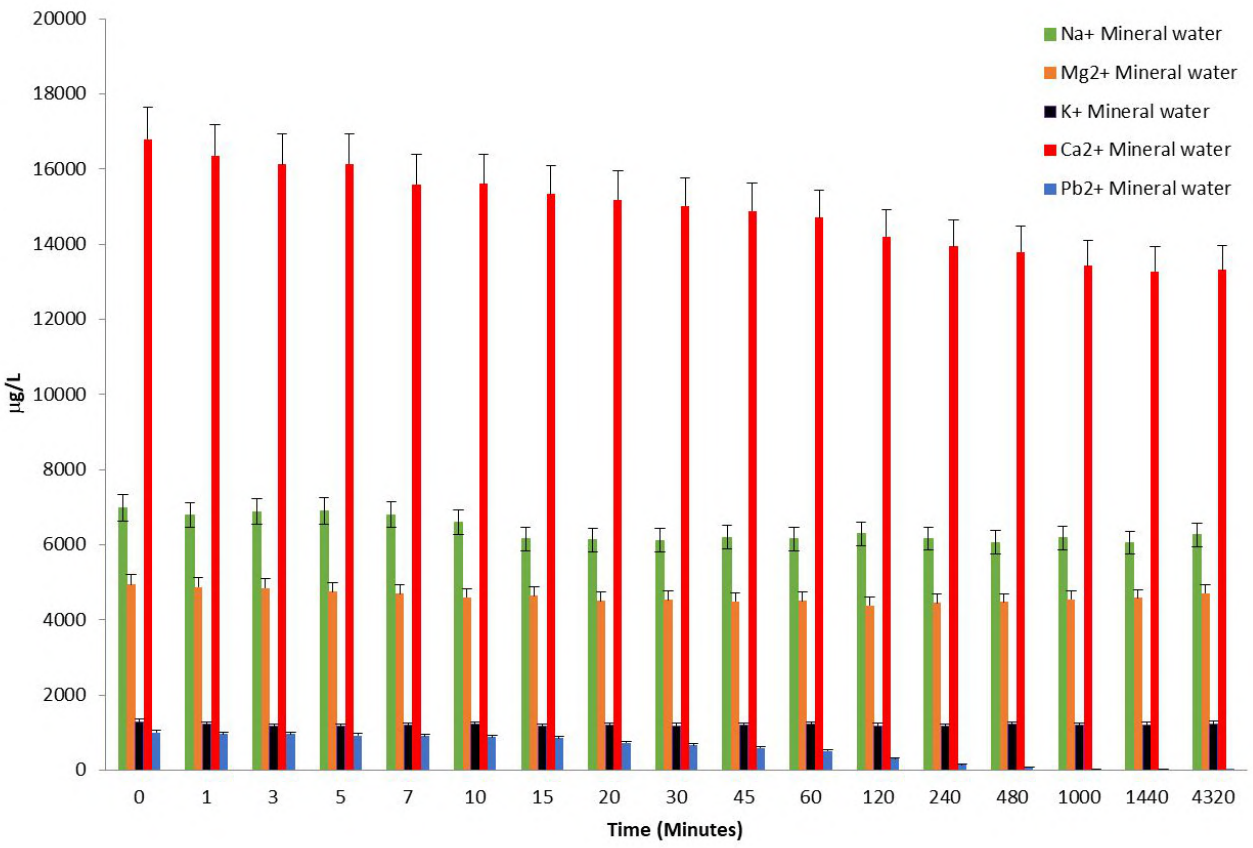

Figure S11. Kinetics and **s**electivity of neat **SWCNT-BP** membrane in mineral water solution with 1000 ppb of [Pb^{2+}]. (Data from Table S7)

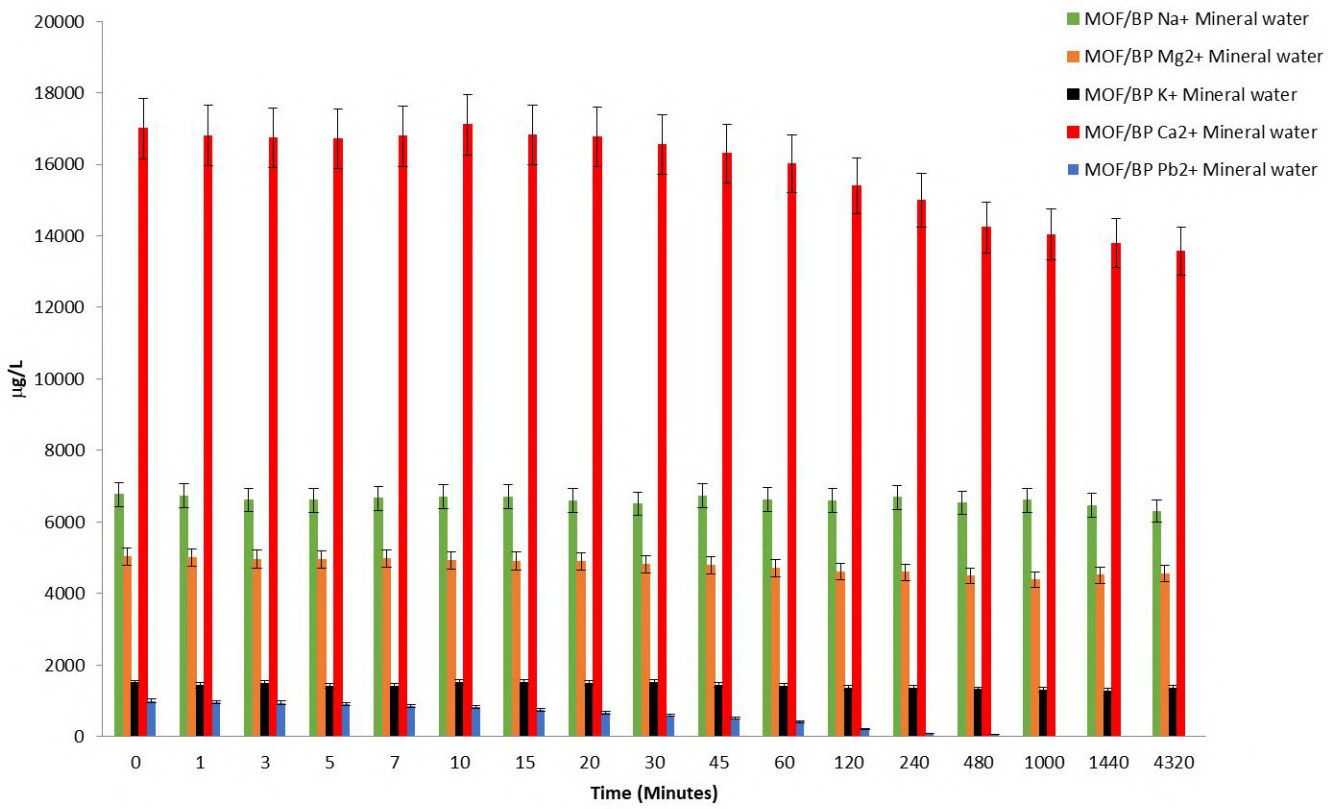

Figure S12. Kinetics and **s**electivity of **MTV-MOF/SWCNT-BP** in mineral water solution with 1000 ppb of [Pb^{2+}]. (Data from Table S8).

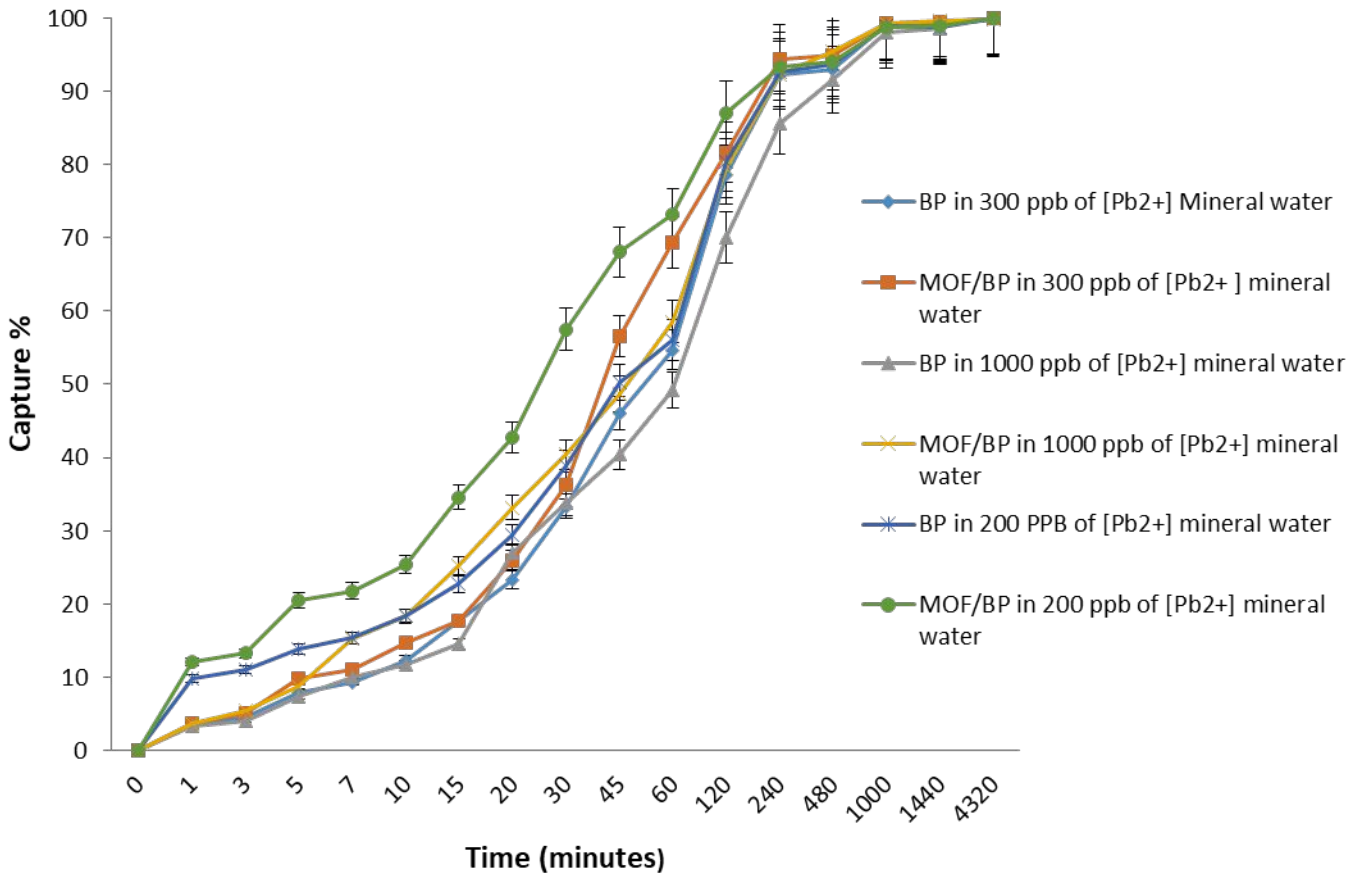

Figure S13. Capture % of Pb^{2+} by **SWCNT-BP** and **MTV-MOF/SWCNT-BP** in mineral water at 200, 300 and 1000 ppb. (Data from Tables S5-S10)

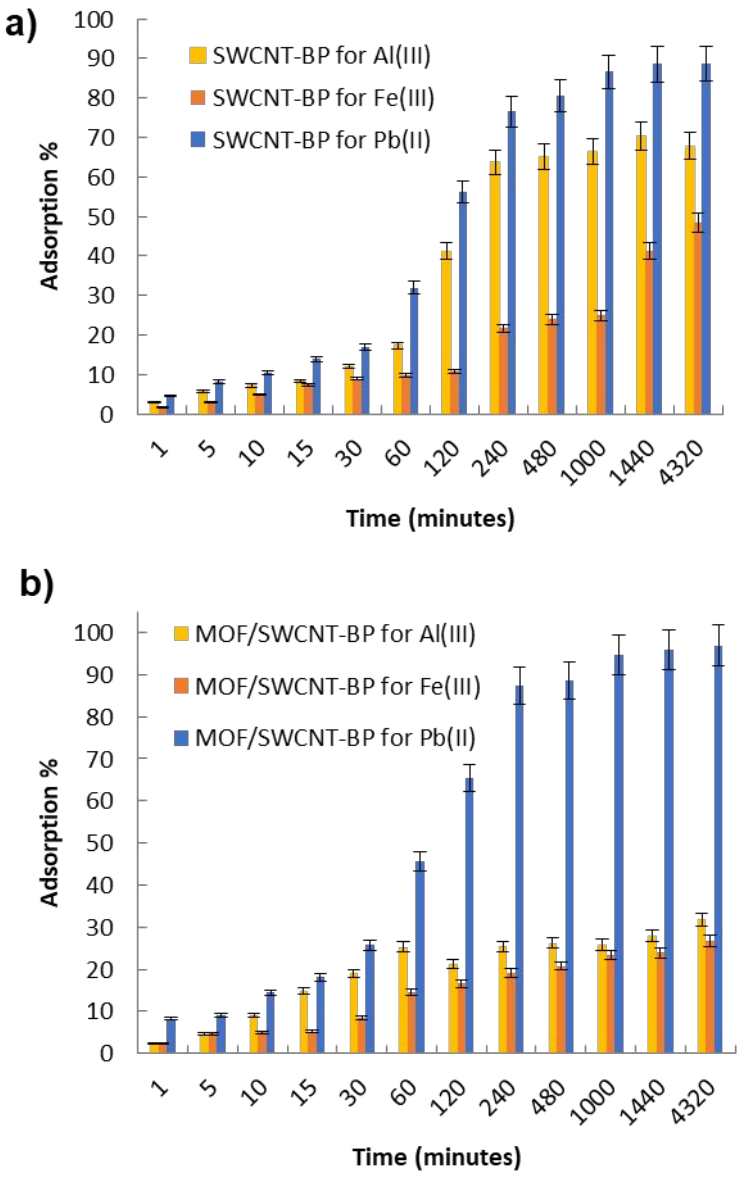

Figure S14. Data for selectivity in 10000 ppb of [Pb^{2+}], [Fe^{3+}], [Al^{3+}] solution for a **SWCNT-BP** (a) and **MTV-MOF/SWCNT-BP** membrane (b) soaked in a volume of 200 mL, in the 0-72 h interval. (Data from Tables S21-S22)

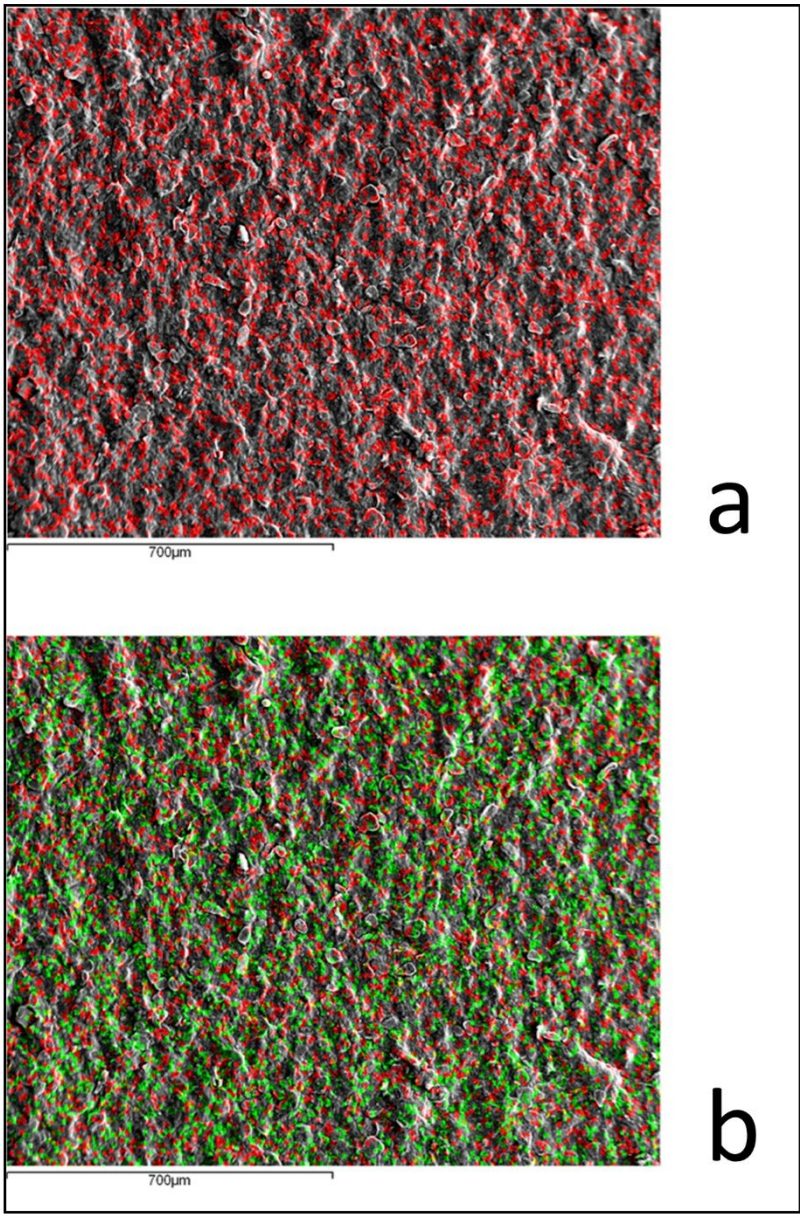

Figure S15. SEM image and the corresponding EDX elemental mapping for Cu and Pb elements from: a) SWCNT-BP and b) a **MTV-MOF/SWCNT-BP** after their use in the capture of Pb(II) (red dots). Green dots in (b) are due to Cu(II) atoms present in **MTV-MOFs**. Images confirm a homogeneous distribution of MTV-MOF in **SWCNT-BP** and a homogeneous adsorption in both membranes of Pb(II).

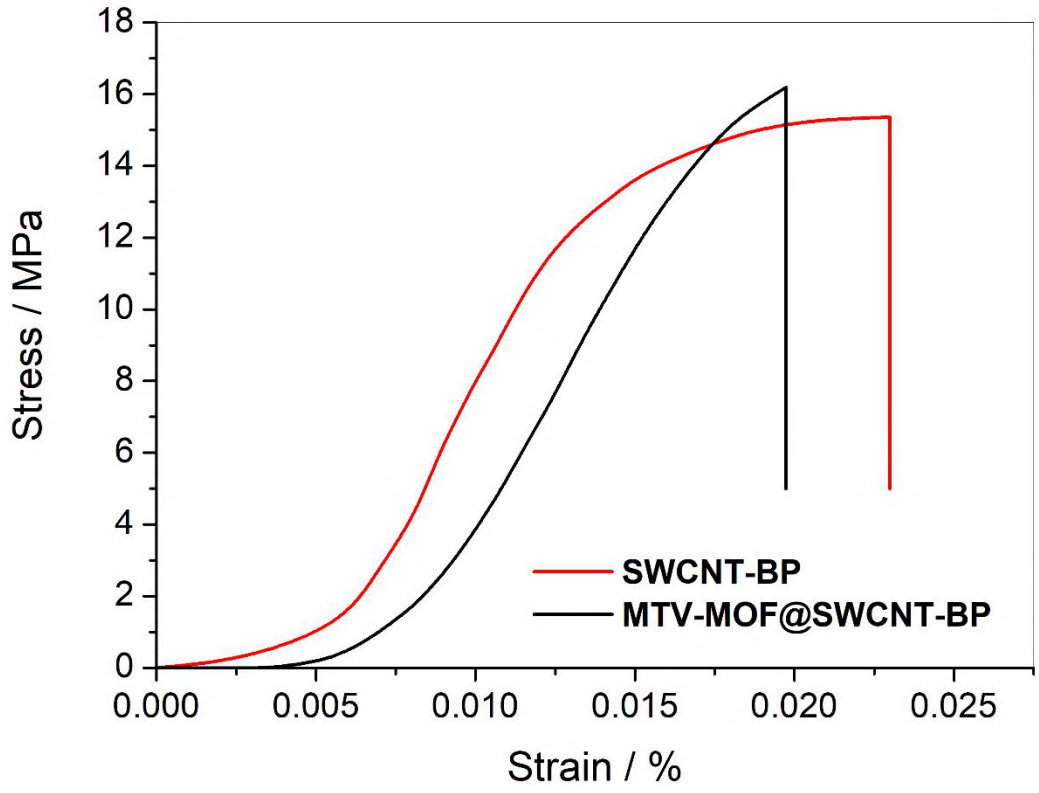

Figure S16. Stress-strain curve for a **SWCNT-BP** and a **MTV-MOF/SWCNT-BP**. The presence of MTV-MOF in SWCNT-BP causes a slight decrease in the Young's modulus from 1.65 ± 0.03 GPa (neat SWCNT-BP) to 1.54 ± 0.02 GPa (**MTV-MOF**/**SWCNT-BP**). Nevertheless, such magnitudes confirm the high mechanical stability of both membranes.

References:

1. Rahbari, M.; Goharrizi, A. S. Adsorption of Lead(II) from Water by Carbon Nanotubes: Equilibrium, Kinetics, and Thermodynamics. *Water Environment Research* **2009**, *81*, 598-607.

2. Forghani, M.; Azizi, A.; Livani, M.J.; Kafshgari, L. A. Adsorption of Lead(II) and Chromium(VI) from Aqueous Environment onto Metal-Organic Framework MIL-100(Fe): Synthesis, Kinetics, Equilibrium and Thermodynamics. *J. Solid State Chem.* **2020**, *291*, 121636.

3. OriginLab Corporation, Northampton, MA, USA.

4. Belhachemi, M.; Addoun, F. Comparative Adsorption Isotherms and Modeling of Methylene Blue onto Activated Carbons. *Appl. Water Sci.* **2011**, *1*, 111–117.

5. Sedeño-Díaz, J. E.; López-López, E.; Mendoza-Martínez, E.; Rodríguez-Romero, A. J.; Morales-García, S. S. Distribution Coefficient and Metal Pollution Index in Water and Sediments: Proposal of a New Index for Ecological Risk Assessment of Metals. *Water*, **2020**, *12*, 29.

6. US EPA 402-R-99-004A. Understanding Variation in Partition Coefficient, Kd, Values. Volume I - Kd Model, Measurement Methods, and Application of Chemical Reaction Codes. Office of Air and Radiation, Washington DC: USA 1999.

7. SAINT, version 6.45, *Bruker Analytical X-ray Systems, Madison, WI*, 2003.

8. Sheldrick, G. M. SADABS Program for Absorption Correction, version 2.10, *Analytical X-ray Systems, Madison, WI*, 2003

9. Sheldrick, G. M. Crystal structure refinement with SHELXL. *Acta Cryst.* **2015,** *C71*, 3-8.

10. Sheldrick, G. M. A short history of SHELX. *Acta Cryst*. **2008**, *A64*, 112–122.

11. SHELXTL-2013/4, *Bruker Analytical X-ray Instruments, Madison, WI*, 2013.

12. Spek, A. L. Structure validation in chemical crystallography *Acta Cryst*. **2009**, *D65*, 148-155.

13. Farrugia, L. J. WinGX and ORTEP for Windows: An Update. *J. Appl. Crystallogr*. **2012**, *45*, 849–854.

14. Palmer, D. C. Zeitschrift fur Krist. *Cryst. Mater*. **2015**, *230*, 559–572.

Chapter 8

molecules

MDPI

Article

GO-SWCNT Buckypapers as an Enhanced Technology for Water Decontamination from Lead

Mariafrancesca Baratta [1,†], Antonio Tursi [1,†], Manuela Curcio [2], Giuseppe Cirillo [2], Fiore Pasquale Nicoletta [2,*] and Giovanni De Filpo [1,*]

[1] Department of Chemistry and Chemical Technologies, University of Calabria, 87036 Rende, Italy; mariafrancesca.baratta@unical.it (M.B.); antonio.tursi@unical.it (A.T.)
[2] Department of Pharmacy, Health and Nutritional Sciences, University of Calabria, 87036 Rende, Italy; manuela.curcio@unical.it (M.C.); giuseppe.cirillo@unical.it (G.C.)
* Correspondence: fiore.nicoletta@unical.it (F.P.N.); giovanni.defilpo@unical.it (G.D.F.); Tel.: +39-09-8449-3194 (F.P.N.); +39-09-8449-2105 (G.D.F.)
† These authors contributed equally to this work.

Abstract: Water decontamination is an important challenge resulting from the incorrect disposal of heavy metal waste into the environment. Among the different available techniques (e.g., filtration, coagulation, precipitation, and ion-exchange), adsorption is considered the cheapest and most effective procedure for the removal of water pollutants. In the last years, several materials have been tested for the removal of heavy metals from water, including metal-organic frameworks (MOFs), single-walled carbon nanotubes (SWCNTs), and graphene oxide (GO). Nevertheless, their powder consistency, which makes the recovery and reuse after adsorption difficult, is the main drawback for these materials. More recently, SWCNT buckypapers (SWCNT BPs) have been proposed as self-standing porous membranes for filtration and adsorption processes. In this paper, the adsorption capacity and selectivity of Pb^{2+} (both from neat solutions and in the presence of other interferents) by SWCNT BPs were evaluated as a function of the increasing amount of GO used in their preparation (GO-SWCNT buckypapers). The highest adsorption capacity, 479 ± 25 mg g^{-1}, achieved for GO-SWCNT buckypapers with 75 wt.% of graphene oxide confirmed the effective application of such materials for cheap and fast water decontamination from lead.

Keywords: lead; heavy metals; single-walled carbon nanotubes; graphene oxide; buckypaper; adsorption

Citation: Baratta, M.; Tursi, A.; Curcio, M.; Cirillo, G.; Nicoletta, F.P., De Filpo, G. GO-SWCN Buckypapers as an Enhanced Technology for Water Decontamination from Lead. *Molecules* **2022**, *27*, 4044. https://doi.org/10.3390/molecules27134044

Academic Editor: Giorgio Vilardi

Received: 30 May 2022
Accepted: 21 June 2022
Published: 23 June 2022

1. Introduction

The incorrect disposal of heavy metal waste from different industrial plants represents a serious hazard for human health and the environment because pollutants can seriously contaminate, even at low doses, freshwater resources essential for all lifeforms [1–4]. Lead is the most frequently found heavy metal in contaminated water resources and, because of its bioaccumulation, can cause several human health problems, including damage to muscles, bones, kidneys, the nervous system, and cancer [5–7]. The World Health Organization fixed in 0.01 mg L^{-1} (10 ppb) the lead ions provisional guideline value for drinkable water [8]. Many technologies, including bio-treatments [9], membrane filtration [10], photocatalysis [11], ion exchange membranes [12], coagulation/chemical precipitation [13], electrochemical technologies [14], and oxidation/reduction [15], have been proposed in order to move heavy metal, and lead in particular, concentrations within the suggested limits from plant effluents. Nevertheless, some drawbacks affect these processes, such as slow and poor removal efficiencies, toxic by-products, and high costs [16,17], which can be generally bypassed by adsorption methods. In fact, adsorption processes are inexpensive and easy to perform and reuse, with no by-products [18].

Several adsorbents have been proposed for the removal of heavy metals from waste-water including activated carbon [19], clays and zeolites [20,21], nanoparticles [22,23], organic resins and polymers [24], metal oxides [25], agricultural waste products [26,27], zero-valent ions [28]. More recently, other materials have been investigated as efficient adsorbents for heavy metals ions, including single and multiwalled carbon nanotubes (SWCNTs and MWCNTs) [29–31], graphene oxides (GOs) [32–34], and organic metal frameworks (MOF) [35,36] as either single components or in mixtures. Despite their enhanced adsorption properties, due to their large surface area, porosity, and the possibility of tuning their interactions with the target pollutants by easy functionalization [37], these materials lack the possibility of easy recovery and regeneration after use due to their powdery consistency. Consequently, several researchers have tried to overcome such drawbacks by assembling such materials in buckypapers (BPs) [38–40].

BPs are films formed by CNTs and CNT bundles self-assembled mainly by π–π and van der Waals interactions [41,42]. Due to such self-standing properties, they are also known as CNT films or CNT papers. In addition, BPs are characterized by a porous structure, low density, and interesting thermal, rheological, and electrical properties [43]. In order to enhance their properties, BPs are used to host other materials such as MOF [36,44] and GO [42,45], leading to the formation of composite materials with superior performance in different fields such as flexible sensors [45], batteries [46], smart packaging [47], artificial muscles [48], fire retardant [49], and membrane-based processes, namely desalinization and catalysis [40,50]. In the literature, few works deal with the application of composite BPs as adsorbent membranes. Recently, SWCNT BPs incorporating MOFs have been proposed as boosted adsorbents for the recovery of rare-earth elements [44] and the selective capture of lead [36] from wastewater. The presence of MOF in SWCNT BPs was found to be beneficial for the adsorption of all tested lanthanides, with the Ce^{3+} recovery reaching the value of 263.30 mg of cerium adsorbed per gram of MOF-SWCNT BP. This was related to the alcohol functionalities of threonine within MOF pores. Similarly, the lead adsorption capacity of neat BPs increased by 42% when 25 wt.% SWCNTs were substituted by MOFs. Moreover, stable BPs for the adsorption of heavy metal ions were obtained by the noncovalent interaction of oxidized CNTs with GO [51]. The presence of nanotubes stabilized the mechanical properties of BPs but reduced the adsorption capacities for all tested heavy metals. In particular, the experimental lead adsorption capacity by BPs with GO content up to 90 wt.% was lower than the experimental maximum loading capacity by neat CNT BPs (163 ± 10 mg g^{-1}) due to the presence of micro- and nano-channels among entangled CNTs.

In this paper, single-walled carbon nanotube/graphene oxide buckypapers (GO-SWCNT BPs) were prepared and characterized as novel membranes for the adsorption of lead from wastewater. The adsorption capacity and selectivity towards Pb^{2+} (both from neat solutions and in the presence of other interferents) by GO-SWCNT BPs were evaluated as a function of the increasing percentage (wt.) of GO used in their preparation. Hybrid membranes showed high lead adsorption capacity and interesting removal properties towards other heavy metal ions, allowing the possibility of multielement decontamination of wastewater.

2. Results

SWCNT BPs and GO-SWCNT BPs were prepared according to the wet method [52,53], including the uniform dispersion of carbonaceous compounds in a surfactant solution, vacuum filtration through a PTFE porous filter (average pore size 5 μm), several washes with methanol, drying, and, finally, peeling off from the PTFE filter.

Under the used conditions reported in the Materials and Methods section, the wet method provided self-standing and flexible BP disks for GO loadings up to 75 wt.% (Figure 1) due to the π–π and van der Waals interaction forces between SWCNTs and GOs. Unfortunately, larger GO amounts gave cracked films (see 85% GO-SWCNT BP picture in Figure 1e). Consequently, successive investigations were limited to BP samples with a maximum GO loading of 75 wt.% (0, 25, 50 and 75 wt.% GO).

As shown in Figure 1f, BPs were characterized by easy detachability from porous PTFE filter and self-sustainability for all studied GO wt. percentages. BPs were flexible disks with an average thickness of around 100 ± 2 μm and an average diameter of 38 ± 1 mm.

Figure 2 shows the morphology of neat SWCNT BP and GO-SWCNT BPs with different GO content (25, 50, and 75 wt.%). SWCNT BP morphology was characterized by the presence of the typical SWCNT bundles and clusters arising from π–π and van der Waals interactions. The found porous structure is expected to give BPs a high permeability and a large contact surface area for heavy metal adsorption. The addition of an increasing amount of GO in SWCNT BPs resulted in increased GO sheets number homogenously hosted inside the membranes.

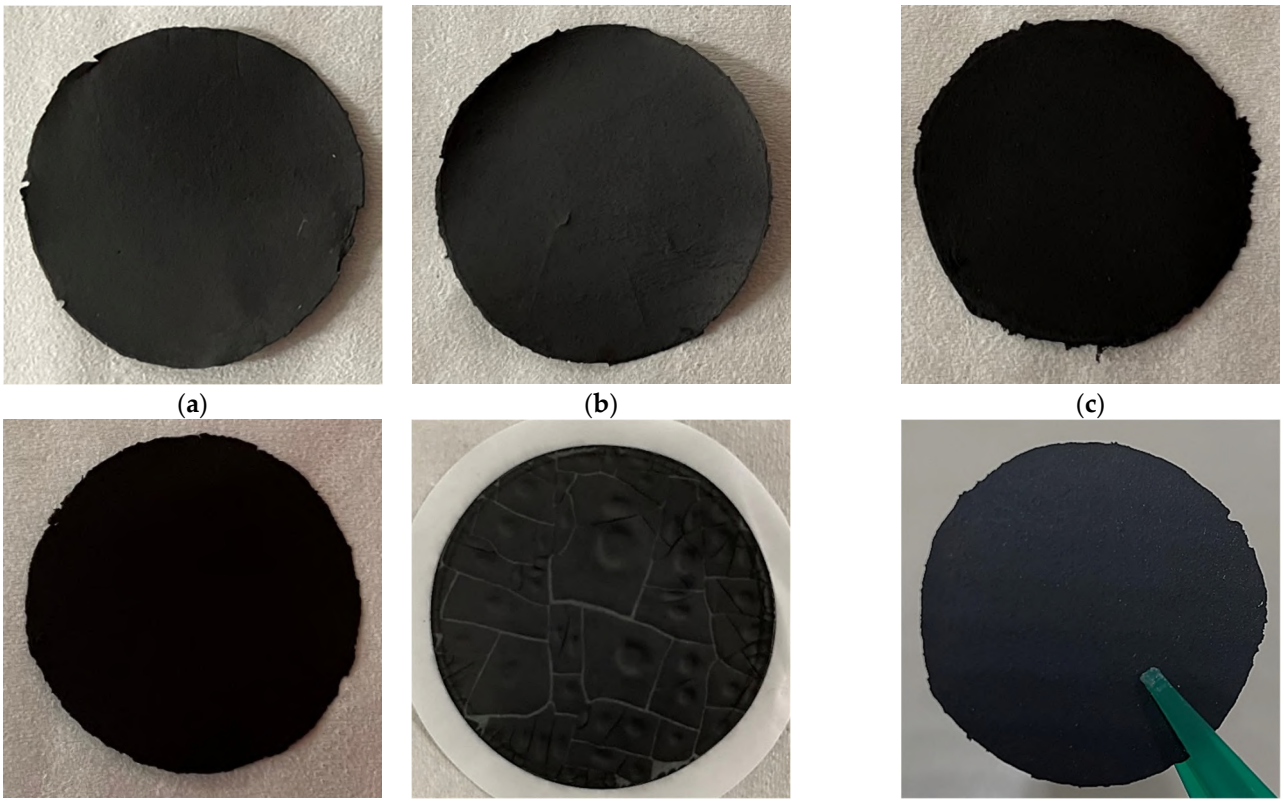

Figure 1. Pictures of (**a**) SWCNT BP, (**b**) 25% GO-SWCNT BP, (**c**) 50% GO-SWCNT BP, (**d**) 75% GO-SWCNT BP, and (**e**) 85% GO-SWCNT BP. All samples, except for 85% GO-SWCNT BP (which showed evident macroscopic cracks), were easy detachable from the porous PTFE filter and resulted in (**f**) self-sustainable and flexible disks.

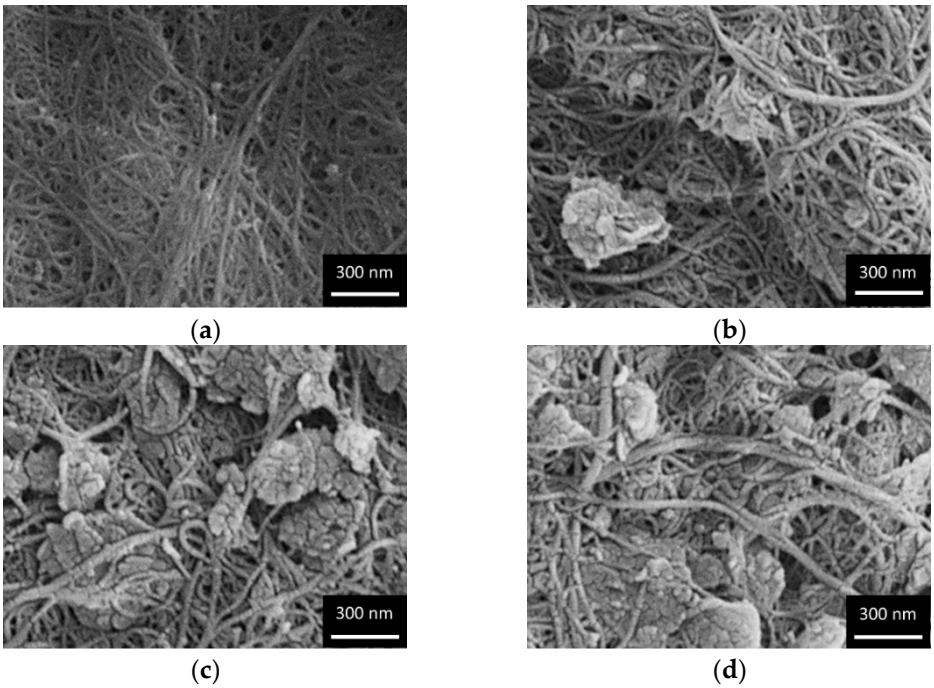

Figure 2. SEM images of (**a**) SWCNT BP, (**b**) 25% GO-SWCNT BP, (**c**) 50% GO-SWCNT BP, and (**d**) 75% GO-SWCNT BP, showing the presence of GO flakes homogeneously embedded in the SWCNT BP network.

Nevertheless, the increasing the number of empty spaces around the GO sheets for BP with higher GO loadings is expected to lead to more fragile BPs with lower mechanical properties. In fact, even if all samples looked like very similar free-standing membranes, both from a macroscopic and microscopic point of view, they were found to be characterized by decreasing values of tensile strength and fracture strain, as reported in Figure 3 and Table 1.

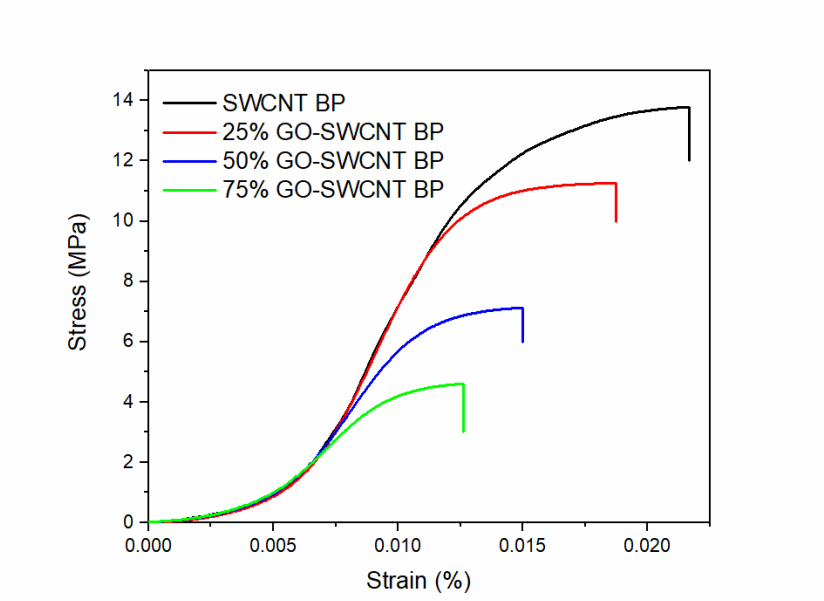

Figure 3. Stress-strain curves of SWCNT BP with different weight percentage of GO.

Despite the slight reduction in the mechanical properties, all investigated BPs can be considered highly stable membranes, and could find important application in adsorption treatments for wastewater.

The increase in GO content was also found to modify the hydrophilicity of BP top surfaces. As shown in Table 1, SWCNT BPs were characterized by lower hydrophilicity (average water contact-angle of 71.3° ± 0.5°) than GO-SWCNT BPs, which showed a gradual decrease in the water contact-angle values from 62.6° ± 0.5° (25% GO-SWCNT BP) to 41.2° ± 0.5° (75% GO-SWCNT BP). Obviously, it is expected that the decrease in water contact-angle values could make GO-SWCNT BPs more effective devices for wastewater treatments than neat SWCNT BPs due to easier wettability. On the contrary, the porosity percentage found for BPs decreased for larger GO amounts due to closer packing between GO sheets.

Table 1. Mechanical properties, water contact-angles, and the porosity of SWCNT BP with different weight percentage of graphene oxide (GO).

Sample	Tensile Strength (MPa)	Fracture Strain (%)	Water Contact-Angle (°)	Porosity (%)
SWCNT BP	13.8 ± 0.9	2.2 ± 0.5	71.3 ± 0.5	74 ± 5
25% GO-SWCNT BP	11.3 ± 0.8	1.9 ± 05	62.6 ± 0.5	70 ± 5
50% GO-SWCNT BP	7.2 ± 0.6	1.5 ± 0.4	51.2 ± 0.5	65 ± 5
75% GO-SWCNT BP	4.7 ± 0.6	1.3 ± 0.4	41.2 ± 0.5	59 ± 5

The lead removal properties of SWCNT and GO-SWCNT membranes were evaluated through adsorption experiments. Membrane disks were immersed in 800 mL beakers with $Pb(NO_3)_2$ water solutions at different lead concentrations (1, 10, and 50 ppm). The kinetic profiles of lead recovery in the 0–72 h interval, are reported in Figure 4.

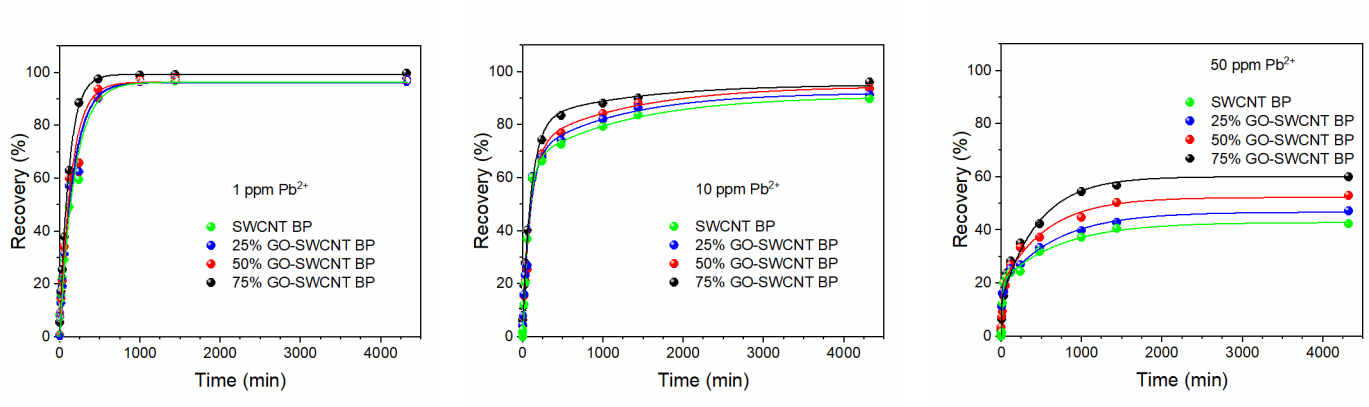

Figure 4. Pb^{2+} recovery by neat SWCNT BP and GO-SWCNT BPs during soaking in 800 mL of aqueous solutions with [Pb^{2+}] of: (**a**) 1 ppm, (**b**) 10 ppm, and (**c**) 50 ppm.

All membranes were able to recover almost 100% of the lead present in the 1 ppm solutions, as seen in Figure 4a. The residual lead concentration was always lower than 10 ppb (7.2, 5.6, 4.6, and 3.1 ppb, respectively for increasing GO amounts), which represents an acceptable limit for drinking water [8]. In particular, 75% GO-SWCNT BPs were able to remove almost all lead ions present in the 1 ppm solution within 8 h. However, slightly different recoveries (ranging from 85% to 95% for increasing GO amounts) were found when 10 ppm lead solution was used (Figure 4b), confirming the positive effect of GO substitution on the adsorption properties of hybrid membranes. For larger concentrations (50 ppm), the lead recovery varied from 42.18% (SWNT BPs) to 47.19%, 53.02%, and 59.95% for GO amounts of 25, 50, and 75 wt.%, respectively. Such results gave a lead adsorption capacity per unit of adsorbent mass of 337 ± 13, 377 ± 9, 424 ± 13, and 479 ± 25

mg g^{-1}, and confirmed again the best adsorption capacity shown by 75% GO-SWCNT BPs. The obtained adsorption capacity per unit of adsorbent mass is larger than the values recently found for the lead removal by MOF powders (108 mg g^{-1}) [54] and BP membranes hosting MOF (310 mg g^{-1}) [36] but lower than the lead adsorption capacity by GO flakes (555 mg g^{-1}) [54]. It is worth noting that, despite the slight reduction in the adsorption capacity (−15%) due to the presence of SWCNTs, 75% of GO-SWCNT BPs are self-standing films, which can be more easily used, recovered, and regenerated than any powder-like adsorbent (see *infra*). The adsorbent physicochemical properties, such as water wettability, surface area, and chemical nature, can affect the adsorption of heavy metals in addition to the operating conditions (e.g., adsorbent amount, temperature, pH and ionic strength values, adsorption time, initial concentration, and interferent presence). The presence of surface functional groups, such as hydroxyl and carboxyl, can improve wettability and heavy metal chelation. Therefore, the increased lead adsorption capacity shown by GO-SWCNT BPs with larger amounts of GO (from 42.18% for SWNT BPs to 59.95% for 75% GO-SWCNT BP) can be attributed to the beneficial presence of functional groups able to enhance membrane wettability and metal chelation and overcome the possible drawbacks due to the reduced porosity (see Table 1).

The beneficial substitution of SWCNT with GO in BPs was further confirmed through kinetic experiments. From the literature [36,38], it is known that the rate equation for Pb^{2+} capture in solutions follows the Lagergren first-order Equation (1):

$$\frac{dq_t}{dt} = k_1(q_e - q_t) \quad (1)$$

where k_1 and q_e are the Lagergren adsorption rate constant (min^{-1}) and the lead adsorption capacity per unit of adsorbent mass (mg g^{-1}) at equilibrium, respectively. The experimental concentrations measured as a function of time, $C(t)$, were used to determine the experimental amount, $q_{exp}(t)$, (mg g^{-1}) of lead adsorbed by BPs, according to the following Equation (2):

$$q_{exp}(t) = \frac{C_0 - C(t)}{m} \times V \quad (2)$$

where C_0 and $C(t)$ are the lead concentration in the solution at time zero and t, respectively. V is the volume of lead solution, and m is the mass of BPs.

Experimental data were well-fitted (R^2 values always larger than 0.975) by non-linear optimization method (OriginPro 2019 Software, OriginLab Corporation, Northampton, MA, USA) [55] with the following Equation (3):

$$q_t = q_e(1 - e^{-k_1 t}) \quad (3)$$

which can be easily obtained from the integration of Equation (1).

As reported in Table 2, fittings of experimental adsorptions at 1 ppm as a function of time showed an increase in the k_1 value for increasing GO amounts incorporated in SWCNT BPs. In fact, the initial k_1 value of 5.44 ± 0.07 × 10^{-3} min^{-1} found for neat SWCNT BP increased to 8.81 ± 0.05 × 10^{-3} min^{-1} for 75% GO-SWCNT BP (increase ≈ 62%).

The found Lagergren adsorption rate constants are of the same order and magnitude as those recently obtained for the lead removal by BP membranes hosting MOF (14.3 ± 0.8 × 10^{-3} min^{-1}) [36], but lower than the lead adsorption rate constant by GO nanosheets (200 × 10^{-3} min^{-1}) [56].

Table 2. Lagergren adsorption rate constant, k_1 (min^{-1}), and lead adsorption capacity per unit of adsorbent mass at equilibrium, q_e (mg g^{-1}), for BPs with different GO loading.

Sample	$k_1 \times 10^3$ (min^{-1})	q_e (mg g^{-1})	R^2
SWCNT BP	5.44 ± 0.07	15.3 ± 0.5	0.9784
25% GO-SWCNT BP	6.07 ± 0.06	15.4 ± 0.4	0.9864
50% GO-SWCNT BP	6.88 ± 0.07	15.4 ± 0.4	0.9864
75% GO-SWCNT BP	8.81 ± 0.05	15.9 ± 0.2	0.9958

To validate the good lead adsorption properties by 75% GO-SWCNT membranes even in the presence of the most found background ions, further adsorption experiments were performed with 1 ppm lead solution prepared with mineral water, where both monovalent and divalent ions (Na^+, K^+, Mg^{2+}, and Ca^{2+}) were present. The initial concentration of such ions was 6.18, 3.90, 5.96, and 15.89 ppm for Na^+, K^+, Mg^{2+}, and Ca^{2+}, respectively. As it is evident from Figure 5a, both the capture performance of hybrid membranes and the selectivity towards Pb^{2+} ions were preserved.

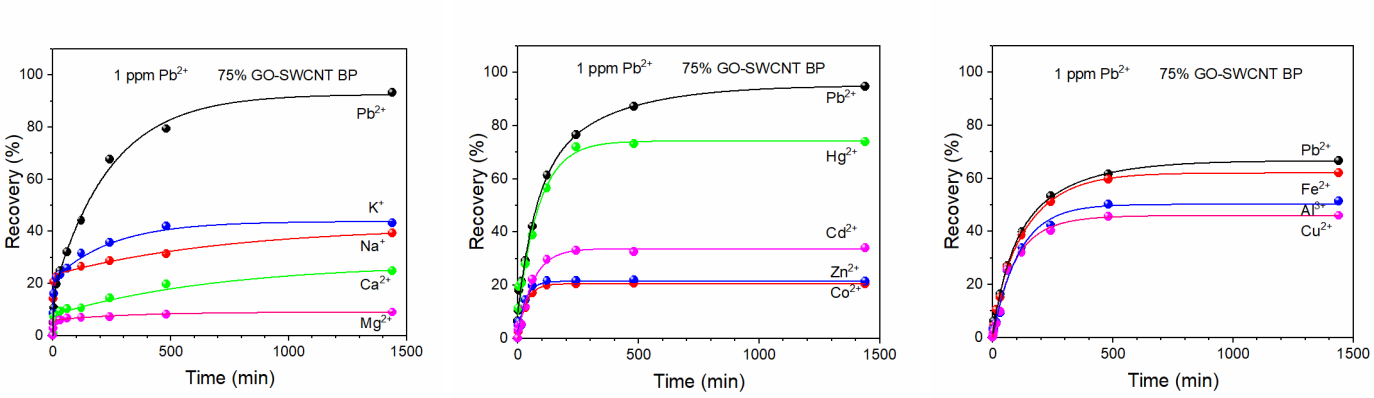

Figure 5. Pb^{2+} recovery by 75% GO-SWCNT BPs during the soaking in 800 mL of: (**a**) a mineral water solution with [Pb^{2+}] of 1 ppm, (**b**) a multielement heavy metal solution with Pb^{2+}, Co^{2+}, Zn^{2+}, Cd^{2+}, and Hg^{2+}, (**c**) a multielement heavy metal solution with Pb^{2+}, Fe^{3+}, Al^{3+}, and Cu^{2+}. The concentration of each heavy metal in the multielement solutions was 1 ppm.

The observed selectivity of 75% GO-SWCNT BPs toward lead was further confirmed when other divalent and potential interferent heavy metals (Co^{2+}, Zn^{2+}, Cd^{2+}, and Hg^{2+}) were present in a simulated wastewater at the concentration of 1 ppm, as shown in Figure 5b. In particular, the Co^{2+}, Zn^{2+}, and Cd^{2+} recovery percentage was lower than one half than the one found for lead.

The lead capture performance was still the highest when 75% GO-SWCNT membranes were soaked in a solution containing 1 ppm of other heavy metal ions easily found in wastewater, such as Fe^{3+}, Al^{3+}, and Cu^{2+}, see Figure 5c.

It is worth noting that, under such drastic experimental conditions, the initial lead concentration of 1 ppm was lowered to the value of about 300 ppb when a 75% GO-SWCNT BP was soaked in the solution beaker, whereas the removal efficiency for Pb^{2+}, Fe^{3+}, Al^{3+}, and Cu^{2+} was around 67%, 62%, 52%, and 46%, respectively. Even if lower than the lead adsorption capacity, the removal percentages of all other tested heavy metals by GO-SWCNT membranes were interesting for wider decontamination of wastewater from such toxic pollutants.

Stability in the adsorption performance after regeneration is an important item for every adsorbent in view of its potential industrial applications. The adsorption performance of 75% GO-SWCNT BP was measured in 1 ppm lead solution after four regeneration processes, performed by soaking the membranes in a 10% (*v*/*v*%) aqueous solution of 2-mercaptoethanol for 24 h in order to favor the release of the adsorbed lead. As shown in Figure 6, the initial recovery found after the first immersion in the lead solution was 99.69% and decreased to 93.42% during the fifth adsorption cycle performed after the fourth regeneration process, confirming the reusability, efficiency, and stability of membranes.

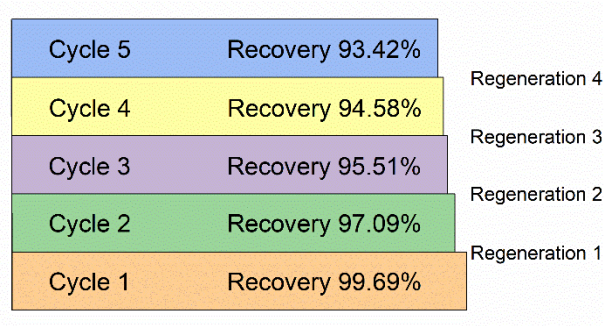

Figure 6. Pb^{2+} adsorption performance by 75% GO-SWCNT BPs after four regeneration processes in a 10% (*v*/*v*%) aqueous solution of 2-mercaptoethanol for 24 h. The initial lead concentration was 1 ppm.

Such properties make GO-SWCNT BPs suitable for industrial wastewater applications, thanks also to their easy scalability as filtration units both in parallel for large-scale treatments and in series for their increased efficiency performance.

Regarding the industrial feasibility and scale-up, at this stage, it is difficult to estimate the operating costs for lead removal by the proposed technology and compare them with those of other existing technologies. According to a previously reported estimation to produce BPs (hosting MOFs at 25 wt.% for a 15 kg scale), the costs of BPs and MOFs were estimated at around 1000 €/kg and less than 4000 €/kg, respectively [36]. Considering that the GO production costs are noticeably lower than those of MOFs [57], it is possible to assess that the production of GO-SWCNT BPs is cheaper than that of MOF-SWCNT BPs or pure-MOF-based devices.

3. Materials and Methods

3.1. Buckypaper Preparation

SWCNT BPs were prepared using mixtures of commercially available single-walled carbon nanotubes, SWCNTs, with a length longer than 5 μm and an average diameter of 1.8 ± 0.1 nm, and commercially available carboxylic acid functionalized SWCNTs (COOH-SWCNTs, 1.0–3.0 atom% carboxylic acid) with average bundle lengths from 0.5 to 1.5 μm and diameters from 4 to 5 nm, as reported in their datasheets from Sigma-Aldrich, Milan, Italy. Briefly, 50 mg SWCNT and COOH-SWCNT mixtures in the ratio 2:1 by weight were dispersed in 250 mL 0.4% TRITON ×100 water solution by an ultrasonic bath (M1800H-E, Bransonic, Danbury, CT, USA) for 30 min, then filtered through poly(tetrafluoroethylene disks (PTFE, diameter = 47 mm, average pore size = 5 μm, Durapore©, Merck KGaA, Darmstadt, Germany) with a vacuum pump (pressure = −0.04 bar), washed several times with methanol and, finally dried at room temperature.

All chemicals were reagent grade and purchased from Sigma-Aldrich, Milan, Italy.

All filtration conditions including the weight percentage between SWCNTs and COOH-SWCNTs, the amount of TRITON ×100, the sonication time, the vacuum depression, the filter porosity, and material were chosen to obtain self-standing and flexible BP disks [36] (Figure 1).

Similarly, single-walled carbon nanotube/graphene oxide buckypapers, GO-SWCNT BPs, were obtained by substituting a given weight amount (25, 50, and 75 wt.%) of SWCNT-COOH-SWCNT mixture with an identical quantity of graphene oxide, (GO, 15–20 sheets, 4–10% edge-oxidized, Sigma-Aldrich, Milan, Italy) and following the procedure previously outlined for the preparation of SWCNT BPs. As shown in Figure 1, BPs were characterized by easy detachability from porous PTFE filter and self-sustainability for all studied GO wt. percentages. The obtained membranes were flexible disks with an average thickness of 100 ± 2 μm and an average diameter of 38 ± 1 mm. The substitution of SWCNT mixture with GO amounts larger than 75 wt.% gave cracked films, as reported in Figure

1e for 85% GO-SWCNT BPs, with difficult detachability and, consequently, broken membranes. Therefore, the maximum GO loading in GO-SWCNT BPs was set at 75 wt.%.

3.2. Characterization Procedure

The morphology of the SWCNT and GO-SWCNT membranes was investigated by a scanning electron microscope (LEO 420, Leica Microsystems, Cambridge, England, accelerating voltage of 10 kV) after their sputtering with an ultrathin gold layer.

Static contact-angle values of SWCNT and GO-SWCNT BPs were obtained with a goniometer (Nordtest, Serravalle Scrivia AL, Italy) at 25 °C. A drop (2 μL) of water was put on five different positions of the sample surface by a micro-syringe, and angle values were evaluated by drawing the tangents on both visible edges of each droplet and calculating the average value of the measurements.

The percentage porosity of BP, *P*(%), was estimated by measuring the weight of a wetting liquid (3M-FC-40, 3M Italia Srl, Pioltello, Milan, Italy) contained in the membrane pores at 25 °C, according to the following Equation (4):

$$P(\%) = \frac{\frac{W_w - W_d}{d_w}}{\frac{W_w - W_d}{d_w} + \frac{W_d}{d_m}} \quad (4)$$

where W_w and W_d are the weight of the wet and dry samples, and d_w and d_m are the density of the wetting liquid (1.855 g cm^{-3}) and BP membranes, respectively."

The tensile strength and fracture strain of SWCNT and GO-SWCNT BPs were measured on rectangular strips (3 cm in length and 5 mm in width) at a strain rate of 0.1 mm min^{-1} with a Sauter TVO-S tensile tester equipped with a Sauter FH-1k digital dynamometer and AFH FAST software (Sauter GmbH, Balingen, Germany).

3.3. Lead Adsorption by SWCNT and GO-SWCNT BPs

Lead adsorption by SWCNT and GO-SWCNT membranes was evaluated at 25 °C in deionized water solutions of $Pb(NO_3)_2$. SWCNT and GO-SWCNT BPs were placed in beakers containing 800 mL $Pb(NO_3)_2$ solution (lead concentration of 1, 10, and 50 ppm) and stirred by an orbital shaker (PSU-10i, Biosan, Italy) at 25 °C.

Mineral water solutions were used to test BP performance in lead (1 ppm) adsorption in the presence of interferent elements commonly found in water, such as Na^+, K^+, Ca^{2+}, and Mg^{2+}. Further investigations on the effect of the interferents' presence on lead removal were performed by measuring the lead adsorption from two different heavy metal multielement solutions, containing Pb^{2+}, Co^{2+}, Zn^{2+}, Cd^{2+}, and Hg^{2+} ions or Pb^{2+}, Fe^{2+}, Al^{3+}, and Cu^{2+} ions. The concentration of each heavy metal was 1 ppm in both multielement solutions.

The effect of pH on lead adsorption was tested at the following values: 4.5, 6, and 8. It was found that a 75% GO-SWCNT BP was able to recover about 99.7% of lead present in an 800 mL solution at a concentration of 1 ppm when the pH value was 6. The capture capacity decreased to about 92.0% and 89.9% when pH was 4.5 and 8, respectively. Consequently, all adsorption experiments were performed at pH 6, if not differently reported.

The heavy metal ion concentrations were determined by inductively coupled plasma-mass spectrometry (ICP-MS iCAP™ TQ Thermo Fisher Scientific, Waltham, MA, USA) equipped with a Peltier cooled high purity quartz baffled cyclonic spray chamber, a concentric borosilicate glass nebulizer, a wide 2.5 mm internal diameter quartz injector, a nickel sample and two skimmer cones with 1.1 mm and 0.5 mm diameter orifices, respectively. The ICP torch was a demountable single-piece quartz torch. Samples were collected by a Thermo Scientific™ Autosampler Housing with a peristaltic pump equipped with three-stop flared PVC pump tubing. A multielement standard solution was used to calibrate the instrument using different analytical concentrations (0.5, 5, 10, 20, 50, and 100 ppb, R^2 of calibration curve ≈ 1, and a limit of detection, LOD, of about

0.015 ppb). Ultrapure deionized water (18.3 MΩ cm, Arioso, Human Corporation, Korea) was used for the preparation of the aqueous solution after filtration by a 0.45 μm filter (Millex Syringe Filter, Merck, Darmstadt, Germany). Each experiment was performed in triplicate, and the results are reported as average values ± 3 SD.

4. Conclusions

In the present work, the preparation and characterization of GO-SWCNT buckypapers was reported, and their efficiency as lead adsorbents was tested as a function of different amounts of graphene oxide present in the membranes. The partial substitution of SWCNTs with GO had a beneficial effect in the adsorption properties of SWCNT BPs, which were still self-standing membranes without any important loss in their mechanical properties and adsorption capacities.

The GO-SWCNT BPs exhibited great capture properties for Pb^{2+} removal from aqueous solutions even in the presence of interferent ions, which could be present in water, such as Na^{+}, K^{+}, Ca^{2+}, and Mg^{2+}, and other heavy metal ions, which could be present in wastewater such as Co^{2+}, Zn^{2+}, Cd^{2+}, Hg^{2+}, Fe^{3+}, Al^{3+}, and Cu^{2+}. The GO-SWCNT membranes were also characterized by interesting capture properties towards all the ions present in the multielement solutions, allowing the possibility of wider decontamination of wastewater from several toxic pollutants at the same time.

For solutions with a lead concentration of 1 ppm, all GO-SWCNT BPs were able to reduce the [Pb^{2+}] to values well below the limit of 10 ppb allowed by WHO for drinkable water. The lead adsorption efficiency of the 75% GO-SWCNT BPs was maintained over five adsorption/four regeneration cycles without any important reduction (less than 7%) in the removal efficiency.

In addition to the above-mentioned features, it is important to emphasize the importance of the easy scalability of the proposed GO-SWCNT BPs as filtration units both in series for an efficiency increase and in parallel for applications in large-scale decontamination plants.

Author Contributions: Conceptualization and methodology, G.C., G.D.F. and F.P.N.; software, G.C. and M.C.; validation, G.D.F. and F.P.N.; formal analysis, G.C., G.D.F. and F.P.N.; investigation, M.B. and A.T.; data curation, M.C., M.B. and A.T.; writing—original draft preparation, G.D.F. and F.P.N.; writing—review and editing, G.D.F., G.C. and F.P.N.; supervision, G.D.F. and F.P.N. All authors have read and agreed to the published version of the manuscript.

Funding: The research activity of M.C. is funded by the Italian Ministry for University and Research under the program PON R&I 2014–2020 Azione IV.6—"Contratti di ricerca su tematiche Green" CUP: H25F21001230004. The research activity of M. B. is funded by a scholarship from Regione Calabria (grant POR Calabria 2014–2020-Azioni 10.5.6 e 10.5.12).

Institutional Review Board Statement: Not applicable.

Informed Consent Statement: Not applicable.

Data Availability Statement: Data are contained within the article.

Conflicts of Interest: The authors declare no conflict of interest.

Sample Availability: Samples are available from the authors.

References

1. Balali-Mood, M.; Naseri, K.; Tahergorabi, Z.; Khazdair, M.R.; Sadeghi, M. Toxic mechanisms of five heavy metals: Mercury, lead, chromium, cadmium, and arsenic. *Front. Pharmacol.* **2021**, *12*, 643972. https://doi.org/10.3389/fphar.2021.643972.
2. Gambhir, R.S.; Kapoor, V.; Nirola, A.; Sohi, R.; Bansal, V. Water pollution: Impact of pollutants and new promising techniques in purification process. *J. Hum. Ecol.* **2012**, *37*, 103–110. https://doi.org/10.1080/09709274.2012.11906453.
3. Lim, J.Y.; Mubarak, N.M.; Abdullah, E.C.; Nizamuddin, S.; Khalid, M.; Inamuddin, Recent trends in the synthesis of graphene and graphene oxide based nanomaterials for removal of heavy metals—A review. *J. Ind. Eng. Chem.* **2018**, *66*, 29–44. https://doi.org/10.1016/j.jiec.2018.05.028.
4. Tchounwou, P.B.; Yedjou, C.G.; Patlolla, A.K.; Sutton, D.J. Heavy metals toxicity and the environment. In *Molecular, Clinical and Environmental Toxicology. Experientia Supplementum*; Luch, A., Ed.; Springer: Basel, Switzerland, 2012; Volume 101, pp. 133–164. https://doi.org/10.1007/978-3-7643-8340-4_6.
5. Payne, M. Lead in drinking water. *Can. Med. Assoc. J.* **2008**, *179*, 253–254. https://doi.org/10.1503/cmaj.071483.
6. Shahat, A.; Awual, M.R.; Khaleque, M.A.; Alam, M.Z.; Naushad, M.; Sarwaruddin Chowdhury, A.M. Large-pore diameter nano–adsorbent and its application for rapid lead (II) detection and removal from aqueous media. *Chem. Eng. J.* **2015**, *273*, 286–295. https://doi.org/10.1016/j.cej.2015.03.073.
7. Zhu, J.; Wei, S.; Chen, M.; Gu, H.; Rapole, S.B.; Pallavkar, S.; Ho, T.C.; Hopper, J.; Guo, Z. Magnetic nanocomposites for environmental remediation. *Adv. Powder Technol.* **2013**, *24*, 459–467. https://doi.org/10.1016/j.apt.2012.10.012.
8. Available online: https://www.who.int/teams/environment-climate-change-and-health/water-sanitation-and-health/water-safety-and-quality/drinking-water-quality-guidelines (accessed on 25 May 2022).
9. Narayani, M.; Shetty, K.V. Chromium–resistant bacteria and their environmental condition for hexavalent chromium removal: A review. *Crit. Rev. Environ. Sci. Technol.* **2013**, *43*, 955–1009. https://doi.org/10.1080/10643389.2011.627022.
10. Hu, M.; Mi, B. Enabling graphene oxide nanosheets as water separation membranes. *Environ. Sci. Technol.* **2013**, *47*, 3715–3723. https://doi.org/10.1021/es400571g.
11. Hoch, L.B.; Mack, E.J.; Hydutsky, B.W.; Hershman, J.M.; Skluzacek, J.M.; Mallouk, T.E. Carbothermal synthesis of carbon–supported nanoscale zero–valent iron particles for the remediation of hexavalent chromium. *Environ. Sci. Technol.* **2008**, *42*, 2600–2605. https://doi.org/10.1021/es702589u.
12. Oehmen, A.; Vergel, D.; Fradinho, J.; Reis, M.A.M.; Crespo, J.G.; Velizarov, S. Mercury removal from water streams through the ion exchange membrane bioreactor concept. *J. Hazard. Mater.* **2014**, *264*, 65–70. https://doi.org/10.1016/j.jhazmat.2013.10.067.
13. Stephenson, R.J.; Duff, S.J.B. Coagulation and precipitation of a mechanical pulping effluent—I. Removal of carbon, colour and turbidity. *Water Res.* **1996**, *30*, 781–792.
14. Tran, T.-K.; Chiu, K.-F.; Lin, C.-Y.; Leu, H.-J. Electrochemical treatment of wastewater: Selectivity of the heavy metals removal process. *Int. J. Hydrogen Energy* **2017**, *42*, 27741–27748. https://doi.org/10.1016/j.ijhydene.2017.05.156.
15. Sun, Y.; Ding, C.; Cheng, W.; Wang, X. Simultaneous adsorption and reduction of U(VI) on reduced graphene oxide-supported nanoscale zerovalent iron. *J. Hazard. Mater.* **2014**, *280*, 399–408. https://doi.org/10.1016/j.jhazmat.2014.08.023.
16. Jung, C.; Heo, J.; Han, J.; Her, N.; Lee, S.-J.; Oh, J.; Ryu, J.; Yoon, Y. Hexavalent chromium removal by various adsorbents: Powdered activated carbon, chitosan, and single/multi-walled carbon nanotubes. *Separ. Purif. Technol.* **2013**, *106*, 63–71. https://doi.org/10.1016/j.seppur.2012.12.028.
17. Li, J.; Wang, X.; Zhao, G.; Chen, C.; Chai, Z.; Alsaedi, A.; Hayat, T.; Wang, X. Metal–organic framework-based materials: Superior adsorbents for the capture of toxic and radioactive metal ions. *Chem. Soc. Rev.* **2018**, *47*, 2322–2356. https://doi.org/10.1039/C7CS00543A.
18. De Gisi, S.; Lofrano, G.; Grassi, M.; Notarnicola, M. Characteristics and adsorption capacities of low-cost sorbents for wastewater treatment: A review. *Sustain. Mater. Technol.* **2016**, *9*, 10–40. https://doi.org/10.1016/j.susmat.2016.06.002.
19. Hadi, P.; To, M.-H.; Hui, C.-W.; Lin, C.S.K.; McKay, G. Aqueous mercury adsorption by activated carbons. *Water Res.* **2015**, *73*, 37–55. https://doi.org/10.1016/j.watres.2015.01.018.
20. Sheng, G.; Yang, S.; Sheng, J.; Hu, J.; Tan, X.; Wang, X. Macroscopic and microscopic investigation of Ni(II) sequestration on diatomite by batch, XPS, and EXAFS techniques. *Environ. Sci. Technol.* **2011**, *45*, 7718–7726. https://doi.org/10.1021/es202108q.
21. Jiménez-Castañeda, M.E.; Medina, D.I. Use of surfactant-modified zeolites and clays for the removal of heavy metals from water. *Water* **2017**, *9*, 235. https://doi.org/10.3390/w9040235.
22. Gupta, V.K.; Nayak, A. Cadmium removal and recovery from aqueous solutions by novel adsorbents prepared from orange peel and Fe_2O_3 nanoparticles. *Chem. Eng. J.* **2012**, *180*, 81–90. https://doi.org/10.1016/j.cej.2011.11.006.
23. Kolluru, S.S.; Agarwal, S.; Sireesha, S.; Sreedhar, I.; Kale, S.R. Heavy metal removal from wastewater using nanomaterials-process and engineering aspects. *Process Saf. Environ. Prot.* **2021**, *150*, 323–355. https://doi.org/10.1016/j.psep.2021.04.025.
24. Bhatti, A.A.; Memon, S.; Memon, N. Dichromate extraction by calix[4]arene appended amberlite XAD–4 resin. *Separ. Sci. Technol.* **2014**, *49*, 664–672. https://doi.org/10.1080/01496395.2013.862722.
25. Dave, P.N.; Chopda, L.V. Application of iron oxide nanomaterials for the removal of heavy metals. *J. Nanotechnol.* **2014**, *2014*, 398569. https://doi.org/10.1155/2014/398569.
26. Nguyen, T.A.H.; Ngo, H.H.; Guo, W.S.; Zhang, J.; Liang, S.; Yue, Q.Y.; Li, Q.; Nguyen, T.V. Applicability of agricultural waste and by-products for adsorptive removal of heavy metals from wastewater. *Bioresour. Technol.* **2013**, *148*, 574–585. https://doi.org/10.1016/j.biortech.2013.08.124.

27. Renu, M.A.; Singh, K.; Upadhyaya, S.; Dohare, R.K.; Removal of heavy metals from wastewater using modified agricultural adsorbents. *Mater. Today Proc.* **2017**, *4*, 10534–10538. https://doi.org/10.1016/j.matpr.2017.06.415.
28. Zou, Y.; Wang, X.; Khan, A.; Wang, P.; Liu, Y.; Alsaedi, A.; Hayat, T.; Wang, X. Environmental remediation and application of nanoscale zero–valent iron and its composites for the removal of heavy metal ions: A review. *Environ. Sci. Technol.* **2016**, *50*, 7290–7304. https://doi.org/10.1021/acs.est.6b01897.
29. Saleh, T.A.; Gupta, V.K.; Column with CNT/magnesium oxide composite for lead(II) removal from water. *Environ. Sci. Pollut. Res.* **2012**, *19*, 1224–1228. https://doi.org/10.1007/s11356-011-0670-6.
30. Kabbashi, N.A.; Atieh, M.A.; Al-Mamun, A.; Mirghami, M.E.S.; Alam, M.D.Z.; Yahya, N. Kinetic adsorption of application of carbon nanotubes for Pb(II) removal from aqueous solution. *J. Environ. Sci.* **2009**, *21*, 539–544. https://doi.org/10.1016/S1001-0742(08)62305-0.
31. Ren, X.; Chen, C.; Nagatsu, M.; Wang, X. Carbon nanotubes as adsorbents in environmental pollution management: A review. *Chem. Eng. J.* **2011**, *170*, 395–410. https://doi.org/10.1016/j.cej.2010.08.045.
32. Wang, H.; Yuan, X.; Wu, Y.; Huang, H.; Zeng, G.; Liu, Y.; Wang, X.; Lin, N.; Qi, Y. Adsorption characteristics and behaviors of graphene oxide for Zn(II) removal from aqueous solution. *Appl. Surf. Sci.* **2013**, *279*, 432–440. https://doi.org/10.1016/j.apsusc.2013.04.133.
33. Zhao, G.; Ren, X.; Gao, X.; Tan, X.; Li, J.; Chen, C.; Huang, Y.; Wang, X. Removal of Pb(II) ions from aqueous solutions on few-layered graphene oxide nanosheets. *Dalton Trans.* **2011**, *40*, 10945–10952. https://doi.org/10.1039/C1DT11005E.
34. Gao, W.; Majumder, M.; Alemany, L.B.; Narayanan, T.N.; Ibarra, M.A.; Pradhan, B.K.; Ajayan, P.M. Engineered graphite oxide materials for application in water purification. *ACS Appl. Mater. Interfaces* **2011**, *3*, 1821–1826. https://doi.org/10.1021/am200300u.
35. Yin, N.; Wang, K.; Xia, Y.; Li, Z. Novel melamine modified metal-organic frameworks for remarkably high removal of heavy metal Pb(II). *Desalination* **2018**, *430*, 120–127. https://doi.org/10.1016/j.desal.2017.12.057.
36. Baratta, M.; Mastropietro, T.F.; Bruno, R.; Tursi, A.; Negro, C.; Ferrando-Soria, J.; Mashin, A.I.; Nezhdanov, A.; Nicoletta, F.P.; De Filpo, G.; et al. Multivariate metal–organic framework/single–walled carbon nanotube buckypaper for selective lead decontamination. *ACS Appl. Nano Mater.* **2022**, *5*, 5223–5233. https://doi.org/10.1021/acsanm.2c00280.
37. Baby, R.; Saifullah, B.; Hussein, M.Z. Carbon nanomaterials for the treatment of heavy metal-contaminated water and environmental remediation. *Nanoscale Res. Lett.* **2019**, *14*, 341. https://doi.org/10.1186/s11671-019-3167-8.
38. Khan, F.S.A.; Mubarak, N.M.; Tan, Y.H.; Khalid, M.; Karri, R.R.; Walvekar, R.; Abdullah, E.C.; Nizamuddin, S.; Mazari, S.A. A comprehensive review on magnetic carbon nanotubes and carbon nanotube-based buckypaper for removal of heavy metals and dyes. *J. Hazard. Mater.* **2021**, *413*, 125375. https://doi.org/10.1016/j.jhazmat.2021.125375.
39. Alshahrani, A.; Alharbi, A.; Alnasser, S.; Almihdar, M.; Alsuhybani, M.; AlOtaibi, B. Enhanced heavy metals removal by a novel carbon nanotubes buckypaper membrane containing a mixture of two biopolymers: Chitosan and i-carrageenan. *Separ. Purif. Technol.* **2021**, *276*, 119300. https://doi.org/10.1016/j.seppur.2021.119300.
40. De Filpo, G.; Pantuso, E.; Mashin, A.I.; Baratta, M.; Nicoletta, F.P. WO_3/buckypaper membranes for advanced oxidation processes. *Membranes* **2020**, *10*, 157. https://doi.org/10.3390/membranes10070157.
41. Rashid, M.H.-O.; Ralph, S.F. Carbon nanotube membranes: Synthesis, properties, and future filtration applications. *Nanomaterials* **2017**, *7*, 99. https://doi.org/10.3390/nano7050099.
42. Patole, S.P.; Arif, M.F.; Susantyoko, R.A.; Almheiri, S.; Kumar, S. A wet-filtration-zipping approach for fabricating highly electroconductive and auxetic graphene/carbon nanotube hybrid buckypaper. *Sci. Rep.* **2018**, *8*, 12188. https://doi.org/10.1038/s41598-018-30009-4.
43. Xia, Q.; Zhang, Z.; Liu, Y.; Leng, J. Buckypaper and its composites for aeronautic applications. *Compos. B Eng.* **2020**, *199*, 108231. https://doi.org/10.1016/j.compositesb.2020.108231.
44. Tursi, A.; Mastropietro, T.F.; Bruno, R.; Baratta, M.; Ferrando-Soria, J.; Mashin, A.I.; Nicoletta, F.P.; Pardo, E.; De Filpo, G.; Armentano, D. Synthesis and enhanced capture properties of a new BioMOF@SWCNT-BP: Recovery of the endangered rare-earth elements from aqueous systems. *ACS Adv. Mater. Interfaces* **2021**, *8*, 2100730. https://doi.org/10.1002/admi.202100730.
45. Huang, J.; Her, S.-C.; Yang, X.; Zhi, M. Synthesis and characterization of multi-walled carbon nanotube/graphene nanoplatelet hybrid film for flexible strain sensors. *Nanomaterials* **2018**, *8*, 786. https://doi.org/10.3390/nano8100786.
46. Huang, J.-Q.; Xu, Z.-L.; Abouali, S.; Garakani, M.A.; Kim, J.-K. Porous graphene oxide/carbon nanotube hybrid films as interlayer for lithium-sulfur batteries. *Carbon* **2016**, *99*, 624–632. https://doi.org/10.1016/j.carbon.2015.12.081.
47. Yuan, G.-J.; Xie, J.-F.; Li, H.-H.; Shan, B.; Zhang, X.-X.; Liu, J.; Li, L.; Tian, Y.-Z. Thermally reduced graphene oxide/carbon nanotube composite films for thermal packaging applications. *Materials* **2020**, *13*, 317. https://doi.org/10.3390/ma13020317.
48. Minett, A.; Fràysse, J.; Gang, G.; Kim, G.-T.; Roth, S. Nanotube actuators for nanomechanics. *Curr. Appl. Phys.* **2002**, *2*, 61–64. https://doi.org/10.1016/S1567-1739(01)00100-6.
49. Kausar, A.; Ilyas, H.; Siddiq, M. Current research status and application of polymer/carbon nanofiller buckypaper: A review. *Polym. Plast. Technol. Eng.* **2017**, *56*, 1780–1800. https://doi.org/10.1080/03602559.2017.1289407.
50. Alshahrani, A.A.; Al-Zoubi, H.; Nghiem, L.D.; in het Panhuis, M. Synthesis and characterisation of MWNT/chitosan and MWNT/chitosan-crosslinked buckypaper membranes for desalination. *Desalination* **2017**, *418*, 60–70. https://doi.org/10.1016/j.desal.2017.05.031.
51. Musielak, M.; Gagor, A.; Zawisza, B.; Talik, E.; Sitko, R. Graphene oxide/carbon nanotube membranes for highly efficient removal of metal ions from water. *ACS Appl. Mater. Interfaces* **2019**, *11*, 28582–28590. https://doi.org/10.1021/acsami.9b11214.

52. Cooper, S.M.; Chuang, H.F.; Cinke, M.; Cruden, B.A.; Meyyappan, M. Gas permeability of a buckypaper membrane. *Nano Lett.* **2003**, *2*, 189–192. https://doi.org/10.1021/nl0259131.
53. Wang, Z.; Liang, Z.Y.; Wang, B.; Zhang, C.; Kramer, L. Processing and property investigation of single-walled carbon nanotube (SWNT) buckypaper/epoxy resin matrix nanocomposites. *Compos. Appl. Sci. Manuf.* **2004**, *35*, 1225–1232. https://doi.org/10.1016/j.compositesa.2003.09.029.
54. Jun, B.-M.; Kim, S.; Kim, Y.; Her, N.; Heo, J.; Han, J.; Jang, M.; Park, C.M.; Yoon, Y. Comprehensive evaluation on removal of lead by graphene oxide and metal organic framework. *Chemosphere* **2019**, *231*, 82–92. https://doi.org/10.1016/j.chemosphere.2019.05.076.
55. Belhachemi, M.; Addoun, F. Comparative adsorption isotherms and modeling of methylene blue onto activated carbons. *Appl. Water Sci.* **2011**, *1*, 111–117. https://doi.org/10.1007/s13201-011-0014-1.
56. Sitko, R.; Turek, E.; Zawisza, B.; Malicka, E.; Talik, E.; Heimann, J.; Gagor, A.; Feist, B.; Wrzalik, R. Adsorption of divalent metal ions from aqueous solutions using graphene oxide. *Dalton Trans.* **2013**, *42*, 5682–5689. https://doi.org/10.1039/C3DT33097D.
57. Ranjan, P.; Agrawal, S.; Sinha, A.; Rao, T.R.; Balakrishnan, J.; Thakur, A.D. Low-cost non-explosive synthesis of graphene oxide for scalable applications. *Sci. Rep.* **2018**, *8*, 12007. https://doi.org/10.1038/s41598-018-30613-4.

molecules

MDPI

Article

Removal of Non-Steroidal Anti-Inflammatory Drugs from Drinking Water Sources by GO-SWCNT Buckypapers

Mariafrancesca Baratta [1,†], Antonio Tursi [1,†], Manuela Curcio [2], Giuseppe Cirillo [2], Aleksey Vladimirovich Nezhdanov [3], Alexandr Ivanovic Mashin [3], Fiore Pasquale Nicoletta [2,*] and Giovanni De Filpo [1,*]

[1] Department of Chemistry and Chemical Technologies, University of Calabria, 87036 Rende, Italy
[2] Department of Pharmacy, Health and Nutritional Sciences, University of Calabria, 87036 Rende, Italy
[3] Applied Physics & Microelectronics, Lobachevsky State University of Nizhni Novgorod, Nizhni Novgorod 603105, Russia
* Correspondence: fiore.nicoletta@unical.it (F.P.N.); giovanni.defilpo@unical.it (G.D.F.); Tel.: +39-098-449-3194 (F.P.N.); +39-098-449-2105 (G.D.F.)
† These authors contributed equally to this work.

Abstract: Pharmaceutical products such as antibiotics, analgesics, steroids, and non-steroidal anti-inflammatory drugs (NSAIDs) are new emerging pollutants, often present in wastewater, potentially able to contaminate drinking water resources. Adsorption is considered the cheapest and most effective technique for the removal of pollutants from water, and, recently, membranes obtained by wet filtration method of SWCNT aqueous solutions (SWCNT buckypapers, SWCNT BPs) have been proposed as self-standing porous adsorbents. In this paper, the ability of graphene oxide/single-walled carbon nanotube composite membranes (GO-SWCNT BPs) to remove some important NSAIDs, namely Diclofenac, Ketoprofen, and Naproxen, was investigated at different pH conditions (pH 4, 6, and 8), graphene oxide amount (0, 20, 40, 60, and 75 wt.%), and initial NSAIDs concentration (1, 10, and 50 ppm). For the same experimental conditions, the adsorption capacities were found to strongly depend on the graphene oxide content. The best results were obtained for 75 wt.% graphene oxide with an adsorption capacity of 118 ± 2 mg g^{-1} for Diclofenac, 116 ± 2 mg g^{-1} for Ketoprofen, and 126 ± 3 mg g^{-1} for Naproxen at pH 4. Overall, the reported data suggest that GO-SWCNT BPs can represent a promising tool for a cheap and fast removal of NSAIDs from drinking water resources, with easy recovery and reusability features.

Keywords: single-walled carbon nanotubes; graphene oxide; buckypaper; non-steroidal anti-inflammatory drugs; water sources; adsorption

Citation: Baratta, M.; Tursi, A.; Curcio, M.; Cirillo, G.; Nezhdanov, A.V.; Mashin, A.I.; Nicoletta, F.P.; De Filpo, G. Removal of Non-Steroidal Anti-Inflammatory Drugs from Drinking Water Sources by GO-SWCNT Buckypapers. *Molecules* **2022**, *27*, 7674. https://doi.org/10.3390/molecules27227674

Academic Editor: Giorgio Vilardi

Received: 11 October 2022
Accepted: 5 November 2022
Published: 8 November 2022

1. Introduction

Emerging pollutant is a general term labeling compounds recently resulting as dangerous for both environment and human health, with an enhanced threat to humans being represented by their increased concentration in water sources and the lack of legal limits at national or international levels.

Nowadays, due to their widespread use to prevent and treat human diseases, pharmaceutical compounds (PCs) represent a new class of emerging pollutants [1]. Their improper disposal and accidental contaminations [2], as well as their excretion and dispersion in wastewater after their assumption, could carry out to their accumulation in fresh water resources. Due to their low molecular weight, polar nature, and hydrophilicity, PCs are not separated by conventional wastewater treatment plants, and thus their persistence and accumulation can cause unforeseen effects on the environment [3–7]. PCs can be detected in aquatic environments around the world [8,9] with concentrations up to several mg L^{-1} as a consequence of their long-term stability [10–12].

In addition, national drinking-water directives generally do not define limits to the PC presence, in spite of any precautionary principle claiming for a complete removal of such pollutants since they can cause acute toxicity, including genotoxicity, endocrine disruption, development of pathogen resistance, and other often unknown effects on public health and environment [13,14].

Non-steroidal anti-inflammatory drugs (NSAIDs) represent the most important class of the new emerging pollutants due to their wide use as analgesic, anti-inflammatory, antipyretic, and pain-relief drugs [15]. Diclofenac (DIC), Ketoprofen (KET), and Naproxen (NAP) are some of the main worldwide used NSAIDs, with a production of many hundreds of tons per year, which can be found at huge concentrations in wastewater, surface water, groundwater, and drinking-water [16].

In the last years, researchers have proposed several technologies for an effective PC removal, including bio-treatment [17], advanced oxidation [18,19], membrane filtration [20,21], and ozonation [22]. Nevertheless, these processes are affected by some drawbacks, such as high costs, toxic by-products, slow and poor removal efficiencies.

Among others, adsorption is considered the cheapest, easiest, and most effective technique for pollutant removal from water with no formation of toxic by-products [23,24]. Several porous materials have been proposed as efficient adsorbents for pharmaceutical compounds thanks to their stable chemical structure, high porosity, easy functionalization, and large adsorption capacities [25,26]. In particular, activated carbons [27,28], waste materials [29,30], metal-organic frameworks (MOFs) [31], magnetic nanoparticles [32,33], single- and multi-walled carbon nanotubes (SWCNTs and MWCNTs) [34,35], and graphene oxide sheets (GO) have been tested for the removal of NSAIDs over the last years [36].

In particular, carbon-based materials were widely explored as promising adsorbents due to their superior surface properties, although they suffer from difficult recovery and reuse as a consequence of their powder consistency. More recently, several research groups have assembled powder adsorbents in porous membranes by either using polymer additives or exploiting the self-assembling properties of some materials [37–39]. Buckypapers (BPs) are self-standing porous membranes obtained by self-assembling SWCNT and/or MWCNT bundles mainly via π-π and van der Waals interactions during the wet filtration of carbon nanotube solutions [40,41]. BPs are characterized by interesting rheological, thermal, and electrical properties [42] and are successfully applied in filtration and adsorption processes. In fact, they show porous structure, low density, easy functionalization, as well as the possibility to host other adsorbents, such as natural polymers [43,44], MOF [45,46], and GO [47,48], to increase the adsorption efficiencies [46,49].

In our previous work, we proved that the partial substitution of SWCNTs with GO in BPs structure allowed the obtainment of self-standing hybrid buckypapers (GO-SWCNT BPs) useful for heavy metal removal with good efficiency [47]. With the present investigation, we aim to test the versatility of these GO-SWCNT BPs, evaluating the possibility of using them as a tool for the removal of NSAIDs (namely DIC, KET, and NAP) from wastewater. In detail, we extensively investigated the effect of key parameters (e.g., different GO wt. contents, pH values, and initial NSAID concentration) to determine the optimal adsorption conditions. Overall, we found that the adsorption capacity towards all NSAIDs increased with the graphene oxide percentage present in the membrane composition, proving the importance of the GO in the membrane composition.

2. Results

The wet method is probably the easiest procedure to obtain carbon nanotube buckypapers with homogeneous morphology [41]. Thus, SWCNT BPs were prepared according to this method by dispersing the SWCNT mixture (SWCNTs and carboxylic acid functionalized SWCNTs in the wt. ratio 2:1) in a TRITON-X100 water solution followed by vacuum filtration through a PTFE 5 μm porous filter. BP membranes were

then washed with methanol several times, dried, and, finally, peeled off from the PTFE filter. GO-SWCNT BPs were prepared similarly to the procedure outlined for pure SWCNT BPs, with the substitution of some percentage (20, 40, 60, and 75 wt.%) of SWCNT mixture with GO (see Materials and Methods section for more details). For all tested wt. ratios, self-standing and flexible BP disks were obtained for a GO loading up to 75 wt.% (Figure 1e), while a further increase in GO amount gave cracked films due to insufficient π-π and van der Waals interaction forces between SWCNT and GO. Such results agree with the decrease in the rheological performance (reduced values of tensile strength and fracture strain) reported in the literature when large GO amounts were used in GO-SWCNT BPs preparation [47].

As reported in Figure 1a,b, BPs looked very similar to the eye independently from the amount of GO present in the BP composition, being black and stable membranes with an average thickness of around 100 ± 2 μm and an average diameter of 38 ± 1 mm. The SEM investigations showed that the SWCNT BP morphology was characterized by the presence of the typical SWCNT clusters and bundles arising from van der Waals and π-π interactions, Figure 1c. It is also evident that the typical large porosity confers high permeability and large contact surface area to BPs, thus allowing for an effective adsorption process. At a microscopic level, the substitution of GO in GO-SWCNT BPs resulted in the presence of GO sheets homogenously hosted inside the SWCNT BP membranes, Figure 1d.

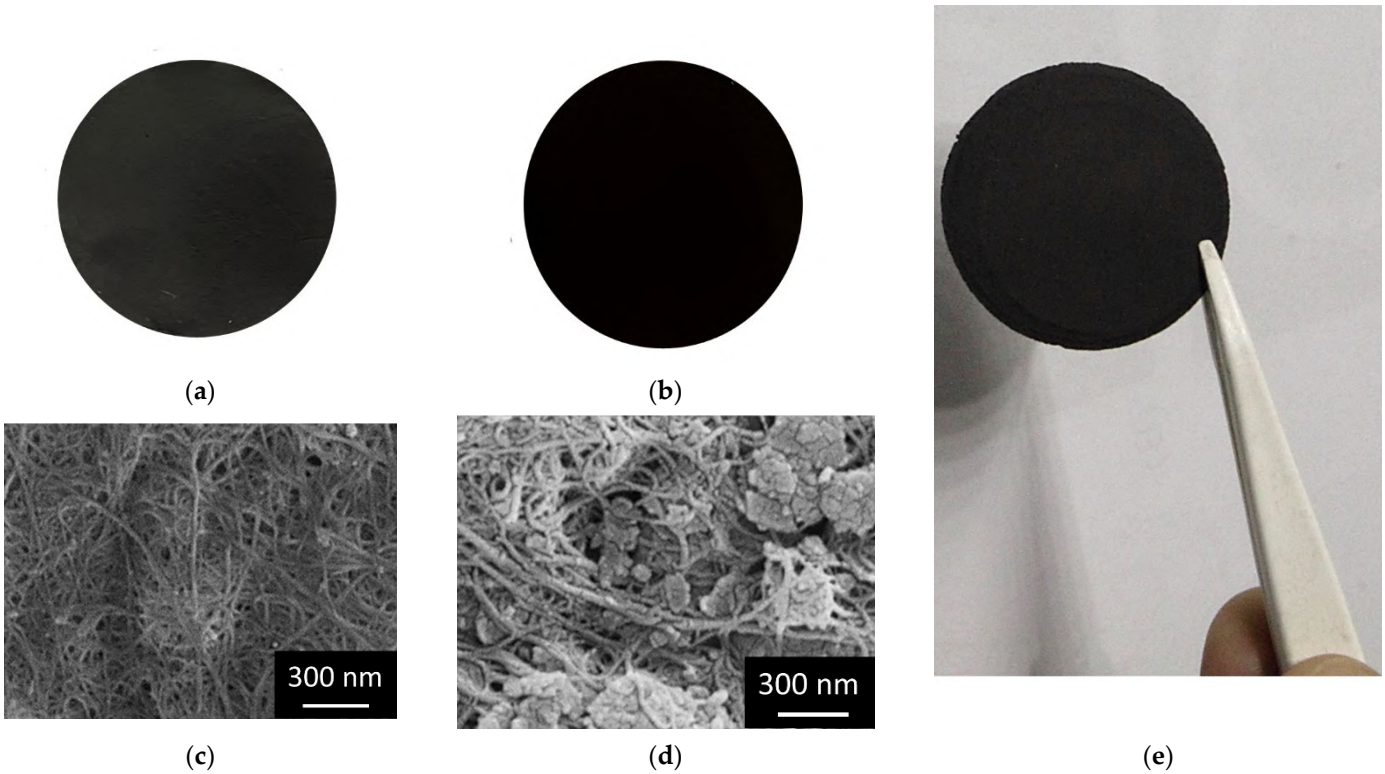

Figure 1. Pictures of (**a**) SWCNT BP and (**b**) 75% GO-SWCNT BP. SEM images of (**c**) SWCNT BP and (**d**) 75% GO-SWCNT BP. The presence of GO flakes embedded in the SWCNT BP network is evident in the latter image. Samples up to 75 wt.% GO were self-sustainable and flexible disks (**e**).

The NSAID removal properties by SWCNT and GO-SWCNT membranes were evaluated through adsorption experiments performed on water solutions of the three most used active compounds (Diclofenac, Ketoprofen, and Naproxen) at three different pH values (4, 6, and 8) and initial concentrations (1, 10, and 50 ppm).

In more detail, membrane disks were immersed in 200 mL beakers with a given NSAID water solution, and the kinetic profiles of drug recovery in the 0–72 h interval were recorded. The recovery percentage was spectro-photochemically obtained by measuring the absorbance of the three NSAIDs at their maximum absorption wavelength (276, 259, and 228 nm for DIC, KET, and NAP, respectively), with Figure 2 showing the UV-Vis adsorption spectra and chemical structure of the three drugs.

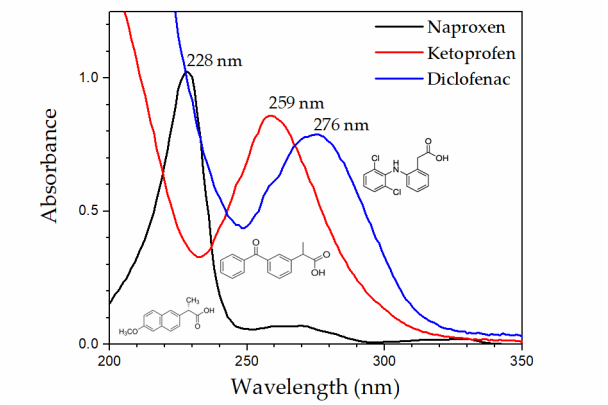

Figure 2. UV-Vis adsorption spectra and chemical structure of NAP, KET, and DIC.

The recovery percentage, *Re*(%), was calculated according to the following Equation (1):

$$Re(\%) = \frac{Abs_0 - Abs_t}{Abs_0} \times 100 \quad (1)$$

where Abs_0 and Abs_t were the drug absorbance at time 0 and t, respectively.

Figure 3 shows the *Re*(%) behavior for the three NSAIDs in water solutions at different pH values and a 10 ppm initial concentration when GO-SWCNT BPs with increasing GO content were used as adsorbents.

The recovery of all NSAIDs as a function of pH after 72 h showed a similar trend with increasing adsorptions found when GO-SWCNT BPs with larger amounts of GO were used. pH 4.0 was the pH value ensuring the largest adsorption for all NSAIDs and GO-SWCNT BPs with the largest GO substitution (75 wt.%) granted the highest recovery values.

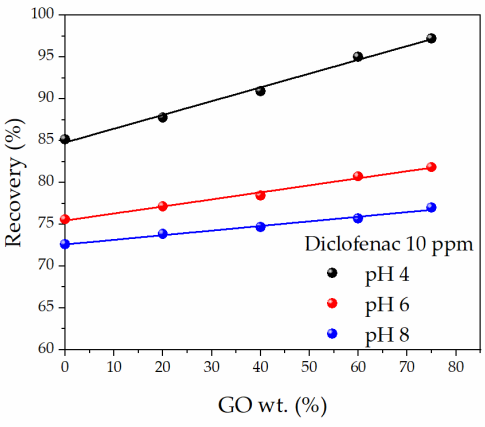

(**a**)

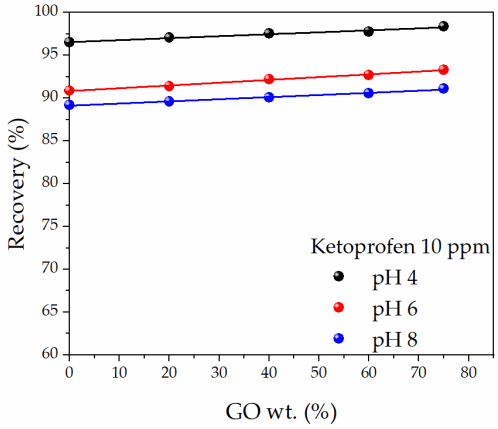

(**b**)

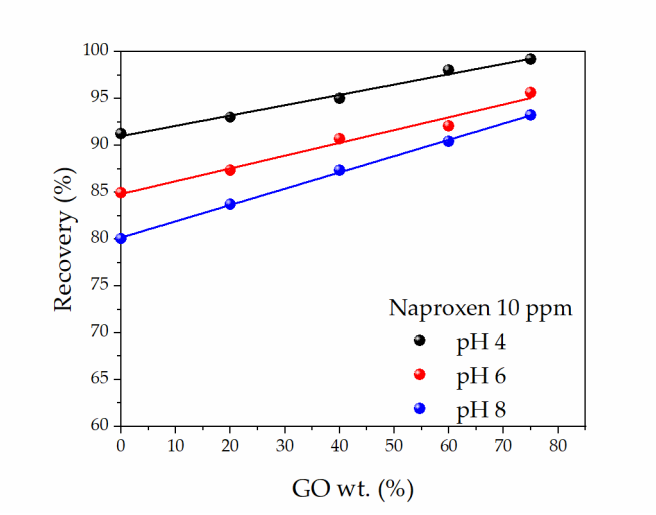

(**c**)

Figure 3. The recovery percentage, *Re*(%), of: (**a**) Diclofenac, (**b**) Ketoprofen, and (**c**) Naproxen water solutions at different pH values and 10 ppm initial concentration as a function of GO content in GO-SWCNT BPs.

In detail, neat SWCNT BPs showed the lowest recovery values (85.16, 96.53, and 91.23% @ pH 4 for DIC, KET, and NAP, respectively), which increased more or less linearly (R^2 values always larger than 0.978) up to 97.2, 98.36, and 99.18% @ pH 4 for 75% GO-SWCNT BPs. Consequently, pH 4 was chosen as the pH value for carrying out the subsequent adsorption experiments. It is worth noting that the recovery could be increased up to the desired value (in accordance with the precautionary principles) also by successive adsorption steps with new or regenerated BPs (see infra).

At pH 4, all membranes were able to recover the major amount of the NSAIDs present in the 1 and 10 ppm solutions (*Re*% larger than 85% in all cases), and the recovery was further increased when membranes with larger GO amounts were used (Figure 4). In these conditions, values larger than 97.2% were obtained when 75% GO-SWCNT BPs were used, confirming the positive effect of GO substitution. At a larger initial concentration (50 ppm), all *Re*(%) were lowered to values ranging from 50 to 64%, with the lowest adsorption value obtained from neat SWCNT BPs (50.91, 57.02, and 53.67% for DIC, KET, and NAP, respectively) and the highest from 75% GO-SWCNT BPs (59.28, 58.75, and 63.54% for DIC, KET, and NAP, respectively).

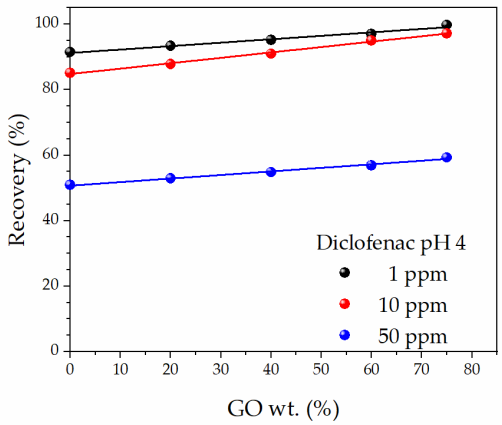

(**a**)

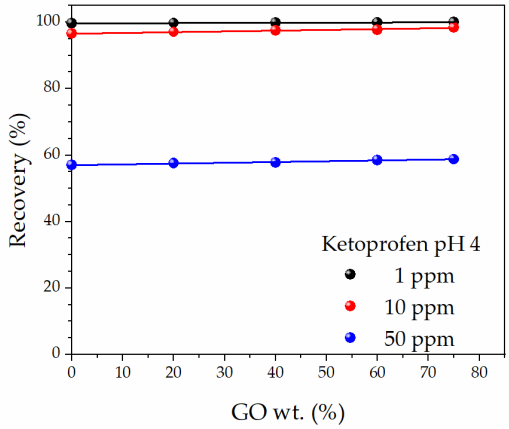

(**b**)

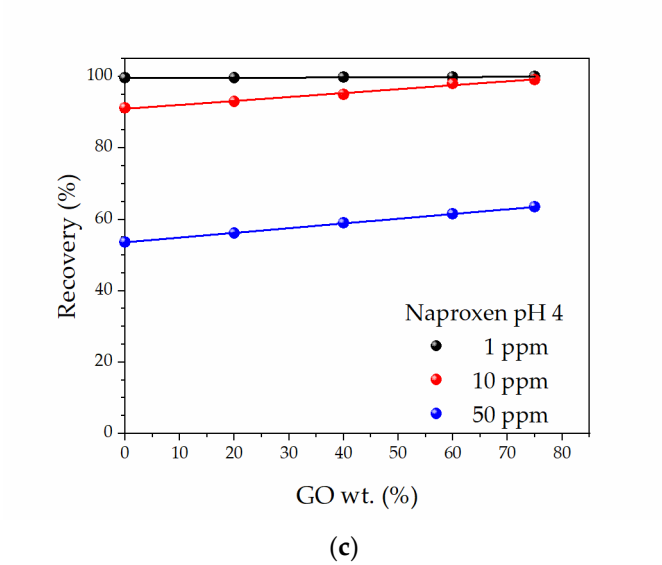

(**c**)

Figure 4. Recovery percentages, *Re*(%), at pH 4 as a function of GO content in GO-SWCNT BPs for: (**a**) Diclofenac, (**b**) Ketoprofen, and (**c**) Naproxen water solutions at different initial concentrations.

Such results gave an NSAID experimental SWCNT BPs adsorption capacity per unit of adsorbent mass, q_{exp} (mg g^{-1}), of 102 ± 2, 114 ± 2, and 108 ± 2 mg g^{-1}, in the case of DIC, KET, and NAP 50 ppm aqueous solutions. q_{exp} was defined as follows (Equation (2)):

$$q_{exp} = \frac{m(NSAID)}{m(membrane)} \quad (2)$$

where *m(NSAID)* was the adsorbed NSAID mass in milligrams, and *m(membrane)* was the SWCNT BP or GO-SWCNT BP mass in grams.

The q_{exp} values increased up to 118 ± 2 (+ 18%), 116 ± 2 (+ 2%), and 126 ± 3 mg g^{-1} (+ 16%) for the adsorption of DIC, KET, and NAP 50 ppm aqueous solutions by 75% GO-SWCNT BPs, confirming once again the best adsorption capacity of 75% GO-SWCNT BPs. The obtained q_{exp} values were higher than those obtained for the adsorption of DIC by rGO flakes (34.1 mg g^{-1}) [50], for DIC and NAP removal by some -COOH multi-walled carbon nanotubes (q_{exp} around 40 mg g^{-1}) [51], or for NAP removal by MOF powders (66.1 mg g^{-1}) (MIL-101-NO_2) [52]. Even if particular GO and MOF samples with comparable NSAID recovery values can be found in the literature [52–56], it is worth noting that GO-SWCNT BPs are self-standing films, which can be more easily used, recovered, and regenerated than any powder-like adsorbent (see infra).

Adsorption, including both chemisorption (involving ionic or covalent bonds) and physisorption (van der Waals forces), is a surface phenomenon where drug molecules accumulate at the interface between an adsorbent and a fluid solution of adsorbate [57]. Generally, the adsorption mechanism is dependent on the chemical nature of active compounds, the adsorbent properties (including chemical nature, number of active sites present, water wettability, and porosity), and the experimental conditions (e.g., initial concentration, ionic strength, pH, temperature, and contact time). Since the same experimental conditions were used for all BPs, the differences in adsorption can arise from their different physico-chemical characteristics. From previous studies [47], we know that the GO substitution in SWCNT BPs causes both a decrease in membrane porosity from around 74 ± 5% (neat SWCNT BP) to around 41 ± 5% (75% GO-SWCNT BP) and a decrease in the water contact angle from 71.3 ± 0.5° (neat SWCNT BP) to 41.2 ± 0.5° (75% GO-SWCNT BP). In addition, we found that the specific surface area changed from a value of 185 ± 20 m^2 g^{-1} (neat SWCNT BP) to 126 ± 15 m^2 g^{-1} (75% GO-SWCNT BP).

On the basis of the available datasheets of SWCNTs, COOH-SWCNTs, and GO, indicating a -COOH group percentage in COOH-SWCNTs of around 1%, and a 4.8%

oxidation at the GO edge, it is possible to speculate that the NSAID adsorption increase with GO amount could be attributed to the presence of a larger number of oxygen groups onto the BP surfaces, as it is known that they favor the adsorption of NSAID molecules by the formation of H-bonding [51,58]. Such chemical functionalities act as active sites for the NSAID capture and are able, at the same time, to improve surface wettability, thus compensating for the detrimental porosity reduction in GO-SWCNT BPs due to the better packaging of GO sheets.

Z-potential measurements, Figure 5a, showed that the pH_{zcp} (the pH value at which the net charge onto the membrane surface is zero) is ≈4.86 and ≈4.41 for SWCNT BPs and 75% GO-SWCNT BPs, respectively. Consequently, BPs possess a net positive surface charge at pH 4, becoming negative at pH 6 and 8 (Z-potential @ pH 8 < Z-potential @ pH 6).

The Z-potential of both membranes becomes more negative at pH 6 due to the ionization of the -COOH groups present on the SWNTs, most probably increase further as a result of the conformational changes of the nanodomains with pH [59]. In addition, when the pH of the solution exceeds the pK_a (4.15, 4.30, and 4.15 for DIC, KET, and NAP, respectively [60]), the active compounds dissociate more easily into their anionic forms. From the speciation diagram determined by the mass law equation (Figure 5b), the investigated NSAID molecules resulted in being in part negatively charged (molar fraction ≈ 40%) at pH 4, and almost all negatively charged at pH 6 and 8 (molar fraction ≈ 98 and ≈100%, respectively). These conditions made the NSAID adsorption onto BPs more favorable at pH 4 because of the presence of attractive electrostatic interactions between the anionic form of NSAID and the positively charged adsorbents and less favorable at pH 6 and 8, where electrostatic repulsions are expected to occur between negatively charged adsorbate and adsorbent, Figure 5c. Even if the BP surface charge at pH 8 is less negative than that at pH 6, the adsorption at the higher pH value could be hindered by the competition among a larger number of negatively charged adsorbent molecules. Therefore, the significant role of electrostatic interactions in the NSAID adsorption process by BPs is evident. The observed decrease of adsorption as a function of pH value agrees with the results previously reported in the literature [61,62]. Nevertheless, other adsorption processes, such as π-π interaction/stacking between SWCNT, GO and NSAID aromatic rings, as well as H-bonds, dispersive forces, and pore filling are expected to play a significant role in the adsorption of active compounds over BPs, accounting for the important recovery amount found at the different pH values [63].

(**a**) (**b**)

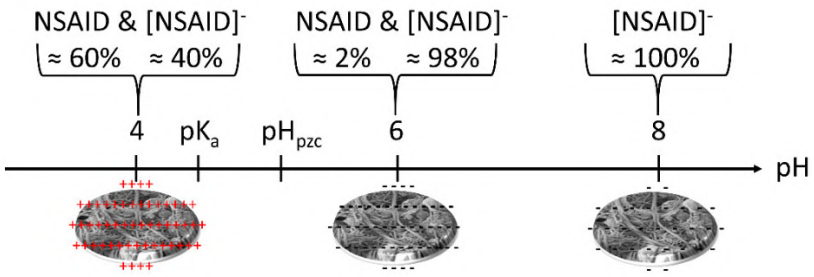

(**c**)

Figure 5. (**a**) Z-potential curves of an SWCNT BP (pH_{zcp} ≈ 4.86) and 75% GO-SWCNT BP (pH_{zcp} ≈ 4.41). The lines are just a guide for the eye. (**b**) Typical speciation diagram determined by the mass law equation for an NSAID. DIC, KET, and NAP are characterized by a pK_a value of 4.15, 4.30, and 4.15, respectively, as reported in [60]. (**c**) Naïve representation of NSAID and NSAID conjugates base *([NSAID]⁻)* molar fractions and charge present on BPs at the investigated pH values (4, 6, and 8).

In order to follow the adsorption of NSAIDs as a function of time at different concentrations (1, 10, and 50 ppm) by neat SWCNT and 75% GO-SWCNT BPs, kinetic experiments were also performed (Figure 6). Experimental data were fitted by a non-linear optimization method [64] with a pseudo-first-order or a pseudo-second-order equation.

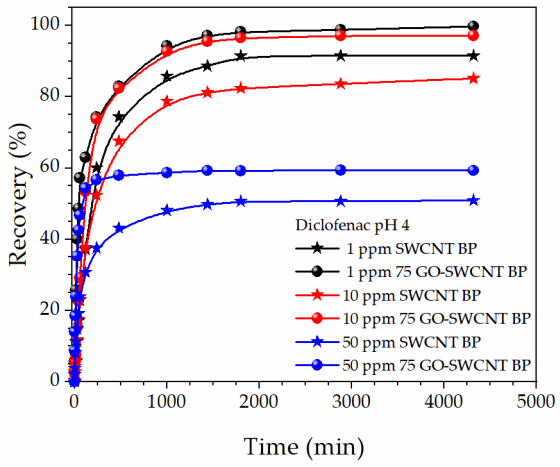

(**a**)

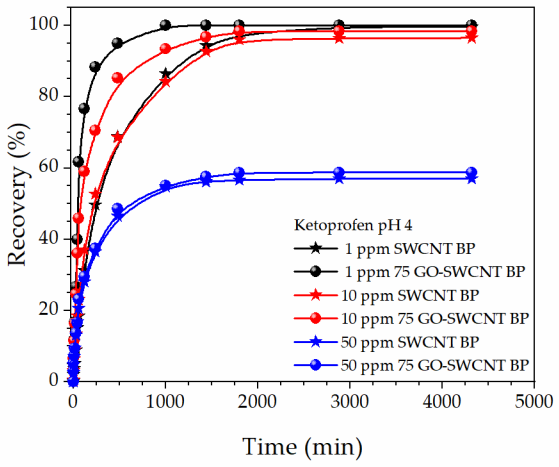

(**b**)

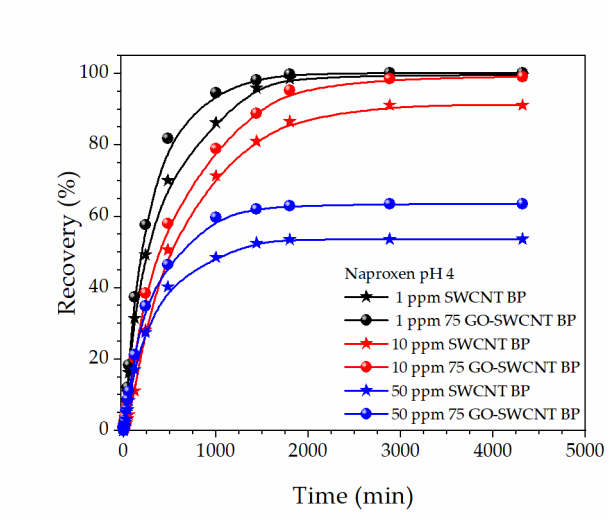

(**c**)

Figure 6. The time-dependent recovery percentage, *Re*(%), of: (**a**) Diclofenac, (**b**) Ketoprofen, and (**c**) Naproxen water solutions at pH 4 and different initial concentrations (1, 10, 50 ppm) for neat SWCNT and 75% GO-SWCNT BPs.

As per results reported in Table 1, the modeling indicated that the adsorption experimental data at 50 ppm were well fitted by the pseudo-second-order model compared to the pseudo-first-order as per their larger R^2 (greater than 0.993), in agreement with the fittings obtained for NSAIDs adsorption by other adsorbents [56].

Table 1. Pseudo-first and pseudo-second-order adsorption rate constants, k_1 (min^{-1}) and k_2 (g mg^{-1} min^{-1}), and adsorption capacity per unit of adsorbent mass at equilibrium, q_e (mg g^{-1}), by SWCNT BPs and 75% GO-SWCNT BPs for the three different NSAIDs (50 ppm).

	Pseudo-First Order Kinetics			**Pseudo-Second Order Kinetics**		
Diclofenac	**$k_1 \times 10^3$ (min^{-1})**	**q_e (mg g^{-1})**	**R^2**	**$k_2 \times 10^4$ (g mg^{-1} min^{-1})**	**q_e (mg g^{-1})**	**R^2**
SWCNT BP	10.1 ± 1.1	96.4 ± 2.5	0.9823	2.6 ± 0.4	103.0 ± 5.4	0.9961
75% GO-SWCNT BP	32.5 ± 2.5	116.1 ± 2.0	0.9752	8.4 ± 1.8	120.5 ± 8.3	0.9914
Ketoprofen	**$k_1 \times 10^3$ (min^{-1})**	**q_e (mg g^{-1})**	**R^2**	**$k_2 \times 10^3$ (g mg^{-1} min^{-1})**	**q_e (mg g^{-1})**	**R^2**
SWCNT BP	6.1 ± 0.7	110.2 ± 3.0	0.9756	1.4 ± 0.3	118.7 ± 8.3	0.9939
75% GO-SWCNT BP	6.4 ± 0.7	112.8 ± 3.1	0.9777	1.5 ± 0.3	121.8 ± 8.8	0.9934
Naproxen	**$k_1 \times 10^3$ (min^{-1})**	**q_e (mg g^{-1})**	**R^2**	**$k_2 \times 10^3$ (g mg^{-1} min^{-1})**	**q_e (mg g^{-1})**	**R^2**
SWCNT BP	2.9 ± 0.1	106.6 ± 0.8	0.9943	5.3 ± 1.1	121.1 ± 9.5	0.9980
75% GO-SWCNT BP	3.2 ± 0.1	125.9 ± 0.8	0.9960	5.7 ± 1.4	142.2 ± 9.4	0.9988

For all investigated NSAIDs, the pseudo-second-order adsorption rate constant, k_2, increases when SWCNT BPs (0.26 ± 0.04, 1.4 ± 0.3, and 5.3 ± 1.1 × 10^{-3} g mg^{-1} min^{-1}, for DIC, KET, and NAP, respectively) are replaced by GO-SWCNT BPs (0.84 ± 0.18, 1.5 ± 0.3, and 5.7 ± 1.4 x 10^{-3} g mg^{-1} min^{-1}, for DIC, KET, and NAP, respectively). The found adsorption rate constants are of the same order and magnitude as those recently obtained for the NSAID adsorption from water by an aluminum-based metal-organic framework, MIL-53, (3.7 and 5.6 × 10^{-3} g mg^{-1} min^{-1} for DIC and NAP, respectively) [61] and by biochar samples

[63], but lower than the adsorption rate constant for DIC adsorption by GO nanosheets ($\approx 10 \times 10^{-3}$ g mg^{-1} min^{-1}) [50,52].

Regeneration and performance stability are important items for any adsorbent in view of potential industrial applications. The adsorption performance of 75% GO-SWCNT BP was measured at pH 4 in a 10 ppm DIC solution after four regeneration cycles, performed by soaking the membranes in ethanol or 24 h in order to favor the release of the adsorbed NSAID. The initial DIC recovery after the first immersion of a 75% GO-SWCNT BP was 97.2%, decreasing to 93.5% after the fourth regeneration cycle, confirming the reusability and stability of GO-SWCNT BP in industrial wastewater applications. In addition, GO-SWCNT BP membranes offer the opportunity for easy scalability as filtration units both in parallel for a large-scale treatment and in series for an increase in the adsorption efficiency.

3. Materials and Methods

3.1. Buckypaper Preparation and Characterization

SWCNT BPs were prepared according to the wet method procedure reported in the literature [47] by using mixtures of commercially available single-walled carbon nanotubes, SWCNTs, (length > 5 μm, and average diameter of 1.4 ± 0.1 nm) and carboxylic acid functionalized SWCNTs (COOH-SWCNTs, 1.00% carboxylic acid, 0.5 < average bundle length < 1.5 μm, and 4 < diameter < 5 nm, as reported in their datasheets from Merck/Sigma Aldrich, Darmstadt, Germany). Briefly, after the dispersion of 50 mg SWCNT and COOH-SWCNT mixtures (wt. ratio 2:1) in a surfactant water solution (250 mL 0.4% TRITON X100) by an ultrasonic bath (M1800H-E, Bransonic, Danbury, CT, USA) for 30 min, the solutions were filtered through poly(tetrafluoroethylene disks (PTFE, diameter = 47 mm, average pore size = 5 μm, Durapore©, Merck, Darmstadt, Germany) by a vacuum pump (pressure = −0.04 bar). Then, BPs were washed several times with methanol, dried at room temperature, and, lastly, peeled off from the PTFE filter.

Single-walled carbon nanotube/graphene oxide buckypapers, GO-SWCNT BPs, were similarly prepared after the substitution of a given weight amount (20, 40, 60, and 75 wt.%) of the SWCNT mixture with an identical quantity of graphene oxide (GO, 15–20 sheets, 4.8% edge-oxidized, Merck/Sigma Aldrich, Darmstadt, Germany). As shown in Figure 1, the wet method gave BPs the aspect of flexible self-standing membranes (average thickness 100 ± 2 μm and average diameter 38 ± 1 mm). The maximum GO loading in GO-SWCNT BPs was limited at 75 wt.% as cracked films were obtained for larger GO amounts. All chemicals were reagent grade and purchased from Merck/Sigma Aldrich, Darmstadt, Germany.

The morphology of buckypapers was investigated by scanning electron microscopy (LEO 420, Leica Microsystems, Cambridge, UK, accelerating voltage of 10 kV) after their sputtering with an ultrathin gold layer.

The surface area of buckypapers was obtained from the N_2 adsorption isotherms at 77 K by a surface area analyzer (Belsorp Mini X, MicrotracBEL, Osaka, Japan) via the Brunauer-Emmett-Teller method. The surface charge of buckypapers was measured by a zeta potential analyzer (SurPASS TM 3, Anton Paar Italia S.R.L., Turin, Italy, equipped with an adjustable gap cell) as a function of pH value (from about pH 9 to pH 3 @ T = 25 °C). A pair of each membrane with a cross-section of 2 × 1 cm^2 was mounted on the sample holders. The changes in pH were achieved by the addition of 0.05 M HCl, and the zeta potential was calculated from streaming potential measurements using the equation by Helmholtz and Smoluchowski [65].

3.2. NSAID Adsorption by Buckypapers

The conditions used for the NSAID adsorption by SWCNT and GO-SWCNT buckypapers were as follows: Buckypaper mass 50 mg, NSAID solution volume 200 mL, NSAID concentration 1, 10, and 50 ppm, contact time 0–4320 min, temperature 25 °C, pH

4, 6, and 8. NSAID concentration was determined by UV-Vis analyses on an Evolution 201 spectrophotometer (ThermoFisher Scientific, Hillsboro, OR, USA) operating with 1.0 cm quartz cells by using the calibration curves of DIC, KET, and NAP. Ultrapure deionized water (18.3 MΩ cm, Arioso, Human Corporation, Korea) was used for the preparation of the aqueous solution after filtration by a 0.45 μm filter (Millex Syringe Filter, Merck, Darmstadt, Germany).

The concentrations of undissociated NSAIDs and their conjugated base, $[NSAID]^-$, as a function of pH were calculated with the following Henderson-Hasselbalch Equation (3):

$$pH = pK_a + log\frac{[NSAID]^-}{NSAID} \quad (3)$$

The speciation diagram clearly indicates that around 60% of all NSAID molecules in the aqueous solution were in a neutral state at pH < 4, Figure 5b.

Kinetic experiments were performed in order to follow the adsorption of NSAIDs as a function of time at different concentrations (1, 10, and 50 ppm) by neat SWCNT and 75% GO-SWCNT BPs.

It is known from the literature [53] that the rate equation for NSAIDS adsorption capacity per unit of adsorbent mass (mg g^{-1}), q_t, by carbonaceous adsorbents can follow either the Lagergren first-order Equation (4) or a pseudo-second-order Equation (5):

$$\frac{dq_t}{dt} = k_1(q_e - q_t) \quad (4)$$

$$\frac{dq_t}{dt} = k_2(q_e - q_t)^2 \quad (5)$$

where k_1 (min^{-1}) and k_2 (g mg^{-1} min^{-1}) are the pseudo-first and pseudo-second order adsorption rate constants, q_e is the NSAID adsorption capacity per unit of adsorbent mass (mg g^{-1}) at equilibrium, respectively. The experimental concentrations measured as a function of time, *C(t)*, were used to determine the experimental amount, $q_{exp}(t)$, (mg g^{-1}) of NSAID adsorbed by BPs, according to the following Equation (6):

$$q_{exp}(t) = \frac{C_0 - C(t)}{m} \times V \quad (6)$$

where C_0 and *C(t)* are the NSAID concentration in the solution at time zero and *t*, respectively. *V* is the volume of NSAID solution, and *m* is the mass of BPs.

Experimental data were fitted by a non-linear optimization method [64] with the following Equations (7) and (8), respectively:

$$q_t = q_e(1 - e^{-k_1 t}) \quad (7)$$

and

$$q_t = \frac{k_2 q_e^2 t}{1 + k_2 q_e t} \quad (8)$$

which can be easily obtained from the integration of Equations (4) and (5).

All measurements were done in triplicate, and data were expressed as means ± SD. The kinetics parameters were calculated by OriginPro 2019 Software (OriginLab Corporation, Northampton, MA, USA).

4. Conclusions

In this work, GO-SWCNT BPs were tested as adsorbent membranes of non-steroidal anti-inflammatory drugs, such as Diclofenac, Ketoprofen, and Naproxen. BPs were prepared with increasing GO wt. contents and their adsorption capacity was measured at different pH values and drug initial concentrations. The maximum NSAID removal was obtained at pH 4 and increased with a larger GO amount. For solutions with a drug concentration of 1 and 10 ppm, 75% GO-SWCNT BPs were able to remarkably reduce the

NSAID amount, with a recovery always higher than 97%, while in the case of 50 ppm solutions, the adsorption capacity increased up to 118, 116, and 126 mg g^{-1} for DIC, KET, and NAP, respectively. The adsorption efficiency was maintained over five adsorption/four regeneration cycles without any important reduction (less than 4%).

This paper confirms that the partial substitution of SWCNTs with GO can increase the adsorption properties of SWCNT BPs towards NSAIDs without affecting their mechanical properties. As a consequence, they can still be used as flexible and self-standing membranes for a cheap and fast removal of NSAIDs from drinking water resources and allow an easier recovery and reuse than powder-like adsorbents can. Finally, it should be emphasized the importance of the easy scalability of the proposed adsorption membranes both in series for an efficiency increase and in parallel for applications in large-scale wastewater treatment plants. Overall, the experimental evidence here reported well addressed the precautionary principles towards the environment and human health, suggesting the adoption of adequate wastewater treatment techniques able to ensure the maximal removal of emerging pollutants, including non-steroidal anti-inflammatory drugs.

Author Contributions: Conceptualization and methodology, G.C., G.D.F., A.I.M. and F.P.N.; software, G.C., M.C. and A.V.N.; validation, G.D.F. and F.P.N.; formal analysis, G.C., G.D.F. and F.P.N.; investigation, M.B. and A.T.; data curation, M.B., M.C., A.V.N. and A.T.; writing—original draft preparation, G.D.F. and F.P.N.; writing—review and editing, G.D.F., G.C. and F.P.N.; supervision, G.D.F. and F.P.N. All authors have read and agreed to the published version of the manuscript.

Funding: The research activity of M.C. is funded by the Italian Ministry for University and Research under the program PON R&I 2014—2020 Azione IV.6—"Contratti di ricerca su tematiche Green" CUP: H25F21001230004. The research activity of M.B. is funded by a scholarship from Regione Calabria (grant POR Calabria 2014—2020—Azioni 10.5.6 e 10.5.12).

Institutional Review Board Statement: Not applicable.

Informed Consent Statement: Not applicable.

Data Availability Statement: Data are contained within the article.

Conflicts of Interest: The authors declare no conflict of interest.

Sample Availability: Samples are available from the authors.

References

1. Stancova, V.; Zikova, A.; Svobodova, Z.; Kloas, W. Effects of the non—Steroidal anti—Inflammatory drug (NSAID) naproxen on gene expression of antioxidant enzymes in zebrafish (*Danio rerio*). *Environ. Toxicol. Pharmacol.* **2015**, *40*, 343–348. https://doi.org/10.1016/j.etap.2015.07.009.
2. Boxall, A.B.A.; Rudd, M.A.; Brooks, B.W.; et al. Pharmaceuticals and personal care products in the environment: What are the big questions? *Environ. Health Perspect.* **2012**, *120*, 1221–1229. https://doi.org/10.1289/ehp.1104477.
3. Ternes, T.A. Occurrence of drugs in German sewage treatment plants and rivers. *Water Res.* **1998**, *32*, 3245–3260. https://doi.org/10.1016/S0043-1354(98)00099-2.
4. Heberer, T. Occurrence, fate and removal of pharmaceutical residues in the aquatic environment: A review of recent research data. *Toxicol. Lett.* **2002**, *131*, 5–17. https://doi.org/10.1016/S0378-4274(02)00041-3.
5. Hernando, M.D.; Mezcua, M.; Fernández-Alba, A.R.; Barceló, D. Environmental risk assessment of pharmaceutical residues in wastewater effluents, surface waters and sediments. *Talanta* **2006**, *69*, 334–342. https://doi.org/10.1016/j.talanta.2005.09.037.
6. Lu, M.-C.; Chen, Y.Y.; Chiou, M.-R.; Chen, M.Y.; Fan, H.-J. Occurrence and treatment efficiency of pharmaceuticals in landfill leachates. *Waste Manag.* **2016**, *55*, 257–264. https://doi.org/10.1016/j.wasman.2016.03.029.
7. Stackelberg, P.E.; Furlong, E.T.; Meyer, M.T.; Zaug, S.D.; Henderson, A.K.; Reissman, D.B. Persistence of pharmaceutical compounds and other organic wastewater contaminants in a conventional drinking-water treatment plant. *Sci. Total Environ.* **2004**, *329*, 99–113. https://doi.org/10.1016/j.scitotenv.2004.03.015.
8. Okuda, T.; Kobayashi, Y.; Nagao, R.; Yamashita, N.; Tanaka, H.; Tanaka, S.; Fujii, S.; Konishi, C.; Houwa, I. Removal efficiency of 66 pharmaceuticals during wastewater treatment process in Japan. *Water Sci. Technol.* **2008**, *57*, 65–71. https://doi.org/10.2166/wst.2008.822.

9. Gulkowska, A.; Leung, H.W.; So, M.K.; Taniyasu, S.; Yamashita, N.; Yeunq, L.W.Y.; Richardson, B.J.; Lei, A.P.; Giesy, J.P.; Lam, P.K.S. Removal of antibiotics from wastewater by sewage treatment facilities in Hong Kong and Shenzhen (China). *Water Res.* **2008**, *42*, 395–403. https://doi.org/10.1016/j.watres.2007.07.031.
10. Manzo, V.; Honda, L.; Navarro, O.; Ascar, L.; Richter, P. Microextraction of nonsteroidal anti-inflammatory drugs from waste water samples by rotating-disk sorptive extraction. *Talanta* **2014**, *128*, 486–492. https://doi.org/10.1016/j.talanta.2014.06.003.
11. Al-Rifai, J.; Gabelish, C.; Schäfer, A. Occurrence of pharmaceutically active and nonsteroidal estrogenic compounds in three different wastewater recycling schemes in Australia. *Chemosphere* **2007**, *69*, 803–815. https://doi.org/10.1016/j.chemosphere.2007.04.069.
12. Kummerer, K. Drugs in the environment: Emission of drugs, diagnostic aids and disinfectants into wastewater by hospitals in relation to other sources—A review. *Chemosphere* **2001**, *45*, 957–969. https://doi.org/10.1016/S0045-6535(01)00144-8.
13. Kosma, C.I.; Lambropoulou, D.A.; Albanis, T.A. Investigation of PPCPs in wastewater treatment plants in Greece: Occurrence, removal and environmental risk assessment. *Sci. Total Environ.* **2014**, *466–467*, 421–438. https://doi.org/10.1016/j.scitotenv.2013.07.044.
14. Lonappan, L.; Brar, S.K.; Das, R.K.; Verma, M.; Surampalli, R.Y. Diclofenac and its transformation products: Environmental occurrence and toxicity—A review. *Environ. Int.* **2016**, *96*, 127–138. https://doi.org/10.1016/j.envint.2016.09.014.
15. Leng, X.-Y.; Liu, C.-N.; Wang, S.-C.; Peng, H.-D.; Wang, D.-G.; Pan, H.-F. Comparison of the efficacy of nonsteroidal anti-inflammatory drugs and opioids in the treatment of acute renal colic: A systematic review and meta-analysis. *Front. Pharmacol.* **2022**, *12*, 728908. https://www.frontiersin.org/articles/10.3389/fphar.2021.728908.
16. Izadi, P.; Izadi, P.; Salem, R.; Papry, S.A.; Magdouli, S.; Pulicharla, R.; Brar, S.K. Non-steroidal anti-inflammatory drugs in the environment: Where were we and how far we have come? *Environ. Pollut.* **2020**, *267*, 115370. https://doi.org/10.1016/j.envpol.2020.115370.
17. Mailler, R.; Gasperi, J.; Chebbo, G.; Rocher, V. Priority and emerging pollutants in sewage sludge and fate during sludge treatment. *Waste Manag.* **2014**, *34*, 1217–1226., https://doi.org/10.1016/j.wasman.2014.03.028.
18. Zhang, H.; Zhang, P.; Ji, Y.; Tian, J.; Du, Z. Photocatalytic degradation of four non-steroidal anti-inflammatory drugs in water under visible light by P25-TiO_2/tetraethyl orthosilicate film and determination via ultra-performance liquid chromatography electrospray tandem mass spectrometry. *Chem. Eng. J.* **2015**, *262*, 1108–1115. https://doi.org/10.1016/j.cej.2014.10.019.
19. Rizzo, L. Bioassays as a tool for evaluating advanced oxidation processes in water and wastewater treatment. *Water Res.* **2011**, *45*, 4311–4340. https://doi.org/10.1016/j.watres.2011.05.035.
20. Vergili, I. Application of nanofiltration for the removal of carbamazepine, diclofenac and ibuprofen from drinking water sources. *J. Environ. Manag.* **2013**, *127*, 177–187. https://doi.org/10.1016/j.jenvman.2013.04.036.
21. Benitez, F.J.; Acero, J.L.; Real, F.J.; Roldán, G.; Rodriguez, E. Ultrafiltration and nanofiltration membranes applied to the removal of the pharmaceuticals amoxicillin, naproxen, metoprolol and phenacetin from water. *J. Chem. Technol. Biotechnol.* **2011**, *86*, 858–866. https://doi.org/10.1002/jctb.2600.
22. Patel, S.; Mondal, S.; Majumder, S.K.; Das, P.; Ghosh, P. Treatment of a pharmaceutical industrial effluent by a hybrid process of advanced oxidation and adsorption. *ACS Omega* **2020**, *5*, 32305–32317. https://doi.org/10.1021/acsomega.0c04139.
23. Yu, Z.; Peldszus, S.; Huck, P.M. Adsorption characteristics of selected pharmaceuticals and an endocrine disrupting compound-naproxen, carbamazepine and nonylphenol-on activated carbon. *Water Res.* **2008**, *42*, 2873–2882. https://doi.org/10.1016/j.watres.2008.02.020.
24. Ahmed, M.J. Adsorption of non-steroidal anti-inflammatory drugs from aqueous solution using activated carbons: Review. *J. Environ. Manag.* **2017**, *190*, 274–282. https://doi.org/10.1016/j.jenvman.2016.12.073.
25. Vona, A.; di Martino, F.; Garcia-Ivars, J.; Pico, Y.; Mendoza-Roca, J.-A.; Iborra-Clar, M.-I. Comparison of different removal techniques for selected pharmaceuticals. *J. Water Process Eng.* **2015**, *5*, 48–57. https://doi.org/10.1016/j.jwpe.2014.12.011.
26. Domínguez, J.R.; González, T.; Palo, P.; Cuerda-Correa, E.M. Removal of common pharmaceuticals present in surface waters by Amberlite XAD-7 acrylic-ester-resin: Influence of pH and presence of other drugs. *Desalination* **2011**, *269*, 231–238. https://doi.org/10.1016/j.desal.2010.10.065.
27. Ternes, T.A.; Meisenheimer, M.; McDowell, D.; Sacher, F.; Brauch, H.J.; Haist-Gulde, B.; Preuss, G.; Wilme, U.; Zulei-Seibert, N. Removal of pharmaceuticals during drinking water treatment. *Environ. Sci. Technol.* **2002**, *36*, 3855–3863. https://doi.org/10.1021/es015757k.
28. Sandoval-González, A.; Robles, I.; Pineda-Arellano, C.A.; Martínez-Sánchez, C. Removal of anti-inflammatory drugs using activated carbon from agro-industrial origin: Current advances in kinetics, isotherms, and thermodynamic studies. *J. Iran. Chem. Soc.* **2022**, *19*, 4017–4033. https://doi.org/10.1007/s13738-022-02588-7.
29. Costa, R.L.T.; do Nascimento, R.A.; de Araújo, R.C.S.; Vieira, M.G.A.; da Silva, M.G.C.; de Carvalho, S.M.L.; de Faria, L.J.G. Removal of non-steroidal anti-inflammatory drugs (NSAIDs) from water with activated carbons synthetized from waste murumuru (*Astrocaryum murumuru Mart.*): Characterization and adsorption studies. *J. Mol. Liq.* **2021**, *343*, 116980. https://doi.org/10.1016/j.molliq.2021.116980.
30. Phasuphan, W.; Praphairaksit, N.; Imyim, A. Removal of ibuprofen, diclofenac, and naproxen from water using chitosan-modified waste tire crumb rubber. *J. Mol. Liq.* **2019**, *294*, 111554. https://doi.org/10.1016/j.molliq.2019.111554.
31. Wang, Y.; Zhang, Y.; Cui, J.; Li, S.; Yuan, M.; Wang, T.; Hu, Q.; Hou, X. Fabrication and characterization of metal organic frameworks/polyvinyl alcohol cryogel and their application in extraction of non-steroidal anti-inflammatory drugs in water samples. *Anal. Chim. Acta* **2018**, *1022*, 45–52, https://doi.org/10.1016/j.aca.2018.03.056.

32. Soares, S.F.; Fernandes, T.; Sacramento, M.; Trindade, T.; Daniel-da-Silva, A.L. Magnetic quaternary chitosan hybrid nanoparticles for the efficient uptake of diclofenac from water. *Carbohydr. Polym.* **2019**, *203*, 35–44. https://doi.org/10.1016/j.carbpol.2018.09.030.
33. Zhang, S.; Dong, Y.; Yang, Z.; Yang, W.; Wu, J.; Dong, C. Adsorption of pharmaceuticals on chitosan-based magnetic composite particles with core-brush topology. *Chem. Eng. J.* **2016**, *304*, 325–334., https://doi.org/10.1016/j.cej.2016.06.087.
34. Hanbali, G.; Jodeh, S.; Hamed, O.; Bol, R.; Khalaf, B.; Qdemat, A.; Samhan, S. Enhanced ibuprofen adsorption and desorption on synthesized functionalized magnetic multiwall carbon nanotubes from aqueous solution. *Materials* **2020**, *13*, 3329. https://doi.org/10.3390/ma13153329.
35. Mazen, N. An overview of carbon-based materials for the removal of pharmaceutical active compounds. In *Carbon-Based Material for Environmental Protection and Remediation*; Bartoli, M., Frediani, M., Rosi, L., Eds.; IntechOpen: London, UK, 2020. https://doi.org/10.5772/intechopen.91934.
36. Mohammadi Nodeh, M.K.; Radfard, M.; Zardari, L.A.; Rashidi Nodeh, H. Enhanced removal of naproxen from wastewater using silica magnetic nanoparticles decorated onto graphene oxide; parametric and equilibrium study. *Sep. Sci. Technol.* **2018**, *53*, 2476–2485. https://doi.org/10.1080/01496395.2018.1457054.
37. Khan, F.S.A.; Mubarak, N.M.; Tan, Y.H.; Khalid, M.; Karri, R.R.; Walvekar, R.; Abdullah, E.C.; Nizamuddin, S.; Mazari, S.A. A comprehensive review on magnetic carbon nanotubes and carbon nanotube-based buckypaper for removal of heavy metals and dyes. *J. Hazard. Mater.* **2021**, *413*, 125375. https://doi.org/10.1016/j.jhazmat.2021.125375.
38. Alshahrani, A.; Alharbi, A.; Alnasser, S.; Almihdar, M.; Alsuhybani, M.; AlOtaibi, B. Enhanced heavy metals removal by a novel carbon nanotubes buckypaper membrane containing a mixture of two biopolymers: Chitosan and i-carrageenan. *Separ. Purif. Technol.* **2021**, *276*, 119300. https://doi.org/10.1016/j.seppur.2021.119300.
39. De Filpo, G.; Pantuso, E.; Mashin, A.I.; Baratta, M.; Nicoletta, F.P. WO_3/buckypaper membranes for advanced oxidation processes. *Membranes* **2020**, *10*, 157. https://doi.org/10.3390/membranes10070157.
40. Rashid, M.H.-O.; Ralph, S.F. Carbon nanotube membranes: Synthesis, properties, and future filtration applications. *Nanomaterials* **2017**, *7*, 99. https://doi.org/10.3390/nano7050099.
41. Patole, S.P.; Arif, M.F.; Susantyoko, R.A.; Almheiri, S.; Kumar, S. A wet-filtration-zipping approach for fabricating highly electroconductive and auxetic graphene/carbon nanotube hybrid buckypaper. *Sci. Rep.* **2018**, *8*, 12188. https://doi.org/10.1038/s41598-018-30009-4.
42. Xia, Q.; Zhang, Z.; Liu, Y.; Leng, J. Buckypaper and its composites for aeronautic applications. *Compos. Part B Eng.* **2020**, *199*, 108231. https://doi.org/10.1016/j.compositesb.2020.108231.
43. Aslam, M.M.-A.; Kuo, H.-W.; Den, W.; Usman, M.; Sultan, M.; Ashraf, H. Functionalized carbon nanotubes (CNTs) for water and wastewater treatment: Preparation to application. *Sustainability* **2021**, *13*, 5717. https://doi.org/10.3390/su13105717.
44. Shawky, H.A.; El-Aassar, A.H.M.; Abo-Zeid, D.E. Chitosan/carbon nanotube composite beads: Preparation, characterization, and cost evaluation for mercury removal from wastewater of some industrial cities in Egypt. *J. Appl. Polym. Sci*. **2012**, *125*, E93–E101. https://doi.org/10.1002/app.35628.
45. Baratta, M.; Mastropietro, T.F.; Bruno, R.; Tursi, A.; Negro, C.; Ferrando-Soria, J.; Mashin, A.I.; Nezhdanov, A.; Nicoletta, F.P.; De Filpo, G.; et al. Multivariate metal–organic framework/single–walled carbon nanotube buckypaper for selective lead decontamination. *ACS Appl. Nano Mater.* **2022**, *5*, 5223–5233. https://doi.org/10.1021/acsanm.2c00280.
46. Tursi, A.; Mastropietro, T.F.; Bruno, R.; Baratta, M.; Ferrando-Soria, J.; Mashin, A.I.; Nicoletta, F.P.; Pardo, E.; De Filpo, G.; Armentano, D. Synthesis and enhanced capture properties of a new BioMOF@SWCNT-BP: Recovery of the endangered rare-earth elements from aqueous systems. *ACS Adv. Mater. Interfaces* **2021**, *8*, 2100730. https://doi.org/10.1002/admi.202100730.
47. Baratta, M.; Tursi, A.; Curcio, M.; Cirillo, G.; Nicoletta, F.P.; De Filpo, G. GO-SWCNT Buckypapers as an enhanced technology for water decontamination from lead. *Molecules* **2022**, *27*, 4044. https://doi.org/10.3390/molecules27134044.
48. Huang, J.; Her, S.-C.; Yang, X.; Zhi, M. Synthesis and characterization of multi-walled carbon nanotube/graphene nanoplatelet hybrid film for flexible strain sensors. *Nanomaterials* **2018**, *8*, 786. https://doi.org/10.3390/nano8100786..
49. Musielak, M.; Gagor, A.; Zawisza, B.; Talik, E.; Sitko, R. Graphene oxide/carbon nanotube membranes for highly efficient removal of metal ions from water. *ACS Appl. Mater. Interfaces* **2019**, *11*, 28582–28590. https://doi.org/10.1021/acsami.9b11214.
50. Jauris, I.M.; Matos, C.F.; Saucier, C.; Lima, E.C.; Zarbin, A.J.G.; Fagan, S.B.; Machado, F.M.; Zanella, I. Adsorption of sodium diclofenac on graphene: A combined experimental and theoretical study. *Phys. Chem. Chem. Phys.* **2016**, *18*, 1526–1536. https://doi.org/10.1039/c5cp05940b.
51. Czech, B.; Oleszczuk, P. Sorption of diclofenac and naproxen onto MWCNT in model wastewater treated by H2O2 and/or UV. *Chemosphere* **2016**, *149*, 272–278. https://doi.org/10.1016/j.chemosphere.2015.12.057.
52. Hiew, B.Y.Z.; Lee, L.Y.; Lee, X.J.; Gan, S.; Thangalazhy-Gopakumar, S.; Lim, S.S.; Pan, G.-T.; Yang, T.C.-K. Adsorptive removal of diclofenac by graphene oxide: Optimization, equilibrium, kinetic and thermodynamic studies. *J. Taiwan Inst. Chem. Eng.* **2019**, 98, 150–162. https://doi.org/10.1016/j.jtice.2018.07.034.
53. Seo, P.W.; Bhadra, B.N.; Ahmed, I.; Khan, N.A.; Jhung, S.H. Adsorptive removal of pharmaceuticals and personal care products from water with functionalized metalorganic frameworks: Remarkable adsorbents with hydrogen-bonding abilities. *Sci. Rep.* **2016**, *6*, 34462. https://doi.org/10.1038/srep34462.
54. Lin, S.; Zhao, Y.; Yun, Y.-S. Highly effective removal of nonsteroidal anti-inflammatory pharmaceuticals from water by Zr(IV)-based metal–organic framework: Adsorption performance and mechanisms. *ACS Appl. Mater. Interfaces* **2018**, *10*, 28076–28085. https://doi.org/10.1021/acsami.8b08596.

55. Bhadra, B.N.; Ahmed, I.; Kim, S.; Jhung, S.H. Adsorptive removal of ibuprofen and diclofenac from water using metal-organic framework-derived porous carbon. *Chem. Eng. J.* **2017**, *314*, 50–58. https://doi.org/10.1016/j.cej.2016.12.127.
56. Liu, W.; Shen, X.; Han, Y.; Liu, Z.; Dai, W.; Dutta, A.; Kumar, A.; Liu, J. Selective adsorption and removal of drug contaminants by using an extremely stable Cu(II)-based 3D metal-organic framework. *Chemosphere* **2019**, *215*, 524–531. https://doi.org/10.1016/j.chemosphere.2018.10.075.
57. Dąbrowski, A. Adsorption-from theory to practice. *Adv. Colloid Interface Sci.* **2001**, *93*, 135–224. https://doi.org/10.1016/S0001-8686(00)00082-8.
58. Song, J.Y.; Jhung, S.H. Adsorption of pharmaceuticals and personal care products over metal-organic frameworks functionalized with hydroxyl groups: Quantitative analyses of H-bonding in adsorption. *Chem. Eng. J.* **2017**, *322*, 366–374. https://doi.org/10.1016/j.cej.2017.04.036.
59. White, B.; Banerjee, S.; O'Brien, S.; Turro, N.J.; Herman, I.P. Zeta-potential measurements of surfactant-wrapped individual single-walled carbon nanotubes. *J. Phys. Chem. C* **2007**, *111*, 13684–13690. https://doi.org/10.1021/jp070853e.
60. Sangster, J. *LOGKOW Databank*; Sangster Res. Lab.: Montreal, QC, Canada. 1994.
61. Karami, A.; Sabouni, R.; Ghommem, M. Experimental investigation of competitive co-adsorption of naproxen and diclofenac from water by an aluminum-based metalorganic framework. *J. Mol. Liq.* **2020**, *305*, 112808. https://doi.org/10.1016/j.molliq.2020.112808.
62. Sun, W.; Li, H.; Li, H.; Li, S.; Cao, X. Adsorption mechanisms of ibuprofen and naproxen to UiO-66 and UiO-66-NH2: Batch experiment and DFT calculation. *Chem. Eng. J.* **2019**, *360*, 645–653. https://doi.org/10.1016/j.cej.2018.12.021.
63. Tomul, F.; Arslan, Y.; Kabak, B.; Trak, D.; Kendüzler, E.; Lima, E.C.; Tran, H.N. Peanut shells-derived biochars prepared from different carbonization processes: Comparison of characterization and mechanism of naproxen adsorption in water. *Sci. Total Env.* **2020**, *726*, 137828. https://doi.org/10.1016/j.scitotenv.2020.137828.
64. Cirillo, G.; Curcio, M.; Madeo, L.F.; Iemma, F.; De Filpo, G.; Hampel, S.; Nicoletta, F.P. Carbon Nanotubes Hybrid Hydrogels for Environmental Remediation: Evaluation of Adsorption Efficiency under Electric Field. *Molecules* **2021**, *26*, 7001. https://doi.org/10.3390/molecules26227001.
65. Chun, M.S.; Lee, S.Y.; Yang, S.M. Estimation of zeta potential by electrokinetic analysis of ionic fluid flows through a divergent microchannel. *J. Colloid Interface Sci.* **2003**, *266*, 120–126. https://doi.org/10.1016/S0021-9797(03)00576-9.

Chapter 9

membranes

MDPI

Article

WO_3/Buckypaper Membranes for Advanced Oxidation Processes

Giovanni De Filpo [1,*], Elvira Pantuso [2], Aleksander I. Mashin [3], Mariafrancesca Baratta [1] and Fiore Pasquale Nicoletta [2,*]

1 Department of Chemistry and Chemical Technologies, University of Calabria, 87036 Rende (CS), Italy; mariafrancesca.baratta@unical.it
2 Department of Pharmacy, Health and Nutritional Sciences, University of Calabria, 87036 Rende (CS), Italy; elvirapnt.ep@gmail.com
3 Applied Physics & Microelectronics, Lobachevsky State University of Nizhni Novgorod, 603950 Nizhni Novgorod, Russian; mashin@unn.ru
* Correspondence: giovanni.defilpo@unical.it (G.D.F.); fiore.nicoletta@unical.it (F.P.N.); Tel.: +39-0984-492095 (G.D.F.); +39-0984-493194 (F.P.N.)

Received: 6 June 2020; Accepted: 18 July 2020; Published: 20 July 2020

Abstract: Photocatalytic materials, such as WO_3, TiO_2, and ZnO nanoparticles, are commonly linked onto porous polymer membranes for wastewater treatment, fouling mitigation and permeation enhancement. Buckypapers (BPs) are entanglements of carbon nanotubes, which have been recently proposed as innovative filtration systems thanks to their mechanical, electronic, and thermal properties. In this work, flexible membranes of single wall carbon nanotubes are prepared and characterized as efficient substrates to deposit by chemical vapor deposition thin layers of WO_3 and obtain, in such a way, WO_3/BP composite membranes for application in advanced oxidation processes. The photocatalytic efficiency of WO_3/BP composite membranes is tested against model pollutants in a small continuous flow reactor and compared with the performance of an equivalent homogeneous WO_3-based reactor.

Keywords: chemical vapor deposition; buckypapers; single wall carbon nanotubes; tungsten trioxide; photocatalysis; membranes

1. Introduction

Advanced oxidation processes, AOPs, allow the mineralization of organic pollutants by the generation of highly reactive hydroxyl radicals [1]. Photocatalytic reactions are particular AOPs, which are carried out when a catalyst is irradiated by a radiation of suitable wavelength [2].

Photocatalysis finds several interesting applications including selective organic reactions, pollutant degradation, photocatalytic surfaces (e.g., tiles, cements, paints, and asphalts), filters for air purification, water splitting in H_2 and O_2, water purification plants, CO_2 reduction to energy fuels and bacterial disinfection [3–8]. Semiconductors are the most common used materials used in photocatalytic processes. Upon irradiation, electrons are promoted from the valence band to the conduction band, generating electron–hole pairs. Electrons and holes can move to the semiconductor surface and generate oxidizing species such as hydroxyl radicals ($OH^{\bullet}$), superoxide anions ($O_2^{-\bullet}$) and hydrogen peroxide molecules (H_2O_2), which are able to react with the present chemical species (dyes, pollutants, and other undesired molecules) and degrade them [9]. Several materials have photocatalytic properties (GaP, GaAs, CdSe, CdS, Fe_2O_3, TiO_2, WO_3, ZnO, SnO_2, and CdS, just to mention a few), however not all of them are sufficiently efficient and stable over time to be used. In fact, GaP, GaAs, CdSe, CdS, or Fe_2O_3 are less stable in the air and degrade more easily. ZnO forms a passivating layer of $Zn(OH)_2$ on

its surface, which seriously compromises its photocatalytic properties [9]. Another important factor determining the choice of a semiconductor is its band-gap value, which must be as small as possible in order to allow the use of electromagnetic radiation with larger wavelengths. Titanium dioxide, TiO_2, and tungsten trioxide, WO_3, are low-cost semiconductor materials characterized by reduced toxicity towards environment and health and relatively low energy band-gaps (3.2 eV and 2.6 eV, respectively), which allow their activation with UV-Vis light (387 nm and 476 nm, respectively) [10].

Further problems for the use of semiconductors in the photocatalytic processes are:

1. The need of high surface area, which can be overcome by using nanometer sized materials; and
2. The semiconductor recovery after their use, which can be solved, for example, by nano-semiconductors with a magnetic core, by chemically cross-linked semiconductor nanoparticles onto polymer or ceramic membranes and, more recently, by vapor deposition of thin semiconductor films onto suitable substrates [11].

Thin film deposition methods can be distinguished in physical vapor deposition, PVD, and chemical vapor deposition, CVD, processes. In both methods, atoms or molecules in their vapor phase are carried onto the substrate surface and settle to form a thin layer [11].

Food, pharmaceutical, and, more in general, chemical plants need efficient separation and purification processes in order to guarantee an efficient treatment of their wastewaters. The removal of toxic pollutants from industrial wastewaters is a challenge due to the facts that they could not be effectively removed by filtration, adsorption, sedimentation, bio-oxidation, chlorination, coagulation, UV, and other classical treatments [12,13] and could represent potential threats to environment and health even at low concentrations (few ng L^{-1}) as a consequence of their bio-accumulation [14,15].

Recently, polymer membranes have been suggested as simple and efficient materials to be used in water treatments including separation, purification, desalinization, recovery of critical raw materials and AOPs [16–19]. In fact, photocatalytic membranes, i.e., membranes with embedded or supported semiconductors by chemical binding, physical blending and vapor deposition, have been prepared in order to reduce/mitigate membrane fouling [20,21], enhance filtration fluxes [22], degrade wastewater pollutants, and remediate the concentrate [23]. Nevertheless, the binding of photocatalysts and polymer functionalization could need several chemical reactions and long cleaning processes, while the physical blending generally alter the mechanical properties of membranes and reduce the photocatalytic performance, as only the catalysts onto the membrane surface can play their photocatalytic activity.

In addition to their potential applications as TV screens, fire protection systems, heat dispersion in microelectronics, electrical-conductive tissue engineering, electromagnetic interferences shielding, electrodes for batteries and supercapacitors, buckypapers (BPs) have been proposed as innovative, high-temperature resistant and lightweight filtration systems. They consist of an entangled assembly of carbon nanotubes (CNTs) obtained by filtration of CNT dispersions through a polymer membrane [24,25]. According to such simple procedure, it is possible to get large-scale BP membranes that merge the mechanical, electronic, and thermal properties of CNTs with the flexibility, porosity, and transport properties of polymer membranes [26]. At a microscopic level, BPs show a highly disordered porous morphology due to π–π and van der Waals interactions between and within bundles of carbon nanotubes [27,28]. Consequently, BPs can result brittle. Such a problem and the risk of nanotubes release can be overcome enhancing the mechanical properties of BPs by polymer intercalation [29,30].

In this work, flexible membranes of single wall carbon nanotubes, SWNT, (or buckypaper, BP) were prepared and characterized as efficient substrates to deposit by CVD thin layers of WO_3 and obtain, in such a way, WO_3/BP composite membranes for application in advanced oxidation processes. The photocatalytic efficiency of WO_3/BP composite membranes was tested against model pollutants (Methylene Blue, Indigo Carmine, and Diclofenac Sodium) in a small continuous flow reactor and compared with the performance of an equivalent homogeneous WO_3-based reactor.

2. Materials and Methods

2.1. Preparation of BP Membranes

Buckypaper membranes were obtained by filtration of SWNT dispersions through PTFE disks (diameter = 47 mm, average pore size = 5 μm, Durapore©, Merck KGaA, Darmstadt, Germany). The average diameter of SWNTs was 1.4 ± 0.1 nm and their length was longer than 5 μm as reported in the datasheet from Sigma-Aldrich, Milan, Italy. Thirty milligrams of SWNTs were dispersed in 200 mL of a 0.4% TRITON X100 water solution by an ultrasonic bath (model M1800H-E, Bransonic, Danbury, CT, USA) for 30 min. Then, solutions were filtered through the PTFE disks with a vacuum pump (pressure = −0.04 bar), washed with 20 mL of methanol and, finally, dried at room temperature. All chemicals were purchased from Sigma-Aldrich, Milan, Italy.

2.2. Deposition of WO_3 onto BP Membranes

The deposition of nanostructured tungsten trioxide onto BP membranes was obtained by reactive RF sputtering using of a tungsten target (purity 99.999%, Goodfellow Cambridge Ltd., Huntingdon, England) in the presence of oxygen (purity 99.999%) as process and reactive gas under different conditions of oxygen flow, sample-target distance, sputtering time, and applied RF process power. The optimal process conditions in term of layer homogeneity and catalyst droplet size were found to be: Oxygen flow 35 mL min^{-1}, sample-target distance 8 cm, sputtering time 30 min, applied RF process power 50 W.

The amorphous WO_3 thin films deposited on BP membranes were converted in monoclinic WO_3 thin films, which are characterized by a larger catalytic activity, by heat treatment at 350 °C for 30 min.

2.3. Characterization of BP and WO_3/BP Membranes

The porosity, P, of BP and WO_3/BP membranes was determined by gravimetric method at 25 °C, measuring the weight of a wetting liquid (3M-FC-40, 3M Italia Srl, Pioltello, Milan, Italy), contained in the membrane pores. The porosity was calculated according to the following Equation (1):

$$P = \frac{\frac{w_w - w_d}{d_w}}{\frac{w_w - w_d}{d_w} + \frac{w_d}{d_m}} \quad (1)$$

where w_w is the weight of the wet samples, w_d the weight of dry samples, d_w the wetting liquid density (1.855 g·cm^{-3}), and d_m is the average membrane density (0.60 ± 0.03 g·cm^{-3} as calculated from measurements of buckypaper weight, thickness, and surface area).

Pore size distribution was evaluated by a capillary flow porometer (CFP-1500 AEXL, PMI Porous Materials Inc., Ithaca, NY, USA). Membranes were fully wetted by keeping them in Porewick® (Sigma-Aldrich, Milan, Italy) for 24 h. Then, nitrogen was gradually allowed to flow into the membrane by increasing its pressure and the registration of gas pressure and permeation flow rate allowed the calculation of the pore size distribution.

The electrical conductivity of membranes was determined from the BP electrical resistance in I–V (current–voltage) measurements by a waveform generator (33220A Agilent, Santa Clara, CA, USA) and a digital multimeter (34410A Agilent, Santa Clara, CA, USA) on BP rectangular strips (width 5 mm and length 3 cm).

The mechanical properties were measured with a Sauter TVO-S tensile tester equipped with a Sauter FH-1k digital dynamometer and AFH FAST software (Sauter GmbH, Balingen, Germany). The rectangular strips (width 5 mm and length 3 cm) were tested at a strain rate of 0.1 mm·min^{-1}. The tests allowed the determination of the tensile strength as the maximum stress, the fracture strain as the percentage of elongation at the breaking point, and the Young's modulus.

Thermogravimetric analysis (TGA, STA 2500 Regulus simultaneous thermal analyzer, Netzsch, Selb, Germany) was employed to assess the BP membrane thermal stability. TGA was carried out

from room temperature to 750 °C with a heating rate of 5 °C/min in a flowing gas mixture consisting of 1% O_2 and 99% Ar at a flow rate of 100 sccm. The average roughness of WO_3/BP surfaces was evaluated by atomic force microscopy (Nanoscope III, Digital Instruments, Santa Barbara, CA, USA). Static contact angle measurements of BP and WO_3/BP membranes were measured with a goniometer (Nordtest, Serravalle Scrivia AL, Italy) at 25 °C. A drop (2 µL) of water was put onto the sample surface by a micro-syringe and measurements were carried out by setting the tangents on both visible edges of the droplet on five different positions of each sample and calculating the average value of the measurements.

The permeation tests were carried out with distilled water using a filtration cell having an active area of 5 cm^2. The feed solution at 25 ± 1 °C was pumped by a gear pump at a transmembrane pressure of 1 bar. The feed flow rate was 250 $mL \cdot min^{-1}$. Permeate samples were collected every 5 min in order to determine the transmembrane flux, J, defined as:

$$J = \frac{V_p}{A\Delta t} \quad (2)$$

where V_p was the permeate volume passed through the membrane in the fixed time interval, Δt, and A was the effective membrane area.

2.4. Photodegradation Experiments

The photoactivity of WO_3/BP membranes was investigated in a small continuous plant with model pollutant water solutions (250 mL) of a cationic dye (Methylene Blue, MB, 5, 10, and 20 ppm), an anionic dye (Indigo Carmine, IC, 20 ppm) and a drug (Diclofenac Sodium, DS, 20 ppm), which were recirculated by a peristaltic system (flow rate 16.6 $mL \cdot min^{-1}$, Masterflex® L/S®, Cole-Parmer Srl, Cernusco sul Naviglio, MI, Italy) through a round cell. All model pollutants were purchased from Sigma-Aldrich, Milan, Italy. The experiment temperature was 25 ± 1 °C being the becker with the pollutant solutions placed in a thermostatic bath (model 1225, VWR, Milan, Italy), which kept constant the flowing solution temperature and avoided the pollutant thermolysis. All model pollutans were purchased from Sigma Aldrich, Milan, Italy. The WO_3/BP membranes divided the cell volume in two compartments: The upper one (thickness 5 mm, photocatalytic area 8 cm^2, irradiated volume 4 cm^3) was equipped with a N-BK7 optical glass window to allow UV-Vis irradiation from a Suntest CPS+ sun simulator (1.5 kW Xenon arc lamp, with an average irradiance of 500 $W \cdot m^{-2}$ in the wavelength range 300 nm–800 nm, see Figure S1 of SI, Atlas, Linsengericht-Altenhaßlau, Germany). The light power of sun simulator was calibrated by a FieldMaxII-TO digital power/energy meter (Coherent Italia S.r.l., Monza, Italy) equipped with a PM10 thermopile. The WO_3 sputtered surface of membranes was exposed to UV light. After irradiation, the solution passed through a quartz flow cuvette placed inside a spectrophotometer able to read at regular intervals (5 min) the absorbance value at the maximum absorption wavelength of MB (665 nm), IC (610 nm), and DS (275 nm). Similarly, the photoactivity of 0.2 mg of monoclinic WO_3 nano-powder (which was the same amount of WO_3 sputtered onto BP membranes) was measured. As each experiment generally lasted 150 min and the recirculation time was around 15 min, the average contact time of solutions with the active photocatalysis region was extimated in 10 min.

The photodegradation of pollutants [31] is generally described by the first-order kinetics

$$\frac{dC}{dt} = -kC \quad (3)$$

where C is the pollutant concentration, k is the rate constant and t is the reaction time. After integration, the following equation is obtained:

$$ln\frac{C(t)}{C_0} = -kt \quad (4)$$

where C_0 and C(t) are the initial concentration and the concentration at time t of the pollutants. The rate constant can be obtained from the slope of the plot of $ln\frac{C(t)}{C_0}$ as a function of t.

Experimental data were corrected by taking into account the effective photon fluence impinging on WO_3 layer (see SI).

The percentage of pollutant removal, %R, was calculated as:

$$\%R = \frac{C_0 - C(t)}{C_0} \times 100 \quad (5)$$

3. Results and Discussion

Several factors influence the BP membrane properties including sonication time of the SWNT solution, the magnitude of the vacuum depression used to filter the SWNT solution, the porosity and material of the filtration membranes. After several trials, which gave unacceptable results, including un-detachable BP from polymer membranes (due to small pore size filtration membrane), and brittle and broken BP (due to fast solvent evaporation), Figure 1a, intact BP were obtained under the optimal conditions reported in the Materials and Methods, Figure 1b. Such BPs are easily detachable from the filtration membranes, Figure 1c, and look like free-standing and flexible disks (average thickness 45 ± 2 μm) as shown in Figure 1d.

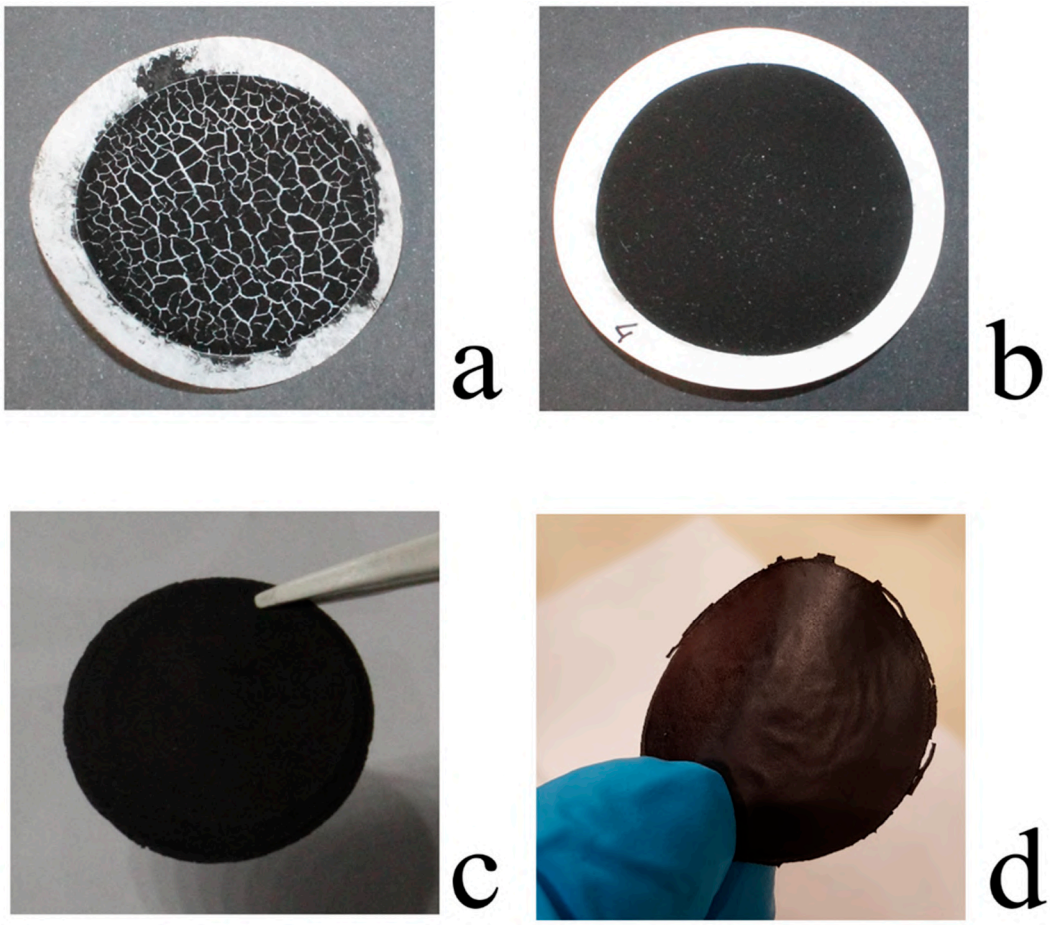

Figure 1. Appearance of buckypaper (BP) membranes under different experimental preparation procedures: (**a**) Brittle and un-detachable BP membrane filtered through a poly (vinylidene fluoride) (PVDF) membrane with reduced pore size; (**b**) whole and detachable; (**c**) free-standing and (**d**) flexible BP membrane obtained under the optimal conditions reported in the Experimental section.

At a microscopic level, BP membranes showed a highly disordered porous morphology due to π–π and van der Waals interactions between and within bundles and clusters of carbon nanotubes, Figure 2a,b.

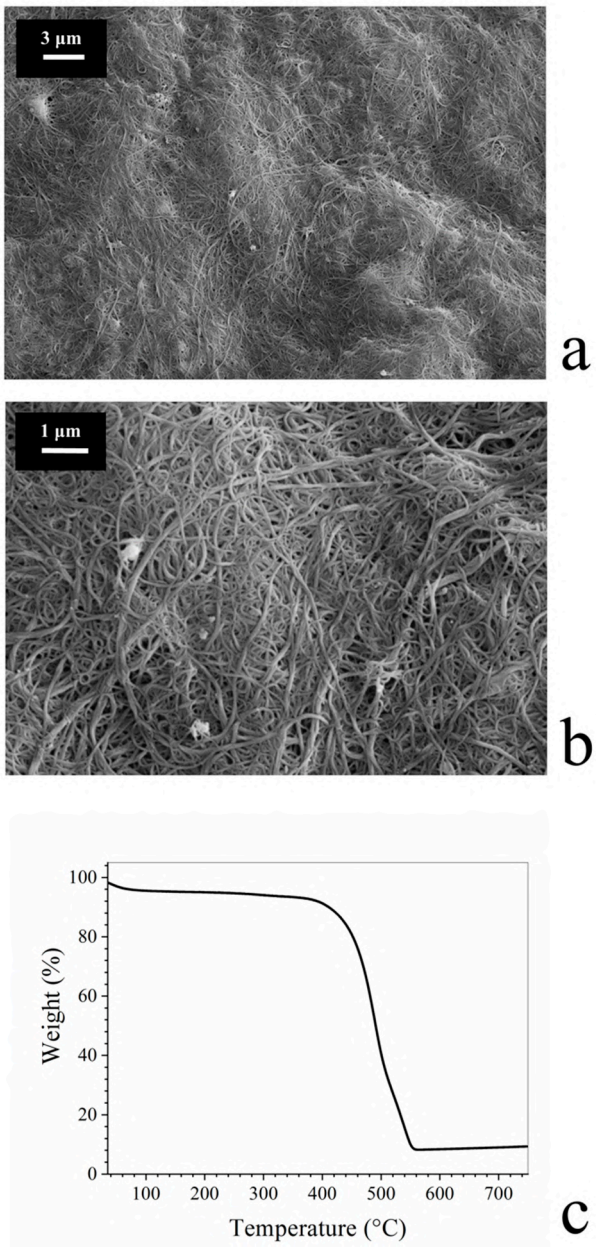

Figure 2. (**a**,**b**) Morphology of BP membranes at two different magnification; (**c**) Thermal stability of BP membranes. The initial weight loss is due to solvent evaporation, while the second one, which starts at around 400 °C, is due to the thermal degradation of single wall carbon nanotubes (SWNTs).

The thermal stability of BP membranes was assessed by TGA. As reported in Figure 2c, after an initial weight loss of about 5% due to water evaporation, BP membranes were found to be stable up to 400 °C. For larger temperatures, the degradation of SWNTs is observed.

Table 1 reports some geometrical data and properties for BP membranes. In particular, density, porosity, and water flow rate values of BPs (0.60 ± 0.03 g·cm^{-3}, 70 ± 5%, and $12{,}500 \pm 100$ L·m^{-2}·h^{-1}·bar^{-1} respectively) fall in the range of values shown by porous polymer membranes, generally used for filtration processes [32]. In addition, the electrical conductivity and the mechanical properties, namely

tensile strenght, fracture strain and Young's modulus, reported in Table 1, allow to consider BPs as strong and conductive membranes [33].

Table 1. Physical-chemical properties of BPs.

Property	Value
Thickness	45 ± 2 μm
Diameter	37.0 ± 0.1 mm
Density	0.60 ± 0.03 g·cm^{-3}
Porosity	70 ± 5 %
Electrical Conductivity	83 ± 4 S cm^{-1}
Tensile strength	11.8 ± 2.2 MPa
Fracture Strain	2.6 ± 0.1%
Young's Modulus	0.9 ± 0.1 GPa
Water Flow Rate	12,500 ± 100 L m^{-2}·h^{-1}·bar^{-1}

In order to give photocatalytic properties to BP membranes, they were covered with thin layers of WO_3 by RF magnetron chemical vapor deposition. CVD is a well-known chemical process for the deposition of desired thin films onto substrate surfaces by chemical reactions among one or more volatile precursors. Nevertheless, the film quality is strongly dependent on the CVD process parameters. Consequently, in this work different sputtering conditions (oxygen flow, sample-target distance, sputtering time, and power) were tested in order to find the optimal set of parameters able to give a homogeneous BP coverage without cracks and small WO_3 nanoparticles to avoid BP membrane occlusion and increase photoactivity.

The best results, in terms of both coverage quality and nanoparticle size, were obtained with the following conditions: Flow(O_2) = 35 mL·min^{-1}, d = 8 cm, t = 30 min, power = 50 W. The WO_3/BP membranes looked like flexible, greenish/yellowish disks as shown in Figure 3a.

Figure 3b shows the morphology of the top surface of a WO_3/BP membrane sputtered under the experimental conditions previously reported. A homogeneous layer of small nanoparticles, with a rather spherical shape and an average diameter of around 50 nm, constitutes the WO_3 coating without cracks and pore occlusion. It is important to remind the presence of BP membrane under the WO_3 layer. Figure 3c shows the picture of a particular faulty WO_3/BP membrane with a small crack, where it is possible to see inside the crack the texture of SWNT bundles, which form the BP substrate.

Figure 4a,b report the pore size distribution of both a pristine BP and a WO_3/BP photocatalytic membrane and the SEM cross section picture of a WO_3/BP membrane, respectively. As shown in Figure 4a both membranes show similar pore size distribution (within experimental errors) with two size populations placed at around 0.160 μm (0.163 ± 0.016 μm and 0.155 ± 0.018 μm, respectively) and at around 0.035 μm (0.037 ± 0.003 μm and 0.035 ± 0.003 μm, respectively) accounting for the presence of a major macroporous structure and a mesoporous structure (inter-tube pores with a size between 2 and 50 nm) formed between SWNT criss-crossings in the sample [34].

It is evident from the cross section of WO_3/BP membrane, that the WO_3 layer is a few tens of nanometers thick, but WO_3 nanoparticles penetrate the BP membrane for ≈ 2 μm, accounting, most likely, for the reduction in the mesopore average size.

However, all the membranes prepared are characterized by a porosity of 70 ± 5%, which is expected to favour the water permeability through them.

The homogeneous covering of BP membranes WO_3 was further assessed by EDX spectroscopy. Figure 5 shows the EDX color mapping images of the border area between a WO_3/BP membrane (lower area) and a BP membrane (i.e., the part of sputtered BP membrane, which was covered by a locking mask, upper area). BP membrane area looks like a red homogeneous region due to the presence of carbon and chemical impurities from SWNT, on the contrary WO_3/BP membrane area looks like a red background covered by yellow and green spots, deriving by the covering of SWNT with WO_3 nanoparticles.

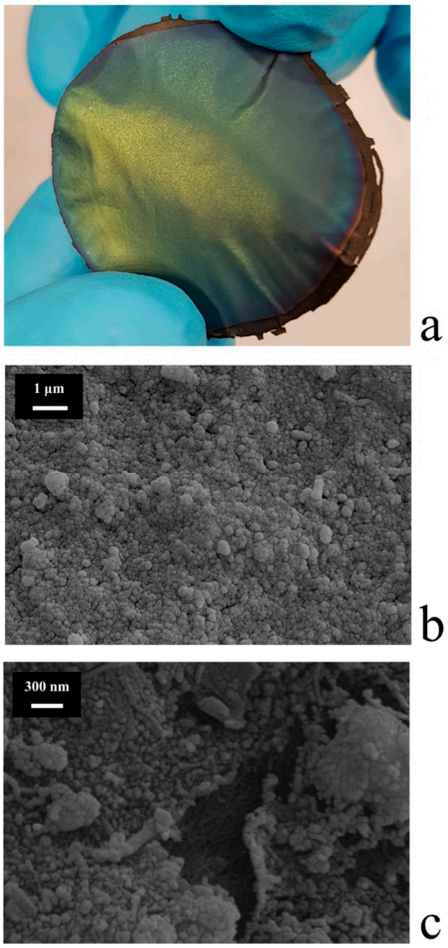

Figure 3. (**a**) Flexible, greenish/yellowish WO_3/BP membranes; (**b**) Morphology of the top surface of a WO_3/BP. The WO_3 coating is a homogeneous layer of small nanoparticles, without cracks and pore occlusion; (**c**) Crack of a faulty WO_3/BP membrane, inside which it is possible to see the texture of BP substrate.

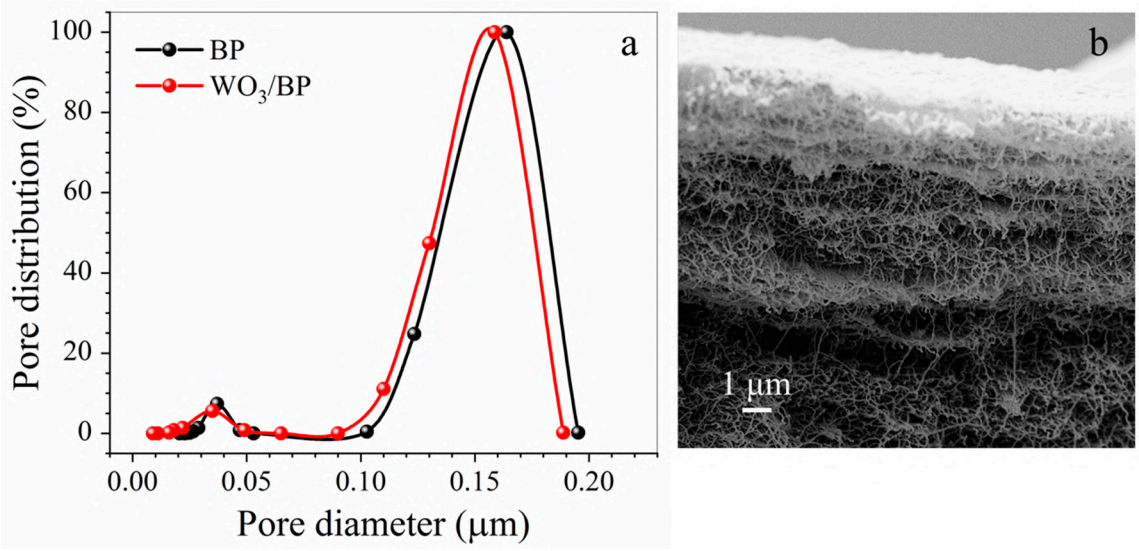

Figure 4. (**a**) Pore size distribution of both a BP membrane (black dots) and a WO_3/BP photocatalytic membrane (red dots); (**b**) SEM cross section picture of a WO_3/BP membrane.

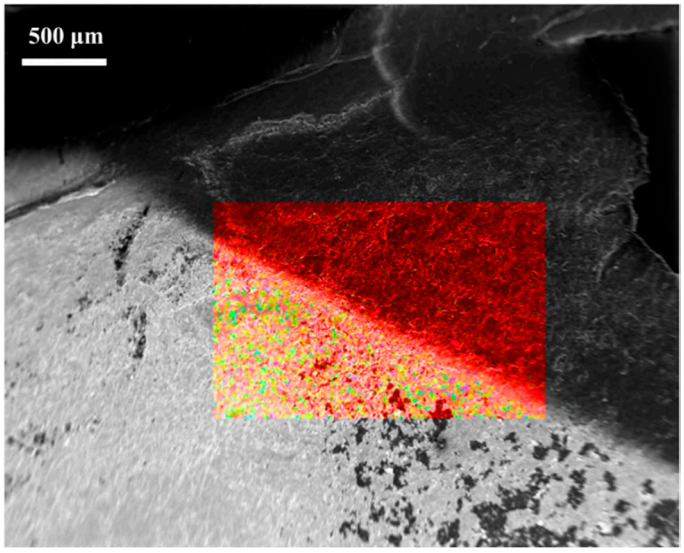

Figure 5. EDX color mapping image and EDX spectra of the border area between a WO_3/BP membrane (lower area) and a BP membrane (upper area).

The WO_3 layer showed an average rms roughness of 0.268 µm as determined by AFM measurements, Figure 6a. Such roughness gives a hydrophilic character to the top surface of WO_3/BP membranes, as confirmed by contact-angle measurements. In fact, the average contact-angle value of WO_3/BP membranes was found to be equal to 57.0° ± 0.5°, which is significantly smaller than the average contact-angle value (119.0° ± 0.5°) shown by a BP, Figure 6b,c. The contact angle values of the WO_3/BP membranes did not change after 3 h continuous irradiation by solar simulator, confirming the stability of WO_3 layer under UV-Vis light. The hydrophilicity of WO_3/BP membranes could result in a possible increase of membrane fouling, i.e., the deposition of organic cakes onto the surfaces, but such possible drawback is overcome by fouling mitigation deriving from the photoactivity of WO_3 layers. Moreover, the increase in hydrophilicity is expected to have a positive effect in the membrane permeation properties and makes such membranes suitable for the filtration of aqueous solutions.

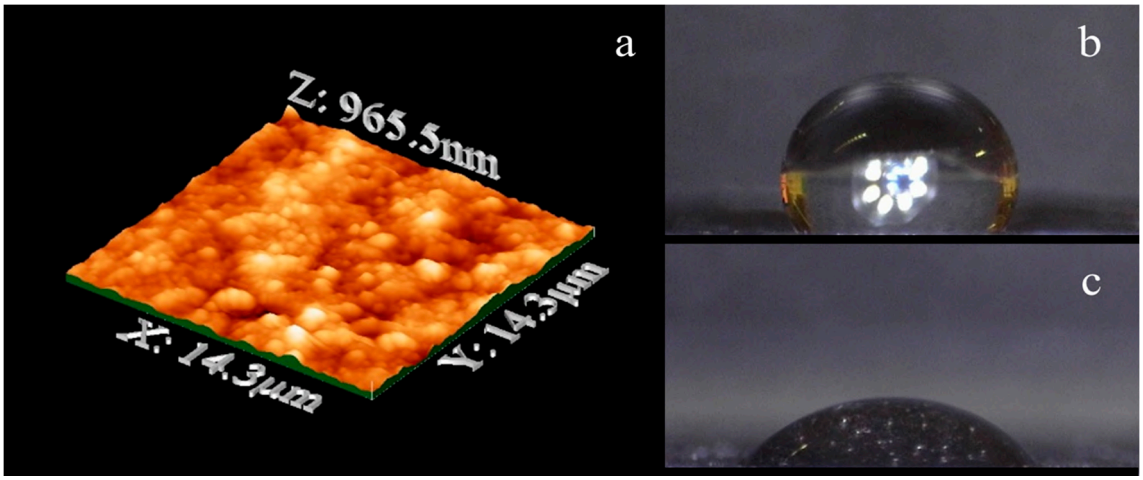

Figure 6. (**a**) AFM topology image of a WO_3/BP membrane. The average rms roughness is 0.268 µm; (**b**) Average contact-angle value of a BP membrane; (**c**) Average contact-angle value of a WO_3/BP membrane.

It is well known that CVD deposition of tungsten trioxide onto substrates gives amorphous WO_3, which is about ten times less photoactive than monoclinic WO_3 [35]. Consequently, WO_3/BP membranes were thermal treated at 350 °C in order to convert the amorphous WO_3 layer into the more

photoactive monoclinic one. Obviously, such treatment was possible thanks to the enhanced thermal properties of BP compared to polymer membranes.

Figure 7a shows the thermal evolution of micro-Raman spectrum of WO_3/BP membranes. The Raman spectrum of as-deposited WO_3 layer shows three main vibrational bands in the range of 200–1000 cm^{-1} observed at 265, 781, and 969 cm^{-1}. The first peak increases in height as a function of the temperature, while the second splits into two intense peaks at around 700 and 800 cm^{-1}. These peaks are the typical Raman peaks of monoclinic crystalline WO_3, which correspond to the stretching vibrations of the bridging oxygen [36,37], and are assigned to WO stretching (ν), WO bending (δ), and OWO deformation (γ) modes, respectively [38,39].

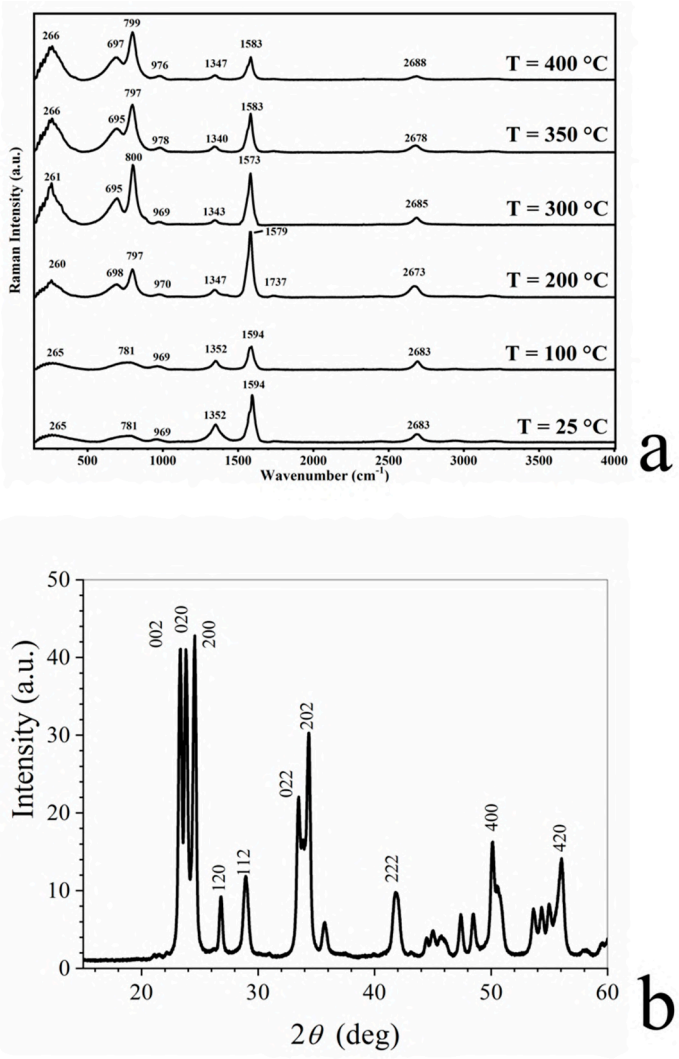

Figure 7. (**a**) Thermal evolution of Raman spectrum of WO_3 deposited onto BP membranes. The peaks at around 700 and 800 cm^{-1} are assigned to WO stretching (ν), WO bending (δ), and OWO deformation (γ) modes, respectively, confirming the monoclinic structure of WO_3; (**b**) X-ray diffraction patterns of WO_3 layer sputtered onto BP membranes. Peaks are related to the reflection planes of the monoclinic phase of WO_3.

The change of amorphous structure of WO_3 to monoclinic WO_3 was further confirmed by XRD as shown in Figure 7b, where the reported peaks are related to the reflection planes of the monoclinic phase of WO_3.

The transmembrane flux WO_3/BP membranes was evaluated in a small continuous plant and found to be $9.4 \times 10^{+3}$ L $m^{-2} \cdot h^{-1} \cdot bar^{-1}$, a value which is slightly lower (−25%) than pristine BP membrane as a consequence of the deposition of WO_3 layer.

The photoactivity of WO_3/BP membranes was tested with model pollutant water solutions (250 mL) of a cationic dye (Methylene Blue, MB, 5, 10, and 20 ppm), an anionic dye (Indigo Carmine, IC, 20 ppm) and a drug (Diclofenac Sodium, DS, 20 ppm), which were recirculated by a peristaltic system through a round cell.

The effect of initial concentrations of Methylene Blue (5, 10, and 20 ppm) on the reaction rate is shown in Figure 8. It is evident that the kinetic constant values decrease with increasing initial concentration (k values were 0.122 ± 0.003, 0.113 ± 0.003, and 0.085 ± 0.002 min^{-1}, respectively). The higher values for the kinetic constant obtained at lower MB concentrations are explained as a consequence of [31,40]:

- The increase of the number of photons available per BM molecule;
- the higher amount of available catalytically active sites per BM molecule; and
- an easier penetration of photons through the less concentrated solutions.

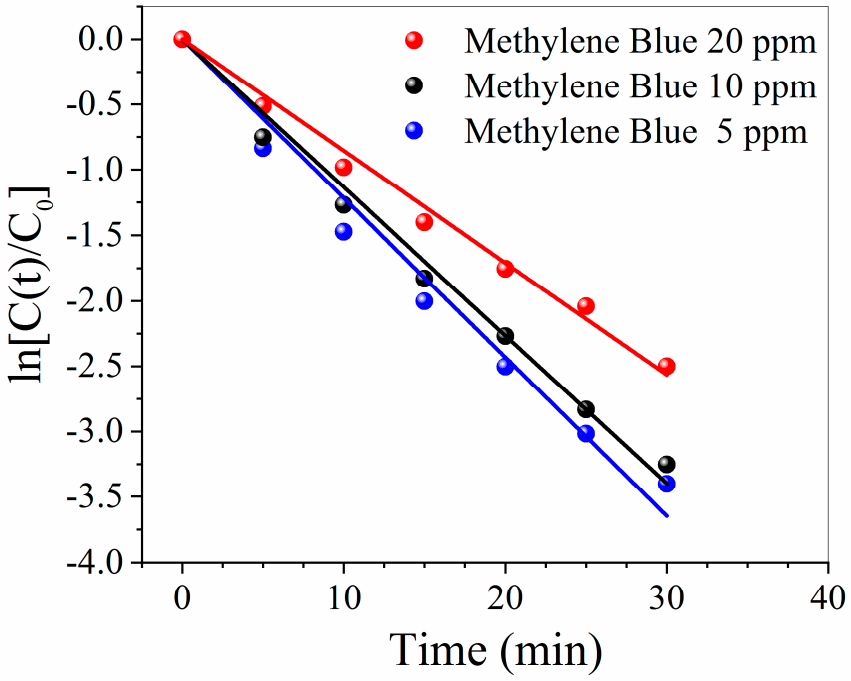

Figure 8. Effect of initial concentrations of Methylene Blue (5, 10, and 20 ppm) on the reaction rate.

Nevertheless, the reported rate constants were corrected for the different photon fluence and their values do not differ so much from the uncorrected ones (0.118 ± 0.003, 0.110 ± 0.002 and 0.082 ± 0.002 min^{-1}, respectively, see SI). Accordingly, the different photon absorption from Methylene Blue solutions at different concentrations is not the major cause for the observed differences in the rate constants for Methylene Blue degradation. Most probably, such differences could arise from the competition of MB molecules towards active surface sites and reactive oxygen species [41].

In all cases the percentage of MB removal within 35 min was larger than 90%. The residual concentration of MB was respectively 0.3, 0.7, and 1.5 ppm, values in agreement with other data present in literature [40]. Removal experiments with no irradiation found very low pollutant adsorption by WO_3/BP membranes. After a 3 h run a WO_3/BP membrane was able to adsorb about 0.003 mg of MB, which was not a significant quantity compared to the weight amount of MB present in the used solutions.

Figure 9 reports the photocatalytical properties of WO_3/BP membranes against water solutions of a cationic dye (Methylene Blue 20 ppm), an anionic dye (Indigo Carmine 20 ppm) and a drug (Diclofenac Sodium 20 ppm), generally used as model pollutants. In all cases WO_3/BP membranes are able to efficiently degrade the water contaminants with a kinetic constant value of 0.085 ± 0.002, 0.064 ± 0.001, and 0.019 ± 0.001 min^{-1}, respectively. Such values are of the same order of magnitude or lower than the kinetic constants against the same pollutants, found with WO_3, TiO_2, or other catalyst nanoparticles dispersed either in the solutions or casted on carbon nanotubes, flakes of graphene oxide or porous polymer membranes [42–50], as no BP bearing photocatalysts, to the knowledge of authors, was ever proposed in literature.

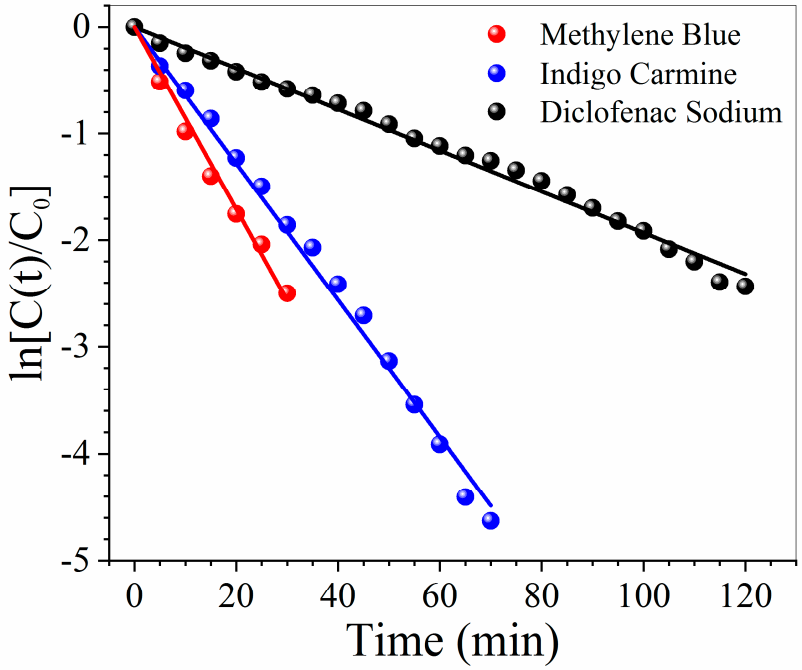

Figure 9. Photoactivity of WO_3/BP membranes against water solutions of a cationic dye (Methylene Blue 20 ppm), an anionic dye (Indigo Carmine 20 ppm) and a drug (Diclofenac Sodium 20 ppm).

Dark changes in absorbance were less than 1%, while UV controls for all three pollutant solutions found that after three hours of irradiation the absorbance changes due to the photolysis through a BP membrane were less than 2%. Such results can be explained by the particular spectrum of solar simulators (see Figure S1), which have only UV-A and UV-B emissions, and by the particular transmittance of N-BK7 optical glass cover, which cuts UV-B emissions with wavelengths lower than 300 nm. The absence of UV-C and lower UV-B wavelengths remarkably reduces the molecular degradation of pollutants by photolysis.

The performance of WO_3/BP membranes was also compared with the photoactivity of 0.2 mg of monoclinic WO_3 nano-powder (the same amount of WO_3 sputtered onto BP membranes).

As shown in Figure 10, the photodegradation of Methylene Blue by both systems (WO_3/BP membrane and monoclinic WO_3 nano-powder) follows a first order kinetics with a rate constant of 0.085 ± 0.002 min^{-1} and 0.029 ± 0.001 min^{-1}, respectively. The enhancement of the photoactivity in WO_3/BP membranes can be due to the presence of BP, as the SWNT substrate prevents the electron/hole pair recombination during photocatalysis and increases the kinetic rate constant [51]. An almost complete photodegradation of Methylene Blue was obtained within ≈ 50 min and ≈ 140 min by using WO_3/BP membranes and WO_3 nano-powder, respectively. Such relatively short degradation times make the WO_3/BP membranes suitable for applications in advanced oxidation processes. In addition, the long-term stability of WO_3/BP membranes was checked by ten cycles of successive photocatalysis processes. Figure 10 shows the morphology and the photocatalycal efficiency of a WO_3/BP membrane

after the tenth photocatalytical cycle of a 20 ppm BM solution, revealing no evident damage in the morphology of WO_3/BP membranes and no important change in the degradation efficiency, being the rate constant value equal to the pristine one within experimental errors (0.081 ± 0.002 min^{-1}). In addition, the morphology of the WO_3/BP membrane, after the tenth photocatalytical cycle, reveals the absence of any cakes on the surface and a morphology similar to that shown in the pristine WO_3/BP membrane (Figure 3b), thanks to its photoactivity and different surface chemistry preventing and destroying any deposition. Further investigations are in progress to test the antifouling activity of WO_3/BP membranes on real industrial wastes rather than on model dye and drug water solutions.

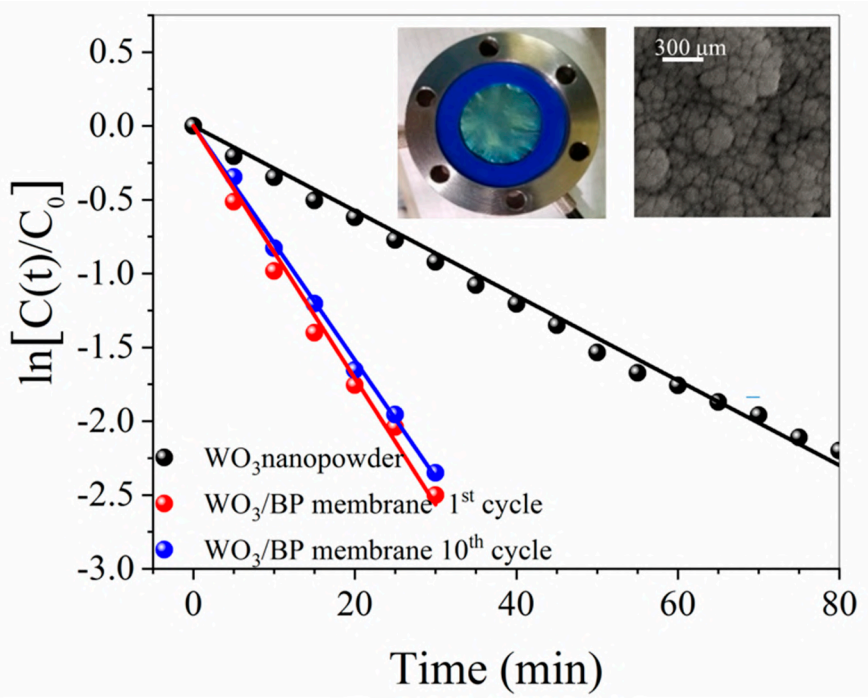

Figure 10. Photodegradation of Methylene Blue by a WO_3/BP membrane (red dots) and by monoclinic WO_3 nanopowder (black dots) in the same amount of WO_3 present on WO_3/BP membrane.

4. Conclusions

A new flexible membrane, based on SWNT and with improved thermal and catalytic properties, was obtained by RF magnetron sputtering of a nanostructured thin layer of tungsten trioxide and successive conversion in the more photoactive monoclinic phase. The WO_3/BP membrane was characterized by SEM, TGA, porosimetry, XRD, EDX, AFM, Raman, contact angle and permeation measurements. The photocatalytic activity of WO_3/BP membranes was tested following the degradation of three different pollutant water solutions in a small continuous plant confirming the beneficial contribution of the hydrophilic WO_3 layer. The degradation kinetics rate of the Methylene Blue by WO_3/BP membranes was about three times that found by an equivalent amount of WO_3 nano-powder.

The main advantages of the proposed WO_3/BP membranes can be summarized in:

1. The possibility to make heterogeneous photocatalytical processes with an easier catalyst recovery and reuse;
2. their application in continuous flow plants;
3. a simpler and cleaner synthetic approach. Chemical vapor deposition processes do not require long and expensive purification procedures, which are necessary in other chemical syntheses, such as solvo-thermal processes. In addition, CVD allows the catalyst amount saving, avoiding its dispersion in the substrate bulk;

4. a higher photocatalytical efficiency, due to the facilitated electron-transfer between carbon nanostrucutres and catalyst nanoparticles, a reduced recombination between electrons and holes [51], and the presence of catalyst nanoparticles with small size just only on the top surface of substrates rather than in the polymer bulk (where they cannot play any catalytic action);
5. the possibility to change the photocatalyst crystal structure in a more photoactive one by thermal annealing processes at temperatures higher than the melting point of commonly used polymer substrate. PTFE, polytetrafluoroethylene, which has one of the highest melting points, melts at 327 °C, a temperature lower than the WO_3 amorphous-monoclinic phase transition temperature. On the contrary, BP membranes result thermally stable up to 400 °C;
6. BPs have both light weight and strong mechanical resistance, and, consequently, are easy to handle. In addition, BPs are resistant to all organic solvents and acid and base solutions, while porous polymer membranes can be damaged; and
7. a green chemisty approach with an almost zero environmental footprint, as the BP preparation is based on rather simple and clean experimental set-ups, which allow the recovery and reuse of solvents, CNT processing waste, end of life BPs and photocatalysts for the preparation of new catalyst/BP membranes.

The improved photoactivity, long-term stability, solvent-free features, fast catalyst recovery and re-use, and the possibility of an easy up-scale make WO_3/BP membranes efficient devices for the pollutant degradation by advanced oxidation processes.

Supplementary Materials: The following are available online at http://www.mdpi.com/2077-0375/10/7/157/s1, Figure S1: Spectrum of Suntest CPS+ sun simulator for three different irradiance values. Reprinted from [S1], with permission from Royal Society of Chemistry, Figure S2: Normalized fluence across solutions of Methylene Blue, Indigo Carmine, and Diclofenac Sodium, Table S1: Fluence uncorrected and fluence corrected rate constants.

Author Contributions: Conceptualization, G.D.F., A.I.M. and F.P.N.; Methodology, G.D.F. and F.P.N.; Supervision, G.D.F.; Writing—review and editing, G.D.F., A.I.M. and F.P.N.; Project administration G.D.F. and F.P.N.; Data curation E.P. and M.B.; Investigation E.P. and M.B.; Formal analysis E.P. and M.B.; Validation, F.P.N. All authors have read and agreed to the published version of the manuscript.

Funding: This research was funded by MIUR, Italian Ministry for University and Research, grant number EX-60/2019.

Acknowledgments: The PhD of M.B. is funded by a scholarship from Regione Calabria (grant POR Calabria 2014-2020—Azioni 10.5.6 e 10.5.12).

Conflicts of Interest: The authors declare no conflict of interest.

References

1. Ollis, D.F.; Pelizzetti, E.; Serpone, N. *Photo-Catalysis Fundamentals and Applications*; Wiley: Hoboken, NJ, USA, 1989.
2. Araña, J.; Herrera Melián, J.A.; Doña Rodríguez, J.M.; González Díaz, O.; Viera, A.; Pérez Peña, J.; Marrero Sosa, P.M.; Jiménez, V.E. TiO_2-photocatalysis as a tertiary treatment of naturally treated wastewater. *Catal. Today* **2002**, *76*, 279–289. [CrossRef]
3. Di Gioia, M.L.; Leggio, A.; Le Pera, A.; Liguori, A.; Siciliano, C. Optically pure N-hydroxy-O-triisopropylsilyl-α-L-amino acid methyl esters from $AlCl_3$-assisted ring opening of chiral oxaziridines by nitrogen containing nucleophiles. *J. Org. Chem.* **2005**, *70*, 10494–10501. [CrossRef] [PubMed]
4. Cho, M.; Chung, H.; Choi, W.; Yoon, J. Linear correlation between inactivation of *E. coli* and OH radical concentration in TiO_2 photocatalytic disinfection. *Water Res.* **2004**, *38*, 1069–1077. [CrossRef] [PubMed]
5. De Filpo, G.; Palermo, A.M.; Tolmino, R.; Formoso, P.; Nicoletta, F.P. Gellan gum hybrid hydrogels for the cleaning of paper artworks contaminated with *Aspergillus versicolor*. *Cellulose* **2016**, *23*, 3265–3279. [CrossRef]
6. Huang, Z.; Maness, P.-C.; Blake, D.; Wolfrum, E.J.; Smolinski, S.L.; Jacoby, W.A. Bactericidal mode of titanium dioxide photocatalysis. *J. Photochem. Photobiol. A* **2000**, *130*, 163–170. [CrossRef]
7. De Filpo, G.; Palermo, A.M.; Munno, R.; Molinaro, L.; Formoso, P.; Nicoletta, F.P. Gellan gum/titanium dioxide nanoparticle hybrid hydrogels for the cleaning and disinfection of parchment. *Int. Biodeterior. Biodegrad.* **2015**, *103*, 51–58. [CrossRef]

8. De Filpo, G.; Palermo, A.M.; Rachiele, F.; Nicoletta, F.P. Preventing fungal growth in wood by titanium dioxide nanoparticles. *Int. Biodeterior. Biodegrad.* **2013**, *85*, 217–222. [CrossRef]
9. Hoffmann, M.R.; Martin, S.T.; Choi, W.Y.; Bahnemann, D.W. Environmental applications of semiconductor photo-catalysis. *Chem. Rev.* **1995**, *95*, 69–96. [CrossRef]
10. Bhatkhande, D.S.; Pangarkar, V.G.; Beenackers, A. Photocatalytic degradation for environmental applications: A review. *J. Chem. Technol. Biotechnol.* **2002**, *77*, 102–116. [CrossRef]
11. De Filpo, G.; Pantuso, E.; Armentano, K.; Formoso, P.; Di Profio, G.; Poerio, T.; Fontananova, E.; Meringolo, C.; Mashin, A.I.; Nicoletta, F.P. Chemical vapor deposition of photocatalyst nanoparticles on PVDF membranes for advanced oxidation processes. *Membranes* **2018**, *8*, 35. [CrossRef]
12. Bhattacharyya, D. Functionalized membranes and environmental applications. *Clean Technol. Environ. Policy* **2007**, *9*, 81–83. [CrossRef]
13. Drioli, E.; Ali, A.; Macedonio, F. Membrane distillation: Recent developments and perspectives. *Desalination* **2015**, *356*, 56–84. [CrossRef]
14. Jones, O.A.H.; Voulvoulis, N.; Lester, J.N. Human pharmaceuticals in the aquatic environment: A review. *Environ. Technol.* **2001**, *22*, 1383–1394. [CrossRef] [PubMed]
15. Ziylan, A.; Ince, N.H. The occurrence and fate of anti-inflammatory and analgesic pharmaceuticals in sewage and fresh water: Treatability by conventional and non-conventional processes. *J. Hazard. Mater.* **2011**, *187*, 24–36. [CrossRef] [PubMed]
16. Formoso, P.; Pantuso, E.; De Filpo, G.; Nicoletta, F.P. Electro-conductive membranes for permeation enhancement and fouling mitigation: A short review. *Membranes* **2017**, *7*, 39. [CrossRef] [PubMed]
17. Nicoletta, F.P.; Cupelli, D.; Formoso, P.; De Filpo, G.; Colella, V.; Gugliuzza, A. Light responsive polymer membranes: A review. *Membranes* **2012**, *2*, 134–197. [CrossRef]
18. Salehi, S.M.; Di Profio, G.; Fontananova, E.; Nicoletta, F.P.; Curcio, E.; De Filpo, G. Membrane distillation by novel hydrogel composite membranes. *J. Membr. Sci.* **2016**, *504*, 220–229. [CrossRef]
19. Salminen, J.; Garbarino, E.; Orveillon, G.; Saveyn, H.; Mateos Aquilino, V.; Llorens González, T.; García Polonio, F.; Horckmans, L.; D'Hugues, P.; Balomenos, E.; et al. *Recovery of Critical and Other Raw Materials from Mining Waste and Landfills: State of Play on Existing Practices*; EUR 29744 EN; Blengini, G.A., Mathieux, F., Mancini, L., Nyberg, M., Viegas, H.M., Eds.; Publications Office of the European Union: Luxembourg, 2019; ISBN 978-92-76-08568-3. [CrossRef]
20. Shon, H.K.; Vigneswaran, S.; Ngo, H.H.; Kim, J.H. Chemical coupling of photocatalysis with flocculation and adsorption in the removal of organic matter. *Water Res.* **2005**, *39*, 2549–2558. [CrossRef]
21. Mozia, S.; Morawski, A.W. Hybridization of photocatalysis and membrane distillation for purification of wastewater. *Catal. Today* **2006**, *118*, 181–188. [CrossRef]
22. Ho, D.P.; Vigneswaran, S.; Ngo, H.H. Integration of photocatalysis and microfiltration in removing effluent organic matter from treated sewage effluent. *Sep. Sci. Technol.* **2010**, *45*, 155–162. [CrossRef]
23. Mendez-Arriaga, F.; Esplugas, S.; Gimenez, J. Photocatalytic degradation of nonsteroidal anti-inflammatory drugs with TiO_2 and simulated solar irradiation. *Water Res.* **2008**, *42*, 585–594. [CrossRef] [PubMed]
24. Kim, Y.A.; Muramatsu, H.; Hayashi, T.; Endo, M.; Terrones, M.; Dresselhaus, M.S. Fabrication of high-purity, double-walled carbon nanotube buckypaper. *Chem. Vap. Depos.* **2006**, *12*, 327–330. [CrossRef]
25. Endo, M.; Muramatsu, H.; Hayashi, T.; Kim, Y.A.; Terrones, M.; Dresselhaus, M.S. Nanotechnology: 'buckypaper' from coaxial nanotubes. *Nature* **2005**, *433*, 476. [CrossRef] [PubMed]
26. Rashid, M.H.-O.; Ralph, S.F. Carbon nanotube membranes: Synthesis, properties, and future filtration applications. *Nanomaterials* **2017**, *7*, 99. [CrossRef]
27. Frizzell, C.J.; Coutinho, D.H.; Balkus, K.J.; Minett, A.I.; Blau, W.J.; Coleman, J.N. Reinforcement of macroscopic carbon nanotube structures by polymer intercalation: The role of polymer molecular weight and chain conformation. *Phys. Rev. B* **2005**, *72*, 245420. [CrossRef]
28. Vohrer, U.; Kolaric, I.; Haque, M.H.; Roth, S.; Detlaff-Weglikowska, U. Carbon nanotube sheets for the use as artificial muscles. *Carbon* **2004**, *42*, 1159–1164. [CrossRef]
29. Coleman, J.N.; Blau, W.J.; Dalton, A.B.; Muñoz, E.; Collins, S.; Kim, B.G.; Razal, J.; Selvidge, M.; Vieiro, G.; Baughman, R.H.; et al. Improving the mechanical properties of single-walled carbon nanotube sheets by intercalation of polymeric adhesives. *Appl. Phys. Lett.* **2003**, *82*, 1682–1684. [CrossRef]
30. Boge, J.; Sweetman, L.J.; Ralph, S.F. The effect of preparation conditions and biopolymer dispersants on the properties of SWNT buckypapers. *J. Mater. Chem. A* **2009**, *19*, 9131–9140. [CrossRef]

31. Zhang, N.; Li, J.M.; Liu, G.G.; Chen, X.L.; Jiang, K. Photodegradation of diclofenac in aqueous solution by simulated sunlight irradiation: Kinetics, thermodynamics and pathways. *Water. Sci. Technol.* **2017**, *75*, 2163–2170. [CrossRef]
32. Russo, F.; Ursino, C.; Avruscio, E.; Desiderio, G.; Perrone, A.; Santoro, S.; Galiano, F.; Figoli, A. Innovative Poly (Vinylidene Fluoride) (PVDF) electrospun nanofiber membrane preparation using DMSO as a low toxicity solvent. *Membranes* **2020**, *10*, 36. [CrossRef]
33. Ashrafi, B.; Guan, J.; Mirjalili, V.; Hubert, P.; Simard, B.; Johnston, A. Correlation between Young's modulus and impregnation quality of epoxy-impregnated SWCNT buckypaper. *Compos. Part A* **2010**, *41*, 1184–1191. [CrossRef]
34. Whitby, R.L.D.; Fukuda, T.; Maekawa, T.; James, S.L.; Mikhalovsk, S.V. Geometric control and tuneable pore size distribution of buckypaper and buckydiscs. *Carbon* **2008**, *46*, 946–956. [CrossRef]
35. Nandiyanto, A.B.-D.; Oktiani, R.; Ragadhita, R.; Sukmafitri, A.; Zaen, R. Amorphous content on the photocatalytic performance of micrometer-sized tungsten. *Arab. J. Chem.* **2020**, *13*, 2912–2924. [CrossRef]
36. de Wijs, G.A.; de Groot, R.A. Amorphous WO_3: A first principles approach. *Electrochim. Acta* **2001**, *46*, 1989–1993. [CrossRef]
37. Tagtstrom, P.; Jansson, U. Chemical vapour deposition of epitaxial WO_3 films. *Thin Solid Film.* **1999**, *352*, 107–113. [CrossRef]
38. Daniel, M.F.; Desbat, B.; Lassegues, J.C.; Gerand, B.; Figlarz, M. Infrared and Raman study of WO_3 tungsten trioxides and WO_3, xH_2O tungsten trioxide tydrates. *J. Solid State Chem.* **1987**, *67*, 235–247. [CrossRef]
39. Díaz-Reyes, J.; Castillo-Ojeda, R.; Galván-Arellano, M.; Zaca-Moran, O. Characterization of WO_3 thin films grown on silicon by HFMOD. *Adv. Condens. Matter Phys.* **2013**, *2013*. [CrossRef]
40. Srinivasan, M.; White, T. Degradation of methylene blue by three-dimensionally ordered macroporous titania. *Environ. Sci. Technol.* **2007**, *41*, 4405–4409. [CrossRef]
41. Wang, W.-Y.; Ku, Y. Photocatalytic degradation of Reactive Red 22 in aqueous solution by UV-LED radiation. *Water Res.* **2006**, *40*, 2249–2258. [CrossRef]
42. Mastropietro, T.F.; Meringolo, C.; Poerio, T.; Scarpelli, F.; Godbert, N.; Di Profio, G.; Fontananova, E. Multistimuli activation of TiO_2/α-alumina membranes for degradation of methylene blue. *Ind. Eng. Chem. Res.* **2017**, *56*, 11049–11057. [CrossRef]
43. Gómez-Solís, C.; Juárez-Ramírez, I.; Moctezuma, E.; Torres-Martínez, L.M. Photodegradation of indigo carmine and methylene blue dyes in aqueous solution by SiC–TiO_2 catalysts prepared by sol–gel. *J. Hazard. Mater.* **2012**, *217–218*, 194–199. [CrossRef] [PubMed]
44. Devarahosahalli Veeranna, K.; Theeta Lakshamaiah, M.; Thimmasandra Naraya, R. Photocatalytic degradation of indigo carmine dye using calcium oxide. *Int. J. Photochem.* **2014**, *2014*. [CrossRef]
45. Sampaio, M.J.; Silva, C.G.; Marques, R.R.N.; Silva, A.M.T.; Faria, J.L. Carbon nanotube–TiO_2 thin films for photocatalytic applications. *Catal. Today* **2011**, *161*, 91–96. [CrossRef]
46. Singh, J.; Chang, Y.-Y.; Koduru, J.R.; Yang, J.-K. Potential degradation of methylene blue (MB) by nano-metallic particles: A kinetic study and possible mechanism of MB degradation. *Environ. Eng. Res.* **2018**, *23*, 1–9. [CrossRef]
47. Sampaio, M.J.; Marques, R.R.N.; Tavares, P.B.; Faria, J.L.; Silva, A.M.T.; Silva, C.G. Tailoring the properties of immobilized titanium dioxide/carbon nanotube composites for photocatalytic water treatment. *J. Environ. Chem. Eng.* **2013**, *1*, 945–953. [CrossRef]
48. Zhou, X.; Shia, T.; Zhou, H. Hydrothermal preparation of ZnO-reduced graphene oxide hybrid with high performance in photocatalytic degradation. *Appl. Surf. Sci.* **2012**, *258*, 6204–6211. [CrossRef]
49. Tian, L.; Ye, L.; Deng, K.; Zan, L. TiO_2/carbon nanotube hybrid nanostructures: Solvothermal synthesis and their visible light photocatalytic activity. *J. Solid State Chem.* **2011**, *184*, 1465–1471. [CrossRef]
50. Bojarska, M.; Nowak, B.; Skowroński, J.; Piątkiewicz, W.; Gradoń, L. Growth of ZnO nanowires on polypropylene membrane surface—Characterization and reactivity. *Appl. Surf. Sci.* **2017**, *391*, 457–467. [CrossRef]
51. Jeevitha, G.; Abhinayaa, R.; Mangalaraj, D.; Ponpandian, N. Tungsten oxide-graphene oxide (WO_3-GO) nanocomposite as an efficient photocatalyst, antibacterial and anticancer agent. *J. Phys. Chem. Solids* **2018**, *116*, 137–147. [CrossRef]

membranes

MDPI

Supporting Information

WO_3/Buckypaper Membranes for Advanced Oxidation Processes

Giovanni De Filpo [1,*], Elvira Pantuso [2], Aleksander I. Mashin [3], Mariafrancesca Baratta [1] and Fiore Pasquale Nicoletta [2,*]

[1] Department of Chemistry and Chemical Technologies, University of Calabria, 87036 Rende (CS), Italy; mariafrancesca.baratta@unical.it
[2] Department of Pharmacy, Health and Nutritional Sciences, University of Calabria, 87036 Rende (CS), Italy; elvirapnt.ep@gmail.com
[3] Applied Physics & Microelectronics, Lobachevsky State University of Nizhni Novgorod, 603950 Nizhni Novgorod, Russian Federation; mashin@unn.ru
* Correspondence: giovanni.defilpo@unical.it (G.D.F.); fiore.nicoletta@unical.it (F.P.N.); Tel.: +39-0984-492095 (G.D.F.), +39-0984-493194 (F.P.N.)

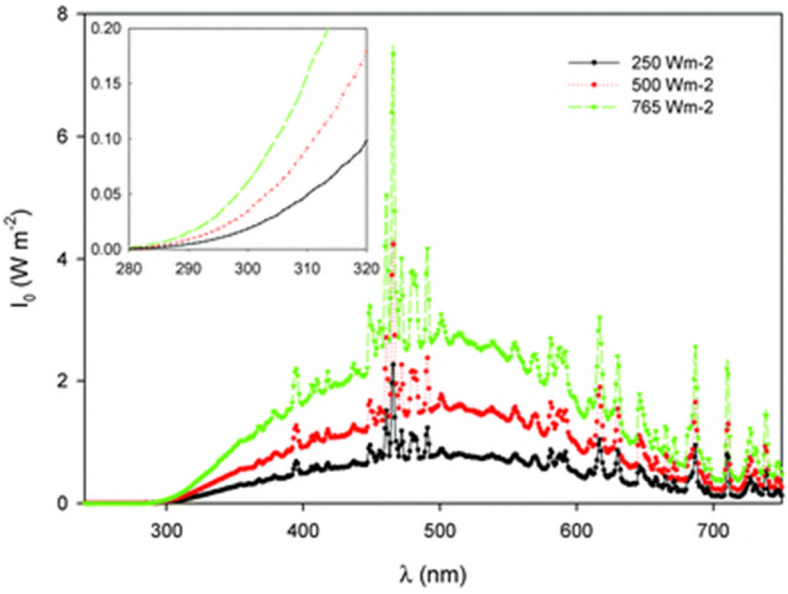

Figure 1. Spectrum of Suntest CPS+ sun simulator for three different irradiance values. Reprinted from [1], with permission from Royal Society of Chemistry.

Fluence Normalization of Kinetic Observations

The activation wavelength of WO_3 (2.6 eV → 476.86 nm ≈ 477 nm) was selected on a FieldMaxII-TO digital power/energy meter (Coherent Italia S.r.l., Monza, Italy) equipped with a PM10 thermopile. Then, the fluence after crossing a 5 mm thick cell containing water (reference) and solutions of Methylene Blue, Indigo Carmine and Diclofenac Sodium at different concentrations (2.5 ppm, 5 ppm, 10 ppm, 15 ppm, and 20 ppm) was measured. The active surface area was fixed in 1 cm^2 by an aluminium mask.

Results are reported in the following Figure S2, where the fluence across dye solutions was normalized to the fluence across water.

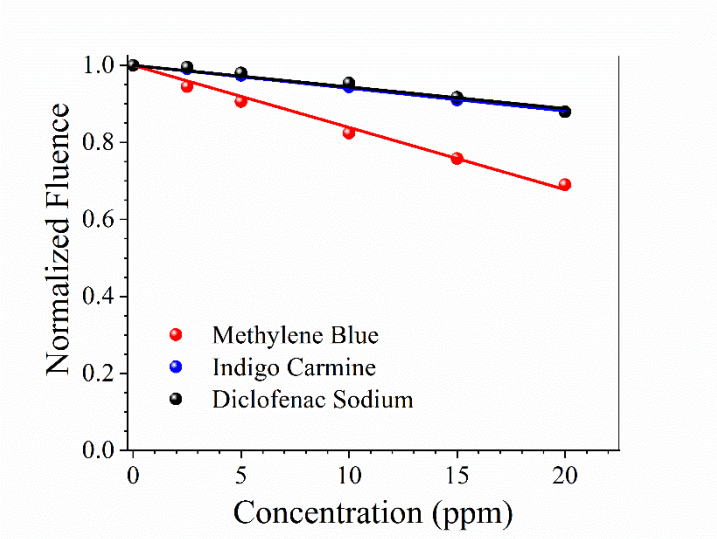

Figure S2. Normalized fluence across solutions of Methylene Blue, Indigo Carmine, and Diclofenac Sodium.

The normalized fluences, NF, were well fitted as function of concentration (ppm) with linear fits ($R^2 > 0.999$) with fixed intercept:
Methylene Blue: NF = 1 - 0.0161 ppm
Indigo Carmine: NF = 1 - 0.0059 ppm
Diclofenac Sodium: NF = 1 - 0.0056 ppm
and used to normalize the kinetic observations.

The rate constants are reported in the following Table S1.

Table S1. Fluence uncorrected and fluence corrected rate constants.

Solution	Uncorrected Rate Constant (min^{-1})	Corrected Rate Constant (min^{-1})
Methylene Blue (5 ppm)	0.118 ± 0.003	0.122 ± 0.003
Methylene Blue (10 ppm)	0.110 ± 0.002	0.113 ± 0.003
Methylene Blue (20 ppm)	0.082 ± 0.002	0.085 ± 0.002
Indigo Carmine (20 ppm)	0.062 ± 0.001	0.064 ± 0.001
Diclofenac Sodium (20 ppm)	0.018 ± 0.001	0.019 ± 0.001
WO_3 nanopowder	0.028 ± 0.001	0.029 ± 0.001
Methylene Blue (20 ppm) 10^{th} run	0.080 ± 0.002	0.081 ± 0.002

The corrected values of rate constants do not differ so much from the uncorrected ones and exclude that the different photon absorption from Methylene Blue solution at different concentrations could be the major cause for the observed differences in the rate constants for Methylene Blue degradation. Most probably, such differences could arise from the competition of MB molecules towards active surface sites and reactive oxygen species [2].

References

1. Weber, J.; Halsall, C.J.; Wargent, J.J.; Nigel D. Paul, N.D. A comparative study on the aqueous photodegradation of two organophosphorus pesticides under simulated and natural sunlight. *J. Environ. Monit.* **2009**, *11*, 654–659. DOI: 10.1039/b811387d

2. Wang, W.-Y., Ku, Y. Photocatalytic degradation of Reactive Red 22 in aqueous solution by UV-LED radiation. *Water Res.* **2006**, *40*, 2249–2258. DOI: 10.1016/j.watres.2006.04.041

Chapter 10

RSC Advances

REVIEW

Cite this: *RSC Adv.*, 2022, **12**, 28318

Microplastics in aquatic systems, a comprehensive review: origination, accumulation, impact, and removal technologies

Antonio Tursi, *[a] Mariafrancesca Baratta, *[a] Thomas Easton, [b] Efthalia Chatzisymeon,*[b] Francesco Chidichimo, *[c] Michele De Biase[c] and Giovanni De Filpo[a]

Received 28th July 2022
Accepted 29th September 2022

DOI: 10.1039/d2ra04713f

rsc.li/rsc-advances

Although the discovery of plastic in the last century has brought enormous benefits to daily activities, it must be said that its use produces countless environmental problems that are difficult to solve. The indiscriminate use and the increase in industrial production of cleaning, cosmetic, packaging, fertilizer, automotive, construction and pharmaceutical products have introduced tons of plastics and microplastics into the environment. The latter are of greatest concern due to their size and their omnipresence in the various environmental sectors. Today, they represent a contaminant of increasing ecotoxicological interest especially in aquatic environments due to their high stability and diffusion. In this regard, this critical review aims to describe the different sources of microplastics, emphasizing their effects in aquatic ecosystems and the danger to the health of living beings, while examining, at the same time, those few modelling studies conducted to estimate the future impact of plastic towards the marine ecosystem. Furthermore, this review summarizes the latest scientific advances related to removal techniques, evaluating their advantages and disadvantages. The final purpose is to highlight the great environmental problem that we are going to face in the coming decades, and the need to develop appropriate strategies to invert the current scenario as well as better performing removal techniques to minimize the environmental impacts of microplastics.

Introduction

Growing environmental alarm has arisen recently due to the presence of plastic waste in aquatic systems. The generation of anthropogenic waste, 70% of which is plastic, has increased exponentially in the last decades.[1] In fact, more than half of plastic becomes waste in less than a year from production and most of it is not recycled or reused. Microplastics are found all over the world, from the poles to the equator, from coastal regions to aquatic ecosystems. Their diffusion is massive due to transport phenomena such as wind and ocean currents which also lead to their presence in other ecosystems.

Since the 3rd industrial revolution in 1950 more than 10 billion tons of plastic have been produced with the annual production rate increasing exponentially. To be more specific, plastic production massively increased from 2 million tons in 1950 to 367 million tons in 2020 (about 0.3 percent less than in 2019 due to the impacts of COVID-19 on the sector).[2] Furthermore, it is estimated that production will further increase to about 600 million tons in 2025 (Fig. 1).[2]

The incredible versatility of plastic materials explains the continuous growth of production year after year as well as their market value.

Of all the plastic produced, recent studies have shown that only 9–10% has been recycled, another 10–11% was incinerated and *ca.* 30% is still in use due to their long lifetime. The remaining 50% has been disposed of in landfills or dispersed into the environment.[2]

One of the biggest problems, in this case, is precisely the fact that much of the plastic dispersed in the environment can easily reach the rivers and oceans. In fact, according to the latest 2020 survey, plastic waste enters the ocean at a rate of approximately 11 million tons per year.[3]

Plastic pollution is particularly acute in estuaries, indicating that terrestrial river input is the preferential way of pollution in coastal and marine environments.[4,5]

Furthermore, the COVID-19 pandemic has triggered an estimated global use of 129 billion masks and 65 billion gloves every month, generating a further release of plastics into the environment and therefore into the oceans.

[a]*Department of Chemistry and Chemical Technologies, University of Calabria, Via P. Bucci, Cubo 15D, 87036 Arcavacata di Rende (CS), Italy. E-mail: antonio.tursi@unical.it*

[b]*School of Engineering, Institute for Infrastructure and Environment, University of Edinburgh, The King's Buildings, Edinburgh EH9 3JL, UK*

[c]*Department of Environmental Engineering, University of Calabria, Via P. Bucci, Cubo 42B, 87036 Arcavacata di Rende (CS), Italy*

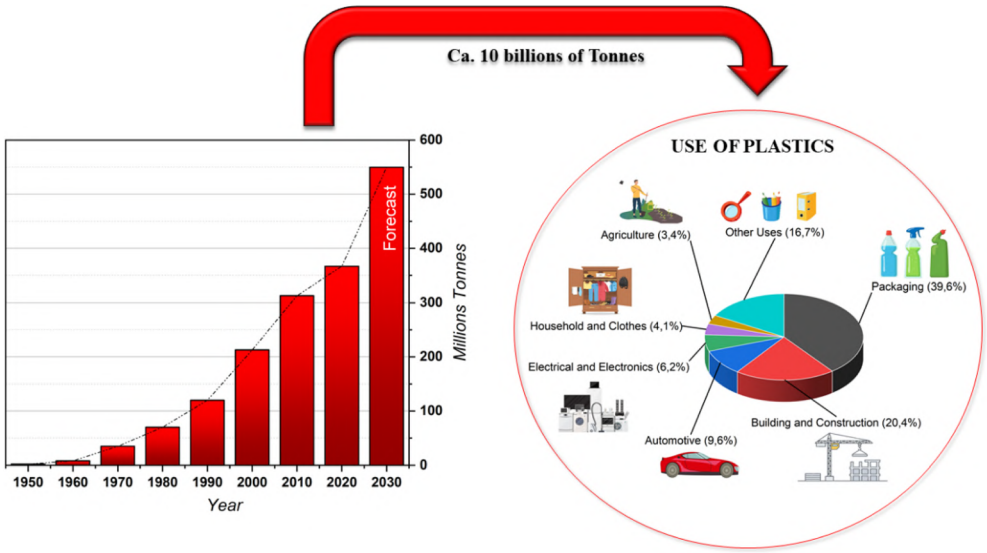

Fig. 1 Annual production of plastics worldwide from 1950 to 2020 (in million metric tons) and their use.[2]

Recent studies provide some truly dramatic evidences; 5.25 trillion macro and micro pieces of plastic float in our ocean with 46 000 pieces in each square mile, weighing up to 269 000 tons.[3] Macroplastics (diameter ≥ 5 mm) are a problem affecting the marine environment both from an aesthetic and environmental point of view with enormous repercussions on the marine biota. For example, plastic ingestion and entanglement in debris are the main cause of injury and death to mammals, fish, reptiles and seabirds.[1,6]

Moreover, microplastics (MP) with diameter < 5 mm can have detrimental impacts to organisms, including humans, since, due to their small size, they bioaccumulate in organisms throughout the food chain. In addition to this, MP can be of greater concern than macroplastics because, due to their high surface area and their distinctly hydrophobic character, they tend to absorb many pollutants such as heavy metals,[7,8] polycyclic aromatic hydrocarbons (PAHs) and polychlorinated biphenyls (PCBs),[9,10] and to transfer them to marine fauna, thus entering the food chain.[11,12] Carpenter and Smith (1972) have been the first to highlight the presence of small plastic fragments in the open sea.[13] Plastic waste can also strongly affect the ecosystem by generating new habitats on floating plastic debris,[14] opacifying the seabed and creating a barrier that interposes between the sea surface and the atmosphere with consequent limitation of gas exchange between the two ecosystems.[6,7] Nowadays, the largest reports of large quantities of plastic waste come mainly from areas located in subtropical latitudes, where concentrations of plastic waste, carried by currents and winds, accumulate on the surface of the sea, forming real oceanic islands called "garbage patches". Mass concentrations per km^2 reach hundreds of kilograms, counting up to one million pieces, for particles with a size > 500 μm. In light of these facts, the pervasiveness of MP waste in aquatic ecosystems as a result of anthropogenic pollution has received scientific attention worldwide. The methods currently being studied for their removal include absorption, filtration, biological degradation and/or chemical treatment processes.

Alongside the aforementioned methods, in recent decades efficient techniques for removing MP from wastewater, a main source of MP discharge to receiving water bodies, have been eagerly required to increase the quality of the final effluents and mitigate MP pollution. Several advanced treatment technologies have been studied through the use of membrane bioreactors for the treatment of the primary effluent and various tertiary treatment technologies such as disc filters, rapid sand filtration and dissolved air flotation for the purification of the secondary effluent.[15,16] However, there is still ample room for improvement and optimization of such ad-hoc technologies until wastewater treatment legislation enforces their application in existing wastewater treatment plants (WWTPs). Furthermore, many recent studies are focusing on the filter systems themselves, investigating the possibility of using natural polymers and eco-friendly materials to replace synthetic ones, in order to reach both comparable remediation efficiencies against several pollutant and plastic waste reduction at the end of their life cycle.[17–21] This review presents recent advances in understanding the impacts of MP on the environment and humans as well as the current state of the art on developing appropriate removal technologies. For this purpose, the major sources of MP pollution and their classification are reported. Recent studies focusing on environmental and human health impacts are reviewed. Furthermore, physical, chemical and biological technologies for MP removal from wastewater are assessed, also considering the latest advances in the scientific field to identify the gaps in the sector and guide future research priorities.

Classification and sources

Plastic classifications

In aquatic systems, plastic particles differ in shape, size, chemical composition and specific density.[22] Currently, the most widely adopted classification is based on their size (Fig. 2).

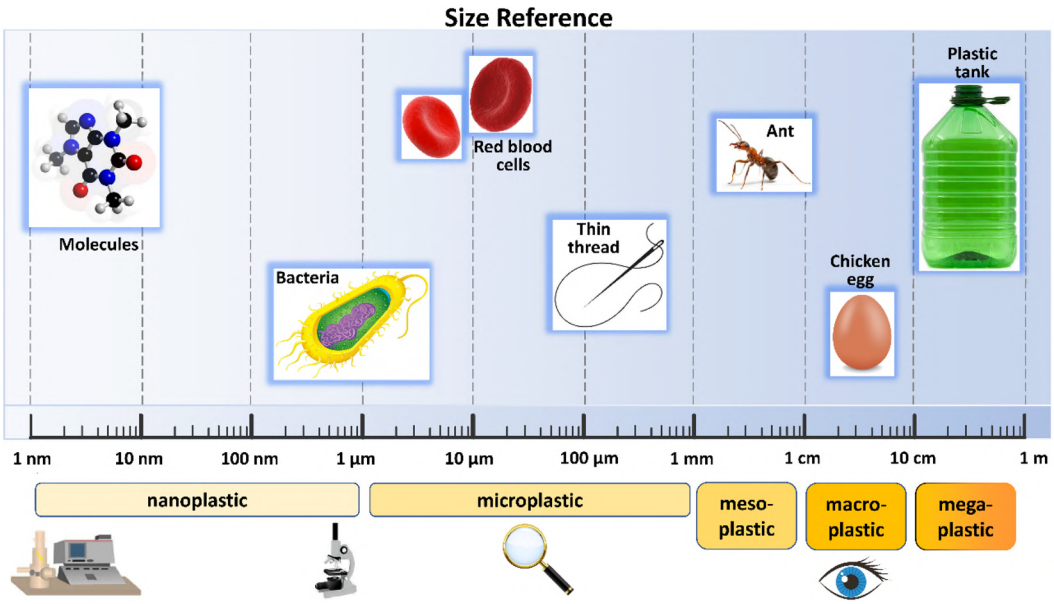

Fig. 2 Size classification of plastic particles.

According to this, plastic debris is divided into four categories: megaplastic (>50 cm), macroplastic (5–50 cm), mesoplastic (0.5–5 cm) and microplastic (<0.5 cm).[23] In 2011, Andrady[24] introduced the concept of nanoplastics, defining them as particles with sizes between 200 nm and 2 µm. A few years later, in 2015, Jambeck *et al.*[25] set the upper size limit of nanoplastics at 100 nm. A brief description of the most common characteristics of the above mentioned plastic is provided below.

Megaplastic (MegP) and macroplastic (MaP) are characterized by large debris, visible to the naked eye. Although they are considered one of the major source of marine plastic pollution, they have garnered increasing attention from the scientific and social community only in recent years.[26,27] Greater amounts of MegP and MaP are released from disposable products, being produced in large quantities and used for a relatively short time.[28] Winton *et al.* (2020), in fact, showed that bottles and lids (7.51% of all litter), bags (5.49%), food wrappers (8.92%), cigarette butts (4.02%), smoking-related packaging (3.40%) and sanitary items (3.72%) are commonly plastic products found on European beaches.[29] The main risk induced by mega/macroplastic for living organisms is represented by the possibility of entanglement and ingestion, which may cause their immediate death by suffocation. This is particularly evident for fish, marine mammals and birds, living in the environments currently most polluted by plastic.[27]

Mesoplastic (MesP), mainly deriving from degradation of macro and megaplastic, exhibits particle sizes between these two classifications. Currently, the number of articles investigating the presence and characteristics of mesoplastic in the marine environment is increasingly growing. Recent studies have shown that MesP density, measured in terms of items per m^2, increases considerably during summer seasons in the most South-American touristic sites.[30] Blettler *et al.* (2017) observed that foam plastics are the dominant mesoplastic category, characterized by many different colors and therefore giving evidence of a high variation in polymer type and origin source.[31] However, the number of MesP particles dispersed in the environment is always smaller than that of MP.[32,33] Isobe *et al.* (2015) found that the concentration of mesoplastic is about 10 times lower than that of MP in East-Asian seas, with a number of collected debris of about 12 000 per MP compared to 780 of MesP and an average concentration of 3.74 and 0.38 pieces per m^3, respectively.[34]

Plastics at different sizes can be generated by fragmentation and degradation of debris[35] due to physical forces, such as waves and currents in aquatic systems, and to environmental and atmospheric conditions, such as solar radiation, pH and temperature. Physical and chemical characteristics of plastics also play a major role in the fragmentation and degradation

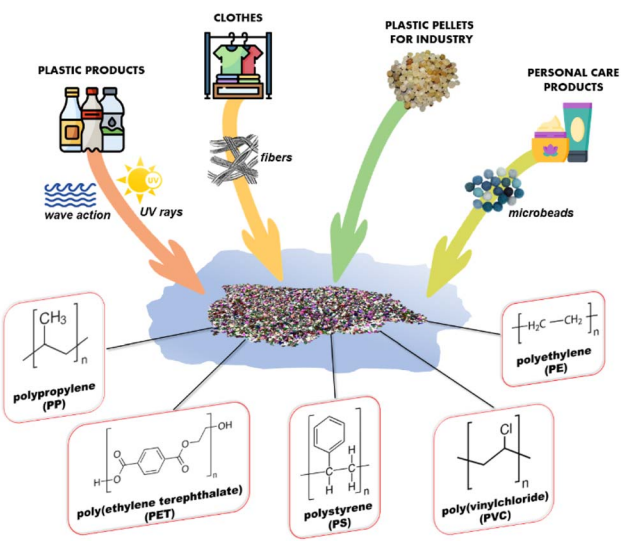

Fig. 3 The main sources of MP pollution and the most common plastic polymers present in the environment.

Table 1 Chemical–physical properties, sources, and average quantities produced annually (2020) of the common microplastic wastes

Plastic class		Specific gravity	Percentage production	Products and typical origin
Polypropylene	PP	0.83–0.85	19.7	Food packaging and wrappers, caps, microwave containers, pipes, automotive parts, *etc.*
Low-density polyethylene	PE-LD	0.91–0.93	17.4	Reusable bags and containers, agricultural film, food packaging film, *etc.*
High-density polyethylene	PE-HD	0.94	12.9	Milk bottles, toys, shampoo bottles, houseware, *etc.*
Poly(vinyl chloride)	PVC	1.38	9.6	Window frames, profiles, floor and wall covering, pipes, cable insulation, garden hoses, *etc.*
Polyethylene terephthalate	PET	1.37	8.4	Bottles for water, soft drinks, juices, cleaners, *etc.*
Polyurethane	PUR	1.05–1.28	7.8	Building insulation, pillows and mattresses, insulating foams for fridges, *etc.*
Polystyrene	PS	1.05	6.1	Food packaging, building insulation, electrical and electronic equipment, eyeglasses frames, *etc.*
Other plastics	—	—	7.4	Phenolic resins, epoxide resins, melamine resins, urea resins, *etc.*
Other thermoplastics	—	—	10.7	Hub caps (ABS); optical fibres (PBT); eyeglasses lenses, roofing sheets (PC); touch screens (PMMA); cable coating in telecommunications (PTFE); aerospace components, medical implants, surgical devices, membranes, protective coatings, *etc.*

processes. The most common plastic polymers present in the environment are polypropylene (PP), poly(ethylene terephthalate) (PET), polyethylene (PE), polystyrene (PS), and poly(vinylchloride) (PVC) (Fig. 3). Their chemical and physical properties, sources, and average quantities produced annually have been reported in Table 1.[24]

Pollution sources

Microplastics pollution sources can be divided into two main groups, namely primary and secondary, based on their origin. The distinction is based on whether the particles were originally produced with those dimensions (primary) or whether they derived from the degradation and/or breakdown processes of larger debris (secondary) (Fig. 4).

Primary sources. The main sources of primary MP are tires, road markings, marine coatings, synthetic textiles, personal care products, plastic pellets, city dust,[36–39] which flow into the environment mainly through domestic sewage, WWTPs or atmospheric events.[40,41] In particular, transporting tires and road wear particles (TRWP) are dispersed through rainwater as

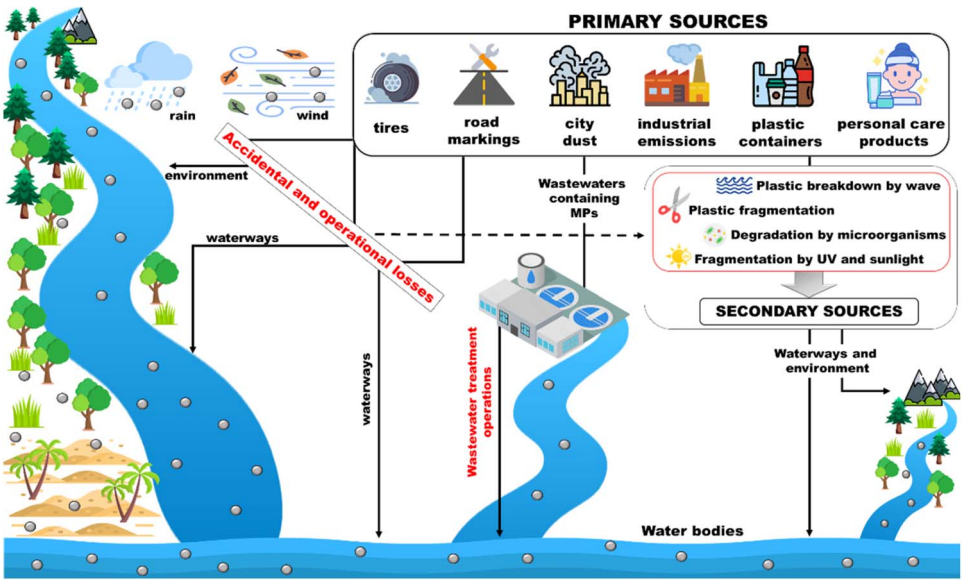

Fig. 4 Primary and secondary sources of MP pollution.

a transport route,[42,43] synthetic fibers deriving from clothing, personal care products like scrubbers in cosmetics, artificial grass, landfills and waste incineration[38,44] are carried by the wind in the aquatic environment or deposited in the terrestrial environment. While large plastic particles can be efficiently removed during wastewater treatment, MP often bypass treatment units, entering and accumulating in the aquatic environment.[45] In fact, most WWTPs are located close to water courses, seas or oceans, thus inducing a more copious and simplified release of microplastics due to the shorter path. For example, in mainland China, more than 50% of wastewater treatment plants (1873 out of 3340), with a treatment capacity of around 10^7 m^3 day^{-1}, are located in coastal regions where their effluents can discharge directly into aquatic ecosystems.[46–48] Recent studies have highlighted that agriculture is also one of the main anthropogenic activities that generates MP pollution mainly in the soil due to the use of sewage sludge as soil improvers and the use of agricultural plastics, such as plastic mulches.[49,50] However, soil MP pollution can be easily transferred to aquatic systems through agricultural runoffs. MP release can also occur at various stages of the life cycle of plastic products (*e.g.* manufacturing, transportation or recycling). Nevertheless, most leaks occur mainly during the use phase of plastic-containing products, which is the main reason that several countries have banned the use of MP in personal care products.[51] In addition, the European Union has called for the use of specially added microplastics (for example in cosmetics and personal care and cleaning products) to be banned by 2020. They have also proposed stricter rules to significantly reduce the unintentional release of microplastics from products such as synthetic fabrics, tires, paints and cigarette butts. The strategy adopted by the EU also includes the use of single-use plastics. In December 2018, European legislators, Parliament and Council, approved a ban on the use of certain single-use plastic products, such as cutlery, plates and balloon sticks, and the obligation for manufacturers of plastic packaging to contribute to the costs of waste collection for these products.

Secondary sources. Secondary MP are defined as micro-waste resulting from the breaking up of larger plastic debris through physical, biological and chemical degradation processes. These processes are mainly (a) photodegradation by sunlight (mainly caused by exposure to UV-B radiation); (b) mechanical degradation such as wave action and sand friction;[52] (c) thermo-oxidative degradation or oxidative erosion; (d) biodegradation by microorganisms that can degrade the hydrocarbons of plastics;[53] and (e) hydrolysis by sea water. Each of these processes can take place individually or simultaneously on a plastic fragment, depending on the ambient environmental conditions. Degradation is usually increased on beaches and offshore, where plastic debris is subjected to more extreme conditions than those found in continental areas or in inland water bodies. All processes can lead to a considerable decrease in the average molecular weight of the polymer and therefore to a drastic reduction of its dimensions, generating secondary MP. In the presence of high oxygen concentrations (*i.e.* in winter and early spring, when the water temperature is low, the dissolved oxygen concentration is high[54]) the degradation processes, especially those of photodegradation or bacterial biodegradation, are much more favoured. In some cases, polymers can self-catalyze the degradation processes leading to the generation of oxygen-rich substances. Such fragmentation and degradation processes increase the availability of plastic debris in the environment, posing additional environmental risks.[55]

Although the degradation processes that can occur in aquatic and coastal environments are different, their biodecomposition rates are not sufficiently fast to cause a beneficial effect towards environmental dispersed plastics.

The slow degradation is mainly due to the temperature, the pH of the sea water but above all to the scarce presence of microbial species capable of degrading these polymers. Furthermore, fouling-defouling, meaning the accumulation of encrustations on the surface of floating plastics, and their subsequent sinking, alternated by the enrichment of foraging bacteria that make the detritus regain buoyancy, can generate a continuous change of environmental conditions along the water column, such as to negatively interfere with the degradation process. Zbyszewski *et al.* (2014)[52] highlighted how studying the degree of surface aging of microplastics can be useful for tracing the history of particles. Furthermore, the evaluation of plastic degradation patterns in different ecosystems is fundamental to understand how particles interact with the environment and how various factors influence their stability, transport and final fate.[56]

Environmental and accumulation cycle of microplastics

Fate and accumulation

The spread and cycle of microplastics from urban and industrial settlements to rivers and lakes, as well as transport to the sea and subsequent marine dispersion on the surface and deep in ocean basins have been intensively studied[57–60] (Fig. 5). Plastic waste is usually generated (a) by the inhabitants, varying according to their habits, geographic location and existing infrastructures; (b) from waste management and treatment, also including collection and transport; (c) from industrial and manufacturing plants (Fig. 5). Plastic waste can take different paths spanning from reuse to recycling, to incineration, to landfill disposal and to dispersion into the environment. The most environmentally friendly practices are reuse or recycling, which keep the plastic in a closed loop (*i.e.* the material remains in the value chain). The local distribution of MP is strictly dependent on the complex interactions between the sources of plastics, their dispersion and the current environmental conditions. Therefore, the distribution and fate of microplastics is highly heterogeneous and challenging to monitor.[24] Despite this, predictive models of MP diffusion have been developed over the last few years. Diffusion processes can be substantially influenced by the geography of the territory, by physical, chemical and biological processes, mainly related to atmospheric conditions, and by the physical properties of the fragments (*e.g.* size, shape, density, buoyancy).[61–63] It has been found that most MP particles released to land will finally end up

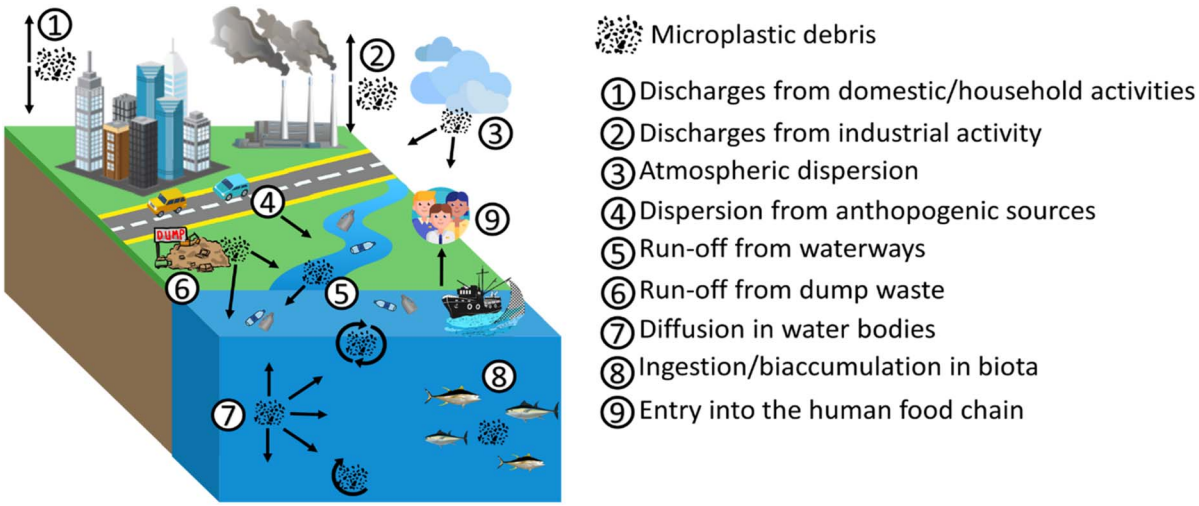

Fig. 5 Pathway example of MP diffusion.

in the marine environment.[25,58,64,65] Especially in coastal regions, terrestrial sources are considered an important contribution to marine plastic debris,[25] with between 1.15–2.41 million tons per year of plastic waste being carried into the ocean by rivers.[64] Schmidt *et al.* (2017)[65] also revealed that rivers are a preferred route contributing between 80% and 94% of the total plastic load entering the seas and oceans. Moreover, a strong correlation between population density and microplastic concentration has been verified. The presence of densely populated regions and inappropriate waste management can generate high levels of contamination.[66–68] From the evidence set out so far, the global distribution of MP in the marine environment is well established. Their ubiquitous presence in the marine ecosystem leads to high interaction with the biota both in surface waters and in the deepest abysses, as well as in sediments.[69] Over 1400 marine species interact, primarily through entanglement and ingestion, with marine plastic debris in different ways.[70] MP are usually mistaken for food due to their micrometric size and variable coloration. A wide variety of marine biota such as corals, zooplankton, phytoplankton, lobsters, sea urchins and fish ingest microplastics and, based on their movements, transfer them to remote or pristine areas.[71] Larger marine biota creatures such as sea turtles, whales, sharks, polar bears and seals are also susceptible to ingesting MP in the oceans.[72] In addition to direct ingestion from water, MP can be ingested from marine biota through their prey.[73,74] In particular, the species that feed on phytoplankton can ingest MP following the formation of the aggregates that the latter generate with photosynthesizing autotrophic organisms. As for the predatory vertebrate species, they can involuntarily ingest MP, confusing the synthetic microparticles for the prey, but also by ingesting invertebrates containing MP (*i.e.* bivalves, amphipods, barnacles, polychaetes) favouring their trophic transfer. Therefore, the variable pathways of MP suggest that all marine organisms, from those inhabiting the abyssal depths to those occupying surface waters and benthic zones, are exposed to MP contamination. This transfer of species to species and the different interactions in the various food compartments ultimately generate channelling towards the human food chain. Microplastics suspended in the ocean water column or dispersed on the sea surface can be transported from their release zone to remote areas[75] (Fig. 6).

However, most of these micro-fragments can accumulate in the central oceanic regions (termed "gyres").[76] An oceanic gyre is a system of ocean currents that move in a circular pattern. They are created by variations in the winds direction and forces generated by the rotation of the Earth. The oceanic gyre is not fixed on a particular point in the ocean but moves to coincide with the wind patterns. These patterns are known to drive the "ocean conveyor belt" that circulates ocean water across the planet. The most notable oceanic gyres include the Indian Ocean Gyre, the North Atlantic Gyre, the South Atlantic Gyre, the North Pacific Gyre, and the South Pacific Gyre. These ocean current systems cause the movement of plastic debris but, at the same time, lead to their accumulation. Cozar *et al.* (2014)[76] estimated that the result of ocean gyres led the Pacific Ocean to contain about 35% of the global amount of ocean plastic.[77] Therefore, non-entrained plastics and MP in gyres can reach remote ocean regions and coasts as a result of ocean transport caused by surface currents, bottom water transport, thermohaline circulation, Coriolis force and friction with air currents.[77]

A further factor linking the MP distribution and the action of the wind is the so-called "Stokes drift", as well as a combination of surface residual currents. These phenomena generate the transport of MP from the open sea to shallow coastal waters.[78,79] The evaluation of the different factors influencing the distribution of microplastics in marine region has allowed to develop models to quantify the expected plastic load in a given region as a function of time, in order to locate areas of high accumulation of debris and potential threats.[76,80]

Many scientists have applied transport models of waterborne materials and particles (oil spills, larvae, sediment) to study the Lagrangian trajectories of surface microplastics.[63,81,82]

The following are the most used models for this purpose:

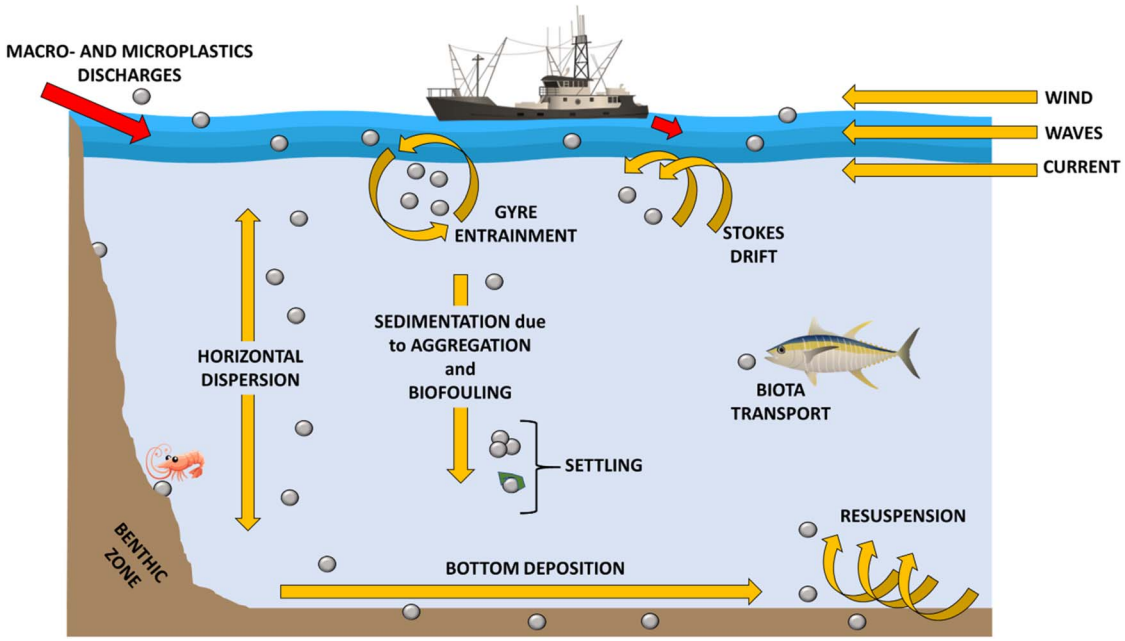

Fig. 6 Microplastic diffusion in the aquatic system.

(1) NEMO: Lagrangian tracking model, used to predict both the accumulation of floating debris and its stranding points in the Mediterranean area.[83] This model, based on repeated 1 year predictions with 24 hours evaluations, took into account an initial homogeneous distribution of marine debris;

(2) MEDSLIK-II: prediction model of the movement of plastic debris in the Adriatic Sea, starting from an estimate of 10 000 tons per year of waste released, with an entry point, at increasing volumes of plastic, identified in the northwest region of the Adriatic, and no defined accumulation points. The model highlights that the main accumulation points are represented by the seabed and coastal areas;[78]

(3) PLETS-2D: Lagrangian model of particle tracking, used to predict the trajectories in 90 days of debris from different entry points. The study showed that wind drift greatly influences particle distribution, generating sources of uncertainty in the mapping of plastic distribution;[84]

(4) Pol3DD: Lagrangian simulation model of particle tracking to predict floating debris in the world ocean. This model highlighted the high concentration of plastic debris in subtropical gyres.[85]

Although many of these models have proved effective, they are subject to uncertainty, both because of the changeableness caused by the short-term variation of abiotic factors, such as the direction and strength of the wind, and because the considered factors are affected by sources of uncertainty determined by the global climate change (coral bleaching,[86] ocean acidification,[87] and ice melt in polar regions[88] affecting our oceans).

Indeed, these changes, in addition to influencing the ability of models to predict the position of plastic aggregates, could also alter geographic areas and ecosystems due to the negative effects of marine plastic pollution.[63]

In addition to induced extrinsic turbulence, a key role also derives from the intrinsic characteristics of microplastics such as size, density and shape that modify their speed of adoption.[62,89,90] Once MP reach the marine ecosystem, their density greatly influences their distribution. Those with a lower density than sea water and a neutral surface charge float to the surface or disperse in the water column, while those with higher density tend to accumulate in benthic environments,[79,89] *i.e.* those ecological zones at the lowest level of a basin or sea, also including the sediment surface and some subsurface layers. Taking into account that more than 65% of the produced plastics have a lower density than sea water, the largest fragments are found floating on the surface or mixed in the surface water column of the oceans.[63,89] At this point, MP are dispersed by dynamic conditions, such as wind strength and geostrophic circulation, resulting in a very wide variability in surface concentrations.[81,91] As far as high-density MP are concerned, these are not floating and tend to settle both in coastal sediments and in the seabed.[92,93] Recently, experimental researches have been conducted to evaluate the sedimentation behavior of high density microplastics (density higher than that of water).[61,94] For example, Ballent *et al.* (2012)[62] studied the sedimentation rate of microplastic pellets having different densities between 1.06 and 1.13 g cm^{-3}. The results showed that the sedimentation rate (which varies from 20 to 60 mm s^{-1}) is directly proportional to the increase in density.

Neutral surface charge MP can be found on the sea surface but also suspended in the water column or lying in the subsoil of deep waters. These considerations emerged following discrepancies found between the expected plastic concentrations and those actually found in surface ocean waters.[76,80]

Recent studies have proved that the highest concentration of microplastics is found in the intermediate part confirming that

the microplastics are distributed vertically inside of the water column, mainly due to the turbulent regimes of the waters, generated by the wind and currents.[95]

Enders *et al.* (2015)[96] examined the vertical dispersion of microplastics as a function of their size. Research results showed that smaller sized microplastics are much more affected by turbulent mixing. While empirical calculations, resulting from the use of the General Ocean Turbulence Model (GOTM), have shown that particle-shaped microplastics have a higher diffusion rate than sheets, which in turn are more affected by turbulent phenomena than fibrous debris.[97]

At the same time, further studies[61] have shown that the sinking speed of microplastic fragments is influenced more by shape rather than density (particles of different forms of polyamide (1.14 g cm^{-3}) sink faster than those of polyvinyl chloride (1.56 g cm^{-3})).

In addition to the characteristics of shape and density, it is also necessary to take into account the phenomenon of biofouling: microorganisms of different nature can rapidly aggregate on the surface of plastic debris and develop biofilms.[24,93,98]

Còzar *et al.* (2014)[76] and Moret-Ferguson *et al.* (2010)[99] hypothesized that the phenomenon of biofouling could increase the density of microplastics to such an extent that particles with a density lower than that of seawater (for example, polyethylene or polypropylene) can reach densities that exceed it, leading to a slow sinking of the particles. At the same time, biofouling can reduce the surface hydrophobicity of microplastics, generating a greater tendency for them to sink:[76,100] plastic particles that would normally float (such as polyethylene and polypropylene) have been found in marine sediments.[101] As reported by Chubarenko *et al.* (2016),[94] heavy microplastic particles take on average less than 24 hours to settle through the 250 m water column, while fibrous plastics, such as polyethylene, take about 6–8 months to sink due to biofouling.

Finally, the sinking speed of microplastics can also be increased by the phenomenon of incorporation into organic aggregates.[102,103] Long *et al.* (2015)[104] found, based on their experimental evidence, that the sinking rate of polystyrene microspheres (2 μm, density of 1.05 g cm^{-3}) embedded in diatom aggregates could reach several hundred meters per day compared to 4 mm per day for freely suspended beads.

Impact on human health

Microplastics represent a huge problem due to their toxicity and persistence in the environment. Their toxicity is mainly attributed to (a) the presence of hazardous chemical additives during their production process, and (b) to the fact that due to their considerable surface area and hydrophobic character, MP are able to absorb and concentrate many organic and inorganic chemical contaminants (indirect toxicity). It was recently observed that MP can absorb chemical pollutants such as polybrominated diphenyl ethers (PBDEs),[105] perfluorochemicals (PFCs),[106] drugs and personal care products (PPCP).[107] The persistent organic pollutants must also be added to the list, better indicated by the acronym POPs. Among them, MP are particularly prone to absorb polycyclic aromatic hydrocarbons (PAHs), polychlorinated biphenyls (PCBs) and organochlorine pesticides such as dichlorodiphenyl trichloroethane (DDTs). The absorption of these pollutants on MP certainly depends on both the type of polymer and its state (rubbery or glassy). Due to their small size, MP can be easily ingested and/or inhaled by organisms. This therefore implies that, through ingestion and/or inhalation, MP and the environmental pollutants they contain enter the circulatory system of organisms, penetrating into the tissues and organs, which is why toxicological studies are necessary to highlight the real risks deriving from the "assumption" of MP.

Human exposure to microplastic

Main sources of human exposure to MP are (a) ingestion, of water or food; (b) inhalation, both of indoor and outdoor air; (c) dermal contact, through indoor dust, personal care products and fabrics. Despite their toxicity, risks for human health deriving from exposure to MP are not simple to assess as most of the developed methods provide quantitative data in terms of MP number, size and shape, failing to translate these in terms of dose or mass. A recent study[108] estimated that the annual amount of MP potentially ingested by a person can fluctuate between 11 845 and 193 200 particles, most of them coming from drinking water consumption.

Inhalation. Due to their low density and small size, suspended MP particles can accumulate in the atmosphere and can be easily inhaled by humans. MP concentration in the air can significantly vary depending on the season, the overall air quality,[109] the characteristics of the particles (density, size, surface charge, hydrophobicity), and the different sampling methods adopted for the analyses. For example, a study in Paris showed that the number of MP in the air significantly increases during the rainy seasons compared to dry ones.[110] The concentration of MP between indoor and outdoor is also significantly different; generally the values are about 5 to 10 times higher for indoor air.[111] However, it should be noted that most of the data are expressed in terms of daily number of fibers, particles, fragments or elements per m^2 (per fallout) or per m^3 (per air), which can differ significantly from day to day. For example, Dris *et al.* (2017) estimated the indoor MP concentration between 0.4 and 56.5 particles per m^3 while the outdoor one was between 0.3 and 1.5 particles per m^3.[112] Taking into account these data, Prata (2018)[113] estimated that an adult man can inhale on average, considering a human tidal volume of 6 L min^{-1}, a daily number of MP particles between 26 and 130. Furthermore, in 2019 Vianello estimated that, in the case of a completely sedentary life, this daily value can reach up to 272.[114]

The presence of MP particles in the air (both indoor and outdoor) is mainly associated with plastic degradation processes, landfills, synthetic textiles, building materials and waste.

Inhaled MP particles accumulate predominantly in the lungs. The pulmonary alveoli have a tissue barrier of less than 1 micron and a large surface area (150 m^2) so they constitute an

optimal adsorption site for MP. The main risks associated with human health involve the appearance of an inflammatory response of the lung tissue, which may also be followed by cytotoxicity and genotoxicity.[115] Xu *et al.* (2019) showed a cytotoxic and genotoxic effect on the pulmonary epithelium and macrophages caused by polystyrene particles of 50 nm size.[116] Lung inflammation can also be chronic, due to the intense release of proinflammatory chemotactic factors, often known as dust overload.[113,117] Also, it was observed[113] that workers in textile factories, exposed to acute and chronic inhalation of MP, can easily be subjected to respiratory tract diseases. Prolonged exposure to MP can also lead to lung diseases, including asthma, pneumoconiosis and extrinsic allergic alveolitis.[108,111,113,118] In addition to the accumulation in the lungs, MP particles are swallowed by macrophages and, since particles of 15–20 microns in size are toxic to them, MP end up being transported also in the lymphatic and cardiovascular system.[119] More recent findings can be found in Yang *et al.* (2022).[120] It must be considered that studies on the effects of MP for inhalation require further investigation in order to quantitatively assess the exposure doses and fully understand the real risks for human health.

Ingestion. As mentioned above, MP can be easily ingested by a large number of organisms due to their very small size, which is considerably smaller than macroplastics. The main sources of microplastics ingestion for humans are food and water.[121] Cox (2019)[122] points out that exposure levels differ between sex categories and age groups since different are lifestyles and diets, with a maximum exposure recorded for male and female adult categories. Recently, Koelmans *et al.* (2019)[123] showed that the amount of MP particles varies in different water matrices, such as treated and untreated wastewater, surface water, tap water and bottled water. Regarding drinking water, a big distinction must be made between tap and bottled water. The number of MP particles, in fact, ranges from 0–61 particles per L for tap water and from 0–10 000 particles per L in the case of bottled water.[111] Currently, the methods used for the treatment of raw water, known as WTPs (water treatment plants), are able to remove at least 70% of the MP present. This percentage can actually increase further, depending on the method type, from 70% in the case of WTP1 (sand filtration) up to a maximum of 85–86% for combined WTP2 (sedimentation + sand filtration) and WTP3 (flotation + sand filtration) treatments.[124] Nevertheless, the high number of MP present in bottled water comes mostly from the container itself and to a lesser extent from the water distribution and bottling processes. In support of this, it has been found that about 80% of MP in bottled water consist of PET, PP, PE, the materials of which caps and bottles are made.[125] Furthermore, the same study[125] has interestingly shown that a considerable number of MP particles are also present in water bottled in glass, leading to the assumption that the plastic cap is the one releasing the greatest amount of microplastics (50 particles per L).[111] Turning to the numbers, Cox *et al.* (2019)[122] showed that on average 90 000 are the MP particles ingested annually by humans only by drinking bottled water, while the amount is about 22 times lower (4000) by drinking tap water.

It is interesting to point out how the presence of MP has also been highlighted in other food beverages such as energy drinks, bottled tea, wine and beer. For example, 2563–5857 MP particles per L were found in white wine from Italy, where the major amount comes from the synthetic stoppers often made of polyethylene, and 10–256 particles per L were found in beer from Germany, even if, in this case, MP sources can be different.[126]

The presence of MP has also been well documented in food. The first evidence dates back in 1960, when plastic fragments were found in the guts of sea birds (the global annual plastic production was less than 25 million tons at that time).[7] Today, the greatest amounts of MP is found in food products such as crustaceans and commercial fish,[127–129] bivalves,[130,131] salt[132] and sugar.[133] Among these sources, sea salt and seafood have aroused particular interest and a greater number of studies have been focused on them. An average concentration of about 0–20 000 MP particles per kg was found in salt but these values can easily vary depending on the geographical origin. For example, Kim *et al.* (2018)[134] showed that sea salt from the coasts of eastern and southern Asia has the highest number of MP particles compared with sea salt from European, North American and Australian coasts. It should be noted that this geographical distribution of MP in sea salt can easily be correlated with the evidence from Lebreton *et al.* (2017), according to which rivers flowing near the coasts of eastern and southern Asia provide the largest contribution to plastic release into the oceans.[64] Seafood is currently ranked as the third cause of human MP consumption, after bottled water and alcohol.[122] Rochman *et al.* (2015)[135] found that each fish species can contain from 25% to 33% of MP, but this percentage rises to about 60% if all marine species are considered. Also, these percentages can change considerably according to the geographical food habits, as some urbanized populations have significantly higher average consumption of seafood than others. For example, anchovy, a fish typically eaten without removing the digestive tract, is a common food in Japan. Given that 2 MP particles can be found in each anchovy,[136] it was estimated that Japanese seafood consumption can result in the accumulation of 154 MP particles per day.[122]

In general, about 90% of ingested MP are eliminated from the human excretory system *via* the feces. The removed MP are usually larger than 150 μm in size while smaller MP can be absorbed much more easily by the human body. In fact it has been shown that MP particles with dimensions smaller than 150 μm can easily cross the gastrointestinal epithelium, MP particles with dimensions of the order of 10 μm can pass through the placenta and the blood–brain barrier and MP particles of smaller dimensions at 2.5 μm are able to reach the systemic circulation by endocytosis.[111] Absorption of MP by the intestinal mucosa is certainly the main route through which MP remain within the human body. In addition, paracellular transport in the intestine and cellular uptake in the lungs must be taken into consideration. Paracellular transport in the gut, in the form of persorption, occurs when the MP particles are of the order of 130 μm.[122] For dimensions of about 10 μm or more, the main route of entry is the absorption by specialized M cells of

intestinal lymphoid tissue (Peyer's spots of the ileum) while smaller MP particles (few microns) can be directly taken up by the gut and lungs cells.[108,122] These compounds are particularly harmful and can cause various types of physiological damage as listed below[108,122]

Disruption of immune function: prolonged exposure to MP can lead to autoimmune diseases or immunosuppression,[109,113] the causes of which are attributable to the release of immunomodulators, to the erroneous activation of immune cells and to oxidative stress.[137] Autoimmune rheumatic disease[138] and systemic lupus erythematosus[139] can also occur.

Translocation to distant tissues: translocation occurs through the circulatory system and produces inflammation following which an immediate increase in the permeability of cell membranes is recorded.[109] Studies have shown that the presence of MP in the circulatory system can cause occlusions and vascular inflammation,[140] pulmonary hypertension,[117] systemic inflammatory response and blood cell cytotoxicity through internalization.[141] Prata *et al.* (2020)[109] also demonstrated that translocation can lead to chronic inflammation, reduced organ function and increased cancer incidence. Furthermore, the presence of MP in bone can cause bone loss by activating osteoclasts.[142,143]

Altering metabolism and energy balance: exposure to MP can cause an alteration of human metabolism either directly or indirectly. In the first case, the activity of metabolic enzymes is compromised or in any case modified, while in the second case the energy balance, the homeostatic balance between energy produced and energy consumed, is interrupted. It has been shown that the most frequently occurring effects are a lowering of nutrient intake, an alteration of the activity of metabolic enzymes and an increase/decrease in energy consumption.[108]

Oxidative stress and cytotoxicity: oxidative stress and, consequently, cytotoxicity are the most common effects generated by MP exposure. Oxidative stress occurs as MP particles can release ROS (reactive oxygen species), created by the manufacturing process of plastics, weathering or exposure to UV light,[144] oxidizing chemicals (such as metals), which easily adsorb on their surface, or oxygen-containing radicals, produced as a result of the inflammatory response.[145,146] Sternschuss *et al.* (2012)[147] showed that the inflammatory response of the human body due to the fitting of limb and joint prostheses containing MP led to the release of free radicals and acute toxicants which completely degraded the prosthesis itself. Oxidative stress and inflammation can lead to cytotoxicity. MP particles, in fact, can be digested and internalized by macrophages.

Neurotoxicity: neurotoxicity occurs due to chronic MP exposure. Direct contact with translocated particles or alteration of the levels of proinflammatory cytokines can lead to the activation of the immune cells in the brain and to oxidative stress, with consequent permanent damage at the neuronal level.[108]

Reproductive toxicity: Chang *et al.* (2020)[148] have shown that MP particles can accumulate in the gonads, leading to a reduction in their reproductive capacity due to the alteration of energy metabolism and oxidative stress.

Carcinogenicity: Chang (2010)[149] showed that chronic irritation and oxidative stress generated by the presence of MP in the human body can lead to the release of pro-inflammatory mediators. Such mediators can involve angiogenesis which, in turn, can lead to the formation of tumors. In 2018, Prata[113] then demonstrated that the same effects, *i.e.* chronic irritation and oxidative stress, can cause the onset of tumors as a result of DNA damage.

Indirect effects through acting as vectors of toxic chemicals and microorganisms: as mentioned above, the MP particles can contain additives, chemical pollutants, metals or other substances that are highly toxic to humans. From a purely numerical point of view, the exposure to toxic agents from MP is irrelevant when compared with the daily intake of MP for food or dust. However, it is the prolonged exposure to toxic agents that can cause the numbers to grow to such an extent that they are considered a real risk factor.[150] It has been shown that BPA, BPS and in general many plastic additives are endocrine-disrupting chemicals (EDCs), leading to a higher incidence of early onset of puberty and genital defects, blood infection and breast cancer.[151,152] Not only toxic agents: the large surface area of MP can also constitute fertile ground for numerous microorganisms such as vibrio spp., one of the most virulent bacteria,[153] or *Folsomia candida*, a soil organism which acts as a promoter of gut microbiome's activities.[154]

Dermal contact. Absorption of MP through the skin is not possible: it has in fact been shown that only particles smaller than 100 nm are able to cross the dermal barrier.[155] However, personal care products such as facemasks, facewashes, hand cleansers and toothpaste contain MP, which can cause skin damage due to local inflammation and cytotoxicity.[72] Schirinzi *et al.* (2017)[156] showed that oxidative stress can also occur in the cells of the dermal epithelium. It should be noted that even plastic products used in surgery can often lead to severe inflammation. To date, there are few studies on the risks due to exposure of MP for dermal contact and therefore greater efforts are required in the coming years to have a much more satisfactory picture of the situation.

Impact on marine habitat-forming species

In the last two decades, numerous studies have been carried out to monitor the presence of plastic in the oceans and the damage that its presence causes to the marine biota. What emerges very clearly is that there is no place that plastic has not reached.[75,80,157–163]

The greater the amount of MP in the marine environment, the greater the bioavailability for marine biota. Numerous studies based on the analysis of the stomachs of marine organisms have revealed the presence of MP inside them, confirming that marine organisms can ingest them.[98,164–166] This is attributed to the fact that marine organisms mistake microplastic particles for food due to their small size, and thus ingest them. The MP uptake by marine biota depends on numerous factors such as density, shape, color, charge, abundance and

aggregation of microplastic particles.[167] Regarding the density, it has been shown that usually the lower density particles are ingested by copepods and are subsequently excreted in the faeces. The sinking speed of these fecal pellets is strictly dependent on the density of the microplastics inside them and this means that they can in turn become nourishment for copepods, polychaetes, crustaceans but also for fish. High density microplastics are usually ingested by benthic invertebrates and deep ocean biota. MP shape influences their dynamics indirectly as it is responsible for the bioavailability and distribution of the MP particles in the marine environment. Generally, spherical shaped particles tend to sink much faster than thin films and plastic fibers of equal density. Shape is also related to the time MP persist in the marine organisms after ingestion and to the excretion process. For example, the amphipod *Hyalella azteca* is able to ingest both MP fibers and spheres.[168] However, the clearance time in the case of fibers is much longer than that for the spheres, thus implying, due to their difficulty in being excreted, fibers have greater toxicity. Generally, irregularly shaped MP particles are more toxic than those of regular shape due to the greater difficulty that organisms have in the process of egestion. MP color is one of the most striking demonstrations of how ingestion of microplastics by marine organisms is due to the fact that they often mistake MP for food. Darker colored MP, especially green microplastic fibers, are easily ingested by flathead gray mullet (*Mugil cephalus*) as they closely resemble marine plankton, which this animal normally feeds on.[169] Another example is that blue polyethylene fragments are ingested by about 80% of the Amberstripe scads (*Decapterus muroadsi*) who mistake them for blue copepods, their prey, being similar to them in color and size.[170] Numerous studies have been carried out and are currently underway to understand how harmful are the side effects on marine biota due to MP ingestion.[72,167,171] It has now been widely demonstrated that damage to the organism can be both physical and chemical and can lead, in the most serious cases, to its death.

Once ingested, the fate of microplastics can follow several paths as described below:

(a) At best, they can be eliminated from the marine organism by excretion or production of pseudofaeces, thus not leading to significant side effects except for the alteration of the organism's energy flow. The function of excretion, in fact, performs two main tasks: to separate the organic material from the inorganic components, that is the MP, and to act as a cleaning mechanism preventing an accumulation of particulate material at the level of the organism gills. It is often observed that excretion occurs a few hours after ingestion of the MP particles. This is due to the fact that, most likely, such organisms are able to recognize MP as low-energy food and consequently remove them.[151] However, pseudofaeces, loaded with microplastics, constitute in turn food for other marine organisms and the problem therefore moves to higher trophic levels.

(b) MP are retained by the organism and cause toxic effects. What occurs is the accumulation of MP in the digestive system, producing physical damage such as injury and clogging, and the appearance of adverse effects such as pathological and oxidative stress, inflammation and liver toxicity, reduced growth rate, false satiation, blocked enzyme production and reproductive complications.

(c) After the digestion process, previously retained MP enter the bloodstream and reach different internal organs and tissues through the translocation phenomenon.

(d) According to the food chain, marine organisms that have ingested MP can in turn constitute food for other organisms, which therefore ingest MP indirectly.

As already pointed out, the toxicity of MP is also attributable to the contaminants and pollutants that they are able to retain on their surface and that can be released into the organism once MP are ingested.

The entire marine biota is affected by the presence of MP. In fact, it has been shown that MP can be ingested by a large number of invertebrate and vertebrate marine organisms including coral, zooplankton, shrimps, bivalves, copepods, mussels, lugworms, oysters, fishes and by larger animals such as turtles, manatees, otters, snakes, sea lions, penguins, seals and whales.[1,160,172]

Currently, with an extension of about 0.2% over the entire oceanic area, coral reefs, having the task of mitigating the effects of the ocean destructive forces on the coasts, constitute the natural habitat of about one third of all marine fish species and thousands of other marine organisms. They mainly feed on phytoplankton and zooplankton, copepods and amphipods. These organisms are all capable of ingesting MP which, consequently, end up in corals too. MP accumulate in the digestive tract of corals, leading some species of hard corals to death and consequently reducing the biodiversity of these environments.[173]

Among the marine organisms, the most affected by MP contamination are planktons, a worrying fact especially considering that they are the nourishment of a large part of the marine biota. Law (2010) showed that microplastics were found in about 60% of the plankton living between the North Atlantic Ocean and the Caribbean Sea.[81] In the report of the Norwegian Institute for Water Research of 2014, Nerland *et al.* demonstrated that MP can cross both cell membranes and cell walls and interfere with the photosynthesis process by reducing the concentration of chlorophyll in the green alga *Scenedesmus obliquus*.[174] Adverse effects include disturbed feeding and digestion due to the accumulation of MP in the digestive tract or in the gut of zooplanktons.[72] Zooplanktons expel MP in the form of faecal pellets. This would not be a problem if it wasn't for the fact that these pellets are nourishment for benthic and pelagic marine organisms, which therefore ingest MP indirectly.[175]

The group of benthic organisms is characterized by a remarkable biodiversity, covering about 98% of the entire marine biota, and includes invertebrates such as lobsters, blue mussels, oysters and barnacles. They are all capable of ingesting MP.[176,177] A 2014 study found that farmed blue mussels from Germany, near the North Sea, contain a number of MP particles equal to 0.36 ± 0.07 particles per g (wet weight) while it is equal to 0.47 ± 0.16 particles per g (wet weight) for oysters farmed in Brittany and France near the North Atlantic Ocean.[178]

MP were found in approximately 36.5% of pelagic and demersal fishes[179] and in approximately 18% of top predators in the central Mediterranean Sea, such as bluefin tuna (*Thunnus thymus*), swordfish (*Xiphias gladius*) and albacore (*Thunnus alalunga*).[180] It has been observed that MP can accumulate in the gut of fishes, causing starvation and malnourishment which can also lead to their death.[181]

Sea birds, which feed on what they find on sea surface, are also affected by the presence of MP in their digestive tract.[72] 30–35% of the MP particles are in the form of industrial pellets. In addition to the process of excretion through the production of faeces, sea birds tend to remove MP from the digestive tract by regurgitation.[182]

At this point the presence of MP was also ascertained in marine mammals, such as whales, harbor seals, sea turtles, and polar bears.[1,183–186] They can ingest MP through three different phenomena: inhalation, feeding or trophic transfer from prey.[187] In 2014, Nerland found that around 60.5% of turtles in Brazil contain MP in their digestive tracts.[174] Whales are another marine mammal particularly affected by MP contamination. This is due to the fact that they often perform a filtering function for seawater so they tend to ingest MP, and to accumulate them in their stomach and liver.[188] Due to the high ingestible quantities of MP, cetaceans are often used as probes to check the level of plastic pollution in the areas where they live by measuring the quantity of phthalates in the blubber of stranded fin whales (*Balaenoptera physalus*).[188] However, these data currently need to be considered cautiously as phthalates can come from various sources.

Removal and treatment technologies

The removal of MP from water is a key challenge in the struggle to mitigate environmental pollution. Traditional water treatment plants are not designed to remove MP and they have been globally identified as a major source of MP to the environment.[16,124,189,190] Hence, it is important to understand our current ability to remove these pollutants *via* engineered treatment methods and identify key opportunities to reduce their concentration in receiving water bodies. For this purpose, several physical, chemical and biological processes for the treatment of MP contaminated water are reviewed below.

Physical processes

Physical separation processes for primary wastewater treatment include screening, skimming and sedimentation. Using these methods, fast and low cost filtering of large contaminants is possible. The ability to remove MP depends on the wastewater characteristics as well as the type of treatment process applied.

Screening and settling. Traditional screening and settling methods may remove significant portions of suspended solids in water. For example, Liu *et al.* (2018)[191] observed that the average size and number of MP fragments present in the water in a Chinese WWTP decreased by 58.8% and 40.7%, respectively, after initial screening and sedimentation. The particles removed were mainly large but the authors also observed the adherence of MP to suspended solids in the water, allowing physical removal of smaller fragments and fibres that might not be expected otherwise. Moreover, screening and sedimentation have reportedly removed up to 88% of anthropogenic solids in a treatment facility in the United States (although this classification includes more than just MP).[192] The importance of plastic density as related to settling velocity during the sedimentation step is highlighted by Iyare *et al.* (2020).[193] The huge variety of polymers in terms of density, shape and type that are found in wastewater can substantially influence their physical separation from water. Settling alone removes an average of 72% of MP particles present in sewage influent but the smallest particles (<27 μm in diameter) are likely to pass unimpeded. As well as failing to capture the smallest particles, reliance on traditional separation processes to remove MP in this way presents another problem of transferring the pollutants from liquid to a concentrated solid waste.[194,195] This can become a serious environmental problem when sludge is recycled for land treatment or disposed of inappropriately; thus potentially allowing MP to find their way back into the water system.[196]

The difference in density between MP and the natural organic matter of water presents an opportunity for physical removal. Several lab scale studies have applied enhanced density separation in salt solution as an isolation method for MP samples in complex matrices such as wastewater or natural water.[197–199] Scaling up this method is challenging due to the large volumes of high cost salt solutions required.[200] Alternatively, enhanced settling *via* coagulation seems promising for large-scale application. Using traditional Fe salt coagulation conditions, the removal of polyethylene (PE) MP was found to be poor with less than 15% removal.[201] However, in the same experimental setup, using a high dose anionic PAM coagulant, removal was increased to over 90%. This can be attributed to the low density of PE that inhibits settling of the produced flocs and reduces the efficiency of the coagulation treatment. An impact of this effect was also observed by Ma *et al.* (2019),[202] where the highest efficiency removal of approximately 60% was achieved for the smallest sized MP. In addition to density, the shape of MP is likely to affect greatly the settling behaviour. Skaf *et al.* (2020) investigated the removal of both fibres and microspheres of PE using an alum coagulation method and they found that both could be adequately removed by sweep flocculation.[203] Less traditional coagulation-like methods such as the bioinspired agglomeration process developed by Herbort *et al.* (2017, 2018)[204,205] suggest targeting specific MP in water. Electrocoagulation methods have also been explored and over 90% removal of PE beads was reported.[206] Despite the progress in the area, the main problem with coagulation based methods is the highly variable nature of MP surfaces. The surface charge is not easily predicted meaning that coagulants specifically designed for MP removal are less efficient than for the removal of organic material.

Filtration and adsorption. Some developed materials for adsorption and activated filtration aim to target MP in water. Biochar offers a low cost option for removal of many pollutant classes, including MP.[207,208] Sun *et al.* (2020)[209] engineered an adsorption separation process relying on a biodegradable chitin

and graphene oxide sponge which is capable of removing up to 89% polystyrene from water. Batch filtration was proposed using a Zr-MOF system with over 95% efficiency for removal of PVDF microplastics.[210] While promising in performance, adsorption and batch filtration treatment pose a challenge in scaling up to meet the needs of a full scale WWTP.

Membrane separation of MP is an option already employed at scale. Malankowska *et al.* (2021) review in detail the advances made in microfiltration, ultrafiltration and nano-filtration methods in the removal of MP.[23] Michielssen *et al.* (2016) suggest retrofitting WWTPs with granular sand filtration and membrane filtration has the highest potential for MP removal in a meta-analysis of available technology.[192] This finding was backed up for large scale studies in a comparison of municipal WWTPs where rapid sand filtration removed 97% of MP.[16] However, the high potential removal efficiency comes at the cost of membrane pore blockage and resulting flux reduction when applying high-pressure filtration techniques. Such issues arose within just 48 h of ultrafiltration when 38% flux reduction occurred due to MP blockage of pores during treatment of MP contaminated water.[211] MP interaction with organic matter in the water may also enhance the rate of membrane fouling. The size of MP in the raw water were found to be the major factor influencing fouling during freshwater ultrafiltration treatment with the most severe effects at a MP size of 1 μm.[212] However, continuous filter module rotation could significantly reduce the fouling and the treatment became more attractive for large scale application. MP in landfill leachate were successfully removed using membrane separation. Interestingly, the researchers identified the re-release of captured MP from the filter back into the effluent suggesting that the particles are not permanently immobilised onto the membrane and may still be released into the environment. Similar removal and re-release behaviour occurred in ultrafiltration membrane treatment of drinking water as well as some MP penetrating the membrane itself.[213] Despite a 98% removal by reverse osmosis treatment, fibers of plastic under 200 μm passed unimpeded indicating that membrane processes alone cannot completely remove MP.

Chemical processes

Effective chemical degradation of polymers could mineralise MP during water treatment and avoid transferring any waste to a new solid phase. Advanced oxidation processes (AOPs) are an effective means to remove biologically recalcitrant contaminants by the generation of non-selective, highly reactive radicals. AOPs are effective in the removal of emerging organic pollutants, such as antibiotics, personal care products, trace organics.[214–216] Recently, their potential application in the rapid degradation of MP is drawing attention.[217] During chemical degradation, the surface of the polymer undergoes chemical change and the MP subsequently fragment.

Photocatalytic treatment. The majority of research published in AOP treatment of MP focuses on photocatalytic methods and is summarised in Table 2. Titania (TiO_2) based photocatalysis is the most common treatment due to its low cost and relatively high radical generating ability.[218] Due to the need for a surface contact during heterogeneous photocatalysis, the morphology of the catalyst is an important area of focus with researchers exploring the use of nanotubes and nanoparticles.

Using TiO_2 doped with C and N, a significant loss of mass of 72% was lost from high density PE beads after an extended treatment time of 50 h.[219] The authors enhanced performance by lowering the water temperature and pH which was attributed to the enhanced radical forming ability of the optimised process as well as changes to plastic properties at low temperature. Nitrogen doped TiO_2 was also utilised in a study focusing on the effect of plastic shape on removal rate.[220] By considering the surface area difference between samples (beads *vs.* flakes) as well as the MP particle size, it was concluded that light illumination was the main factor affecting removal. Furthermore, it was observed that the low density PE flakes, an insoluble water pollutant, were floating on the water surface blocking light and oxygen from reaching the submerged catalyst. This probably resulted in generating fewer radicals thus yielding a removal efficiency less than 5%. Similarly, a low removal in water was also observed during treatment of polystyrene (PS) with TiO_2, which was attributed to low transmittance of UV light.[221] Removal of the MP from water by physical means prior to AOP treatment allowed effective oxidation but this can limit the practical applicability of the method at large scale.

Other catalyst doping strategies have been explored such as the use of Pt doped ZnO based AOP.[222] It was found that the proportion of carbonyl and vinyl surface groups on a low density PE film was increased when treated, which indicates surface oxidation. As well as doping, the effect of synthesis conditions on MP removal has been explored. The synthesis method employed for catalyst preparation was investigated by comparing traditional sol–gel and bio derived N-doped TiO_2, with an improvement in MP removal observed for the latter green-synthesised material.[223] Synthesis of ZnO catalysts was tuned to produce a variety of nanorod lengths and the effect of their morphology on plastic removal was studied.[224] High surface area ZnO supported on a glass fibre substrate enabled trapping of low density MP in place in contact with the catalyst for continuous flow treatment.[225] In the first AOP treatment specifically reported for fibre degradation, a combination of UVC irradiation and TiO_2 photocatalysis achieved 97% mass reduction of polyamide in 48 hours.[226] Less common materials have also been investigated such as a PMS carbon nanospring based catalyst and hydroxy-rich ultrathin sheets[227,228] and TiO_2 supported on β-SiC alveolar foams.[229]

Fenton and Fenton-like treatment. Fenton based AOPs combine hydrogen peroxide and Fe(II) ions to produce oxidizing hydroxyl radicals, activated by light or heat.[230] A few of these treatment methods have recently been applied for MP removal and are summarised in Table 2.

Many of the Fenton based treatment processes reported in the literature were developed with the aim of accelerating the ageing of MP in order to study the change in adsorption or transport behaviour.[231–233] Although not aimed at removing MP completely, these studies provide important insight into how plastic degradation is initiated by Fenton processes and could

Table 2 Advanced oxidation treatment methods for microplastic removal from wastewater

AOP	MP targeted	Monitoring methods	AOP performance	Other parameters	Ref.
C,N–TiO_2 photocatalysis	Polyethylene (PE) beads	Mass loss, FTIR measured carbonyl index (CI), microscopy	50 h, mass loss 72% and large increase in CI	Visible light LED (400–800 nm), temperature 0–40 °C, pH 3–11, lamp distance 25 cm, 4 L^{-1} MPs, 4 g L^{-1} catalyst (optimum removal at pH 3, 0 °C)	219
N–TiO_2 photocatalysis	PE beads and flakes	Mass loss, CI	50 h, mass loss < 5% for all (4.6% HDPE and 1.8% LDPE)	Visible light LED (400–800 nm), pH 3, room temperature, 4 g L^{-1} MPs, lamp distance 21.5 cm	220
ZnO nanorod photocatalysis	PE film	Microscopy (SEM), mechanical change, CI	175 h, CI increase of 30%	Visible light 50 W dichroic halogen ambient air. Deionised water	224
N–TiO_2 photocatalysis	PE beads	Mass loss, SEM, CI	8 h, mass loss < 3% in aqueous solution	27 W visible fluorescent lamp (400–800 nm), room temperature, lamp distance 12 cm, 2 g L^{-1} MPs	223
PMS/carbon nanospring photocatalysis	PE	Mass loss, CI, SEM	8 h, 40% mass loss	pH 3–11, MPs 5–12 g L^{-1}, temperature 25–160 °C (>150 °C optimum)	227
ZnO photocatalyst supported on glass fibre	Polypropylene (PP)	Size change, CI, SEM	456 h, 65% reduction in volume	Visible light 60 mW cm^2, 300 mL min^{-1} continuous flow treatment of 10^4 particles per L	225
TiO_2 nanoparticle photocatalyst film	Polystyrene (PS)	Diameter change, DRIFTS, GC-MS	24 h required for removal of 400 nm starting diameter particles	254 nm UV irradiation	221
ZnO nanorod photocatalysis with Pt modification	PE film	CI, SEM	175 h	Visible light 50 W, room temperature, lamp distance 10 cm	222
TiO_2	Polyamide (PA) fibre	Mass loss, CI, total organic carbon (TOC), SEM	48 h, 94% mass loss	UVA irradiation, room temperature, 5 lamp photo reactor	226
Modified TiO_2 photocatalysis	Poly(methyl methacrylate) (PMMA), PS	TOC	7 h, flow reactor	UVA irradiation 112 W m^2	229
Hydroxy-rich ultrathin BiOCl photocatalysis	PE	Mass loss	5 h, 6% mass loss	250 W of 420 nm irradiation; MP and catalyst 1 g L^{-1}	228
Photo-Fenton	PS	SEM, CI, HPLC/MS, contact angle, C : O atomic ratio (XPS)	108 h, CI increase	500 W mercury lamp, 12 g L^{-1} MPs	231
Fenton	PS and high density PE	Size distribution, CI, C : O ratio by XPS	1–30 days	pH 4, 3 mM Fe, 4.5 mg mL^{-1} H_2O_2	232
Fenton	PE, PP, polyvinyl chloride (PVC), nylon	Microscopy	10 min, minor surface area decrease	Room temperature, pH 5, 7 g L^{-1} MPs, 3–10 mg mL^{-1} Fe	233
Thermal Fenton	PE, PS, PP and polyethylene terephthalate (PET)	Mass loss, CI, DSC to determine crystallinity, XRD, SEM, Raman spectroscopy, particle sizing by zetasizer	16 h, 96% mass loss	4 mM Fe^{2+}, 300 mM H_2O_2	234
Heterogeneous photo Fenton/photocatalysis	PP, PVC	FTIR, particle diameter by microscopy	7 days, 94–96% size reduction	Nano zero valent iron and combined with ZnO/SnO_x photocatalysis, 60 mW cm^2 visible light	235
Ozonation	PE	FTIR, XPS	60–180 min, increase in CI	Ozone 4–7 mg L^{-1}	236

Table 2 (*Contd.*)

AOP	MP targeted	Monitoring methods	AOP performance	Other parameters	Ref.
Ozonation	Mixed MPs obtained from real wastewater	Particle counting	99.2% removal after tertiary treatment (this includes removal *via* other methods during the treatment process)	Ozone 12.6 mg L^{-1} for 1 min during tertiary treatment	237
Ozonation, H_2O_2/ozone	PE, PP, PS	Adsorption, XRD, SEM, FTIR	10 min, ozone dose of 88 mg L^{-1}	$O_3 : H_2O_2$ molar ratio of 0.5	238

be harnessed for water treatment applications. For example, during Fenton treatment of PS and HDPE over long timescales, issues with the deposition of ferric hydroxide were observed thus leading to poor removal from water, despite steps taken to mitigate this.[232] Thermal methods of activating the Fenton reaction can offer an alternative mechanism of action, as explored by Hu *et al.* (2022).[234] A high mass loss of plastic was observed for a range of polymers but the treatment required the use of high temperatures in order to break down the crystallinity of the plastics, which limits its applicability at large scale. Furthermore, combining heterogeneous systems (*i.e.* solid iron on a supporting matrix) with photocatalysis resulted in significant reduction in size of PVC and PP particles after 7 days.[235]

Ozone and peroxide based treatment. Ozone has been applied either on its own,[236,237] or in combination with radical generating hydrogen peroxide[238] to degrade MP. In the latter case, a 10 minutes treatment affected the surface chemistry and associated adsorption behaviour of several types of plastic. Although the treatment is not directly designed for removal, the resulting change in adsorbance properties is relevant to understanding how MP treated with AOPs may carry additional micro pollutants through the water treatment process and therefore extending the treatment duration may be an option for investigation. Similarly, Zafar *et al.* (2021) considered the effect of ozone treatment on the surface of PE particles and found that reaction time was more effective in increasing the oxygen prevalence on the surface compared to ozone dose.[236] Hidayaturrahman *et al.* (2019) reported that ozonation combined with primary, secondary and coagulation steps removed 99.2% of MP in a full-scale treatment plant.[237] While reasonably high removal performance is possible, slow reaction rates currently limit the applicability of AOPs in water treatment. Long contact times of several hours are not feasible in a high throughput system. In order to bring AOPs into the focus for water treatment, improvements to the rate of degradation are essential.

Biological processes

Biodegradation of plastic is an intensive area of research and has potential for application in wastewater treatment.[239–241] Traditional water treatment systems typically involve an element of biodegradation for the removal of organic matter. In most cases, these systems fail to adequately remove MP, leading researchers to explore alternatives. In a systematic review for MP removal, Iyare *et al.* (2020)[242] identified that 19 out of 21 traditional wastewater treatment systems included activated sludge treatment as a secondary step. On average, activated sludge could reportedly remove 16% of MP from the water (across a broad range of 0.2–52%). Alongside limited effectiveness, relying only on traditional water treatment methods like this can create further challenges. Physical transfer of MP out of the wastewater moves the plastic pollution into another part of the water treatment process – the sludge. Also, MP can affect the activity of bacteria used for organic matter decomposition as well as cause issues downstream in sludge treatment.[191,243,244] Wei *et al.* (2021) showed that PET MP inhibited aerobic

digestion of waste activated sludge (WAS) by approximately 10%, which was attributed to its influence on microbial communities.[244] In another study, anaerobic digestion of WAS was found to be impeded by the presence of PVC MP. Moreover, bisphenol A leaching out of the plastics was linked to a decrease in methane production and inhibition of the treatment in this case.[245] Biofiltration of wastewater was identified as a more effective biological secondary step for MP removal than activated sludge with an average of 19% from the treatment systems surveyed.[242] However, the presence of MP in these systems drastically impedes the effectiveness of treatment for other contaminants. Membrane bioreactors (MBR) reportedly experience immediate decline in removal of organic matter from 80% to below 50% upon addition of PVC MP.[246] This was attributed to an increase in membrane fouling as a result of MP build up. In order to avoid these knock on effects to treatment system performance, the presence of MP needs to be taken into account when (re)designing water and wastewater treatment processes. Developing biological treatments specifically aimed at combatting plastics is a challenging area of research but is clearly required to overcome the shortcomings of traditional WWTPs. Outwith the context of wastewater treatment, bacteria, bacterial consortia[247–250] and fungi[251,252] have been investigated for their ability to degrade plastics. Microbial digestion is an extremely attractive option to solve the problem of plastic waste in a potentially sustainable way. One of the main hurdles in each case is the lengthy treatment times required (many reported biodegradation options take weeks or months) for it to be effective for large scale application. In 60 days, PE was biodegraded by a specifically isolated microbial consortium to reduce its mass by just 14.7%.[250] PET increased crystallinity and reduced in particle diameter as a result of bacterial degradation in a high pH process over 48 h but complete removal was not achieved.[253] Using a surfactant to improve interfacial activity, bacterial degradation of PET reached 11% mass loss in 5 days.[254] As well as the lengthy digestion times required, biological systems are likely to struggle to cope with the diverse nature of our plastic waste. Enzymatic digestion relies on specific target groups in the polymer chain being broken. To tackle the huge range of polymers present in our waste, a great many different plastic digesting microorganisms will be required.[255] As it stands, these engineered systems are not currently capable of treating the high flow of microplastics in our water treatment systems due to the long timescales required but are under constant development as reviewed comprehensively elsewhere.[256]

As previously discussed, a broad range of polymer types and MP shapes are present in the environment. Lab scale treatment studies have focused on a number of different MP subtypes. It is important to consider the effect of this when evaluating the efficacy of a reported treatment system. Fig. 7 shows the papers discussed in this section, broken down by which MP types and shapes are focused on. Furthermore, Fig. 8 highlights the performance of treatment technologies reviewed here in terms of MP removal from water. It can be observed that primary treatment (screening, settling, sedimentation) can remove about 50–90% of MP from wastewater, while adsorption and filtration are able to remove more than 95%. The percentages for advanced oxidation processes can span from very low to almost complete removal of MP. For biological engineered technologies the removal can be up to 20%. Physical treatment methods offer reasonably consistent high removal rates but are hampered by the production of solid waste and process problems such as membrane blockage. Chemical and biological treatment methods are an area of intense research and have the potential to effectively destroy MP if the rate of degradation can be significantly improved. Further research into these important water treatment systems is required to further understand their potential in tackling MP pollution.

Monitoring and treatment technologies: future perspectives

Currently, the most common chemical techniques used for the identification of MP are generally based on electronic

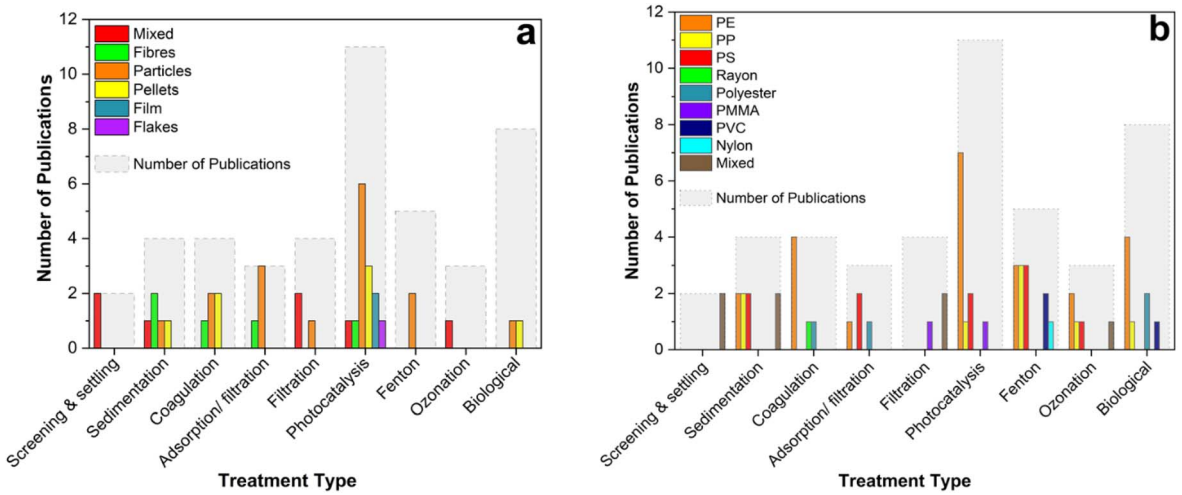

Fig. 7 (a) Publications reviewed considering water treatment for the removal of microplastics broken down by plastic shape. (b) Publications reviewed considering water treatment for the removal of microplastics broken down by polymer type.

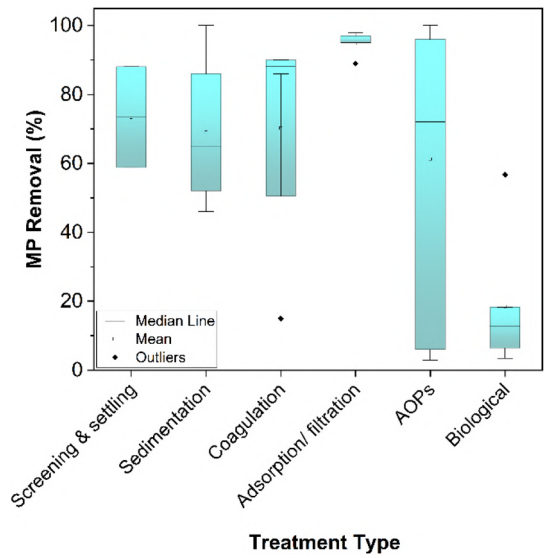

Fig. 8 Summary of the reported microplastic removal performance of water treatment technologies reviewed.

microscopies (SEM, TEM), on Fourier transformed infrared (FT-IR) and Raman spectroscopies (micro-Raman and micro-FT-IR for smaller particles) and on thermal identification (DSC, TGA). Detection of polymer type and better quantification of MP in collected samples are achieved by using more performant analytical techniques, such as thermal chromatography, usually coupled with mass spectrometry (Pyro-GC/MS), to ensure highly sensitive MP detection.[257–261]

Considering the global emergency due to plastic pollution, it is increasingly important for the scientific community to develop and/or improve technologies and methods that can guarantee a better quantification of MP, both during the extraction and analysis phases.[262]

In this regard, Silva *et al.* (2020) implemented the μ-FTIR hyperspectral imagining technique using a new machine learning approach to quantify and characterize microplastic particles.[263] Cashman *et al.* (2022) developed a new method of extracting MP from marine sediments in order to obtain significantly higher extraction yields than standard methods.[264] Castelvetro *et al.* (2021) proposed an alternative approach combining wet chemical techniques of extraction with analytical quantification techniques such as reverse phase HPLC and size exclusion chromatography for the determination and quantification of MP in marine sediments and freshwater.[261]

At the same time, the world scientific community is also striving to develop new technologies focused on preventing plastic waste from entering the environment. The latest scientific advances and technologies available in this area are collected in the Plastic Pollution Prevention and Collection Technology Inventory (**https://nicholasinstitute.duke.edu/plastics-technology-inventory**), created to help local governments and non-governmental organizations with the aim of helping to solve the hotspots of marine plastic pollution.[265]

The Plastic Pollution Prevention and Collection Technology Inventory currently contains 52 technologies (developed starting from 20 July 2020) with the aim of:

(1) Prevent plastic pollution from entering the environment;

(2) Collect existing marine plastic pollution.

The technologies in the inventory are classified according to the remediation strategy (prevention or collection), the plastic type or the inventory category (laundry balls, textile fibers, personal care products, disposable products, *etc.*).

In order to minimize plastic in the environment, the scientific community is also thinking about a final destination for plastics collected through the exploration of innovative recycling solutions, such as plastic-to-fuel and bioremediation.[266–268]

Conclusions

While progress has been made in addressing the global plastics challenge, commitments from governments and industry will reduce the annual volume of plastic flowing into the ocean by only about 7% by 2040.

A great deal of attention has been paid to tackling the problem of microplastic pollution in water with physical, chemical and biological treatment options explored by recent research. Considering the complexity and scale of microplastics present in our water, a universally effective treatment solution has not emerged. Incorporation of several innovative steps such as advanced oxidation and targeted biological degradation into broader treatment systems may effectively remove microplastics. Updates to traditional methods to deal with an increased plastic load in our wastewater are required or treatment infrastructure faces the possibility of process problems as well as release to the environment.

Together with innovative techniques, existing plastic waste recycling systems should be improved to prevent microplastics release from the inland to the sea and this task can and must be reached in a short time. The same goes for municipal sewage treatment processes which in many cases do not even include microplastics removal units. This environmental problem, common to the governments and the communities of all countries, must trigger practical policies and measures to ensure conservation actions for the aquatic ecosystem.

Author contributions

Project conceptualization, methodology, and supervision, A. T., M. B., F. C., E. C. and G. D. F.; administration, funding acquisition, E. C. and G. D. F.; methodology, investigation, data analysis, writing—original draft preparation, A. T., M. B., F. C., T. E., E. C. and M. D. B.; writing—review and editing, A. T., M. B., F. C., T. E., E. C., and G. D. F. All authors contributed to the discussion, reviews and approval of the manuscript for publication.

Conflicts of interest

There are no conflicts to declare.

Acknowledgements

This work was supported by a NERC Doctoral Training Partnership grant (NE/S007407/1) and by a scholarship from Regione Calabria (grant POR Calabria 2014–2020 – Azioni 10.5.6 e 10.5.12) for the PhD of M. B. For the purpose of open access, the authors has applied a Creative Commons Attribution (CC BY) licence to any Author Accepted Manuscript version arising from this submission.

References

1 J. G. B. Derraik, *Mar. Pollut. Bull.*, 2002, **44**, 842–852.
2 R. Geyer, J. R. Jambeck and K. L. Law, *Sci. Adv.*, 2017, **3**, e1700782.
3 The PEW Charitable Trusts, **https://www.pewtrusts.org/en/research-and-analysis/articles/2020/07/23/breaking-the-plastic-wave-top-findings**, accessed September 2022.
4 A. Gallagher, A. Rees, R. Rowe, J. Stevens and P. Wright, *Mar. Pollut. Bull.*, 2016, **102**, 243–249.
5 S. S. Sadri and R. C. Thompson, *Mar. Pollut. Bull.*, 2014, **81**, 55–60.
6 M. R. Gregory, *Philos. Trans. R. Soc., B*, 2009, **364**, 2013–2025.
7 M. Cole, P. Lindeque, C. Halsband and T. S. Galloway, *Mar. Pollut. Bull.*, 2011, **62**, 2588–2597.
8 J. Wang, J. Peng, Z. Tan, Y. Gao, Z. Zhan, Q. Chen and L. Cai, *Chemosphere*, 2017, **171**, 248–258.
9 C. G. Avio, S. Gorbi and F. Regoli, *Mar. Environ. Res.*, 2017, **128**, 2–11.
10 J. P. G. L. Frias, P. Sobral and A. M. Ferreira, *Mar. Pollut. Bull.*, 2010, **60**, 1988–1992.
11 A. Bakir, S. J. Rowland and R. C. Thompson, *Environ. Pollut.*, 2014, **185**, 16–23.
12 A. Bakir, S. J. Rowland and R. C. Thompson, *Estuarine, Coastal Shelf Sci.*, 2014, **140**, 14–21.
13 E. J. Carpenter and K. L. Smith, *Science*, 1972, **175**, 1240–1241.
14 M. Rumbak, *Am. J. Med. Sci.*, 2016, **351**, 606.
15 J. Talvitie, A. Mikola, O. Setälä, M. Heinonen and A. Koistinen, *Water Res.*, 2017, **109**, 164–172.
16 J. Talvitie, A. Mikola, A. Koistinen and O. Setälä, *Water Res.*, 2017, **123**, 401–407.
17 A. Tursi, N. De Vietro, A. Beneduci, A. Milella, F. Chidichimo, F. Fracassi and G. Chidichimo, *J. Hazard. Mater.*, 2019, **373**, 773–782.
18 A. Tursi, F. Chidichimo, R. Bagetta and A. Beneduci, *Water*, 2020, **12**, 1–20.
19 A. Tursi, V. Gallizzi, F. Olivito, V. Algieri, A. De Nino, L. Maiuolo and A. Beneduci, *J. Hazard. Mater. Lett.*, 2022, **3**, 100060.
20 L. Pugliese, M. De Biase, F. Chidichimo, G. J. Heckrath, B. V. Iversen, C. Kjærgaard and S. Straface, *Ecol. Eng.*, 2020, **156**, 105968.
21 N. De Vietro, A. Tursi, A. Beneduci, F. Chidichimo, A. Milella, F. Fracassi, E. Chatzisymeon and G. Chidichimo, *Photochem. Photobiol. Sci.*, 2019, **18**, 2248–2258.
22 K. Duis and A. Coors, *Environ. Sci. Eur.*, 2016, **28**, 1–25.
23 M. Malankowska, C. Echaide-Gorriz and J. Coronas, *Environ. Sci.: Water Res. Technol.*, 2021, **7**, 243–258.
24 A. L. Andrady, *Mar. Pollut. Bull.*, 2011, **62**, 1596–1605.
25 J. Jambeck, R. Geyer, C. Wilcox, T. R. Siegler, M. Perryman, A. Andrady, R. Narayan and K. L. Law, *Science*, 2015, **347**, 768–771.
26 T. van Emmerik, *Microplastics and Nanoplastics*, 2021, **1**, 4–5.
27 L. G. A. Barboza, A. Cózar, B. C. G. Gimenez, T. L. Barros, P. J. Kershaw and L. Guilhermino, *Macroplastics pollution in the marine environment*, Elsevier Ltd, 2nd edn, 2018.
28 S. Lechthaler, K. Waldschläger, G. Stauch and H. Schüttrumpf, *Environments*, 2020, **7**, 1–30.
29 D. J. Winton, L. G. Anderson, S. Rocliffe and S. Loiselle, *Sci. Total Environ.*, 2020, **704**, 135242.
30 C. Rodríguez, M. Fossatti, D. Carrizo, L. Sánchez-García, F. Teixeira de Mello, F. Weinstein and J. P. Lozoya, *Sci. Total Environ.*, 2020, **721**, 137734.
31 M. C. M. Blettler, M. A. Ulla, A. P. Rabuffetti and N. Garello, *Environ. Monit. Assess.*, 2017, **189**, 581.
32 S. Gündoğdu and C. Çevik, *Mar. Pollut. Bull.*, 2017, **118**, 341–347.
33 C. Scopetani, D. Chelazzi, T. Martellini, J. Pellinen, A. Ugolini, C. Sarti and A. Cincinelli, *Mar. Pollut. Bull.*, 2021, **171**, 112712.
34 A. Isobe, K. Uchida, T. Tokai and S. Iwasaki, *Mar. Pollut. Bull.*, 2015, **101**, 618–623.
35 L. K. Law and C. R. Thompson, *Science*, 2014, **345**, 144–145.
36 C. Lassen, S. F. Hansen, K. Magnusson, N. B. Hartmann, P. Rehne Jensen, T. G. Nielsen and A. Brinch, *Microplastics: occurrence, effects and sources of releases*, 2015.
37 Norwegian Environment Agency, **https://www.miljodirektoratet.no/globalassets/publikasjoner/m321/m321.pdf**, accessed September 2022.
38 K. Magnusson, K. Eliasson, A. Fråne, K. Haikonen, J. Hultén, M. Olshammar, J. Stadmark and A. Voisin, *Swedish sources and pathways for microplastics to the marine environment*, IVL Svenska Miljöinstitutet, 2016, vol. C183, pp. 1–89.
39 J. Q. Jiang, *Sustainable Production and Consumption*, 2018, **13**, 16–23.
40 Z. Long, Z. Pan, W. Wang, J. Ren, X. Yu, L. Lin, H. Lin, H. Chen and X. Jin, *Water Res.*, 2019, **155**, 255–265.
41 M. A. Browne, P. Crump, S. J. Niven, E. Teuten, A. Tonkin, T. Galloway and R. Thompson, *Environ. Sci. Technol.*, 2011, **45**, 9175–9179.
42 K. M. Unice, M. P. Weeber, M. M. Abramson, R. C. D. Reid, J. A. G. van Gils, A. A. Markus, A. D. Vethaak and J. M. Panko, *Sci. Total Environ.*, 2019, **646**, 1639–1649.
43 P. Jan Kole, A. J. Löhr, F. G. A. J. Van Belleghem and A. M. J. Ragas, *Int. J. Environ. Res. Public Health*, 2014, **14**, 1265.
44 R. Dris, J. Gasperi, M. Saad, C. Mirande and B. Tassin, *Mar. Pollut. Bull.*, 2016, **104**, 290–293.

45 F. Murphy, C. Ewins, F. Carbonnier and B. Quinn, *Environ. Sci. Technol.*, 2016, **50**, 5800–5808.
46 A. Beljanski, *Proceedings of the National Conference on Undergraduate Research (NCUR)*, University of North Carolina Asheville, 2016.
47 J. Sun, X. Dai, Q. Wang, M. C. M. van Loosdrecht and B. J. Ni, *Water Res.*, 2019, **152**, 21–37.
48 S. A. Carr, J. Liu and A. G. Tesoro, *Water Res.*, 2016, **91**, 174–182.
49 A. Rodríguez-Seijo and R. Pereira, *Bioremediation of Agricultural Soils*, CRC Press, 2019, pp. 45–60.
50 L. Nizzetto, M. Futter and S. Langaas, *Environ. Sci. Technol.*, 2016, **50**, 10777–10779.
51 E. Kentin and H. Kaarto, *Review of European, Comparative & International Environmental Law*, 2018, **27**, 254–266.
52 M. Zbyszewski, P. L. Corcoran and A. Hockin, *J. Great Lakes Res.*, 2014, **40**, 288–299.
53 E. R. Zettler, T. J. Mincer and L. A. Amaral-Zettler, *Environ. Sci. Technol.*, 2013, **47**, 7137–7146.
54 O. Bozorg-Haddad, M. Delpasand and H. A. Loáiciga, in *Economical, Political, and Social Issues in Water Resources*, ed. O. Bozorg-Haddad, Elsevier, 2021, pp. 217–257.
55 R. C. Thompson, C. J. Moore, F. S. V. Saal and S. H. Swan, *Philos. Trans. R. Soc., B*, 2009, **364**, 2153–2166.
56 A. Ballent, P. L. Corcoran, O. Madden, P. A. Helm and F. J. Longstaffe, *Mar. Pollut. Bull.*, 2016, **110**, 383–395.
57 M. S. Bank and S. V. Hansson, *Microplastic in the Environment: Pattern and Process*, 2022, pp. 1–16.
58 R. C. Hale, M. E. Seeley, M. J. La Guardia, L. Mai and E. Y. Zeng, *J. Geophys. Res.: Oceans*, 2020, **125**, 1–40.
59 A. A. Horton, A. Walton, D. J. Spurgeon, E. Lahive and C. Svendsen, *Sci. Total Environ.*, 2017, **586**, 127–141.
60 X. Peng, M. Chen, S. Chen, S. Dasgupta, H. Xu, K. Ta, M. Du, J. Li, Z. Guo and S. Bai, *Geochemical Perspectives Letters*, 2018, **9**, 1–5.
61 N. Kowalski, A. M. Reichardt and J. J. Waniek, *Mar. Pollut. Bull.*, 2016, **109**, 310–319.
62 A. Ballent, A. Purser, P. de Jesus Mendes, S. Pando and L. Thomsen, *Biogeosciences*, 2012, **9**, 18755–18798.
63 Y. Li, H. Zhang and C. Tang, *Anthropocene Coasts*, 2020, **3**, 6–13.
64 L. C. M. Lebreton, J. Van Der Zwet, J. W. Damsteeg, B. Slat, A. Andrady and J. Reisser, *Nat. Commun.*, 2017, **8**, 1–10.
65 C. Schmidt, T. Krauth and S. Wagner, *Environ. Sci. Technol.*, 2017, **51**, 12246–12253.
66 M.-L. Pedrotti, S. Petit, A. Elineau, S. Bruzaud, J.-C. Crebassa, B. Dumontet, E. Martí, G. Gorsky and A. Cózar, *PLoS One*, 2016, **11**(8), e0161581.
67 F. A. E. Lots, P. Behrens, M. G. Vijver, A. A. Horton and T. Bosker, *Mar. Pollut. Bull.*, 2017, **123**, 219–226.
68 S. Zhao, L. Zhu and D. Li, *Environ. Pollut.*, 2015, **206**, 597–604.
69 A. Mathalon and P. Hill, *Mar. Pollut. Bull.*, 2014, **81**, 69–79.
70 R. J. E. Vroom, A. A. Koelmans, E. Besseling and C. Halsband, *Environ. Pollut.*, 2017, **231**, 987–996.
71 S. Chatterjee and S. Sharma, *Field Actions Science Reports*, 2019, **19**, 54–61.
72 S. Sharma and S. Chatterjee, *Environ. Sci. Pollut. Res.*, 2017, **24**, 21530–21547.
73 A. J. R. Watts, C. Lewis, R. M. Goodhead, S. J. Beckett, J. Moger, C. R. Tyler and T. S. Galloway, *Environ. Sci. Technol.*, 2014, **48**, 8823–8830.
74 D. S. Green, B. Boots, D. J. Blockley, C. Rocha and R. Thompson, *Environ. Sci. Technol.*, 2015, **49**, 5380–5389.
75 J. A. Ivar do Sul, M. F. Costa, M. Barletta and F. J. A. Cysneiros, *Mar. Pollut. Bull.*, 2013, **75**, 305–309.
76 A. Cózar, F. Echevarría, J. I. González-Gordillo, X. Irigoien, B. Úbeda, S. Hernández-León, Á. T. Palma, S. Navarro, J. García-de-Lomas, A. Ruiz, M. L. Fernández-de-Puelles and C. M. Duarte, *Proc. Natl. Acad. Sci. U. S. A.*, 2014, **111**, 10239–10244.
77 N. A. C. Welden and A. L. Lusher, *Integr. Environ. Assess. Manage.*, 2017, **13**, 483–487.
78 S. Liubartseva, G. Coppini, R. Lecci and S. Creti, *Mar. Pollut. Bull.*, 2016, **103**, 115–127.
79 A. Isobe, K. Kubo, Y. Tamura, S. Kako, E. Nakashima and N. Fujii, *Mar. Pollut. Bull.*, 2014, **89**, 324–330.
80 M. Eriksen, L. C. M. Lebreton, H. S. Carson, M. Thiel, C. J. Moore, J. C. Borerro, F. Galgani, P. G. Ryan and J. Reisser, *PLoS One*, 2014, **9**, 1–15.
81 L. K. Law, *Science*, 2010, **329**, 1185–1188.
82 J. T. Potemra, *Mar. Pollut. Bull.*, 2012, **65**, 42–50.
83 J. Mansui, A. Molcard and Y. Ourmières, *Mar. Pollut. Bull.*, 2015, **91**, 249–257.
84 D. Neumann, U. Callies and M. Matthies, *Mar. Pollut. Bull.*, 2014, **86**, 219–228.
85 L. C. M. Lebreton, S. D. Greer and J. C. Borrero, *Mar. Pollut. Bull.*, 2012, **64**, 653–661.
86 O. Hoegh-Guldberg, *Mar. Freshwater Res.*, 1999, **50**, 839–866.
87 S. C. Doney, V. J. Fabry, R. A. Feely and J. A. Kleypas, *Annual Review of Marine Science*, 2009, **1**, 169–192.
88 J. C. Comiso, C. L. Parkinson, R. Gersten and L. Stock, *Geophys. Res. Lett.*, 2008, **35**, 1–6.
89 T. Kukulka, G. Proskurowski, S. Morét-Ferguson, D. W. Meyer and K. L. Law, *Geophys. Res. Lett.*, 2012, **39**, 1–6.
90 F. Galgani, G. Hanke and T. Maes, In *Marine Anthropogenic Litter*, ed. M. Bergmann, L. Gutow and M. Klages, Springer International Publishing, Cham, 2015, ch. 2, pp. 29–56.
91 E. A. Howell, S. J. Bograd, C. Morishige, M. P. Seki and J. J. Polovina, *Mar. Pollut. Bull.*, 2012, **65**, 16–22.
92 L. C. Woodall, A. Sanchez-Vidal, M. Canals, G. L. J. Paterson, R. Coppock, V. Sleight, A. Calafat, A. D. Rogers, B. E. Narayanaswamy and R. C. Thompson, *R. Soc. Open Sci.*, 2014, **1**, 140317.
93 K. Zhang, X. Xiong, H. Hu, C. Wu, Y. Bi, Y. Wu, B. Zhou, P. K. S. Lam and J. Liu, *Environ. Sci. Technol.*, 2017, **51**, 3794–3801.
94 I. Chubarenko, A. Bagaev, M. Zobkov and E. Esiukova, *Mar. Pollut. Bull.*, 2016, **108**, 105–112.
95 L. D. K. Kanhai, K. Gårdfeldt, O. Lyashevska, M. Hassellöv, R. C. Thompson and I. O'Connor, *Mar. Pollut. Bull.*, 2018, **130**, 8–18.

96 K. Enders, R. Lenz, C. A. Stedmon and T. G. Nielsen, *Mar. Pollut. Bull.*, 2015, **100**, 70–81.
97 J. Reisser, B. Slat, K. Noble, K. Du Plessis, M. Epp, M. Proietti, J. De Sonneville, T. Becker and C. Pattiaratchi, *Biogeosciences*, 2015, **12**, 1249–1256.
98 M. Cole, P. Lindeque, E. Fileman, C. Halsband, R. Goodhead, J. Moger and T. S. Galloway, *Environ. Sci. Technol.*, 2013, **47**, 6646–6655.
99 S. Morét-Ferguson, K. L. Law, G. Proskurowski, E. K. Murphy, E. E. Peacock and C. M. Reddy, *Mar. Pollut. Bull.*, 2010, **60**, 1873–1878.
100 D. Lobelle and M. Cunliffe, *Mar. Pollut. Bull.*, 2011, **62**, 197–200.
101 C. J. Moore, S. L. Moore, M. K. Leecaster and S. B. Weisberg, *Mar. Pollut. Bull.*, 2001, **42**, 1297–1300.
102 J. Zhao, W. Ran, J. Teng, Y. Liu, H. Liu, X. Yin, R. Cao and Q. Wang, *Sci. Total Environ.*, 2018, **640–641**, 637–645.
103 L. Van Cauwenberghe, A. Vanreusel, J. Mees and C. R. Janssen, *Environ. Pollut.*, 2013, **182**, 495–499.
104 M. Long, B. Moriceau, M. Gallinari, C. Lambert, A. Huvet, J. Raffray and P. Soudant, *Mar. Chem.*, 2015, **175**, 39–46.
105 P. Wardrop, J. Shimeta, D. Nugegoda, P. D. Morrison, A. Miranda, M. Tang and B. O. Clarke, *Environ. Sci. Technol.*, 2016, **50**, 4037–4044.
106 F. Wang, K. M. Shih and X. Y. Li, *Chemosphere*, 2015, **119**, 841–847.
107 C. Wu, K. Zhang, X. Huang and J. Liu, *Environ. Sci. Pollut. Res.*, 2016, **23**, 8819–8826.
108 A. Rahman, A. Sarkar, O. P. Yadav, G. Achari and J. Slobodnik, *Sci. Total Environ.*, 2021, **757**, 143872.
109 J. C. Prata, J. P. da Costa, I. Lopes, A. C. Duarte and T. Rocha-Santos, *Sci. Total Environ.*, 2020, **702**, 134455.
110 R. Dris, J. Gasperi, V. Rocher, M. Saad, N. Renault and B. Tassin, *Environ. Chem.*, 2015, **12**, 592–599.
111 K. Kannan and K. Vimalkumar, *Front. Endocrinol.*, 2021, **12**, 1–19.
112 R. Dris, J. Gasperi, C. Mirande, C. Mandin, M. Guerrouache, V. Langlois and B. Tassin, *Environ. Pollut.*, 2017, **221**, 453–458.
113 J. C. Prata, *Environ. Pollut.*, 2018, **234**, 115–126.
114 A. Vianello, R. L. Jensen, L. Liu and J. Vollertsen, *Sci. Rep.*, 2019, **9**, 1–11.
115 K. Donaldson, V. Stone, P. S. Gilmour, D. M. Brown and W. Macnee, *Philos. Trans. R. Soc., A*, 2000, **358**, 2741–2749.
116 M. Xu, G. Halimu, Q. Zhang, Y. Song, X. Fu, Y. Li, Y. Li and H. Zhang, *Sci. Total Environ.*, 2019, **694**, 133794.
117 S. L. Wright and F. J. Kelly, *Environ. Sci. Technol.*, 2017, **51**, 6634–6647.
118 S. E. Turcotte, A. Chee, R. Walsh, F. C. Grant, G. M. Liss, A. Boag, L. Forkert, P. W. Munt and M. D. Lougheed, *Chest*, 2013, **143**, 1642–1648.
119 A. D. Vethaak and H. A. Leslie, *Environ. Sci. Technol.*, 2016, **50**, 6825–6826.
120 X. Yang, Y. B. Man, M. H. Wong, R. B. Owen and K. L. Chow, *Sci. Total Environ.*, 2022, **825**, 154025.
121 T. S. Galloway, in *Marine Anthropogenic Litter*, ed. M. Bergmann, L. Gutow and M. Klages, Springer International Publishing, Cham, 2015, ch, 13, pp. 343–366.
122 K. D. Cox, G. A. Covernton, H. L. Davies, J. F. Dower, F. Juanes and S. E. Dudas, *Environ. Sci. Technol.*, 2019, **53**, 7068–7074.
123 A. A. Koelmans, N. H. Mohamed Nor, E. Hermsen, M. Kooi, S. M. Mintenig and J. De France, *Water Res.*, 2019, **155**, 410–422.
124 M. Pivokonsky, L. Cermakova, K. Novotna, P. Peer, T. Cajthaml and V. Janda, *Sci. Total Environ.*, 2018, **643**, 1644–1651.
125 D. Schymanski, C. Goldbeck, H. U. Humpf and P. Fürst, *Water Res.*, 2018, **129**, 154–162.
126 V. C. Shruti, F. Pérez-Guevara, I. Elizalde-Martínez and G. Kutralam-Muniasamy, *Environ. Pollut.*, 2021, **268**, 115811.
127 S. Karbalaei, P. Hanachi, T. R. Walker and M. Cole, *Environ. Sci. Pollut. Res.*, 2018, **25**, 36046–36063.
128 F. Bessa, P. Barría, J. M. Neto, J. P. G. L. Frias, V. Otero, P. Sobral and J. C. Marques, *Mar. Pollut. Bull.*, 2018, **128**, 575–584.
129 D. Neves, P. Sobral, J. L. Ferreira and T. Pereira, *Mar. Pollut. Bull.*, 2015, **101**, 119–126.
130 A. Naji, M. Nuri and A. D. Vethaak, *Environ. Pollut.*, 2018, **235**, 113–120.
131 J. Li, X. Qu, L. Su, W. Zhang, D. Yang, P. Kolandhasamy, D. Li and H. Shi, *Environ. Pollut.*, 2016, **214**, 177–184.
132 A. Karami, A. Golieskardi, C. Keong Choo, V. Larat, T. S. Galloway and B. Salamatinia, *Sci. Rep.*, 2017, **7**, 1–11.
133 G. Liebezeit and E. Liebezeit, *Food Addit. Contam., Part A*, 2013, **30**, 2136–2140.
134 J. S. Kim, H. J. Lee, S. K. Kim and H. J. Kim, *Environ. Sci. Technol.*, 2018, **52**, 12819–12828.
135 C. M. Rochman, A. Tahir, S. L. Williams, D. V. Baxa, R. Lam, J. T. Miller, F. C. Teh, S. Werorilangi and S. J. Teh, *Sci. Rep.*, 2015, **5**, 1–10.
136 K. Tanaka and H. Takada, *Sci. Rep.*, 2016, **6**, 1–8.
137 S. C. L. Farhat, C. A. Silva, M. A. M. Orione, L. M. A. Campos, A. M. E. Sallum and A. L. F. Braga, *Autoimmun. Rev.*, 2011, **11**, 14–21.
138 S. Bernatsky, A. Smargiassi, C. Barnabe, L. W. Svenson, A. Brand, R. V. Martin, M. Hudson, A. E. Clarke, P. R. Fortin, A. van Donkelaar, S. Edworthy, P. Bélisle and L. Joseph, *Environ. Res.*, 2016, **146**, 85–91.
139 E. C. Fernandes, C. A. Silva, A. L. F. Braga, A. M. E. Sallum, L. M. A. Campos and S. C. L. Farhat, *Arthritis Care Res.*, 2015, **67**, 1609–1614.
140 C. Campanale, C. Massarelli, I. Savino, V. Locaputo and V. F. Uricchio, *Int. J. Environ. Res. Public Health*, 2020, **17**, 1212.
141 L. Canesi, C. Ciacci, E. Bergami, M. P. Monopoli, K. A. Dawson, S. Papa, B. Canonico and I. Corsi, *Mar. Environ. Res.*, 2015, **111**, 34–40.
142 A. Liu, L. Richards, C. L. Bladen, E. Ingham, J. Fisher and J. L. Tipper, *Acta Biomater.*, 2015, **23**, 38–51.

143 R. T. Ormsby, M. Cantley, M. Kogawa, L. B. Solomon, D. R. Haynes, D. M. Findlay and G. J. Atkins, *Acta Biomater.*, 2016, **33**, 242–251.

144 B. Gewert, M. M. Plassmann and M. Macleod, *Environ. Sci.: Processes Impacts*, 2015, **17**, 1513–1521.

145 A. Valavanidis, T. Vlachogianni, K. Fiotakis and S. Loridas, *Int. J. Environ. Res. Public Health*, 2013, **10**, 3886–3907.

146 F. J. Kelly and J. C. Fussell, *Atmos. Environ.*, 2012, **60**, 504–526.

147 G. Sternschuss, D. R. Ostergard and H. Patel, *J. Urol.*, 2012, **188**, 27–32.

148 X. Chang, Y. Xue, J. Li, L. Zou and M. Tang, *J. Appl. Toxicol.*, 2020, **40**, 4–15.

149 C. Chang, *J. Autoimmun.*, 2010, **34**, J234–J246.

150 A. Bakir, I. A. O'Connor, S. J. Rowland, A. J. Hendriks and R. C. Thompson, *Environ. Pollut.*, 2016, **219**, 56–65.

151 F. Ribeiro, J. W. O'Brien, T. Galloway and K. V. Thomas, *TrAC, Trends Anal. Chem.*, 2019, **111**, 139–147.

152 S. Mishra, C. charan Rath and A. P. Das, *Mar. Pollut. Bull.*, 2019, **140**, 188–197.

153 I. V. Kirstein, S. Kirmizi, A. Wichels, A. Garin-Fernandez, R. Erler, M. Löder and G. Gerdts, *Mar. Environ. Res.*, 2016, **120**, 1–8.

154 D. Zhu, Q. L. Chen, X. L. An, X. R. Yang, P. Christie, X. Ke, L. H. Wu and Y. G. Zhu, *Soil Biol. Biochem.*, 2018, **116**, 302–310.

155 M. Revel, A. Châtel and C. Mouneyrac, *Current Opinion in Environmental Science and Health*, 2018, **1**, 17–23.

156 G. F. Schirinzi, I. Pérez-Pomeda, J. Sanchís, C. Rossini, M. Farré and D. Barceló, *Environ. Res.*, 2017, **159**, 579–587.

157 D. K. A. Barnes, F. Galgani, R. C. Thompson and M. Barlaz, *Philos. Trans. R. Soc., B*, 2009, **364**, 1985–1998.

158 A. L. Lusher, V. Tirelli, I. O'Connor and R. Officer, *Sci. Rep.*, 2015, **5**, 1–9.

159 R. W. Obbard, S. Sadri, Y. Q. Wong, A. A. Khitun, I. Baker and C. Richard, *Earth's Future*, 2014, **2**, 315–320.

160 J. A. Ivar Do Sul and M. F. Costa, *Environ. Pollut.*, 2014, **185**, 352–364.

161 L. D. K. Kanhai, C. Johansson, J. P. G. L. Frias, K. Gardfeldt, R. C. Thompson and I. O'Connor, *Deep Sea Res., Part I*, 2019, **145**, 137–142.

162 M. Claessens, L. Van Cauwenberghe, M. B. Vandegehuchte and C. R. Janssen, *Mar. Pollut. Bull.*, 2013, **70**, 227–233.

163 L. Van Cauwenberghe, L. Devriese, F. Galgani, J. Robbens and C. R. Janssen, *Mar. Environ. Res.*, 2015, **111**, 5–17.

164 M. C. Fossi, L. Marsili, M. Baini, M. Giannetti, D. Coppola, C. Guerranti, I. Caliani, R. Minutoli, G. Lauriano, M. G. Finoia, F. Rubegni, S. Panigada, M. Bérubé, J. Urbán Ramírez and C. Panti, *Environ. Pollut.*, 2016, **209**, 68–78.

165 C. M. Rochman, E. Hoh, T. Kurobe and S. J. Teh, *Sci. Rep.*, 2013, **3**, 1–7.

166 E. M. Duncan, A. C. Broderick, W. J. Fuller, T. S. Galloway, M. H. Godfrey, M. Hamann, C. J. Limpus, P. K. Lindeque, A. G. Mayes, L. C. M. Omeyer, D. Santillo, R. T. E. Snape and B. J. Godley, *Global Change Biol.*, 2019, **25**, 744–752.

167 H. Ma, S. Pu, S. Liu, Y. Bai, S. Mandal and B. Xing, *Environ. Pollut.*, 2020, **261**, 114089.

168 S. Y. Au, T. F. Bruce, W. C. Bridges and S. J. Klaine, *Environ. Toxicol. Chem.*, 2015, **34**, 2564–2572.

169 L. T. O. Cheung, C. Y. Lui and L. Fok, *Int. J. Environ. Res. Public Health*, 2018, **15**, 597.

170 N. C. Ory, P. Sobral, J. L. Ferreira and M. Thiel, *Sci. Total Environ.*, 2017, **586**, 430–437.

171 H. S. Auta, C. U. Emenike and S. H. Fauziah, *Environ. Int.*, 2017, **102**, 165–176.

172 S. Kühn, E. L. Bravo Rebolledo and J. A. van Franeker, in *Marine Anthropogenic Litter*, ed. M. Bergmann, L. Gutow and M. Klages, Springer International Publishing, Cham, 2015, pp. 75–116.

173 C. Ferrier-Pagès, J. Witting, E. Tambutté and K. P. Sebens, *Coral Reefs*, 2003, **22**, 229–240.

174 I. L. Nerland, C. Halsband, I. Allan and K. V. Thomas, *Norwegian Institute for Water Research, Report No. 6754–2014*, 2014, pp. 1–71.

175 O. Setälä, V. Fleming-Lehtinen and M. Lehtiniemi, *Environ. Pollut.*, 2014, **185**, 77–83.

176 R. C. Thompson, Y. Olson, R. P. Mitchell, A. Davis, S. J. Rowland, A. W. G. John, D. McGonigle and A. E. Russell, *Science*, 2004, **304**, 838.

177 E. R. Graham and J. T. Thompson, *J. Exp. Mar. Biol. Ecol.*, 2009, **368**, 22–29.

178 L. Van Cauwenberghe and C. R. Janssen, *Environ. Pollut.*, 2014, **193**, 65–70.

179 A. L. Lusher, M. McHugh and R. C. Thompson, *Mar. Pollut. Bull.*, 2013, **67**, 94–99.

180 T. Romeo, B. Pietro, C. Pedà, P. Consoli, F. Andaloro and M. C. Fossi, *Mar. Pollut. Bull.*, 2015, **95**, 358–361.

181 C. M. Boerger, G. L. Lattin, S. L. Moore and C. J. Moore, *Mar. Pollut. Bull.*, 2010, **60**, 2275–2278.

182 V. A. Lindborg, J. F. Ledbetter, J. M. Walat and C. Moffett, *Mar. Pollut. Bull.*, 2012, **64**, 2351–2356.

183 C. R. McMahon, D. Holley and S. Robinson, *Wildl. Res.*, 1999, **26**, 839–846.

184 S. D. Goldsworthy, M. A. Hindell and H. M. Crowley, in *Marine mammal research in the Southern hemisphere: status, ecology and medicine*, ed. M. A. Hindell and C. Kemper, Surrey Beatty & Sons, Chipping Norton, NSW, 1997, vol. 1, pp. 151–163.

185 L. J. Zantis, E. L. Carroll, S. E. Nelms and T. Bosker, *Environ. Pollut.*, 2021, **269**, 116142.

186 E. L. Bravo Rebolledo, J. A. Van Franeker, O. E. Jansen and S. M. J. M. Brasseur, *Mar. Pollut. Bull.*, 2013, **67**, 200–202.

187 A. Lusher, in *Marine Anthropogenic Litter*ed. M. Bergmann, L. Gutow and M. Klages, Springer International Publishing, Cham, 2015, ch. 10, pp. 245–307.

188 M. C. Fossi, C. Panti, C. Guerranti, D. Coppola, M. Giannetti, L. Marsili and R. Minutoli, *Mar. Pollut. Bull.*, 2012, **64**, 2374–2379.

189 K. Magnusson, F. Norén, Screening of microplastic particles in and down-stream a wastewater treatment plant, IVL Swedish Environmental Research Institute, 2014, vol. C55, 1–20.

190 S. Ziajahromi, P. A. Neale, L. Rintoul and F. D. L. Leusch, *Water Res.*, 2017, **112**, 93–99.
191 X. Liu, W. Yuan, M. Di, Z. Li and J. Wang, *Chem. Eng. J.*, 2019, **362**, 176–182.
192 M. R. Michielssen, E. R. Michielssen, J. Ni and M. B. Duhaime, *Environ. Sci.: Water Res. Technol.*, 2016, **2**, 1064–1073.
193 P. U. Iyare, S. K. Ouki and T. Bond, *Environ. Sci.: Water Res. Technol.*, 2020, **6**, 2664–2675.
194 S. S. Alavian Petroody, S. H. Hashemi and C. A. M. van Gestel, *Chemosphere*, 2021, **278**, 130471.
195 E. D. Okoffo, E. Donner, S. P. McGrath, B. J. Tscharke, J. W. O'Brien, S. O'Brien, F. Ribeiro, S. D. Burrows, T. Toapanta, C. Rauert, S. Samanipour, J. F. Mueller and K. V. Thomas, *Water Res.*, 2021, **201**, 117367.
196 E. Zilinskaite, M. Futter and D. Collentine, *Frontiers in Sustainable Food Systems*, 2022, **6**, 1–13.
197 J. S. Hanvey, P. J. Lewis, J. L. Lavers, N. D. Crosbie, K. Pozo and B. O. Clarke, *Anal. Methods*, 2017, **9**, 1369–1383.
198 M. Lares, M. C. Ncibi, M. Sillanpää and M. Sillanpää, *Environ. Sci. Pollut. Res.*, 2019, **26**, 12109–12122.
199 R. M. Blair, S. Waldron, V. R. Phoenix and C. Gauchotte-Lindsay, *Environ. Sci. Pollut. Res.*, 2019, **26**, 12491–12504.
200 Z. Wang, T. Lin and W. Chen, *Sci. Total Environ.*, 2020, **700**, 134520.
201 B. Ma, W. Xue, Y. Ding, C. Hu, H. Liu and J. Qu, *J. Environ. Sci.*, 2019, **78**, 267–275.
202 B. Ma, W. Xue, C. Hu, H. Liu, J. Qu and L. Li, *Chem. Eng. J.*, 2019, **359**, 159–167.
203 D. W. Skaf, V. L. Punzi, J. T. Rolle and K. A. Kleinberg, *Chem. Eng. J.*, 2020, **386**, 123807.
204 A. F. Herbort and K. Schuhen, *Environ. Sci. Pollut. Res.*, 2017, **24**, 11061–11065.
205 A. F. Herbort, M. T. Sturm and K. Schuhen, *Environ. Sci. Pollut. Res.*, 2018, **25**, 15226–15234.
206 W. Perren, A. Wojtasik and Q. Cai, *ACS Omega*, 2018, **3**, 3357–3364.
207 Z. Wang, M. Sedighi and A. Lea-Langton, *Water Res.*, 2020, **184**, 116165.
208 V. Siipola, S. Pflugmacher, H. Romar, L. Wendling and P. Koukkari, *Appl. Sci.*, 2020, **10**, 788.
209 C. Sun, Z. Wang, L. Chen and F. Li, *Chem. Eng. J.*, 2020, **393**, 124796.
210 Y. J. Chen, Y. Chen, C. Miao, Y. R. Wang, G. K. Gao, R. X. Yang, H. J. Zhu, J. H. Wang, S. L. Li and Y. Q. Lan, *J. Mater. Chem. A*, 2020, **8**, 14644–14652.
211 M. Enfrin, J. Lee, P. Le-Clech and L. F. Dumée, *J. Membr. Sci.*, 2020, **601**, 117890.
212 J. Li, B. Wang, Z. Chen, B. Ma and J. P. Chen, *Chem. Eng. J.*, 2021, **410**, 128174.
213 H. Ding, J. Zhang, H. He, Y. Zhu, D. D. Dionysiou, Z. Liu and C. Zhao, *Sci. Total Environ.*, 2021, **755**, 142658.
214 T. Makropoulou, I. Kortidis, K. Davididou, D. E. Motaung and E. Chatzisymeon, *Journal of Water Process Engineering*, 2020, **36**, 101299.
215 D. Kanakaraju, B. D. Glass and M. Oelgemöller, *J. Environ. Manage.*, 2018, **219**, 189–207.
216 Y. Deng and R. Zhao, *Curr. Pollut. Rep.*, 2015, **1**, 167–176.
217 S. Kim, A. Sin, H. Nam, Y. Park, H. Lee and C. Han, *Chem. Eng. J. Adv.*, 2022, **9**, 100213.
218 M. I. Stefan, *Advanced Oxidation Processes for Water Treatment: Fundamentals and Applications*, IWA Publishing, 2017.
219 M. C. Ariza-Tarazona, J. F. Villarreal-Chiu, J. M. Hernández-López, J. Rivera De la Rosa, V. Barbieri, C. Siligardi and E. I. Cedillo-González, *J. Hazard. Mater.*, 2020, **395**, 122632.
220 B. E. Llorente-García, J. M. Hernández-López, A. A. Zaldívar-Cadena, C. Siligardi and E. I. Cedillo-González, *Coatings*, 2020, **10**, 658.
221 I. Nabi, A. U. R. Bacha, K. Li, H. Cheng, T. Wang, Y. Liu, S. Ajmal, Y. Yang, Y. Feng and L. Zhang, *iScience*, 2020, **23**, 101326.
222 T. S. Tofa, F. Ye, K. L. Kunjali and J. Dutta, *Catalysts*, 2019, **9**, 819.
223 M. C. Ariza-Tarazona, J. F. Villarreal-Chiu, V. Barbieri, C. Siligardi and E. I. Cedillo-González, *Ceram. Int.*, 2019, **45**, 9618–9624.
224 T. S. Tofa, K. L. Kunjali, S. Paul and J. Dutta, *Environ. Chem. Lett.*, 2019, **17**, 1341–1346.
225 A. Uheida, H. G. Mejía, M. Abdel-Rehim, W. Hamd and J. Dutta, *J. Hazard. Mater.*, 2021, **406**, 124299.
226 J. M. Lee, R. Busquets, I. C. Choi, S. H. Lee, J. K. Kim and L. C. Campos, *Water*, 2020, **12**, 1–20.
227 J. Kang, L. Zhou, X. Duan, H. Sun, Z. Ao and S. Wang, *Matter*, 2019, **1**, 745–758.
228 R. Jiang, G. Lu, Z. Yan, J. Liu, D. Wu and Y. Wang, *J. Hazard. Mater.*, 2021, **405**, 124247.
229 P. H. Allé, P. Garcia-Muñoz, K. Adouby, N. Keller and D. Robert, *Environ. Chem. Lett.*, 2021, **19**, 1803–1808.
230 Z. S. B. de Souza, M. P. Silva, T. J. M. Fraga and M. A. Motta Sobrinho, *Environ. Sci. Pollut. Res.*, 2021, **28**, 23912–23928.
231 P. Liu, K. Lu, J. Li, X. Wu, L. Qian, M. Wang and S. Gao, *J. Hazard. Mater.*, 2020, **384**, 121193.
232 P. Liu, L. Qian, H. Wang, X. Zhan, K. Lu, C. Gu and S. Gao, *Environ. Sci. Technol.*, 2019, **53**, 3579–3588.
233 A. S. Tagg, J. P. Harrison, Y. Ju-Nam, M. Sapp, E. L. Bradley, C. J. Sinclair and J. J. Ojeda, *Chem. Commun.*, 2017, **53**, 372–375.
234 K. Hu, P. Zhou, Y. Yang, T. Hall, G. Nie, Y. Yao, X. Duan and S. Wang, *ACS ES&T Engg*, 2022, **2**, 110–120.
235 V. Piazza, A. Uheida, C. Gambardella, F. Garaventa, M. Faimali and J. Dutta, *Frontiers in Marine Science*, 2022, **8**, 1–15.
236 R. Zafar, S. Y. Park and C. G. Kim, *Environmental Engineering Research*, 2021, **26**, 200410–200412.
237 H. Hidayaturrahman and T. G. Lee, *Mar. Pollut. Bull.*, 2019, **146**, 696–702.
238 T. Gomes de Aragão Belé, T. F. Neves, J. Cristale, P. Prediger, M. Constapel and R. F. Dantas, *Journal of Water Process Engineering*, 2021, **41**, 102072.
239 P. Ebrahimbabaie, K. Yousefi and J. Pichtel, *Sci. Total Environ.*, 2022, **806**, 150603.
240 T. Ahmed, M. Shahid, F. Azeem, I. Rasul, A. A. Shah, M. Noman, A. Hameed, N. Manzoor, I. Manzoor and

S. Muhammad, *Environ. Sci. Pollut. Res.*, 2018, **25**, 7287–7298.
241 M. Sillanpää, A. Khadir and S. S. Muthu, *Microplastics Pollution in Aquatic Media: Occurrence, Detection, and Removal*, Springer Nature, Singapore, 2022.
242 P. U. Iyare, S. K. Ouki and T. Bond, *Environ. Sci.: Water Res. Technol.*, 2020, **6**, 2664–2675.
243 P. Campo, A. Holmes and F. Coulon, *MethodsX*, 2019, **6**, 2776–2781.
244 W. Wei, X. Chen, L. Peng, Y. Liu, T. Bao and B. J. Ni, *Water Res.*, 2021, **190**, 116731.
245 W. Wei, Q.-S. Huang, J. Sun, J.-Y. Wang, S.-L. Wu and B.-J. Ni, *Environ. Sci. Technol.*, 2019, **53**, 2509–2517.
246 L. Li, D. Liu, K. Song and Y. Zhou, *Mar. Pollut. Bull.*, 2020, **150**, 110724.
247 H. S. Auta, C. U. Emenike, B. Jayanthi and S. H. Fauziah, *Mar. Pollut. Bull.*, 2018, **127**, 15–21.
248 J. Yang, Y. Yang, W.-M. Wu, J. Zhao and L. Jiang, *Environ. Sci. Technol.*, 2014, **48**, 13776–13784.
249 H. J. Jeon and M. N. Kim, *Biodegradation*, 2013, **24**, 89–98.
250 S. Y. Park and C. G. Kim, *Chemosphere*, 2019, **222**, 527–533.
251 A. Paço, K. Duarte, J. P. da Costa, P. S. M. Santos, R. Pereira, M. E. Pereira, A. C. Freitas, A. C. Duarte and T. A. P. Rocha-Santos, *Sci. Total Environ.*, 2017, **586**, 10–15.
252 R. Sangeetha Devi, V. Rajesh Kannan, D. Nivas, K. Kannan, S. Chandru and A. Robert Antony, *Mar. Pollut. Bull.*, 2015, **96**, 32–40.
253 J. Gong, T. Kong, Y. Li, Q. Li, Z. Li and J. Zhang, *Polymers*, 2018, **10**, 1326.
254 X. Li, H. Wu, J. Gong, Q. Li, Z. Li and J. Zhang, *Environ. Technol.*, 2022, 1–10.
255 S. Miri, R. Saini, S. M. Davoodi, R. Pulicharla, S. K. Brar and S. Magdouli, *Chemosphere*, 2022, **286**, 131670.
256 J. Ru, Y. Huo and Y. Yang, *Front. Microbiol.*, 2020, **11**, 442.
257 E. Duemichen, P. Eisentraut, M. Celina and U. Braun, *J. Chromatogr. A*, 2019, **1592**, 133–142.
258 K. Matsui, T. Ishimura, M. Mattonai, I. Iwai, A. Watanabe, N. Teramae, H. Ohtani and C. Watanabe, *J. Anal. Appl. Pyrolysis*, 2020, **149**, 104834.
259 J. La Nasa, G. Biale, D. Fabbri and F. Modugno, *J. Anal. Appl. Pyrolysis*, 2020, **149**, 104841.
260 A. Käppler, M. Fischer, B. M. Scholz-Böttcher, S. Oberbeckmann, M. Labrenz, D. Fischer, K.-J. Eichhorn and B. Voit, *Anal. Bioanal. Chem.*, 2018, **410**, 5313–5327.
261 V. Castelvetro, A. Corti, G. Biale, A. Ceccarini, I. Degano, J. La Nasa, T. Lomonaco, A. Manariti, E. Manco, F. Modugno and V. Vinciguerra, *Environ. Sci. Pollut. Res.*, 2021, **28**, 46764–46780.
262 S. Jung, S. H. Cho, K. H. Kim and E. E. Kwon, *Chem. Eng. J.*, 2021, **422**, 130154.
263 V. H. Da Silva, F. Murphy, J. M. Amigo, C. Stedmon and J. Strand, *Anal. Chem.*, 2020, **92**, 13724–13733.
264 M. A. Cashman, T. Langknecht, D. El Khatib, R. M. Burgess, T. B. Boving, S. Robinson and K. T. Ho, *Mar. Pollut. Bull.*, 2022, **174**, 113254.
265 E. Schmaltz, E. C. Melvin, Z. Diana, E. F. Gunady, D. Rittschof, J. A. Somarelli, J. Virdin and M. M. Dunphy-Daly, *Environ. Int.*, 2020, **144**, 106067.
266 M. U. Sheth, S. K. Kwartler, E. R. Schmaltz, S. M. Hoskinson, E. J. Martz, M. M. Dunphy-Daly, T. F. Schultz, A. J. Read, W. C. Eward and J. A. Somarelli, *Frontiers in Marine Science*, 2019, **6**, 1–10.
267 C. Mohanraj, T. Senthilkumar and M. Chandrasekar, *Int. J. Energy Res.*, 2017, **41**, 1534–1552.
268 V. Tournier, C. M. Topham, A. Gilles, B. David, C. Folgoas, E. Moya-Leclair, E. Kamionka, M.-L. Desrousseaux, H. Texier, S. Gavalda, M. Cot, E. Guémard, M. Dalibey, J. Nomme, G. Cioci, S. Barbe, M. Chateau, I. André, S. Duquesne and A. Marty, *Nature*, 2020, **580**, 216–219.

Conclusions

Briefly resuming, the present work concerns the preparation of two different typologies of buckypaper membranes: a) nanofillers doped BPs; b) semiconductor/BP membranes. Even if both typologies were employed for pollutants removal from water, nanofillers doped BPs were designed for contaminants recovery through adsorption processes while semiconductor/BP membranes were investigated for degradation of organic pollutants through photocatalysis. Considering the scientific results obtained, the following conclusions can be derived.

Nanofillers doped BPs

MOF/BPs. MOF/BPs are one of the first examples of MOF-carbon-based materials designed for applications in the field of recovery and water remediation. Concerning the work described in this thesis, two different MOFs were incorporated in the structure of buckypaper membranes. In the case of bioMOF, prepared from the natural amino acid L-threonine, the obtained BioMOF@SWCNT-BP membrane was tested for lanthanides recovery from water solutions. Adsorption capacity of the membrane was investigated both in static and dynamic conditions and is not influenced by pH of lanthanide solutions. Compared with the neat SWCNT membrane, BioMOF@SWCNT-BP is able to increase significantly Ce^{3+} recovery when higher concentrations of lanthanide solutions were employed, reaching a maximum adsorption capacity of 263 mg g^{-1} of Ce^{3+} adsorbed per gram of BioMOF@SWCNT-BP.

When the multivariate MOF (MTV-MOF), synthesized using oxamidato ligands of derivatives of the amino acids methionine and methylcysteine, is incorporated in the buckypaper membrane, lead adsorption capacity of the prepared MTV-MOF/SWCNT-BP was evaluated. Both membranes, the neat SWCNT-BP and MTV-MOF/SWCNT-BP, exhibited high recovery efficiencies for lead even when higher concentrations of the metal (up to 100 ppm) were tested. Furthermore, when the lead concentration ranges between 200 ppb and 1000 ppb, adsorption experiments showed that the lead content is reduced well

below the current established limit of 10 ppb set by EPA and WHO for drinking water, with MTV-MOF/SWCNT-BP driving to a faster and better removal of Pb^{2+} from water solutions. The behaviour of MTV-MOF/SWCNT-BP differs significantly from SWCNT-BP in terms of selectivity, where the MOF doped BP membrane exceed by more than 42% SWCNT-BP performances in the recovery of Pb^{2+} from highly concentrated multicomponent solutions (Na^{+}, K^{+}, Mg^{2+}, Ca^{2+}), over a wide range of lead concentrations. Higher selectivity of MTV-MOF/SWCNT-BP for lead is also maintained when capture properties of the membrane were evaluated in a highly concentrated multi-metal solution containing Pb^{2+}, Al^{3+}, Fe^{3+} (10 ppm for each metal), preserving removal efficiencies of up 97% for lead.

GO/BPs. Great removal efficiencies of GO for water pollutants have guided to the preparation of GO/BPs membranes in order to enhance adsorption properties of both materials and overcome one of the major drawbacks of GO powder: GO recovery and recycle at the end of each adsorption process. The optimal ratio GO:CNTs = 75:25 (weight percentage) allows to prepare a self-standing BP membrane, without altering substantially the mechanical and chemical stability of the pristine buckypapers. GO/BPs were then investigated in adsorption experiments for lead and non-steroidal anti-inflammatory drugs recovery. Great capture properties of GO-SWCNT BPs have been observed for lead when several initial concentrations were investigated, ranging from 1 to 50 ppm, ensuring a removal efficiency until to 60% for the highly concentrated lead solution and a maximum adsorption capacity of 479 mg g^{-1}. GO-SWCNT BPs also exhibited great selectivity for Pb^{2+} in the presence of interferent ions, which could be present in water, such as Na^{+}, K^{+}, Ca^{2+}, and Mg^{2+}, and other heavy metal ions, which could be present in wastewater such as Co^{2+}, Zn^{2+}, Cd^{2+}. Similar lead recovery efficiencies have been observed for Hg^{2+}, Fe^{3+}, Al^{3+}, and Cu^{2+} when these interfering metals are also present in the initial solution, suggesting the possibility of simultaneously decontamination of wastewater from several toxic pollutants.

Diclofenac (DIC), Ketoprofen (KET) and Naproxen (NAP) were selected as reference pollutants for the NSAIDs category and capture properties of GO-SWCNT BPs for these organic pollutants were investigated. Adsorption capacity of GO-SWCNT BP membranes is little influenced by pH solutions, with better recovery efficiencies reached for pH=4. After optimization of pH conditions, adsorption experiments were performed for each drug at pH=4 in the concentration interval 1-10-50 ppm. Adsorption capacity of GO-SWCNT BPs increased up to 118, 116, and 126 mg g^{-1} for DIC, KET, and NAP, respectively, maintaining these removal efficiencies even after four regeneration cycles, without any important reduction (less than 4%).

Semiconductor/BP membranes

A nanostructured thin layer of the semiconductor WO_3 has been deposited through RF magnetron sputtering on buckypaper surface. Photocatalytic efficiency of WO_3/BP membrane has been tested in a small continuous plant for degradation of two organic dyes, Methylene Blue (cationic dye) and Indigo Carmine (anionic dye), and the non-steroidal anti-inflammatory drug Diclofenac, starting from an initial solution concentration of 20 ppm for each pollutant. WO_3/BP membranes are able to efficiently degrade the water contaminants, with a degradation kinetics three times greater than that of WO_3 nano-powder in the case of Methylene Blue.

In conclusion, nanofillers doped buckypaper membranes are biocompatible and highly stable adsorbent membranes to be efficiently employed in pollutants recovery from wastewater. Smoothness and sustainability of the membrane preparation strategy by using the wet method, and easy recovery of adsorbents, which can be quickly regenerated and recycled, are among the major advantages attributable to these novel membranes, representing a viable solution to be extended to the whole recovery of contaminants from wastewater. Furthermore, the improved photoactivity, fast catalyst recovery and easy scale-up process observed for WO_3/BP membranes open the door to the application of these membranes, structured in the form of semiconductor/buckypapers, in the field of photocatalytic processes and, more

in general, of advanced oxidation processes, for totally degradation of pollutants from water in view of more environmental and sustainable approaches for water remediation.

Bibliography

1 United Nations General Assembly, *The human right to water and sanitation : resolution / adopted by the General Assembly*, UN, [New York], 2010-08-03, 2010.

2 United Nations, *Hum. Rights Instruments, Vol. I. Compil. Gen. Comments Gen. Recomm. Adopt. by Hum. Rights Treaty Bodies - HRI/GEN/1/Rev.9*, 2002, **2003**, 97–113.

3 A. Hamdy, in *Water demand management in the Mediterranean, progress and policies*, Zaragoza, 2007.

4 M. M. Mekonnen and A. Y. Hoekstra, *Sci. Adv.*, 2016, **2**, e1500323.

5 C. J. Vörösmarty, P. B. McIntyre, M. O. Gessner, D. Dudgeon, A. Prusevich, P. Green, S. Glidden, S. E. Bunn, C. A. Sullivan, C. R. Liermann and P. M. Davies, *Nature*, 2010, **467**, 555–561.

6 W. H. Organization and U. N. C. F. (UNICEF), *Progress on drinking water, sanitation and hygiene: 2017 update and SDG baselines*, World Health Organization, 2017.

7 A. Gürses, M. Açıkyıldız, K. Güneş and M. S. Gürses, in *A. Gürses et al., Dyes and Pigments, SpringerBriefs in Green Chemistry for Sustainability*, 2016, pp. 13–29.

8 R. Al-Tohamy, S. S. Ali, F. Li, K. M. Okasha, Y. A. G. Mahmoud, T. Elsamahy, H. Jiao, Y. Fu and J. Sun, *Ecotoxicol. Environ. Saf.*, 2022, **231**, 113160.

9 A. Gürses, M. Açıkyıldız, K. Güneş and M. S. Gürses, in *A. Gürses et al., Dyes and Pigments, SpringerBriefs in Green Chemistry for Sustainability*, 2016, pp. 69–83.

10 C. Lakshmi, *Res. J. Chem. Sci. Res. J. Chem. Sci*, 2014, **4**, 87–96.

11 D. B. Rodriguez-Amaya, *Curr. Opin. Food Sci.*, 2016, **7**, 20–26.

12 A. Khan and M. Alam, *J. Appl. Pharm. Sci. Res.*, 2019, **2**, 1–6.

13 M. Berradi, R. Hsissou, M. Khudhair, M. Assouag, O. Cherkaoui, A. El Bachiri and A. El Harfi, *Heliyon*, 2019, **5**, e02711.

14 V. K. Balakrishnan, S. Shirin, A. M. Aman, S. R. de Solla, J. Mathieu-Denoncourt and V. S. Langlois, *Chemosphere*, 2016, **146**, 206–215.

15 O. M. Rodriguez-Narvaez, J. M. Peralta-Hernandez, A. Goonetilleke and E. R. Bandala, *Chem. Eng. J.*, 2017, **323**, 361–380.

16 J. Rivera-Utrilla, M. Sánchez-Polo, M. Á. Ferro-García, G. Prados-Joya and R. Ocampo-Pérez, *Chemosphere*, 2013, **93**, 1268–1287.

17 T. Heberer, *Toxicol. Lett.*, 2002, **131**, 5–17.

18 T. Heberer, *J. Hydrol.*, 2002, **266**, 175–189.

19 O. F. S. Khasawneh and P. Palaniandy, *Process Saf. Environ. Prot.*, 2021, **150**, 532–556.

20 F. Spataro, N. Ademollo, T. Pescatore, J. Rauseo and L. Patrolecco, *Microchem. J.*, 2019, **148**, 634–642.

21 R. Kumar, A. K. Sarmah and L. P. Padhye, *J. Environ. Manage.*, 2019, **233**, 649–659.

22 H. B. Quesada, A. T. A. Baptista, L. F. Cusioli, D. Seibert, C. de Oliveira Bezerra and R. Bergamasco, *Chemosphere*, 2019, **222**, 766–780.

23 N. A. H. Ismail, S. Y. Wee, D. E. M. Haron, N. H. Kamarulzaman and A. Z. Aris, *Mar. Pollut. Bull.*, 2020, **150**, 110735.

24 F. Pomati, S. Castiglioni, E. Zuccato, R. Fanelli, D. Vigetti, C. Rossetti and D. Calamari, *Environ. Sci. Technol.*, 2006, **40**, 2442–2447.

25 A. Sapkota, A. R. Sapkota, M. Kucharski, J. Burke, S. McKenzie, P. Walker and R. Lawrence, *Environ. Int.*, 2008, **34**, 1215–1226.

26 N. G. H. Taylor, D. W. Verner-Jeffreys and C. Baker-Austin, *Trends Ecol. Evol.*, 2011, **26**, 278–284.

27 M. Pei, B. Zhang, Y. He, J. Su, K. Gin, O. Lev, G. Shen and S. Hu, *Environ. Int.*, 2019, **131**, 105026.

28 J. Margot, L. Rossi, D. A. Barry and C. Holliger, *WIREs Water*, 2015, **2**, 457–487.

29 J. M. Brausch and G. M. Rand, *Chemosphere*, 2011, **82**, 1518–1532.

30 G. S. Dhillon, S. Kaur, R. Pulicharla, S. K. Brar, M. Cledón, M. Verma and R. Y. Surampalli, *Int. J. Environ. Res. Public Health*, 2015, **12**, 5657–5684.

31 L. Yao, Y.-Z. Lv, L.-J. Zhang, W.-R. Liu, J.-L. Zhao, Y.-Y. Yang, Y.-W. Jia, Y.-S. Liu, L.-Y. He and G.-G. Ying, *Sci. Total Environ.*, 2019, **665**, 810–819.

32 T. Ahmad, M. Rafatullah, A. Ghazali, O. Sulaiman, R. Hashim and A. Ahmad, *J. Environ. Sci. Heal. - Part C Environ. Carcinog. Ecotoxicol. Rev.*, 2010, **28**, 231–271.

33 M. Köck-Schulmeyer, M. Villagrasa, M. López de Alda, R. Céspedes-Sánchez, F. Ventura and D. Barceló, *Sci. Total Environ.*, 2013, **458–460**, 466–476.

34 K. H. Kim, E. Kabir and S. A. Jahan, *Sci. Total Environ.*, 2017, **575**, 525–535.

35 S. Mostafalou and M. Abdollahi, *Toxicol. Appl. Pharmacol.*, 2013, **268**, 157–177.

36 E. Corsini, M. Sokooti, C. L. Galli, A. Moretto and C. Colosio, *Toxicology*, 2013, **307**, 123–135.

37 A. F. Gilca, C. Teodosiu, S. Fiore and C. P. Musteret, *Chemosphere*, 2020, **259**, 127476.

38 M. Yang and X. Zhang, *Trends Environ. Anal. Chem.*, 2016, **10**, 24–34.

39 S. D. Richardson and T. A. Ternes, *Anal. Chem.*, 2014, **86**, 2813–2848.

40 J. Li, W. Wang, B. Moe, H. Wang and X. F. Li, *Chem. Res. Toxicol.*, 2015, **28**, 306–318.

41 E. D. Wagner, K. M. Hsu, A. Lagunas, W. A. Mitch and M. J. Plewa, *Mutat. Res. - Genet. Toxicol. Environ. Mutagen.*, 2012, **741**, 109–115.

42 S. D. Richardson, F. Fasano, J. J. Ellington, F. G. Crumley, K. M. Buettner, J. J. Evans, B. C. Blount, L. K. Silva, T. J. Waite, G. W. Luther, A. B. Mckague, R. J. Miltner, E. D. Wagner and M. J. Plewa, *Environ. Sci. Technol.*, 2008, **42**, 8330–8338.

43 S. W. Krasner, H. S. Weinberg, S. D. Richardson, S. J. Pastor, R. Chinn, M. J. Sclimenti, G. D. Onstad and A. D. Thruston, *Environ. Sci. Technol.*, 2006, **40**, 7175–7185.

44 J. Briffa, E. Sinagra and R. Blundell, *Heliyon*, 2020, **6**, e04691.

45 J. C. Lee, Y. O. Son, P. Pratheeshkumar and X. Shi, *Free Radic. Biol. Med.*, 2012, **53**, 742–757.

46 A. T. Jan, M. Azam, K. Siddiqui, A. Ali, I. Choi and Q. M. R. Haq, *Int. J. Mol. Sci.*, 2015, **16**, 29592–29630.

47 M. Bilal, I. Ihsanullah, M. Younas and M. Ul Hassan Shah, *Sep. Purif. Technol.*, 2022, **278**, 119510.

48 K. S. Mohammed Abdul, S. S. Jayasinghe, E. P. S. Chandana, C. Jayasumana and P. M. C. S. De Silva, *Environ. Toxicol. Pharmacol.*, 2015, **40**, 828–846.

49 P. Holmes, K. A. F. James and L. S. Levy, *Sci. Total Environ.*, 2009, **408**, 171–182.

50 M. Boskabady, N. Marefati, T. Farkhondeh, F. Shakeri, A. Farshbaf and M. H. Boskabady, *Environ. Int.*, 2018, **120**, 404–420.

51 D. L. Ozsvath, *Rev. Environ. Sci. Biotechnol.*, 2009, **8**, 59–79.

52 S. Ghosh, A. Malloum, C. A. Igwegbe, J. O. Ighalo, S. Ahmadi, M. H. Dehghani, A. Othmani, Ö. Gökkuş and N. M. Mubarak, *J. Mol. Liq.*, 2022, **346**, 118257.

53 A. Rasool, A. Farooqi, T. Xiao, W. Ali, S. Noor, O. Abiola, S. Ali and W. Nasim, *Environ. Geochem. Health*, 2017, **40**, 1265–1281.

54 J. Chen, H. Qian, H. Wu, Y. Gao and X. Li, *Environ. Earth Sci.*, 2017, **76**, 1–15.

55 M. Kupiec, P. Pieńkowski, B. Bosiacka, I. Gutowska, P. Kupnicka, A. Prokopowicz, D. Chlubek and I. Baranowska-Bosiacka, *Int. J. Environ. Res. Public Health*, 2019, **16**, 819.

56 R. Geyer, J. R. Jambeck and K. L. Law, *Sci. Adv.*, 2017, **3**, e1700782.

57 S. Sharma and S. Chatterjee, *Environ. Sci. Pollut. Res.*, 2017, **24**, 21530–21547.

58 M. Smith, D. C. Love, C. M. Rochman and R. A. Neff, *Curr. Environ. Heal. reports*, 2018, **5**, 375–386.

59 J. G. B. Derraik, *Mar. Pollut. Bull.*, 2002, **44**, 842–852.

60 S. Lechthaler, K. Waldschläger, G. Stauch and H. Schüttrumpf, *Environ. - MDPI*, 2020, **7**, 1–30.

61 L. G. A. Barboza, A. Cózar, B. C. G. Gimenez, T. L. Barros, P. J. Kershaw and L. Guilhermino, in *World Seas: An Environmental Evaluation Volume III: Ecological Issues and Environmental Impacts*, Elsevier Ltd., Second Edi., 2018, pp. 305–328.

62 J. Q. Jiang, *Sustain. Prod. Consum.*, 2018, **13**, 16–23.

63 F. Murphy, C. Ewins, F. Carbonnier and B. Quinn, *Environ. Sci. Technol.*, 2016, **50**, 5800–5808.

64 H. S. Auta, C. U. Emenike and S. H. Fauziah, *Environ. Int.*, 2017, **102**, 165–176.

65 L. C. M. Lebreton, S. D. Greer and J. C. Borrero, *Mar. Pollut. Bull.*, 2012, **64**, 653–661.

66 J. Kaiser, *Science*, 2010, **328**, 1506.

67 C. J. Moore, S. L. Moore, M. K. Leecaster and S. B. Weisberg, *Mar. Pollut. Bull.*, 2001, **42**, 1297–1300.

68 M. Eriksen, L. C. M. Lebreton, H. S. Carson, M. Thiel, C. J. Moore, J. C. Borerro, F. Galgani, P. G. Ryan and J. Reisser, *PLoS One*, 2014, **9**, 1–15.

69 E. Van Sebille, M. H. England and G. Froyland, *Environ. Res. Lett.*, 2012, **7**, 044040.

70 M. Eriksen, N. Maximenko, M. Thiel, A. Cummins, G. Lattin, S. Wilson, J. Hafner, A. Zellers and S. Rifman, *Mar. Pollut. Bull.*, 2013, **68**, 71–76.

71 L. Fok and P. K. Cheung, *Mar. Pollut. Bull.*, 2015, **99**, 112–118.

72 M. Claessens, S. De Meester, L. Van Landuyt, K. De Clerck and C. R. Janssen, *Mar. Pollut. Bull.*, 2011, **62**, 2199–2204.

73 T. Gouin, N. Roche, R. Lohmann and G. Hodges, *Environ. Sci. Technol.*, 2011, **45**, 1466–1472.

74 S. Mishra, C. charan Rath and A. P. Das, *Mar. Pollut. Bull.*, 2019, **140**, 188–197.

75 I. A. Kane and M. A. Clare, *Front. Earth Sci.*, 2019, **7**, 80.

76 J. Zalasiewicz, C. N. Waters, J. A. Ivar do Sul, P. L. Corcoran, A. D. Barnosky, A. Cearreta, M. Edgeworth, A. Gałuszka, C. Jeandel, R. Leinfelder, J. R. McNeill, W. Steffen, C. Summerhayes, M. Wagreich, M. Williams, A. P. Wolfe and Y. Yonan, *Anthropocene*, 2016, **13**, 4–17.

77 A. Rahman, A. Sarkar, O. P. Yadav, G. Achari and J. Slobodnik, *Sci. Total Environ.*, 2021, **757**, 143872.

78 K. D. Cox, G. A. Covernton, H. L. Davies, J. F. Dower, F. Juanes and S. E. Dudas, *Environ. Sci. Technol.*, 2019, **53**, 7068–7074.

79 J. P. S. Cabral, *Int. J. Environ. Res. Public Health*, 2010, **7**, 3657–3703.

80 R. D. Arnone and J. P. Walling, *J. Water Health*, 2007, **5**, 149–162.

81 P. K. Pandey, P. H. Kass, M. L. Soupir, S. Biswas and V. P. Singh, *AMB Express*, 2014, **4**, 1–16.

82 O. Savichtcheva and S. Okabe, *Water Res.*, 2006, **40**, 2463–2476.

83 K. G. Field and M. Samadpour, *Water Res.*, 2007, **41**, 3517–3538.

84 D. A. Holcomb and J. R. Stewart, *Curr. Environ. Heal. Reports*, 2020, **7**, 311–324.

85 P. Gwimbi, M. George and M. Ramphalile, *Environ. Health Prev. Med.*, 2019, **24**, 1–7.

86 A. Kongprajug, N. Chyerochana, S. Rattanakul, T. Denpetkul, W. Sangkaew, P. Somnark, Y. Patarapongsant, K. Tomyim, M. Sresung, S. Mongkolsuk and K. Sirikanchana, *Water Res.*, 2021, **203**, 117479.

87 WHO, *Guidelines for drinking water quality - Fourth edition incorporating the first and second addenda*, 2022, vol. 4.

88 U.S. EPA, *National Primary Drinking Water Guidelines*, 2009, vol. 1.

89 G. Lofrano and J. Brown, *Sci. Total Environ.*, 2010, **408**, 5254–5264.

90 C. Prasse, D. Stalter, U. Schulte-Oehlmann, J. Oehlmann and T. A. Ternes, *Water Res.*, 2015, **87**, 237–270.

91 A. K. J. A. K. J. Dr. B. C. Punmia, B. C. Punmia, A. K. Jain and A. K. Jain, *Waste Water Engineering*, Laxmi Publications Pvt Limited, 1998.

92 K. B. Newhart, R. W. Holloway, A. S. Hering and T. Y. Cath, *Water Res.*, 2019, **157**, 498–513.

93 J. I. Kroschwitz, Kirk-Othmer and A. Seidel, *Kirk-Othmer Encyclopedia of Chemical Technology*, J. Wiley, 2004.

94 W. Bourgeois, J. E. Burgess and R. M. Stuetz, *J. Chem. Technol. Biotechnol.*, 2001, **76**, 337–348.

95 K. Lenz, S. N. Mahnik, N. Weissenbacher, R. M. Mader, P. Krenn, S. Hann, G. Koellensperger, M. Uhl, S. Knasmüller, F. Ferk, W. Bursch and M. Fuerhacker, *Water Sci. Technol.*, 2007, **56**, 141–149.

96 A. Q. Nguyen, H. P. Vu, L. N. Nguyen, Q. Wang, S. P. Djordjevic, E. Donner, H. Yin and L. D. Nghiem, *Sci. Total Environ.*, 2021, **783**, 146964.

97 E. M. Carstea, J. Bridgeman, A. Baker and D. M. Reynolds, *Water Res.*, 2016, **95**, 205–219.

98 F. Ejeian, P. Etedali, H. A. Mansouri-Tehrani, A. Soozanipour, Z. X. Low, M. Asadnia, A. Taheri-Kafrani and A. Razmjou, *Biosens. Bioelectron.*, 2018, **118**, 66–79.

99 A. Sonune and R. Ghate, *Desalination*, 2004, **167**, 55–63.

100 W. A. Shewa and M. Dagnew, *Sustain.*, 2020, **12**, 5928.

101 Y. J. Chan, M. F. Chong, C. L. Law and D. G. Hassell, *Chem. Eng. J.*, 2009, **155**, 1–18.

102 X. Shi, O. Lefebvre, K. K. Ng and H. Y. Ng, *Bioresour. Technol.*, 2014, **153**, 79–86.

103 H. Huang, C. Peng, P. Peng, Y. Lin, X. Zhang and H. Ren, *Appl. Microbiol. Biotechnol.*, 2019, **103**, 1115–1129.

104 A. van Haandel and J. van der Lubbe, *Handbook of Biological Wastewater Treatment*, IWA Publishing, 2012.

105 M. C. Collivignarelli, A. Abbà, I. Benigna, S. Sorlini and V. Torretta, *Sustain.*, 2018, **10**, 1–21.

106 S. Monarca, D. Feretti, C. Collivignarelli, L. Guzzella, I. Zerbini, G. Bertanza and R. Pedrazzani, *Water Res.*, 2000, **34**, 4261–4269.

107 C. Pironti, F. Dell'Annunziata, R. Giugliano, V. Folliero, M. Galdiero, M. Ricciardi, O. Motta, A. Proto and G. Franci, *Sci. Total Environ.*, 2021, **797**, 149206.

108 E. Veschetti, D. Cutilli, L. Bonadonna, R. Briancesco, C. Martini, G. Cecchini, P. Anastasi and M. Ottaviani, *Water Res.*, 2003, **37**, 78–94.

109 S. W. Krasner, P. Westerhoff, B. Chen, B. E. Rittmann and G. Amy, *Environ. Sci. Technol.*, 2009, **43**, 8320–8325.

110 Y. Luo, L. Feng, Y. Liu and L. Zhang, *Sep. Purif. Technol.*, 2020, **238**, 116405.

111 A. Dell'Erba, D. Falsanisi, L. Liberti, M. Notarnicola and D. Santoro, *Desalination*, 2007, **215**, 177–186.

112 J. Le Roux, M. J. Plewa, E. D. Wagner, M. Nihemaiti, A. Dad and J. P. Croué, *J. Environ. Sci. (China)*, 2017, **58**, 135–145.

113 T. K. Das, *Clean Prod. Process.*, 2001, **3**, 69–80.

114 Y. Deng and R. Zhao, *Curr. Pollut. Reports*, 2015, **1**, 167–176.

115 J. M. Poyatos, M. M. Muñio, M. C. Almecija, J. C. Torres, E. Hontoria and F. Osorio, *Water. Air. Soil Pollut.*, 2010, **205**, 187–204.

116 C. V. Rekhate and J. K. Srivastava, *Chem. Eng. J. Adv.*, 2020, **3**, 100031.

117 M. E. Borges, T. Hernández and P. Esparza, *Clean Technol. Environ. Policy*, 2014, **16**, 431–436.

118 O. K. Dalrymple, D. H. Yeh and M. A. Trotz, *J. Chem. Technol. Biotechnol.*, 2007, **82**, 121–134.

119 A. Bernabeu, R. F. Vercher, L. Santos-Juanes, P. J. Simón, C. Lardín, M. A. Martínez, J. A. Vicente, R. González, C. Llosá, A. Arques and A. M. Amat, *Catal. Today*, 2011, **161**, 235–240.

120 R. Saravanan, F. Gracia and A. Stephen, in *Nanocomposites for Visible Light-induced Photocatalysis*, eds. M. M. Khan, D. Pradhan and Y. Sohn, Springer Cham, 1st edn., 2017, pp. 19–40.

121 C. W. Lai, K. M. Lee and J. C. Juan, in *Nanocomposites for Visible Light-induced Photocatalysis*, eds. M. M. Khan, D. Pradhan and Y. Sohn, Springer Cham, 1st edn., 2017, pp. 175–201.

122 R. Ameta and S. C. Ameta, in *Photocatalysis - Principles and Applications*, eds. R. Ameta and S. C. Ameta, CRC Press, Boca Raton, 1st edn., 2016, pp. 17–34.

123 U. G. Akpan and B. H. Hameed, *J. Hazard. Mater.*, 2009, **170**, 520–529.

124 J. Qiu, M. Li, M. Ding and J. Yao, *Renew. Sustain. Energy Rev.*, 2022, **154**, 111820.

125 G. Li Puma, A. Bono, D. Krishnaiah and J. G. Collin, *J. Hazard. Mater.*, 2008, **157**, 209–219.

126 J. Velásquez, S. Valencia, L. Rios, G. Restrepo and J. Marín, *Chem. Eng. J.*, 2012, **203**, 398–405.

127 X. Liu, Q. Chen, L. Lv, X. Feng and X. Meng, *Catal. Commun.*, 2015, **58**, 30–33.

128 A. Di Mauro, M. Cantarella, G. Nicotra, G. Pellegrino, A. Gulino, M. V. Brundo, V. Privitera and G. Impellizzeri, *Sci. Rep.*, 2017, **7**, 1–12.

129 R. Saravanan, E. Sacari, F. Gracia, M. M. Khan, E. Mosquera and V. K. Gupta, *J. Mol. Liq.*, 2016, **221**, 1029–1033.

130 R. A. Rakkesh, D. Durgalakshmi and S. Balakumar, in *Nanocomposites for Visible Light-induced Photocatalysis*, eds. M. M. Khan, D. Pradhan and Y. Sohn, Springer Cham, 1st edn., 2017, pp. 107–127.

131 R. Marschall and L. Wang, *Catal. Today*, 2014, **225**, 111–135.

132 A. Kudo, R. Niishiro, A. Iwase and H. Kato, *Chem. Phys.*, 2007, **339**, 104–110.

133 E. Kowsari, in *Nanocomposites for Visible Light-induced Photocatalysis*, eds. M. M. Khan, D. Pradhan and Y. Sohn, Springer Cham, 1st edn., 2017, pp. 203–249.

134 Y. Zhang, N. Zhang, Z. R. Tang and Y. J. Xu, *ACS Nano*, 2012, **6**, 9777–9789.

135 X. Yang, H. Cui, Y. Li, J. Qin, R. Zhang and H. Tang, *ACS Catal.*, 2013, **3**, 363–369.

136 S. Zhang, B. Li, X. Wang, G. Zhao, B. Hu, Z. Lu, T. Wen, J. Chen and X. Wang, *Chem. Eng. J.*, 2020, **390**, 124642.

137 A. Babuponnusami and K. Muthukumar, *J. Environ. Chem. Eng.*, 2014, **2**, 557–572.

138 S. Guerra-Rodríguez, E. Rodríguez, D. N. Singh and J. Rodríguez-Chueca, *Water (Switzerland)*, 2018, **10**, 1828.

139 M. Brienza and I. A. Katsoyiannis, *Sustain.*, 2017, **9**, 1–18.

140 M. Takht Ravanchi, T. Kaghazchi and A. Kargari, *Desalination*, 2009, **235**, 199–244.

141 M. Catarino and A. Mendes, *Innov. Food Sci. Emerg. Technol.*, 2011, **12**, 330–337.

142 F. Salehi, *Food Bioprod. Process.*, 2014, **92**, 161–177.

143 A. Ambrosi, N. S. M. Cardozo and I. C. Tessaro, *Food Bioprocess Technol.*, 2014, **7**, 921–936.

144 A. Ali, R. A. Tufa, F. Macedonio, E. Curcio and E. Drioli, *Renew. Sustain. Energy Rev.*, 2018, **81**, 1–21.

145 N. K. Khanzada, M. U. Farid, J. A. Kharraz, J. Choi, C. Y. Tang, L. D. Nghiem, A. Jang and A. K. An, *J. Memb. Sci.*, 2020, **598**, 117672.

146 A. G. T. Fane, R. Wang and Y. Jia, *Membrane and Desalination Technologies*, 2011.

147 E. O. Ezugbe and S. Rathilal, *Membranes*, 2020, **10**, 89.

148 H. Al Abdulgader, V. Kochkodan and N. Hilal, *Sep. Purif. Technol.*, 2013, **116**, 253–264.

149 W. L. Ang, A. W. Mohammad, Y. H. Teow, A. Benamor and N. Hilal, *Sep. Purif. Technol.*, 2015, **152**, 23–31.

150 W. L. Ang, A. W. Mohammad, A. Benamor and N. Hilal, *Desalination*, 2016, **390**, 25–32.

151 N. Rosman, W. N. W. Salleh, M. A. Mohamed, J. Jaafar, A. F. Ismail and Z. Harun, *J. Colloid Interface Sci.*, 2018, **532**, 236–260.

152 P. Le-Clech, *Appl. Microbiol. Biotechnol.*, 2010, **88**, 1253–1260.

153 C. Stoquart, P. Servais, P. R. Bérubé and B. Barbeau, *J. Memb. Sci.*, 2012, **411–412**, 1–12.

154 E. Saljoughi and S. M. Mousavi, *Sep. Purif. Technol.*, 2012, **90**, 22–30.

155 W. Zhang, Z. Shi, F. Zhang, X. Liu, J. Jin and L. Jiang, *Adv. Mater.*, 2013, **25**, 2071–2076.

156 B. Fryczkowska, A. Machnicka, D. Biniaś, C. Ślusarczyk and J. Fabia, *Membranes (Basel).*, 2020, **10**, 58.

157 H. R. Lohokare, M. R. Muthu, G. P. Agarwal and U. K. Kharul, *J. Memb. Sci.*, 2008, **320**, 159–166.

158 A. Lee, J. W. Elam and S. B. Darling, *Environ. Sci. Water Res. Technol.*, 2016, **2**, 17–42.

159 I. Pinnau and B. D. Freeman, *ACS Symp. Ser.*, 1999, **744**, 1–22.

160 A. Rahimpour, *Desalination*, 2011, **265**, 93–101.

161 E. Yuliwati and A. F. Ismail, *Desalination*, 2011, **273**, 226–234.

162 Y. Zhang, Y. Wan, G. Pan, X. Wei, Y. Li, H. Shi and Y. Liu, *J. Memb. Sci.*, 2019, **573**, 11–20.

163 S. K. Nemani, R. K. Annavarapu, B. Mohammadian, A. Raiyan, J. Heil, M. A. Haque, A. Abdelaal and H. Sojoudi, *Adv. Mater. Interfaces*, 2018, **5**, 1–26.

164 F. A. Jung, M. Schart, L. Bührend, E. Meidinger, J. J. Kang, B. J. Niebuur, S. Ariaee, D. S. Molodenskiy, D. Posselt, H. Amenitsch, C. Tsitsilianis and C. M. Papadakis, *Adv. Funct. Mater.*, 2021, **31**, 2102905.

165 D. Fournier, R. Hoogenboom, H. M. L. Thijs, R. M. Paulus and U. S. Schubert, *Macromolecules*, 2007, **40**, 915–920.

166 B. Yang, X. Yang, B. Liu, Z. Chen, C. Chen, S. Liang, L. Y. Chu and J. Crittenden, *J. Memb. Sci.*, 2017, **541**, 558–566.

167 D. Menne, F. Pitsch, J. E. Wong, A. Pich and M. Wessling, *Angew. Chemie - Int. Ed.*, 2014, **53**, 5706–5710.

168 S. Loeb and S. Sourirajan, in *Saline Water Conversion—II*, AMERICAN CHEMICAL SOCIETY, 1963, vol. 38, pp. 117–132.

169 J. J. Qin, Y. Li, L. S. Lee and H. Lee, *J. Memb. Sci.*, 2003, **218**, 173–183.

170 V. Vatanpour, M. E. Pasaoglu, H. Barzegar, O. O. Teber, R. Kaya, M. Bastug, A. Khataee and I. Koyuncu, *Chemosphere*, 2022, **295**, 133914.

171 A. Mansourizadeh and A. Javadi Azad, *J. Polym. Res.*, 2014, **21**, 375.

172 S. P. Nunes, P. Z. Culfaz-Emecen, G. Z. Ramon, T. Visser, G. H. Koops, W. Jin and M. Ulbricht, *J. Memb. Sci.*, 2020, **598**, 117761.

173 H. Guo, S. Zhao, X. Wu and H. Qi, *Microporous Mesoporous Mater.*, 2018, **260**, 125–131.

174 M. B. Asif and Z. Zhang, *Chem. Eng. J.*, 2021, **418**, 129481.

175 F. E. Bortot Coelho, N. N. Kaiser, G. Magnacca and V. M. Candelario, *J. Eur. Ceram. Soc.*, 2021, **41**, 7792–7806.

176 K. H. Park, P. F. Sun, E. H. Kang, G. D. Han, B. J. Kim, Y. Jang, S. H. Lee, J. H. Shim and H. D. Park, *Sep. Purif. Technol.*, 2021, **272**, 118935.

177 Q. Chang, J. er Zhou, Y. Wang, J. Liang, X. Zhang, S. Cerneaux, X. Wang, Z. Zhu and Y. Dong, *J. Memb. Sci.*, 2014, **456**, 128–133.

178 E. Luster, D. Avisar, I. Horovitz, L. Lozzi, M. A. Baker, R. Grilli and H. Mamane, *Nanomaterials*, 2017, **7**, 1–19.

179 P. Jarvis, I. Carra, M. Jafari and S. J. Judd, *Water Res.*, 2022, **215**, 118269.

180 C. Algieri and E. Drioli, *Sep. Purif. Technol.*, 2022, **278**, 119295.

181 N. Kosinov, J. Gascon, F. Kapteijn and E. J. M. Hensen, *J. Memb. Sci.*, 2016, **499**, 65–79.

182 M. Drobek, C. Yacou, J. Motuzas, A. Julbe, L. Ding and J. C. Diniz da Costa, *J. Memb. Sci.*, 2012, **415**–**416**, 816–823.

183 F. Gallucci, L. Paturzo and A. Basile, *Chem. Eng. Process. Process Intensif.*, 2004, **43**, 1029–1036.

184 A. Campanile, B. Liguori, C. Ferone, D. Caputo and P. Aprea, *Sci. Rep.*, 2022, **12**, 1–10.

185 S. Iijima, *Nature*, 1991, **354**, 56–58.

186 M. S. Dresselhaus, G. Dresselhaus, P. C. Eklund and A. M. Rao, in *The Physics of Fullerene-Based and Fullerene-Related Materials*, ed. W. Andreoni, Springer Netherlands, Dordrecht, 2000, pp. 331–379.

187 S. Reich, C. Thomsen and J. Maultzsch, *Carbon Nanotubes: Basic Concepts and Physical Properties*, Wiley, 2008.

188 M. F. L. De Volder, S. H. Tawfick, R. H. Baughman and A. J. Hart, *Science*, 2013, **339**, 535–539.

189 S. Chopra, K. McGuire, N. Gothard, A. M. Rao and A. Pham, *Appl. Phys. Lett.*, 2003, **83**, 2280–2282.

190 Y. Li, H. Liu, C. Yang, M. Zhu and T. Chen, *Diam. Relat. Mater.*, 2019, **100**, 107567.

191 S. Zhang, A. Hao, N. Nguyen, A. Oluwalowo, Z. Liu, Y. Dessureault, J. G. Park and R. Liang, *Carbon N. Y.*, 2019, **144**, 628–638.

192 M. Jung, Y. soon Lee, S. G. Hong and J. Moon, *Cem. Concr. Res.*, 2020, **131**, 106017.

193 Q. Xia, Z. Zhang, Y. Liu and J. Leng, *Compos. Part B Eng.*, 2020, **199**, 108231.

194 F. S. A. Khan, N. M. Mubarak, Y. H. Tan, M. Khalid, R. R. Karri, R. Walvekar, E. C. Abdullah, S. Nizamuddin and S. A. Mazari, *J. Hazard. Mater.*, 2021, **413**, 125375.

195 V. N. Popov, *Mater. Sci. Eng. R Reports*, 2004, **43**, 61–102.

196 J. Prasek, J. Drbohlavova, J. Chomoucka, J. Hubalek, O. Jasek, V. Adam and R. Kizek, *J. Mater. Chem.*, 2011, **21**, 15872–15884.

197 G. D. Nessim, *Nanoscale*, 2010, **2**, 1306–1323.

198 M. Baro, D. Gogoi, A. R. Pal, N. C. Adhikary, H. Bailung and J. Chutia, *Chem. Vap. Depos.*, 2014, **20**, 161–169.

199 G. Allaedini, S. M. Tasirin and P. Aminayi, *J. Alloys Compd.*, 2015, **647**, 809–814.

200 K. A. Shah and B. A. Tali, *Mater. Sci. Semicond. Process.*, 2016, **41**, 67–82.

201 J. Sengupta and C. Jacob, *J. Nanoparticle Res.*, 2010, **12**, 457–465.

202 Ihsanullah, *Sep. Purif. Technol.*, 2019, **209**, 307–337.

203 M. H. O. Rashid and S. F. Ralph, *Nanomaterials*, 2017, **7**, 99.

204 M. D. Rein, O. Breuer and H. D. Wagner, *Compos. Sci. Technol.*, 2011, **71**, 373–381.

205 J. DeGraff, R. Liang, M. Q. Le, J. F. Capsal, F. Ganet and P. J. Cottinet, *Mater. Des.*, 2017, **133**, 47–53.

206 H. Papa, M. Gaillard, L. Gonzalez and J. Chatterjee, *Biosensors*, 2014, **4**, 449–460.

207 J. Che, P. Chen and M. B. Chan-Park, *J. Mater. Chem. A*, 2013, **1**, 4057–4066.

208 U. Vohrer, I. Kolaric, M. H. Haque, S. Roth and U. Detlaff-Weglikowska, *Carbon N. Y.*, 2004, **42**, 1159–1164.

209 X. Yang, J. Lee, L. Yuan, S. R. Chae, V. K. Peterson, A. I. Minett, Y. Yin and A. T. Harris, *Carbon N. Y.*, 2013, **59**, 160–166.

210 L. F. Dumée, K. Sears, J. Schütz, N. Finn, C. Huynh, S. Hawkins, M. Duke and S. Gray, *J. Memb. Sci.*, 2010, **351**, 36–43.

211 A. Lee, S. Beak, S. Lee, G. Kim, D. chul Lee, S. Kim, Y. Sung and H. Jeong, *Diam. Relat. Mater.*, 2020, **110**, 108152.

212 A. Alshahrani, A. Alharbi, S. Alnasser, M. Almihdar, M. Alsuhybani and B. AlOtaibi, *Sep. Purif. Technol.*, 2021, **276**, 119300.

213 A. S. Brady-Estévez, S. Kang and M. Elimelech, *Small*, 2008, **4**, 481–484.

214 L. J. Sweetman, L. Nghiem, I. Chironi, G. Triani, M. In Het Panhuis and S. F. Ralph, *J. Mater. Chem.*, 2012, **22**, 13800–13810.

215 L. Sweetman, *University Of Wollongong Thesis Collection 1954-2016*, 2012.

216 J. Boge, L. J. Sweetman, M. In Het Panhuis and S. F. Ralph, *J. Mater. Chem.*, 2009, **19**, 9131–9140.

217 J. Dechnik, J. Gascon, C. J. Doonan, C. Janiak and C. J. Sumby, *Angew. Chemie - Int. Ed.*, 2017,

56, 9292–9310.

218 L. M. Robeson, *J. Memb. Sci.*, 2008, **320**, 390–400.

219 D. R. Paul and D. R. Kemp, *J. Polym. Sci. Polym. Symp.*, 1973, **93**, 79–93.

220 Y. Cheng, Y. Ying, S. Japip, S. D. Jiang, T. S. Chung, S. Zhang and D. Zhao, *Adv. Mater.*, 2018, **30**, 1–20.

221 S. L. Hou, J. Dong, X. L. Jiang, Z. H. Jiao and B. Zhao, *Angew. Chemie - Int. Ed.*, 2019, **58**, 577–581.

222 D. Alezi, Y. Belmabkhout, M. Suyetin, P. M. Bhatt, L. J. Weseliński, V. Solovyeva, K. Adil, I. Spanopoulos, P. N. Trikalitis, A. H. Emwas and M. Eddaoudi, *J. Am. Chem. Soc.*, 2015, **137**, 13308–13318.

223 J. Della Rocca, D. Liu and W. Lin, *Acc. Chem. Res.*, 2011, **44**, 957–968.

224 C. Crivello, S. Sevim, O. Graniel, C. Franco, S. Pane, J. Puigmarti-Luis and D. Munoz-Rojas, *Mater. Horizons*, 2021, **8**, 168–178.

225 C. H. Kang, Y. F. Lin, Y. S. Huang, K. L. Tung, K. S. Chang, J. T. Chen, W. S. Hung, K. R. Lee and J. Y. Lai, *J. Memb. Sci.*, 2013, **438**, 105–111.

226 M. Etxeberria-Benavides, O. David, T. Johnson, M. M. Łozińska, A. Orsi, P. A. Wright, S. Mastel, R. Hillenbrand, F. Kapteijn and J. Gascon, *J. Memb. Sci.*, 2018, **550**, 198–207.

227 J. Gao, H. Mao, H. Jin, C. Chen, A. Feldhoff and Y. Li, *Microporous Mesoporous Mater.*, 2020, **297**, 110030.

228 S. Xu, H. Zhang, F. Yu, X. Zhao and Y. Wang, *Sep. Purif. Technol.*, 2018, **206**, 80–89.

229 J. H. Cavka, S. Jakobsen, U. Olsbye, N. Guillou, C. Lamberti, S. Bordiga and K. P. Lillerud, *J. Am. Chem. Soc.*, 2008, **130**, 13850–13851.

230 D. Jiang, G. Fang, Y. Tong, X. Wu, Y. Wang, D. Hong, W. Leng, Z. Liang, P. Tu, L. Liu, K. Xu, J. Ni and X. Li, *ACS Catal.*, 2018, **8**, 11973–11978.

231 B. M. Jarai, Z. Stillman, L. Attia, G. E. Decker, E. D. Bloch and C. A. Fromen, *ACS Appl. Mater. Interfaces*, 2020, **12**, 38989–39004.

232 N. W. Ockwig, A. P. Co, M. O. Keeffe, A. J. Matzger and O. M. Yaghi, *Science (80-.).*, 2005, **310**, 1166–1171.

233 C. R. Deblase and W. R. Dichtel, *Macromolecules*, 2016, **49**, 5297–5305.

234 P. Küsgens, M. Rose, I. Senkovska, H. Fröde, A. Henschel, S. Siegle and S. Kaskel, *Microporous Mesoporous Mater.*, 2009, **120**, 325–330.

235 M. Baghbanzadeh, D. Rana, C. Q. Lan and T. Matsuura, *Sep. Purif. Rev.*, 2016, **45**, 141–167.

236 Y. Zhao, B. T. Jung, L. Ansaloni and W. S. W. Ho, *J. Memb. Sci.*, 2014, **459**, 233–243.

237 A. F. Ismail, P. S. Goh, S. M. Sanip and M. Aziz, *Sep. Purif. Technol.*, 2009, **70**, 12–26.

238 M. Hossein, D. Abadi, D. Hua and T. Chung, *J. Memb. Sci.*, 2018, **548**, 319–331.

239 Y. Shen, H. Wang, J. Liu and Y. Zhang, *ACS Sustain. Chem. Eng.*, 2015, **3**, 1819–1829.

240 R. Mukherjee, P. Bhunia and S. De, *Chem. Eng. J.*, 2016, **292**, 284–297.

241 H. P. Ngang, B. S. Ooi, A. L. Ahmad and S. O. Lai, *Chem. Eng. J.*, 2012, **197**, 359–367.

242 V. Vatanpour, S. Siavash, A. Reza, E. Salehi, S. Zinadini and H. Ahmadi, *Desalination*, 2012, **292**, 19–29.

243 M. S. Jyothi, V. Nayak, M. Padaki, R. G. Balakrishna and A. F. Ismail, *Desalination*, 2014, **354**, 189–199.

244 O. Agboola, J. Maree and R. Mbaya, *Environ. Chem. Lett.*, 2014, **12**, 241–255.

245 W. J. Lau, A. F. Ismail, P. S. Goh, N. Hilal and B. S. Ooi, *Sep. Purif. Rev.*, 2015, **44**, 135–156.

246 A. Bonilla-Petriciolet, D. I. Mendoza-Castillo and H. E. Reynel-Ávila, *Adsorption processes for water treatment and purification*, Springer International Publishing, 2017.

247 C. H. Giles, T. H. MacEwan, S. N. Nakhwa and D. Smith, *J. Chem. Soc.*, 1960, 3973–3993.

248 I. Langmuir, *J. Am. Chem. Soc.*, 1918, **40**, 1361–1403.

249 S. Brunauer, P. H. Emmett and E. Teller, *J. Am. Chem. Soc.*, 1938, **60**, 309–319.

250 D. M. Ruthven, *Principles of Adsorption and Adsorption Processes*, Wiley, 1984.

251 R. Leyva-Ramos and C. J. Geankoplis, *Chem. Eng. Sci.*, 1985, **40**, 799–807.

252 H. Qiu, L. Lv, B. C. Pan, Q. J. Zhang, W. M. Zhang and Q. X. Zhang, *J. Zhejiang Univ. Sci. A*, 2009, **10**, 716–724.

253 S. Lagergren, in *Kungliga Svenska Vetenskapsakademiens Handlingar*, 1898, pp. 1–39.

254 J. Zeldowitsch, *Acta Physicochim URSS*, 1934, **1**, 364.

255 V. Kumar, S. K. Dwivedi and S. Oh, *J. Water Process Eng.*, 2022, **45**, 102518.

256 J. P. Vareda, A. J. M. Valente and L. Durães, *J. Environ. Manage.*, 2019, **246**, 101–118.

257 D. Rusiecka, M. Gledhill, A. Milne, E. P. Achterberg, A. L. Annett, S. Atkinson, A. Birchill, J. Karstensen, M. Lohan, C. Mariez, R. Middag, J. M. Rolison, T. Tanhua, S. Ussher and D. Connelly, *Geophys. Res. Lett.*, 2018, **45**, 2734–2743.

258 A. Srivastava, N. A. Siddiqui, R. K. Koshe and V. K. Singh, in *Advances in Health and Environment Safety*, eds. N. Siddiqui, S. Tauseef and K. Bansal, Springer, Singapore, 2018, pp. 279–296.

259 B. F. Swaringen, E. Gawlik, G. D. Kamenov, N. E. McTigue, D. A. Cornwell and J. C. J. Bonzongo, *Environ. Res.*, 2022, **204**, 112025.

260 J. Clausen and S. C. Rastogi, *Br. J. Ind. Med.*, 1977, **34**, 208–215.

261 R. M. Harrison and R. Perry, *Atmos. Environ.*, 1977, **11**, 847–852.

262 K. J. Pieper, R. Martin, M. Tang, L. Walters, J. Parks, S. Roy, C. Devine and M. A. Edwards, *Environ. Sci. Technol.*, 2018, **52**, 8124–8132.

263 A. L. Wani, A. Ara and J. A. Usmani, *Interdiscip. Toxicol.*, 2016, **8**, 55–64.

264 G. Pinon-Lataillade, A. Thoreux-Manlay, H. Coffigny, G. Monchaux, R. Masse and J.-C. Soufir, *Hum. \& Exp. Toxicol.*, 1993, **12**, 165–172.

265 EPA, *EPA Enforcement Actions Help Protect Vulnerable Communities from Lead-Based Paint Health Hazards,* 2017.

266 Y. Xie and D. E. Giammar, *Water Res.*, 2011, **45**, 6525–6534.

267 P. Hore, K. Alex-Oni, S. Sedlar and D. Nagin, *J. Public Heal. Manag. Pract.*, 2019, **25**, S63–S70.

268 J. Sun, L. Wu and Y. Li, *J. Taiwan Inst. Chem. Eng.*, 2017, **78**, 219–229.

269 S. Koushkbaghi, A. Zakialamdari, M. Pishnamazi, H. F. Ramandi, M. Aliabadi and M. Irani, *Chem. Eng. J.*, 2018, **337**, 169–182.

270 J. E. Efome, D. Rana, T. Matsuura and C. Q. Lan, *Chem. Eng. J.*, 2018, **352**, 737–744.

271 N. Ghaemi, S. Zereshki and S. Heidari, *Process Saf. Environ. Prot.*, 2017, **111**, 475–490.

272 Y. Li, D. Han, S. Han, X. Zhu, L. Hu, Z. Zhang and Y. Liu, *Int. J. Hydrogen Energy*, 2009, **34**, 1399–1404.

273 P. C. Dent, *J. Appl. Phys.*, 2012, **111**, 1–7.

274 D. Natarajan, Z. Ye, L. Wang, L. Ge and J. L. Pathak, *Rare earth smart nanomaterials for bone tissue engineering and implantology: Advances, challenges, and prospects*, 2022, vol. 7.

275 A. R. Jha, *Rare Earth Materials: Properties and Applications*, CRC Press, 2014.

276 A. Shahbaz, *Miner. Eng.*, 2022, **184**, 107632.

277 A. Bashiri, A. Nikzad, R. Maleki, M. Asadnia and A. Razmjou, *Membranes*, 2022, **12**, 1–23.

278 Q. Chen, X. Ma, X. Zhang, Y. Liu and M. Yu, *J. Rare Earths*, 2018, **36**, 1190–1197.

279 C. F. Croft, M. I. G. S. Almeida, R. W. Cattrall and S. D. Kolev, *J. Memb. Sci.*, 2018, **545**, 259–265.

280 Y. Wang, L. Chen, Y. Yan, J. Chen, J. Dai and X. Dai, *J. Memb. Sci.*, 2020, **610**, 118263.

281 D. Comandella, W. Bonani, J. B. Ciscar, J. Ponti, M. Cologna, K. Popa and D. Gilliland, *RSC Adv.*, 2021, **11**, 19351–19362.

282 Y. Sun, D. Shao, C. Chen, S. Yang and X. Wang, *Environ. Sci. Technol.*, 2013, **47**, 9904–9910.

283 K. Li, Q. Gao, G. Yadavalli, X. Shen, H. Lei, B. Han, K. Xia and C. Zhou, *ACS Appl. Mater. Interfaces*, 2015, **7**, 21047–21055.

284 K. Brune and P. Patrignani, *J. Pain Res.*, 2015, **8**, 105–118.

285 N. Y. Mlunguza, S. Ncube, P. Nokwethemba Mahlambi, L. Chimuka and L. M. Madikizela, *J. Environ. Chem. Eng.*, 2019, **7**, 103142.

286 A. E. B. Kermia, D. Fouial-Djebbar and M. Trari, *Comptes Rendus Chim.*, 2016, **19**, 963–970.

287 E. Carmona, V. Andreu and Y. Picó, *Sci. Total Environ.*, 2014, **484**, 53–63.

288 A. Eslami, M. M. Amini, A. R. Yazdanbakhsh, N. Rastkari, A. Mohseni-Bandpei, S. Nasseri, E. Piroti and A. Asadi, *Environ. Monit. Assess.*, 2015, **187**, 1–15.

289 J. Gao, J. Huang, W. Chen, B. Wang, Y. Wang, S. Deng and G. Yu, *Front. Environ. Sci. Eng.*, 2016, **10**, 491–501.

290 M. Taheran, M. Naghdi, S. K. Brar, E. J. Knystautas, M. Verma and R. Y. Surampalli, *ACS Sustain. Chem. Eng.*, 2017, **5**, 10430–10438.

291 A. Ikhlaq, D. R. Brown and B. Kasprzyk-Hordern, *Appl. Catal. B Environ.*, 2014, **154**–**155**, 110–122.

292 A. Kaur, A. Umar and S. K. Kansal, *Appl. Catal. A Gen.*, 2016, **510**, 134–155.

293 M. J. Ahmed, *J. Environ. Manage.*, 2017, **190**, 274–282.

294 L. A. Al-Khateeb, W. Hakami and M. A. Salam, *J. Mol. Liq.*, 2017, **241**, 733–741.

295 M. Zambianchi, M. Durso, A. Liscio, E. Treossi, C. Bettini, M. L. Capobianco, A. Aluigi, A. Kovtun, G. Ruani, F. Corticelli, M. Brucale, V. Palermo, M. L. Navacchia and M. Melucci, *Chem. Eng. J.*, 2017, **326**, 130–140.

296 L. M. Madikizela, N. T. Tavengwa and L. Chimuka, *J. Pharm. Biomed. Anal.*, 2018, **147**, 624–633.